Title

Searches for Electroweak Production of Compressed Supersymmetry in Events with Soft Leptons, Missing Transverse Momentum, and a Hard Jet in the ATLAS Detector

Author

Schier, Sheena Calie

Publication Date

2018

UNIVERSITY OF CALIFORNIA
SANTA CRUZ

SEARCHES FOR ELECTROWEAK PRODUCTION OF COMPRESSED SUPERSYMMETRY IN EVENTS WITH SOFT LEPTONS, MISSING TRANSVERSE MOMENTUM, AND A HARD JET IN THE ATLAS DETECTOR

A dissertation submitted in partial satisfaction of the
requirements for the degree of

DOCTOR OF PHILOSOPHY

in

PHYSICS

by

Sheena Calie Schier

June 2018

The Dissertation of Sheena Calie Schier
is approved:

Professor Abraham Seiden, Chair

Professor Jason Nielsen

Professor Michael Hance

Dean Tyrus Miller
Vice Provost and Dean of Graduate Studies

Table of Contents

List of Figures **vi**

List of Tables **xiv**

Abstract **xvi**

Dedication **xviii**

Acknowledgments **xix**

1 Introduction **1**

I Theoretical Motivation and Experimental Setup **5**

2 Theoretical Background and Motivation **6**
- 2.1 The Standard Model of Particle Physics 7
- 2.2 Shortcomings of the Standard Model 11
- 2.3 Supersymmetry 13
  - 2.3.1 Minimal Supersymmetric Model (MSSM) 14
  - 2.3.2 Phenomenology of Directly Produced Higgsinos and Sleptons in Compressed Scenarios 18

3 The LHC and The ATLAS Experiment **24**
- 3.1 The Large Hadron Collider Machine 24
- 3.2 The ATLAS Experiment 28
  - 3.2.1 Inner Tracking Detector 30
  - 3.2.2 Calorimeters 35
  - 3.2.3 Muon System 37
  - 3.2.4 Trigger System 38

II Method 39

4 Data Collection and Simulated Events 40
4.1 Data . . . 40
4.2 Simulated Signal Samples . . . 42
4.3 Simulated SM Background Samples . . . 48

5 Physics Object Reconstruction and Identification 51
5.1 The Building Blocks . . . 52
5.2 Particle Identification and Reconstruction . . . 55
5.3 Special Treatment of Reconstructed Objects . . . 62

6 Signal Region Optimization 68
6.1 Discriminating Variables . . . 69
6.2 Signal Region Definitions . . . 72
6.2.1 Common Preselection . . . 73
6.2.2 Model-Specific Signal Regions . . . 79
6.2.3 SR Acceptance and Efficiency . . . 84

7 Background Estimation 87
7.1 Summary of estimation strategy . . . 87
7.2 Irreducible Backgrounds . . . 90
7.2.1 Top Control Region (CR-top) . . . 91
7.2.2 Ditau Control Region (CR-tau) . . . 94
7.2.3 Diboson Validation Region (VR-VV) . . . 97
7.2.4 Different Flavor Validation Regions (VR-DF) . . . 97
7.3 Drell-Yan Background . . . 100

8 Fake Factor Method 102
8.1 Introduction . . . 102
8.2 Description of Fake Factor Method . . . 104
8.3 Fake Factor Method Applied to Low-p_{T} Di-lepton Events . . . 107
8.3.1 ID & Anti-ID Lepton Definitions . . . 108
8.3.2 Fake Factor Measurement . . . 115
8.4 Same-Sign Validation Regions (VR-SS) . . . 133

III Analysis and Results 136

9 Systematic Uncertianties 137
9.1 Experimental Uncertainties . . . 138
9.1.1 CP Group Uncertainties . . . 138
9.1.2 Fake Factor Uncertainties . . . 139
9.2 Theoretical Uncertainties . . . 142

9.2.1 Uncertainty on Simulated Signal Events 142
9.2.2 Uncertainty on Simulated Background Events 142

10 Statistical Analysis **147**
10.1 Test Statistics and p-values 148
10.2 Fit Stategies 151
10.3 Nuisance Parameter Pulls 152

11 Results **155**
11.1 Background-Only Fit 155
11.2 Model-Independent Upper Limits on New Physics 159
11.3 Model Dependent Sensitivity with Shape Fit 161

12 Interpretations **165**
12.1 Compressed Higgsino 166
12.2 Compressed Wino 166
12.3 Compressed Slepton 169

13 Conclusion **171**

Bibliography **176**

A Signal Acceptance and Efficiency **186**
A.1 Acceptance 186
A.1.1 Efficiency 193
A.1.2 Efficiency within Acceptance 199
A.1.3 Signal Leakage 205
A.1.4 Acceptance*Efficiency 211

B Trial invisible mass m_χ in $m_{\mathbf{T2}}^{m_\chi}$ **217**

List of Figures

2.1 Schematic of supersymmetry particle spectrum 14
2.2 Feynman diagram of direct Higgsino production (left), and schematic of electroweakino mass spectrum (right) 18
2.3 Feynman diagram of direct slepton production (left) and schematic of electroweakino and slepton mass spectrum 19
2.4 SUSY cross-sections in LHC pp collisions [25] 20
2.5 Feynman diagram of direct Higgsino production in one compressed scenario. Red arrows point out features like the soft leptons from the off-shell Z boson decay, or the ISR jet boosting the system, increasing the $E_{\mathrm{T}}^{\mathrm{miss}}$, and forcing a large angular separation between the jet and $E_{\mathrm{T}}^{\mathrm{miss}}$. 22

3.1 Schematic of the LHC layout [23] 26
3.2 Cut-away view of the complete ATLAS Detector [60] 30
3.3 Layout of the ALTAS Inner Detector 31
3.4 Layout of the ALTAS Inner Detector 32
3.5 ATLAS simulation of material in the Pixel and SCT detectors in terms of the differential radiation length projected on the $r - z$ plane [4]. . . . 34
3.6 Picture of the ATLAS Calorimeters 35

4.1 Cumulative luminosity versus time delivered to (green) and recorded by (yellow) ATLAS during stable beams for *pp* collisions at 13 TeV in 2015 (left) and 2016 (right). 41
4.2 Cross-sections for electroweakino $\tilde{\chi}$ and slepton $\tilde{\ell}$ pair production in LHC pp collisions at $\sqrt{s} = 13$TeV from LHC SUSY Cross-sections Working Group and Refs. [40, 41]. Total cross-sections are exhibited according to production process, with electroweakinos labelled as either being wino $\tilde{W}$ or Higgsino $\tilde{H}$ and slepton by their right- and left-handed chirality. . . . 43
4.3 Kinematics distributions in electroweakino signal samples, with decays simulated with MadSpin and parton showing performed by PYTHIA v8.186. 47

5.1 Sketch of ATLAS tracking parameters at the perigee in the $x-y$ plane (left) and the $r-z$ plane (right) [55]. In this diagram, the $r-z$ plane is denoted as $R-z$. 54
5.2 Schematic of an electron's flight in the ATLAS [73] 55
5.3 Electron efficiency as a function of η (left) and E_{T} (right) in the *Loose*, *Medium*, and *Tight* LH identification algorithms 57
5.4 Reconstruction efficiency for *Medium* muon identification working point as a function of muon p_{T}, in the region $0.1 < |\eta| < 2.5$ [8]. 58
5.5 Signal lepton efficiencies for electrons and muons, averaged over all Higgsino and slepton samples. Efficiencies are shown for leptons within detector acceptance, and with lepton p_{T} within a factor of 3 of $\Delta\ m(\tilde{l}\tilde{\chi}_1^0)$ for slepton samples or within a factor of 3 of $\Delta\ m(\tilde{\chi}_2^0\tilde{\chi}_1^0)/2$ for Higgsino samples. Uncertainty bands represent the range of efficiencies observed across all signal samples for the given p_{T} bin. The η dependence is consistent with values reported in ATLAS combined performance papers, shown in Figures 5.3 and 5.4. 60
5.6 Dilepton Δ R distribution before LepIsoCorrection (top) and after LepIsoCorrection (bottom) for the ee-channel (left) and $\mu\mu$-channel (right), using electroweakino signal samples with $\mathrm{m}(\tilde{\chi}_2^0, \tilde{\chi}_1^0) = (110, 100)\mathrm{GeV}$. . . 65
5.7 Dilepton invariant mass distribution before LepIsoCorrection (top) and after LepIsoCorrection (bottom) for the ee-channel (left) and $\mu\mu$-channel (right), using electroweakino signal samples with $\mathrm{m}(\tilde{\chi}_2^0\tilde{\chi}_1^0)$ $(110, 100)\mathrm{GeV}$. 66
5.8 Impact of the `NearbyLepIsoCorrection` tool on the efficiency of low-mass dilepton pairs in data. The data are shown in a region with $\Delta\phi(E_{\mathrm{T}}^{\mathrm{miss}}, p_t^{j1}) <$ 1.5 to avoid the signal region. Events are triggered with the inclusive-$E_{\mathrm{T}}^{\mathrm{miss}}$ trigger. The red trend shows events with two baseline leptons without applying any isolation; the green shows the impact of applying `GradientLoose` isolation; the blue shows the result of the `NearbyLepIsoCorrection` applied to the `GradientLoose` sample. 67

6.1 Schematic illustrating the fully leptonic $(Z \to \tau\tau)$ + jets system motivating the construction of $m_{\tau\tau}$. 71
6.2 Leading lepton p_{T}, subleading lepton p_{T}, and $\Delta R_{\ell\ell}$ distributions after the background-only fit with all common preselection cuts applied. The category 'Others' contains rare backgrounds from triboson, Higgs boson, and three or four top-quark production processes. The first (last) bin includes underflow (overflow). Benchmark Higgsino $\tilde{H}$ and slepton $\tilde{\ell}$ signals are overlaid as dashed lines. Orange arrows in the Data/SM panel indicate values that are beyond the y-axis range. 75

6.3 Distributions of $E_{\mathrm{T}}^{\mathrm{miss}}$, $p_{\mathrm{T}}(j_1)$, and $\Delta\phi(j_1), p_{\mathrm{T}}^{\mathrm{miss}}$ after the background-only fit with all common preselection cuts applied. Blue arrows in the upper panel denote the final requirement used to define the common SR, otherwise all selections are applied. The category 'Others' contains rare backgrounds from triboson, Higgs boson, and three or four top-quark production processes. The first (last) bin includes underflow (overflow). Benchmark Higgsino $\tilde{H}$ and slepton $\tilde{\ell}$ signals are overlaid as dashed lines. Orange arrows in the Data/SM panel indicate values that are beyond the y-axis range. 77
6.4 Distributions of $\min\Delta\phi(jets, p_{\mathrm{T}}^{\mathrm{miss}})$, number of b-jets, and $m_{\tau\tau}$ after the background-only fit with all common preselection cuts applied. Blue arrows in the upper panel denote the final requirement used to define the common SR, otherwise all selections are applied. The category 'Others' contains rare backgrounds from triboson, Higgs boson, and three or four top-quark production processes. The first (last) bin includes underflow (overflow). Benchmark Higgsino $\tilde{H}$ and slepton $\tilde{\ell}$ signals are overlaid as dashed lines. 78
6.5 Feynman diagram of direct Higgsino (left), and direct slepton (right) production. 80
6.6 Distributions after the background-only fit of kinematic variables used to define selections common to all signal regions, i.e. not including requirements specific to the electroweakino or slepton SR definitions. Benchmark Higgsino $\tilde{H}$ and slepton $\tilde{\ell}$ signals are overlaid as dashed lines. Orange arrows in the Data/SM panel indicate values that are beyond the y-axis range. 81
6.7 Distributions of $E_{\mathrm{T}}^{\mathrm{miss}}/H_{\mathrm{T}}^{\mathrm{lep}}$ for the Higgsino (left) and slepton (right) selections, after applying all signal region cuts except those on the $E_{\mathrm{T}}^{\mathrm{miss}}/H_{\mathrm{T}}^{\mathrm{lep}}$, $m_{\ell\ell}$, or m_{T2}^{100}. The red solid line indicates the cut applied in the signal region; events in the region below the red line are rejected. 82
6.8 Signal acceptance (left) and efficiency (right) for electroweakino $\tilde{\chi}_2^0$, $\tilde{\chi}_1^0$ production in the most inclusive Higgsino signal region SR-$m_{\ell\ell}$ $[1, 60]$GeV (top) and for slepton pair production in the most inclusive slepton signal region SR-m_{T2}^{100} $[100, \infty]$GeV (bottom) 86

7.1 CR-top $ee + \mu\mu + e\mu + \mu e$ channel, pre-fit distributions. 92
7.2 CR-top $ee + \mu\mu + e\mu + \mu e$ channel, pre-fit distributions. 93
7.3 CR-tau $ee + \mu\mu + e\mu + \mu e$ channel, pre-fit distributions. 95
7.4 CR-tau $ee + \mu\mu + e\mu + \mu e$ channel, pre-fit distributions. 96
7.5 VR-VV $ee + \mu\mu + e\mu + \mu e$ channel, pre-fit distributions. 98
7.6 VR-VV $ee + \mu\mu + e\mu + \mu e$ channel, pre-fit distributions. 99
7.7 Data events passing inclusive $E_{\mathrm{T}}^{\mathrm{miss}}$ triggers with opposite sign baseline leptons in the dilepton invariant mass $m_{\ell\ell}$ spectrum. The $\Delta\phi(j_1, \mathbf{p}_{\mathrm{T}}^{\mathrm{miss}})$ variable is inverted to ensure this is orthogonal to the signal region. . . 101

8.1 Cross-section of $W(\rightarrow \ell\nu)$+jets binned in exclusive jet-multiplicity [7] (left), and SUSY cross-sections [25] (right) in LHC pp collisions 104
8.2 Schematic illustrating the fake factor method to estimate the fake lepton contribution in the signal region. 106
8.3 Fake electron composition as a function of electron p_{T} (top left), electron η (top right), m_{T}, (bottom left) and $E_{\mathrm{T}}^{\mathrm{miss}}$ (bottom right). All distributions correspond to events in the m_{T} measurement region, except the m_{T} distribution itself. 110
8.4 Anti-ID muon composition in events with exactly zero b-jets(left) and one or more b-jets(right) as a function of m_{T}, $E_{\mathrm{T}}^{\mathrm{miss}}$, muon p_{T}, and muon η. All but the m_{T} distribution correspond to events with $m_{\mathrm{T}} < 40$GeV. . . 114
8.5 The ID electron (left) and anti-ID electron (right) p_{T} distributions for pre-scaled single-lepton-trigger, normalized to 1 pb^{-1}. Blue curve: 5 GeV trigger threshold, red curve: 10 GeV threshold, magenta curve: 15 GeV threshold, green curve: 20 GeV threshold. 116
8.6 The $E_{\mathrm{T}}^{\mathrm{miss}}$ distributions for ID (left) and anti-ID (right) electrons in FF sample. MC is rescaled to match data in the $E_{\mathrm{T}}^{\mathrm{miss}} > 200$GeV region. . . 117
8.7 $\mathrm{m_T}$ distributions for ID (left) and anti-ID (right) electrons in the FF sample. MC has been scaled to the data in the $E_{\mathrm{T}}^{\mathrm{miss}} > 200$GeV region. 118
8.8 p_{T} distributions of ID (left) and anti-ID (right) electrons in FF sample for events with $m_{\mathrm{T}} < 40$GeV. MC has been rescaled to match data for $E_{\mathrm{T}}^{\mathrm{miss}} > 200$GeV. 119
8.9 Electron fake factors *before* requiring a jet with $p_{\mathrm{T}} > 100$GeV, as a function of electron p_{T} (left) and leading jet p_{T} (right). The average electron fake factor over all p_{T} is 0.267. 120
8.10 Electron fake factors as a function of electron p_{T} in the measurement region $m_{\mathrm{T}} < 40$GeV and leading jet $p_{\mathrm{T}} > 100$GeV. Fake factors for electron p_{T} $4.5-5$GeV are taken to be the same as electron p_{T} $5-6$GeV. A red line marks the average electron fake factor over all electron p_{T}; 0.211. 121
8.11 Electron fake factors binned in alternative kinematic variable in the measurement region $m_{\mathrm{T}} < 40$GeV and leading jet $p_{\mathrm{T}} > 100$GeV. A red line marks the average electron fake factor over all electron p_{T}. 122
8.12 Relative uncertainties on electron fake factors binned in electron p_{T}. . . 123
8.13 The ID (left) and anti-ID (right) muon p_{T} distributions for pre-scaled single-muon triggers, normalized to 1 pb^{-1}. Blue curve: 4 GeV trigger threshold, red curve: 10 GeV threshold, magenta curve: 14 GeV threshold, green curve: 18 GeV trigger threshold. 124
8.14 The $E_{\mathrm{T}}^{\mathrm{miss}}$ distributions for ID (left) and anti-ID (right) muons in muon FF samples for events with exactly zero b-jets (top), and events with at least one b-jet (bottom). MC is scaled to match the data in the region $E_{\mathrm{T}}^{\mathrm{miss}} > 200$GeV. 125

8.15 The m_{T} distributions for ID (left) and anti-ID (right) muons in muon FF samples for events with exactly zero b-jets (top), and events with one or more b-jets (bottom). MC is scaled to the data in the region $E_{\mathrm{T}}^{\mathrm{miss}} > 200$GeV. 126
8.16 ID (left) and anti-ID (right) muon p_{T} in the fake factor measurement region $m_{\mathrm{T}} < 40$GeV for events with exactly zero b-jets (top), and events with one or more b-jets (bottom). MC has been rescaled to the data in the region $E_{\mathrm{T}}^{\mathrm{miss}} > 200$GeV. 127
8.17 Muon fake factors *before* requiring a hard jet of $p_{\mathrm{T}} > 100$GeV, computed from muon FF samples as a function of muon p_{T} (top-left), as a function of leading jet p_{T} (top-right), and as a function of b-jet multiplicity (bottom). A red line marks the average muon fake factor over all muon p_{T}.128
8.18 Muon fake factors as a function of muon p_{T} in events with exactly zero b-jets (left) and one or more b-jets (right). A red line denotes the average muon fake factor over all muon p_{T}. 130
8.19 Muon fake factors as a function of muon η in events with exactly zero b-jets (left) and one or more b-jets (right). 130
8.20 Muon fake factors as a function of $\Delta\phi_{jet-E_{\mathrm{T}}^{\mathrm{miss}}}$ in events with exactly zero b-jets (left) and one or more b-jets (right). 131
8.21 Muon fake factors as a function of the jet multiplicity in events with exactly zero b-jets (left) and one or more b-jets (right). 131
8.22 Muon fake factors as a function of the average number of interactions per bunch crossing in events with exactly zero b-jets (left) and one or more b-jets (right). 132
8.23 Muon fake factors as a function of the number of primary vertices in events with exactly zero b-jets (left) and one or more b-jets (right). . . . 132
8.24 Relative uncertainties on muon fake factors versus muon p_{T} in zero b-jets bin (left) and one or more b-jets bin (right). 133
8.25 Fake lepton composition as a function of subleading lepton p_T, with and without prompt (“Isolated” plus “lep→gamma→lep”) leptons, for opposite sign muon pairs in the signal region. Top left: SR iso, top right: SR no iso, bottom left: ssSR iso, bottom right: ssSR no iso. 134
8.26 Distributions after the background-only fit for the same-sign validation regions, where the subleading lepton is either the electron $ee + \mu e$ (top) or muon $\mu\mu + e\mu$ (bottom). The category “Others” contains rare backgrounds from triboson, Higgs boson, and the multi-top processes. The last bin includes overflow. 135

9.1 QCD scale, α_s and PDF uncertainties on the shape and normalization of the diboson background in the Higgsino (left) and slepton (right) signal regions, but with no lepton flavor requirement. 144

9.2 QCD scale, α_s and PDF uncertainties on the shape and normalization of the $Z \to \tau\tau$ background in the Higgsino (left) and slepton (right) signal regions, but with no lepton flavor requirement. 145
9.3 QCD scale and PDF uncertainties on the shape and normalization of the $t\bar{t}$ background in the Higgsino (left) and slepton (right) signal regions, but with no lepton flavor requirement. 146

10.1 Fit parameters for background-only fit in various configurations of the regions allowed to be treated as constraining. 153
10.2 Ranking of systematics impact on μ_{signal} in the most inclusive Higgsino (left) and slepton (right) signal regions 154

11.1 Summary of Monte Carlo yields in control, validation and signal regions in a background-only fit using data only in the two CRs to constrain the fit. 156
11.2 Kinematic distributions of data and expected backgrounds after the background-only fit. Top left plot shows the sub-leading lepton p_{T} distribution in the different-flavor validation region VRDF-m_{T2}^{100}; the top right plot shows the m_{T2}^{100} distribution in the diboson validation region VR-VV (top right); the sub-leading lepton p_{T} distribution in the bottom right plot and the $m_{\ell\ell}$ distribution in the bottom left are shown in the same-sign validation region VR-SS inclusive of lepton flavor. Background processes containing fewer than two prompt leptons are categorized as “Fake/nonprompt.” The category “Others” contains rare backgrounds from triboson, Higgs boson, and multi-top processes. The last bin includes overflow. 157
11.3 Kinematic distributions after the background-only fit showing the data as well as the expected background in the most inclusive electroweakino SR$\ell\ell$-$m_{\ell\ell}$ $[1, 60]$ (top) and slepton m_{T2}^{100} $[100, \infty]$ (bottom) signal regions. The arrow in the $E_{\mathrm{T}}^{\mathrm{miss}}/H_T^{lep}$ variables indicates the minimum value of the requirement imposed in the final SR selection. The $m_{\ell\ell}$ and m_{T2}^{100} distributions (right) have all the SR requirements applied. Background processes containing fewer than two prompt leptons are categorized as “Fake/nonprompt.” The category “Others” contains rare backgrounds from triboson, Higgs boson, and multi-top processes. The last bin includes overflow. The dashed lines represent benchmark signal samples corresponding to the Higgsino $\widetilde{H}$ and slepton $\tilde{\ell}$ simplified models. Orange arrows in the Data/SM panel indicate values that are beyond the y-axis range. 158

11.4 Comparison of observed and expected event yields after the exclusion fit. Background processes containing fewer than two prompt leptons are categorized as "Fake/nonprompt." The category "Others" contains rare backgrounds from triboson, Higgs boson, and multi-top processes. Uncertainties in the background estimates include both the statistical and systematic uncertainties, where σ_{tot} denotes the total uncertainty. 164

12.1 Expected 95% CL exclusion sensitivity (blue dashed line) with $\pm 1\sigma_{\text{exp}}$ (yellow band) from experimental systematics and observed limits (red solid) with $\pm 1\sigma_{\text{theory}}$ (dotted red) from signal cross section uncertainties. A shape fit of Higgsino signals to the $m_{\ell\ell}$ spectrum is used to derive the limit is displayed in the $m(\tilde{\chi}_2^0) - m(\tilde{\chi}_1^0)$ vs $m(\tilde{\chi}_2^0)$ plane. The chargino $\tilde{\chi}_1^{\pm}$ mass is assumed to be half way between the two lightest neutralinos. The gray region denotes the lower chargino mass limit from LEP [13]. . 167
12.2 Expected 95% CL exclusion sensitivity (blue dashed line) with $\pm 1\sigma_{\text{exp}}$ (yellow band) from experimental systematic uncertainties and observed limits (red solid line) with $\pm 1\sigma_{\text{theory}}$ (dotted red line) from signal cross-section uncertainties for simplified models direct wino production. A shape fit of wino signals to the $m_{\ell\ell}$ spectrum is used to derive the limit is displayed in the $m(\tilde{\chi}_2^0) - m(\tilde{\chi}_1^0)$ vs $m(\tilde{\chi}_2^0)$ plane. The chargino $\tilde{\chi}_1^{\pm}$ mass is assumed equal to the $m(\tilde{\chi}_2^0)$ mass. The gray region denotes the lower chargino mass limit from LEP [13], and the blue region in the lower plot indicates the limit from the 2ℓ+3ℓ combination of ATLAS Run 1. 168
12.3 Expected 95% CL exclusion sensitivity (blue dashed line) with $\pm 1\sigma_{\text{exp}}$ (yellow band) from experimental systematics and observed limits (red solid) with $\pm 1\sigma_{\text{theory}}$ (dotted red) from signal cross section uncertainties. A shape fit of slepton signals to the m_{T2}^{100} spectrum is used to derive the limit projected into the $m(\tilde{\ell}) - m(\tilde{\chi}_1^0)$ vs $m(\tilde{\ell})$ plane. The slepton $\tilde{\ell}$ refers to a 4-fold mass degenerate system of left- and right-handed selectron and smuon. The gray region denotes a conservative right-handed smuon $\tilde{\mu}_R$ mass limit from LEP [13], while the blue region is the 4-fold mass degenerate slepton limit from ATLAS Run 1 [6]. 170

13.1 Summary plot for compressed electroweak searches, including combined LEP limits in grey. The ATLAS Run 2 disappearing track analysis, which targets mass-splittings $\mathcal{O}(1)$GeV, is shown in orange. The two-soft-lepton analysis described in this thesis is shown in light blue. 175

A.1 **Slepton**. 188
A.2 **N2N1**. 189
A.3 **N2C1p**. 190
A.4 **N2C1m**. 191
A.5 **C1C1**. 192
A.6 **Slepton Efficiency**. 194

A.7 **N2N1 Efficiency**. 195
A.8 **N2C1p Efficiency**. 196
A.9 **N2C1m Efficiency**. 197
A.10 **C1C1 Efficiency**. 198
A.11 **Slepton Efficiency within acceptance**. 200
A.12 **N2N1 Efficiency within acceptance**. 201
A.13 **N2C1p Efficiency within acceptance**. 202
A.14 **N2C1m Efficiency within acceptance**. 203
A.15 **C1C1 Efficiency with acceptance**. 204
A.16 **Slepton Signal Leakage**. 206
A.17 **N2N1 Signal Leakage**. 207
A.18 **N2C1p Signal Leakage**. 208
A.19 **N2C1m Signal Leakage**. 209
A.20 **C1C1 Signal Leakage**. 210
A.21 **Slepton Acceptance*Efficiency**. 212
A.22 **N2N1 Acceptance*Efficiency**. 213
A.23 **N2C1p Acceptance*Efficiency**. 214
A.24 **N2C1m Acceptance*Efficiency**. 215
A.25 **C1C1 Acceptance*Efficiency**. 216

B.1 m_{T2}^{0}. Using $E_{\mathrm{T}}^{\mathrm{miss}}/H_{\mathrm{T}}^{\mathrm{leptons}} > 5$. 220
B.2 m_{T2}^{25}. Using $E_{\mathrm{T}}^{\mathrm{miss}}/H_{\mathrm{T}}^{\mathrm{leptons}} > 5$. 221
B.3 m_{T2}^{50}. Using $E_{\mathrm{T}}^{\mathrm{miss}}/H_{\mathrm{T}}^{\mathrm{leptons}} > 5$. 222
B.4 m_{T2}^{75}. Using $E_{\mathrm{T}}^{\mathrm{miss}}/H_{\mathrm{T}}^{\mathrm{leptons}} > 5$. 223
B.5 m_{T2}^{100}. Using $E_{\mathrm{T}}^{\mathrm{miss}}/H_{\mathrm{T}}^{\mathrm{leptons}} > 5$. 224
B.6 m_{T2}^{120}. Using $E_{\mathrm{T}}^{\mathrm{miss}}/H_{\mathrm{T}}^{\mathrm{leptons}} > 5$. 225
B.7 m_{T2}^{150}. Using $E_{\mathrm{T}}^{\mathrm{miss}}/H_{\mathrm{T}}^{\mathrm{leptons}} > 5$. 226
B.8 m_{T2}^{175}. Using $E_{\mathrm{T}}^{\mathrm{miss}}/H_{\mathrm{T}}^{\mathrm{leptons}} > 5$. 227
B.9 m_{T2}^{200}. Using $E_{\mathrm{T}}^{\mathrm{miss}}/H_{\mathrm{T}}^{\mathrm{leptons}} > 5$. 228
B.10 m_{T2}^{250}. Using $E_{\mathrm{T}}^{\mathrm{miss}}/H_{\mathrm{T}}^{\mathrm{leptons}} > 5$. 229
B.11 m_{T2}^{300}. Using $E_{\mathrm{T}}^{\mathrm{miss}}/H_{\mathrm{T}}^{\mathrm{leptons}} > 5$. 230
B.14 m_{T2}^{200} shape fit. Using $E_{\mathrm{T}}^{\mathrm{miss}}/H_{\mathrm{T}}^{\mathrm{leptons}} > \mathrm{Max}\left(5, 15 - 2 \cdot \left[m_{\mathrm{T2}}^{200}/\ \mathrm{GeV} - 200\right]\right)$.233

List of Tables

2.1 Strong and EW boson spin, mass, $SU(3)_C$ and $SU(2)_L$ multiplet representations, and $U(1)_Y$ value. 10
2.2 Description of fermion mass, electric charge Q, $SU(3)_C$ and $SU(2)_L$ multiplet representations, and $U(1)_Y$ value. 11
2.3 SUSY MSSM spectrum in $SU(3)_C, SU(2)_L, U(1)_Y$ multiplet representation. 14

3.1 Luminosity parameters in Equation 3.3, corresponding to ATLAS peak luminosity $L \sim 10^{34}\mathrm{cm}^{-2}\mathrm{s}^{-1}$ 27

4.1 Evolution of lowest unprescaled $E_{\mathrm{T}}^{\mathrm{miss}}$ trigger threshold and corresponding total integrated luminosity from the start of 2015 to the end of 2016. All through 2015 the lowest unprescaled $E_{\mathrm{T}}^{\mathrm{miss}}$ trigger threshold was 70GeV, and it increased to 90GeV at the start of 2016. By July of 2016, the threshold rose to 110GeV. 42
4.2 Summary of the Monte Carlo generators used for each SM background sample production. 49

5.1 Summary of object definitions 61

6.1 Summary of common Higgsino and slepton SR cuts 73
6.2 Higgsino specific SR cuts and definitions. SR definitions are expressed as bins in $m_{\ell\ell}$. 83
6.3 Slepton specific signal region cuts 84

7.1 Background estimation summary 90

8.1 Pre-scaled single-lepton triggers from 2015+2016 used to compute lepton fake factors. 108
8.2 Summary of electron definitions. 109
8.3 Summary of muon definitions. 112
8.4 Single-Electron triggers and their corresponding p_{T} range. 116
8.5 ID and anti-ID normalization scale factors calculated in $E_{\mathrm{T}}^{\mathrm{miss}} > 200\mathrm{GeV}$.. 117

8.6 Single-muon triggers used for fake factor computation and their corresponding p_{T} range. 124
8.7 ID and anti-ID muon scale factors calculated in $E_{\mathrm{T}}^{\mathrm{miss}} > 200\mathrm{GeV}$ separated by muon definition and 125

11.1 Breakdown of yields and upper limits. 160
11.2 Observed event yields and exclusion fit results with the signal strength parameter set to zero for the exclusive electroweakino and slepton signal regions. Background processes containing fewer than two prompt leptons are categorized as "Fake/nonprompt." The category "Others" contains rare backgrounds from triboson, Higgs boson, and multi-top processes. Uncertainties in the fitted background estimates combine statistical and systematic uncertainties. 162
11.3 Observed event yields and exclusion fit results with the signal strength parameter set to zero for the exclusive electroweakino and slepton signal regions. Background processes containing fewer than two prompt leptons are categorized as "Fake/nonprompt." The category "Others" contains rare backgrounds from triboson, Higgs boson, and multi-top processes. Uncertainties in the fitted background estimates combine statistical and systematic uncertainties. 163

Abstract

Searches for Electroweak Production of Compressed Supersymmetry in Events with Soft Leptons, Missing Transverse Momentum, and a Hard Jet in the ATLAS Detector

by

Sheena Calie Schier

Supersymmetry (SUSY) is an extension of the Standard Model that predicts a boson (fermion) partner for each fermion (boson) in the Standard Model. Weak-scale SUSY is attractive for reasons like improving gauge coupling unification, reducing fine-tuning in the Higgs sector and providing a dark matter candidate. This thesis presents a dedicated search for direct production of new, colorless, weak-scale states with compressed mass spectra in final states characterized by soft visible decay products. This analysis uses pp collisions at $\sqrt{s} = 13$ TeV at the Large Hadron Collider and collected by the ATLAS experiment during 2015 and 2016 corresponding to 36.1 fb^{-1} of integrated luminosity. This analysis selects events with two soft electrons or muons, an intermediate amount of missing transverse momentum ($E_{\mathrm{T}}^{\mathrm{miss}}$), and a hard jet. Backgrounds with two prompt leptons are estimated with Monte Carlo simulation, while reducible backgrounds are estimated with a mix of Monte Carlo and data-driven methods. Results are consistent with Standard Model expectations and used to put limits on compressed supersymmetric states. Limits are extended on compressed electroweak SUSY model for the first time since the Large Electron Positron Collider (LEP).

To my father,

Lecil Charles Schier,

the person who taught me at the age of 7 that the grass in not green.

Acknowledgments

Many people made this academic journey possible, and while I think them all in my heart, I would like to name a few individually.

My parents, Bonnie and Charlie Schier, were the most influential people in my life growing up. They molded me into the person I am, by giving me the ultimate freedom to define myself and inspiring the courage to discover my own path through the conundrum of life.

Lastly, I want to thank my love, Mike Spooner. You were my light when the world ceased to exist.

Chapter 1

Introduction

Since the world's first particle accelerator went online in the 1930s at the Cavendish Laboratory, colliding protons against a fixed lithium target, particle collisions have been providing physicists with portals into the subatomic realm where quantum physics is the supreme ruler. Progressively, accelerators have become more and more powerful, and the depth at which physicists can peer into the atom, into the structure of neutrons and protons, and eventually into interactions of the most fundamental, has hastened. Today, we stand at the frontier of high energy physics experiments, with the Standard Model of Particle Physics in hand, a theory that could appear as a complete map of fundamental particles and interactions, to guide us through the sea of quantum possibilities, while astronomical observations, for one, give us the distinct sense that we are holding only a small slice of the key.

Another historic event in the 1930s was the first hint of dark matter in astronomical observation. J.H. Oort, the namesake of the Oort Cloud, measured the velocities of stars using their Doppler shifts. Surprisingly, the galactic mass that binds stars in their gravitational orbits should not be strong enough to overcome their velocities, and the stars should escape. It wasn't until 1973, that Vera Rubin, with her studies or galactic rotations [66, 65], actually opened the eyes of science to the alarming possibility of a new kind of matter, so different from the electrically interacting matter that makes our universe observable, that we call it "dark". Dark matter is now observed to be so abundant in the universe, we believe there is four times more of it than the matter that constitutes all the stars, planets, gas clouds, and anything else made of Standard Model particles [43]. But this extraordinary matter might not be completely dark. It might couple to the Standard Model extremely weakly, and when it does, we hope to be there to witness.

The European Organization for Nuclear Research, or Conseil Européen pour la Recherche Nuclèaire (CERN), began as an official scientific union between 12 European countries in 1954, when engineers started digging the first hole near Geneva, Switzerland, which marked the beginning of a new era of particle collisions. Experiments at CERN have been heroes in electroweak physics, with discoveries of the $W^{\pm}$ and Z^{0} bosons in 1983 at the Super Proton Synchrotron (SPS), and the discovery of what so far looks sufficiently like the Standard Model Higgs boson in 2012 at the Large Hadron Collider (LHC). Currently, the LHC is the largest and most powerful accelerator on Earth, colliding protons with a center-of-mass energy of 13 TeV. With this machine, we step into the energy scales of the early universe before thermal freeze-out, when the universe became too cold for dark matter production or any other interaction at the dark matter physics-scale. There is a chance the LHC will produce dark matter particles if they interact with the electroweak force. There is also the chance to produce a plethora of other particles that do not account for dark matter, but are motivated by predictive new physics models.

Some of these models predict a new symmetry, and with this new symmetry, a new particle paired to each Standard Model constituent. A generic extension of the SM that introduces a new weak multiplet would naturally have a similar structure as the W and Z bosons with nearly degenerate masses. If the lightest neutral weak particle is stable it may explain the abundance of dark matter in the universe. On the occasion that the candidate dark matter particle would produce an overabundance of dark matter, this can be mitigated by the coannihilation of dark matter with some other similar-mass state, as a way to dilute the DM abundance in the early universe. This requires semi-compressed spectra between the lightest neutral weak particle and the coannihilation states. If any of these particles exist, the LHC may be capable of producing them, but if their mass spectra are compressed, meaning the masses are within a few GeV of each other, the signatures of these events will be hard to resolve in a detector. It takes dedicated teams and a lot of strategy to do physics at the edge of detector limits.

This thesis presents a search for new compressed electroweak physics marked by soft, low-momentum leptons and a sufficient amount of energy deduced to have left the detector unseen. The analysis is broken into three parts. Part 1 will engage the theories that give context to this search and will also describe the LHC and the particle detector used for the experiment. Part 2 will describe all the work done in performing the analysis, and Part 3 will overview the uncertainties, results, and interpretations.

Enjoy.

Part I

Theoretical Motivation and Experimental Setup

Chapter 2

Theoretical Background and Motivation

To any curious mind staring into the starry deep late in the night, or gazing at pictures from the Hubble Space Telescope, the universe can seem deeply mysterious, as a vast space containing a rich spectrum of matter moving and transforming via some set of complex mechanisms. Although this mysterious sense of the universe rings true in the mind of even the most learned physics scholar, large leaps have been made in understanding the true nature of the matter and forces that make up the observable universe. In the last century, particle physicists have constructed a theory that incorporates all the directly observed fundamental particles and explains their existence and interactions in simplicity through field equations that describe the fundamental forces in the universe. This theory is called the Standard Model of Particle Physics (SM) and, apart from gravity being far too weak to be described by particle interactions [34], is internally complete in that every piece of the SM has been observed according to prediction.

But the story doesn't end here. There are reasons to think the accomplished Standard Model is a low-scale approximation of a much larger theory. Some reasons are philosophical in nature; we want to understand why the SM has its structure, or lack confidence in a theory that is so incredibly fine-tuned as the Standard Model. Other reasons come from observations that we can not be resolved with SM predictions, like the abundance of dark matter that drives massive galaxies to rotate contrary to predictive models accounting only for gravity and SM particles and forces.

The proceeding structure of this chapter is as follows: Section 2.1, summarizes the Standard Model of Particle Physics, and Section 2.2 reviews some of the shortcomings of the Standard Model. Supersymmetry is introduced in Section 2.3 as a suitable contender for physics beyond the Standard Model; and lastly, Section 2.3.2 describes the phenomenology of supersymmetric Higgsinos and sleptons in compressed scenarios.

2.1 The Standard Model of Particle Physics

The Standard Model of Particle Physics provides a quantum description of three of the four known fundamental forces; the electromagnetic force, the strong force, and the weak force. It leaves out the gravitational force because the strength of gravitational interactions is several orders of magnitude lower than the other three forces, which leads to intrinsic incompatibilities in a description of quantum gravitational interactions at energies below the Planck scale, $M_P \approx 10^{19}$ GeV. The SM was pieced together throughout the second half of the twentieth century by several progressive discoveries, and we now know that the fundamental components of nature separate into two distinct categories: fermions and bosons. These two types of particles are characterized by their spin, and ultimately play completely different roles in the state and phenomena of the universe. [74]

The main ingredients of the Standard Model are a set of Dirac fermion fields having specific muliplet representations in group theory given by the $SU(3)_C \times SU(2)_L \times U(1)_Y$ gauge group. In SM quantum field theory (QFT), called the "Yang Mills theory" [79], fermion interactions are mediated by gauge bosons.

Gauge invariance in QFT demands the existence of gauge boson fields, which occur in two independent sectors: the electroweak sector, described by quantum electroweak dynamics (QED), and the strong sector, described by quantum chromodynamics (QCD). Glashow, Salam, and Weinberg first presented the structure for the electroweak model in the 1960's [44, 68, 77]. The $SU(2)_L \otimes U(1)_Y$ symmetry of quantum flavor dynamics (QFD) produces the photon γ and the massive bosons, $W^{\pm}$ and Z^0. $U(1)_Y$ is a mathematical group described by unitary 1×1 matrices generated by weak-hypercharge symmetry Y, defined as

$$Y = 2(Q - T_3) \tag{2.1}$$

, where Q is the electromagnetic charge, and T_3 is the z-component of the weak isospin[1]. This symmetry produces the B^0 gauge boson. Similarly, $SU(2)_L$ represents a group of unitary 2×2 matrices with determinant 1. These are generated by a left-handed chiral

---

[1] Weak isospin is the charge associated with the $SU(2)_L$ symmetry. $SU(2)_L$ multiplets are often called *isospin multiplets*.

symmetry [53] that produces the $W^{\pm}$ and W^0, or W_3 gauge bosons. If this were a perfect symmetry, these gauge bosons would be mass eigenstates with mass equal to zero. But the observed electroweak gauge bosons are not massless; therefore, the symmetry must be broken. The mass eigenstates of the photon and the neutral vector boson Z^0 are formed by the mixing of the neutral B and W_3 states, shown in Eq 2.2.

$$\begin{pmatrix} \gamma \\ Z^0 \end{pmatrix} = \begin{pmatrix} \cos\theta_W & \sin\theta_W \\ \sin\theta_W & \cos\theta_W \end{pmatrix} \begin{pmatrix} B^0 \\ W_3^0 \end{pmatrix} \tag{2.2}$$

In Eq 2.2, θ_W is the weak mixing angle [27].

In the wake of electroweak symmetry breaking, an external mechanism called the *Higgs mechanism* is needed to provide the masses of the $W^{\pm}$ and Z^0. To generate the masses of the charged and neutral electroweak bosons, the Higgs Mechanism is expressed as two scalar fields, producing a chiral doublet, as in Equation 2.3.

$$\phi = \begin{pmatrix} \phi^+ \\ \phi^0 \end{pmatrix} = \frac{1}{\sqrt{2}} \begin{pmatrix} \phi_1 + i\phi_2 \\ \phi_3 + i\phi_4 \end{pmatrix} \Rightarrow \begin{pmatrix} H_u^+ & H_u^0 \\ H_d^- & H_d^0 \end{pmatrix} \tag{2.3}$$

The u and d subscripts in Equation 2.3 mean *up* and *down*, referring to the relative direction of the weak isospin. The two charged and one neutral boson states provide the longitudinal degrees of freedom to the $W^{\pm}$ and the Z^0 bosons, and the last neutral boson provides the SM Higgs, which, until recently, remained the last missing piece of the Standard Model. The squared mass of the Higgs, seen in Equation 2.4, is quadratically sensitive to the scale (Λ) at which particle couplings to the Higgs turn on. In the SM, Λ is the weak-scale $\sim$ 100 GeV.

$$m_H^2 = (m_H^2)_0 + \frac{kg^2\Lambda^2}{16\pi^2} \tag{2.4}$$

The first term in Equation 2.4 is the bare Higgs mass, and the second term adds the one-loop radiative correction to the Higgs mass. Here, g is an electroweak coupling, and k is a constant that scales the coupling; calculable in the low-energy effective theory, it is expected to be of $\mathcal{O}(1)$ [62]. The $SU(3)_C$ represents a group of unitary 3×3 matrices with determinant 1 generated by color symmetry. The gauge invariance imposed on this symmetry produces a color octet of massless gluons. The gauge bosons (plus the Higgs) masses and their $SU(3)_C \times SU(2)_L \times U(1)_Y$ multiplet representations are summarized in Table 2.1. All bosons are integer-spin particles.

State	Spin	Mass	$SU(3)_C$	$SU(2)_L$	$U(1)_Y$
g	1	0	**8**	**1**	0
$W^{\pm}$	1	80.4 GeV	**1**	**3**	0
Z^0	1	91.2 GeV	**1**	**3**	0
γ	1	0	**1**	**1**	0
H^0	0	125 GeV	**1**	**2**	±1

Table 2.1: Strong and EW boson spin, mass, $SU(3)_C$ and $SU(2)_L$ multiplet representations, and $U(1)_Y$ value.

Fermions are 1/2-integer-spin particle that fall into two categorizes, leptons and quarks. Leptons carry electromagnetic and weak isospin charge, but do not carry strong color charge. The leptons consists of three generations of isospin doublets which contain the electron, muon, and tau-lepton with their associated neutrino partners. Quarks are strongly charged particles that also carry weak isospin and fractional electromagnetic charge. Like the leptons, there are three quark families, each forming an isospin doublet and consisting of an up-type and a down-type quark. The fermion masses and multiplet representations are summarized in Table 2.2.

State	Mass	Q	$SU(3)_C$	$SU(2)_L$	$U(1)_Y$
leptons			**1**	**2**	-1
$\begin{pmatrix} e^- \\ \nu_e \end{pmatrix}$	0.511 MeV < 2 eV	-1 0			
$\begin{pmatrix} \mu^- \\ \nu_\mu \end{pmatrix}$	105.7 MeV < 0.19 MeV	-1 0			
$\begin{pmatrix} \tau^- \\ \nu_\tau \end{pmatrix}$	1.78 GeV < 18.2 MeV	-1 0			
quarks			**3**	**2**	1/3
$\begin{pmatrix} d \\ u \end{pmatrix}$	5 MeV 2 MeV	$-1/3$ $2/3$			
$\begin{pmatrix} s \\ c \end{pmatrix}$	≈ 100 MeV ≈ 1 GeV	$-1/3$ $2/3$			
$\begin{pmatrix} b \\ t \end{pmatrix}$	4.19 GeV < 172.0 GeV	$-1/3$ $2/3$			

Table 2.2: Description of fermion mass, electric charge Q, $SU(3)_C$ and $SU(2)_L$ multiplet representations, and $U(1)_Y$ value.

2.2 Shortcomings of the Standard Model

As mentioned before, the Standard Model of Particle Physics in all its glory has limitations.

- The inability to explain dark matter [26]
- The hierarchy problem in relation to M_W/M_P
- Neutrino masses and mixing [52, 42, 10]
- CP-violation in the early universe [67]

Dark matter is proposed to make up about 80% of the matter in the universe, and yet, unlike matter from SM particles, does not interact with the electromagnetic or the strong forces, and possibly not even the weak force. The fact that the SM only accounts for 20% of the matter in the universe is perplexing, but there are hints to what type of new particles we should be looking for. First, we know that dark matter does not interact via the electromagnetic force; otherwise photon radiation would be observed. We have no reason to believe it interacts via the weak force, but it could, and for experimental purposes we often assume that it does. Another important quality of dark matter is that it is stable enough to statically populate the universe. This also relates to the relic abundance of dark matter, which is the measured abundance of dark matter “frozen” into existence in the early universe once it cooled to the point that dark matter could no longer be produced. This puts theorized constraints on the masses of dark matter candidates. We also know from cosmological dark matter mapping, like from recent Dark Energy Survey [35], that it must have the ability to cluster; therefore it should not be extremely light and relativistic. The most popular theory about the characteristics of dark matter refer to what is called the 'WIMP Miracle', which broadly assumes dark matter to be a stable, Weakly Interacting Massive Particle (WIMP) [51, 57].

The hierarchy between the weak scale and the Planck scale is a problem of the SM because the Higgs potential is quite sensitive to new physics in any sensible extension to the SM. Quantum loop corrections from any particle that couples to the Higgs potential can cause quadratic divergences in the Higgs mass through Λ, as in Equation 2.4. Supersymmetry, introduced in the next section, has the benefit of cancelling these diverging mass corrections by adding new particles to the spectrum with corrections opposite to those from SM particles. The only other option in extending the

SM is to make the rather *ad hoc* assumption that none of the undiscovered high-mass particles or condensates from new physics far above the weak scale couple in any way to the Higgs potential.

2.3 Supersymmetry

Supersymmetry offers an extension to the Standard Model by extending the Poincare symmetry of quantum field theory to $SO(10)_{SUSY}$ [56]. This extension leads to a boson-fermion symmetry that can be expressed by a supersymmetric transformation operator which carries 1/2-integer spin angular momentum that transforms boson states to fermion states, and vice versa. If unbroken, this symmetry generates a supersymmetric partner for all Standard Model particles, with each pair being equivalent in mass and all other quantum numbers, but differing intrinsically by half-integer spin. So, each SM fermion has a scalar supersymmetric partner, and each SM boson has a fermionic supersymmetric partner.

According to this symmetry, assuming it is a perfect symmetry, these new particles should have already been observed with their SM masses, but this is not the case. In order for this theory to remain viable, the new symmetry must be broken in a way that preserves the fermion-boson symmetry and all observations of the Standard Model while allowing fermion-boson partners to be decoupled in mass [47]. If the effective scale of supersymmetry breaking is near the weak scale, no unnatural cancellations need to be added to Equation 2.4 to keep the Higgs mass near the electroweak scale and free of

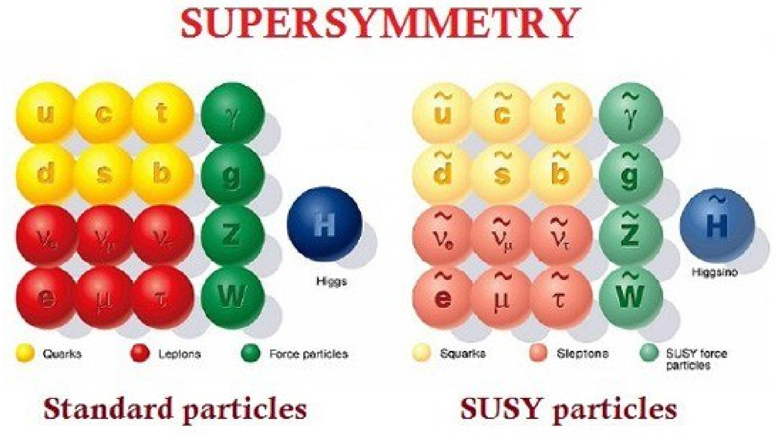

Figure 2.1: Schematic of supersymmetry particle spectrum

quadratic divergences due to quantum corrections.

A detailed description of the various models for mediating this symmetry-breaking and communicating it the visible sector of observable particles is beyond the scope of this thesis, but a very clear explanation by Howard Haber can be found in the Supersymmetry (Theory) chapter in the Particle Data Group [62]. This search targets SUSY models that have undergone soft-breaking in the SUSY electroweak sector.

2.3.1 Minimal Supersymmetric Model (MSSM)

Spin 0	Spin $\frac{1}{2}$	Spin 1	$SU(3)_C, SU(2)_L, U(1)_Y$
$(\tilde{u}\ \tilde{d})$	$(u\ d)$		$(\mathbf{3}, \mathbf{2}, 1/6)$
$(\tilde{e}\ \tilde{\nu})$	$(e\ \nu)$		$(\mathbf{1}, \mathbf{2}, -1/2)$
$(H_u^+\ H_u^0)$ $(H_d^0\ H_d^-)$	$(\tilde{H}_u^+\ \tilde{H}_u^0)$ $(\tilde{H}_0^+\ \tilde{H}_d^-)$		$(\mathbf{1}, \mathbf{2}, +1/2)$ $(\mathbf{1}, \mathbf{2}, -1/2)$
	$\tilde{g}$	g	$(\mathbf{8}, \mathbf{1}, 0)$
	$\tilde{W}^\pm\ \tilde{W}^0$ $\tilde{B}^0$	$W^\pm\ W^0$ B^0	$(\mathbf{1}, \mathbf{3}, 0)$ $(\mathbf{1}, \mathbf{1}, 0)$

Table 2.3: SUSY MSSM spectrum in $SU(3)_C, SU(2)_L, U(1)_Y$ multiplet representation.

Supersymmetric extensions to the SM are free to include multiple sectors and new sets of supersymmetric partners. A Minimal Supersymmetric extension to the Standard Model (MSSM) adds the minimal number of new states needed to complete the theory, and most importantly, just one new Higgs doublet. The general MSSM has 124 free parameters, many of which are related to each other only through some unknown SUSY breaking mechanism. Observed or inferred constraints can be placed on many of the 100-plus parameters, reducing this number down to 19. Among these is the top quark mass [24]. Table 2.3 shows the particle content in the MSSM. In this table, $(e\ \nu)$ stands for all three generations of SM lepton, and $(u\ d)$ refers to the three generations of quark. Both chiral representation of the Higgs fields are shown explicitly. In the MSSM, these form chiral supermultiplets with their superpartners; three generations of *sleptons* $(\tilde{e}\ \tilde{\nu})$, three generations of *squarks* $(\tilde{u}\ \tilde{d})$, and four new spin-1 Higgsino fields. The name for all supersymmetric quark partners and supersymmetric lepton partners is just the SM partner name with an *s* in front. This *s* does not mean *supersymmetric*; but rather, it means *scalar*, which refers to a particle with spin angular momentum 0, as seen in Table 2.3. The names for SM boson partners have the suffix *ino*.

Standard model gauge bosons and their superpartners, typically referred to as *gauginos*, form gauge supermultiplets. The superpartner to the gluon g is the spin-1/2 color-octet *gluino* $\tilde{g}$. The spin-1 gauge eigenstates that mix to form the SM vector bosons are the W^+, W^0, W^-, and B^0. Their spin-1/2 superpartners are the *winos* and *binos*: $\tilde{W}^+$, $\tilde{W}^0$, $\tilde{W}^-$, and $\tilde{B}^0$. Like with SM gauge bosons, their mass eigenstates are not necessarily pure weak eigenstates. There can be mixing between the electroweak gauginos and the Higgsinos to form the charged and neutral SUSY mass eigenstates called the *charginos* and *neutralinos*. There are two charged states ($\tilde{\chi}_1^\pm$, $\tilde{\chi}_2^\pm$) and four light neutral states ($\tilde{\chi}_1^0$, $\tilde{\chi}_2^0$, $\tilde{\chi}_3^0$, $\tilde{\chi}_4^0$), and can be referred to together as *electroweakinos*.

The MSSM is defined to conserve R-parity. All SM particles have R-parity +1, while all SUSY particles have R-parity -1. R-parity is defined as:

$$P_R = (-1)^{3(B+L)+2s} \tag{2.5}$$

where B and L are the baryon number and lepton number defined in Section 2.1. The conservation of R-parity means that, in the collision of two R-parity even SM particles, R-parity odd SUSY particles must be produced in pairs, and the subsequent decay chain of each must end with the lightest SUSY particle (LSP) in the MSSM model. The LSP must be stable since the only kinematically available decays are to lighter SM particles, which would violate R-parity conservation. The stability of a weakly interacting LSP in R-parity conserving models can make them good candidates for dark matter.

Of the 19 free parameters in the constrained MSSM, only a handful determine the chargino and neutralino masses; M_1, M_2, μ, and $\tan\beta$. M_1 and M_2 are the bino and wino mass parameters, μ is the Higgsino mass parameter, and $\tan\beta$ is the ratio of the vacuum expectation values of the two Higgs doublets:

$$\tan\beta = \nu_u/\nu_d \tag{2.6}$$

The chargino and neutralino mass mixing matrices are shown in Equations 2.7 and 2.8.

$$M_{\chi^\pm} = \begin{pmatrix} M_2 & \sqrt{2}M_W \sin\beta \\ \sqrt{2}M_W \cos\beta & \mu \end{pmatrix} \tag{2.7}$$

$$M_{\chi^0} = \begin{pmatrix} M_1 & 0 & -M_Z \cos\beta \sin\theta_W & M_Z \sin\beta \sin\theta_W \\ 0 & M_2 & M_Z \cos\beta \cos\theta_W & -M_Z \sin\beta \cos\theta_W \\ -M_Z \cos\beta \sin\theta_W & M_Z \cos\beta \cos\theta_W & 0 & -\mu \\ M_Z \sin\beta \sin\theta_W & -M_Z \sin\beta \cos\theta_W & -\mu & 0 \end{pmatrix} \tag{2.8}$$

In these equations, $\cos\beta$ and $\sin\beta$ are the x- and y-components of $\tan\beta$. The structure of wino/bino/higgsino mixing and relative mass spectrum of the lightest electroweakinos is governed by the relative magnitudes of the mass parameters M_1, M_2, and μ in Equations 2.7 and 2.8. When $|\mu| \ll |M_1|, |M_2|$, the lightest mass eigenstates of the mass mixing matrices are mostly Higgsino with little or no wino/bino mixing. In this case, the lightest stable SUSY particle is the Higgsino $\tilde{\chi}_1^0$, and is called the Higgsino LSP. When the eigenstates are purely Higgsino, the solution gives a fully degenerate set of electroweakinos[2], and there needs to be some level of wino/bino mixing added to get larger differences between the lightest and next-to-lightest chargino and neutralino masses [29]. Another relevant scenario, $|M_1| < |M_2| \ll |\mu|$, leads to wino-dominated $\tilde{\chi}_1^\pm$ and $\tilde{\chi}_2^0$ states that are nearly mass degenerate and $\mathcal{O}(10$ GeV$)$ heavier than the bino LSP $\tilde{\chi}_1^0$. This is the order of mixing assumed for the compressed slepton model interpretations where the slepton masses are in between the bino LSP and the heavier winos. For these scenarios to be compressed, mass-splittings between the $\tilde{\chi}_1^0$ and the sleptons are of $\mathcal{O}(1$ GeV$)$. Other scenarios can occur as well. For example, the Higgsino-bino

---

[2] Small mass splittings of order 200 MeV occur through radiative corrections.

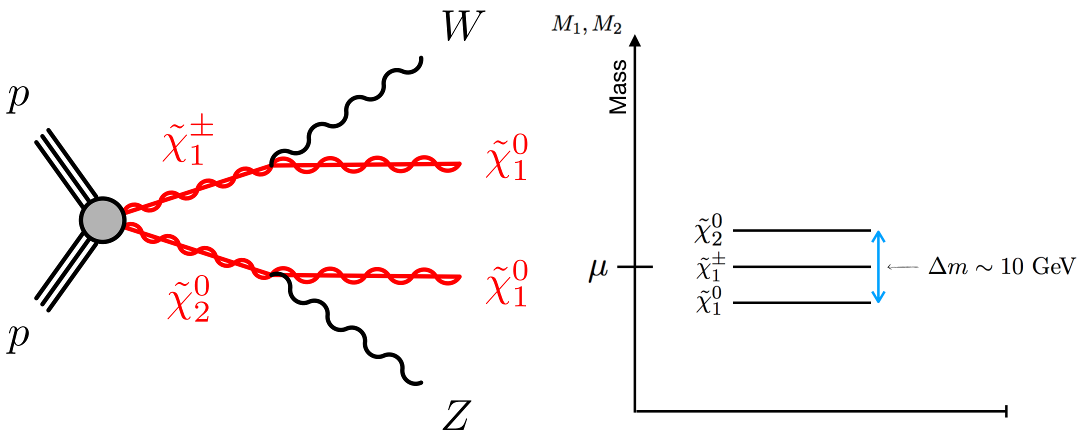

Figure 2.2: Feynman diagram of direct Higgsino production (left), and schematic of electroweakino mass spectrum (right)

model $|\mu| \sim |M_1| \ll |M_2|$, the Higgsino-wino model $|\mu| \sim |M_2| \ll |M_1|$ and the wino-bino model $|M_1| \sim |M_2| \ll |\mu|$ display mass spectra related to $\Delta(\mu, M_1)$, $\Delta(\mu, M_2)$ and $\Delta(M_1, M_2)$ respectively [63].

2.3.2 Phenomenology of Directly Produced Higgsinos and Sleptons in Compressed Scenarios

This analysis targets direct production of compressed electroweakinos that decay to Higgsino LSPs, as in Figure 2.2, and direct production of compressed sleptons that decay to bino LSPs , as in Figure 2.3. Small mass splittings among the electroweakinos come from the Higgsino scenario with $\mu \ll M_1, M_2$, and in order for supersymmetry breaking to occur at the correct scale without any unnatural corrections, the parameter μ must be near the weak scale ≈ 100 GeV. This sets the Higgsinos masses near the

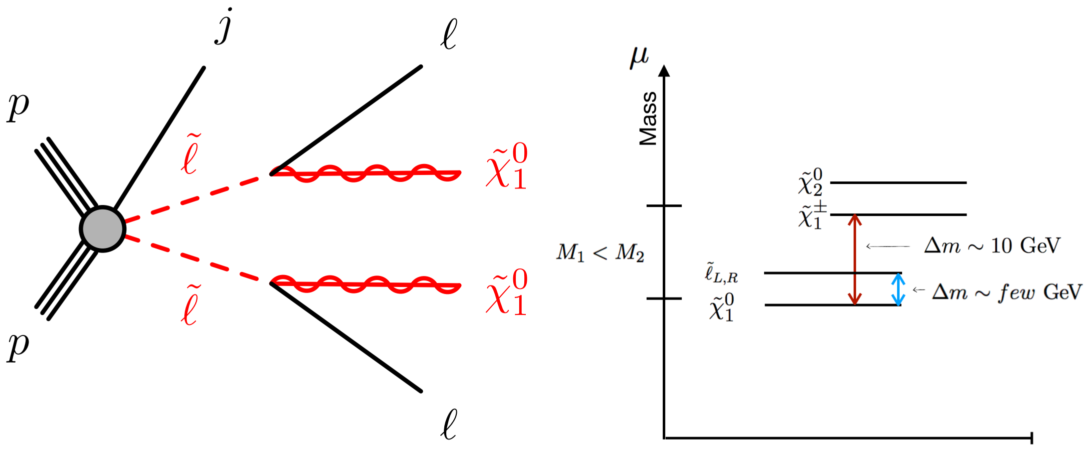

Figure 2.3: Feynman diagram of direct slepton production (left) and schematic of electroweakino and slepton mass spectrum

weak scale, while allowing the winos and binos, with masses given by M_1 and M_2, to still be heavy. The slepton model assumes $|M_1| < |M_2| \ll |\mu|$ with the slepton mass just above the LSP mass [37]. In the natural scenario, M_1 and M_2 are near the weak scale, and the bino becomes a valid dark matter candidate, except that it leads to a higher dark matter relic abundance than measured with the WMAP [71] and Planck [30] experiments. If the slepton has a mass slightly above the LSP mass, then coannihilation could reduce the dark matter abundance [46]. So far, there is no sign of the colored SUSY sector, so we can ignore the colored states altogether by assuming there masses are very large.

One way to search for Higgsinos is through direct production of squarks that then decay to Higgsinos, but these particles have little effect on the mass of the Higgs, and may naturally have masses well beyond the reach of the LHC. In direct squark

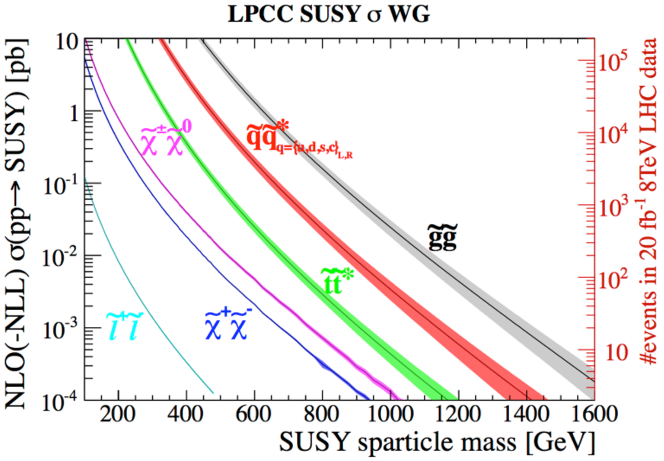

Figure 2.4: SUSY cross-sections in LHC pp collisions [25]

production, Higgsino models are very sensitive to the spectrum of light SUSY particles. Direct Higgsino or slepton production depends only weakly on the spectrum of the SUSY sector, and therefore, retain sensitivity to a large range of weak-scale SUSY models. Unfortunately, the direct production of electroweakinos, including Higgsinos, has small cross-sections $\sim$ 1 pb, and the slepton cross-sections are even smaller, limiting the search sensitivity at the LHC. Figure 2.4 shows the cross-sections for the SUSY particles in the MSSM as a function of mass. Electroweakino and slepton pair-production cross-sections are more than 10^2 and 10^3 times smaller than squark pair-production cross-sections.

When the electroweakino mass-splittings are close to the mass of the W boson, Standard Model W and Z bosons are produced on-shell, at their nominal masses, and about 30% of the time will decay to electrons, muons, or tau-leptons. In this case, analyses have been performed in both ATLAS and CMS to search for the three leptons from the W and Z boson decays, where the Z boson can be reconstructed from an opposite-sign-same-flavor lepton pair. These searches also require a substantial amount of missing transverse momentum from the lightest neutral electroweakinos. When the mass-splittings fall below the W boson mass, the W and Z bosons are produced off-shell, they are lighter than their nominal $80 - 90$ GeV mass, and the leptons from these decays become less energetic, or *softer*. When the leptons become very soft, triggering and lepton reconstruction become challenging; therefore, dedicated efforts are needed to probe model space where the electroweakino mass-splittings are less than $\sim$ 60 GeV. For final states with soft leptons and $E_{\mathrm{T}}^{\mathrm{miss}}$, requiring a hard ISR jet in the event helps sculpt the kinematic signature in a way that makes the decays of the nearly degenerate particles more distinguishable from the backgrounds. Figure 2.5 points out some of the kinematic features of direct production of compressed electroweakinos with an ISR jet. The jet boosts the system, increases the $E_{\mathrm{T}}^{\mathrm{miss}}$, and forces a large angular separation between the leading jet in the system and the intermediate amount of $E_{\mathrm{T}}^{\mathrm{miss}}$. Having more $E_{\mathrm{T}}^{\mathrm{miss}}$ associated with the LSPs is also important for triggering, as $E_{\mathrm{T}}^{\mathrm{miss}}$ might be the most efficient object on which to trigger. These characteristics are also relevant for compressed slepton production with hadronic ISR.

Another important feature is that the dilepton invariant mass ($m_{\ell\ell}$) distribution in electroweakino production is linked to the mass splitting between the lightest and next-to-lightest neutralino through the mass of the very off-shell Z. We can exploit the dilepton invariant mass for the electroweakinos, through what is called the kinematic end-point, which is a strict limit on the dilepton invariant mass set by $m(\tilde{\chi}_2^0) - m(\tilde{\chi}_1^0)$. The sleptons do not have the same sensitivity in $m_{\ell\ell}$, but instead show angular corre-

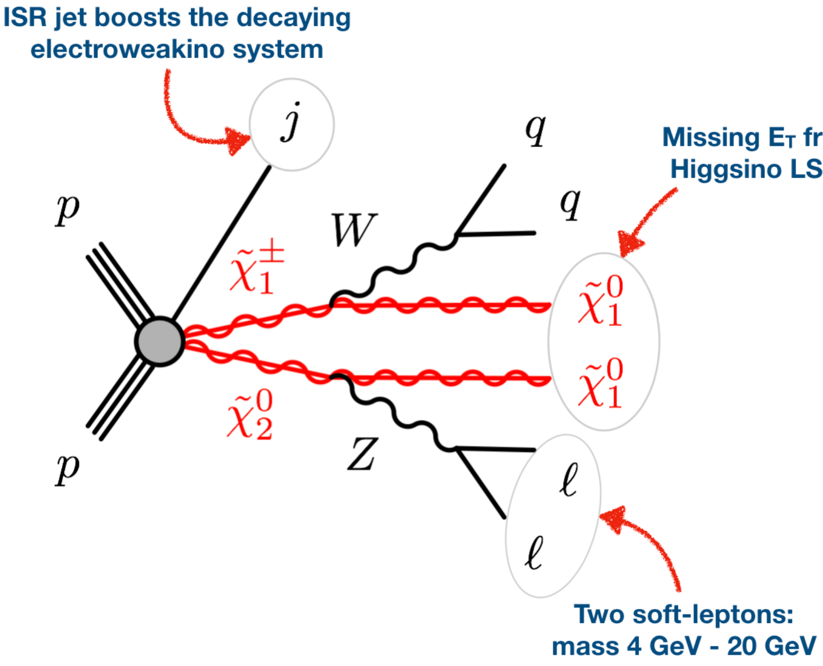

Figure 2.5: Feynman diagram of direct Higgsino production in one compressed scenario. Red arrows point out features like the soft leptons from the off-shell Z boson decay, or the ISR jet boosting the system, increasing the $E_{\mathrm{T}}^{\mathrm{miss}}$, and forcing a large angular separation between the jet and $E_{\mathrm{T}}^{\mathrm{miss}}$.

lations between the SM leptons and $E_{\mathrm{T}}^{\mathrm{miss}}$ coming from the bino LSP. This relationship is expressed through a variable called the *stransverse mass* (M_{T2}), which is defined in Chapter 6, and is subject to kinematic boundaries set by the mass of the LSP and its difference from the slepton masses.

Chapter 3

The LHC and The ATLAS Experiment

This chapter gives an overview of the LHC and the ATLAS detector used for this physics analysis. First, the LHC is introduced in Section 3.1, then a review of the ATLAS detector is given in Section 3.2. This section is broken into smaller pieces that detail the ATLAS subdetectors and trigger system.

3.1 The Large Hadron Collider Machine

The Large Hadron Collider (LHC) is a circular proton accelerator and collider at CERN [38], operating in the 26.7 km-long tunnel that was originally built for the Large Electron-Positron Collider (LEP). In the tunnel, there are two separate vacuum beam pipes with counter-rotating proton beams that are accelerated to the TeV energy scale by a gigantic super-conducting magnet system. To reach LHC energies, the proton beams first move through a stream of smaller accelerator structures that increase the kinetic energy of the beam at each step, until the beam is finally injected into the LHC, which is still the largest and most powerful accelerator in the world. There are two transfer tunnels, each about 2.5 km long, that join the LHC to the SPS, now acting as the injector for the LHC. The LHC tunnel is broken into octants with eight straight sides and eight curves. This is not an LHC design, but rather an artifact of LEP [2]. That being said, each octants is considered as a reference point around the ring; for instance, octant 1 is centered around “point 1”, octant 2 is centered around ”point 2”, and so on. The beams collide at four interaction points located approximately 100 m underground, and surrounding each interaction point is a physics detector apparatus to collect data from the proton collisions. The four different detector experiments are ALICE, LHC-B, CMS, and ATLAS [32]. Figure 3.1 depicts the tunnel octants and the beam injection and dump points. It also shows the placement of the four detectors; ATLAS is located at point 1.

The primary objective of the LHC is produce the Higgs boson, which was discovered by both ATLAS and CMS in 2012, and to expose Beyond Standard Model (BSM) physics. To attempt these goals, the accelerator was designed to supply proton collisions with enough center-of-mass energy to produce a Higgs with mass above 100 GeV and to unlock possible new physics interactions at the 100 GeV - multi-TeV scale. The initial aim was a proton-proton center-of-mass energy of 14 TeV, but due to instabilities in the magnet system at such high energy, only 13 TeV has successfully been achieved. Many BSM theories predict new particle interactions with weak-scale cross-sections or lower, creating the need for enough luminosity to measure these low probability events. The machine luminosity (L) depends only on beam parameters, as

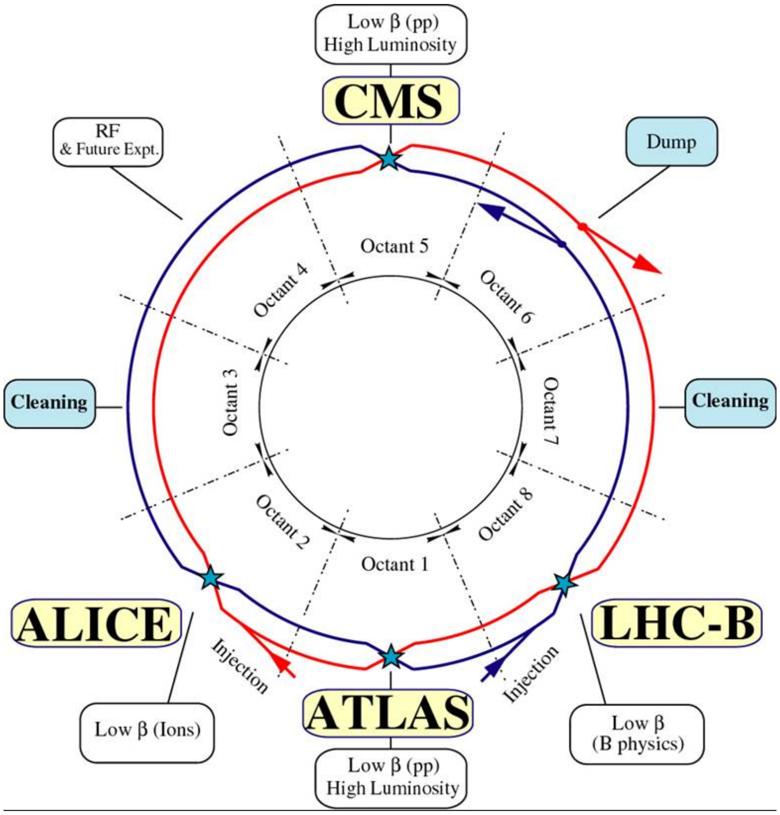

Figure 3.1: Schematic of the LHC layout [23]

expressed in Eq 3.1.

$$L = \frac{N_p^2 f}{4\epsilon\beta^\star} F \tag{3.1}$$

In the numerator of Eq 3.1, N_p is the number of particles per bunch and f is the bunch crossing frequency. In the denominator of Eq 3.1, ϵ is the transverse beam emittance and $\beta^\star$ in the amplitude function at the collision point. The geometric luminosity reduction factor F is due to the beams crossing at an angle at the interaction points rather than directly head-on, and is about equal to 1 [75]. Luminosity is generally in units of $\mathrm{cm}^{-2}\mathrm{s}^{-1}$, and these units are better understood by rewriting $\epsilon\beta^\star$ of Equation 3.1 in terms of bunch cross-section σ:

$$\epsilon\beta^\star = 4\pi\sigma^2 \tag{3.2}$$

$$L = \frac{N_p^2 f}{4\pi\sigma^2} \tag{3.3}$$

ATLAS, one of the high luminosity experiments at the LHC, recorded a peak luminosity in 2016 above $L = 10^{34}\mathrm{cm}^{-2}\mathrm{s}^{-1}$, for which the values corresponding to Equation 3.3 are shown in Table 3.1.

Parameter	Value
N_p	1.15×10^{11} protons
f	$40 \times 10^6 \mathrm{s}^{-1}$
σ	16×10^{-4} cm^2

Table 3.1: Luminosity parameters in Equation 3.3, corresponding to ATLAS peak luminosity $L \sim 10^{34}\mathrm{cm}^{-2}\mathrm{s}^{-1}$

3.2 The ATLAS Experiment

The general design for detectors at the LHC is informed by the benchmark physics goals and the experimental environment and constraints [11]. The high energy and luminosity demands make radiation-hard sensor elements and read-out electronics a necessity. Large numbers of interactions per bunch crossing, called pileup, create the need for highly granular detectors to resolve the separate events in space. To search for new physics, a detector needs to be as general as possible, meaning it tries to see everything. This requires a high acceptance in pseudorapidity with coverage over nearly the full azimuthal angle of the detector, high track reconstruction efficiency and good resolution on charged-particle momentum measurements. Fairly precise electromagnetic calorimetry is also needed for efficient electron and photon identification. Now that we understand these demands, we turn to a description of the ATLAS detector.

The ATLAS experiment is a general purpose detector apparatus [5] that almost completely covers the entire solid angle around one of the LHC beam collision points. ATLAS recorded its first LHC pp collisions in 2009 at center-of-mass energy 7 TeV, and has since recorded events at several different center-of-mass energies, including the most extensive energy reach in history at 13 TeV. ATLAS achieves central coverage in the symmetric cylindrical barrel, and forward-backward detecting capabilities in the end-caps. The complete detector system is 44 m long, 25 m in diameter, and weighs 4000 tons. The ATLAS detector, shown in Figure 3.2, is comprised of several sub-detector systems, each calibrated and optimized for a different observational purpose. The sub-detectors, listed in order from the beam pipe outward, are: the inner tracking detector, the electromagnetic calorimeter, the hadronic calorimeter, and the muon spectrometer. Together, these sub-detectors measure the energy and momentum of a variety of particles and reconstruct the dynamics of each recorded event.

ATLAS uses a right-handed coordinate system with the center of the detector as the origin. The z-axis runs through the center of the barrel along the beam pipe, and the y-axis points upward through the barrel from the origin. The x-axis points outward from the origin, perpendicular to both the y- and z-axes. Cylindrical coordinates (r, ϕ) map out the transverse plane, where r is the radius in the plane, and ϕ is the azimuthal angle around the z-axis. The pseudorapidity η, given by Eq 3.4, is a transformation of the polar angle θ that is commonly used in particle detector experiments. At $\theta = \pi/2$, $\eta = 0$; at $\theta = \pi/18$, $\eta = 2.88$; as θ approaches zero, η approaches infinity.

$$\eta = -\ln[\tan(\theta/2)] \tag{3.4}$$

The combination of the detector systems provide charged particle measurements and efficient lepton and photon measurements out to $|\eta| < 2.4$. Missing transverse momentum ($p_{\mathrm{T}}^{\mathrm{miss}}$) is the negative vector sum of the transverse momentum of all the visible objects in the detector, and is often referred to by the same nomenclature as the scalar magnitude, missing transverse energy ($E_{\mathrm{T}}^{\mathrm{miss}}$). Jets and $E_{\mathrm{T}}^{\mathrm{miss}}$ are reconstructed using the full set of information out to $|\eta| < 4.9$.

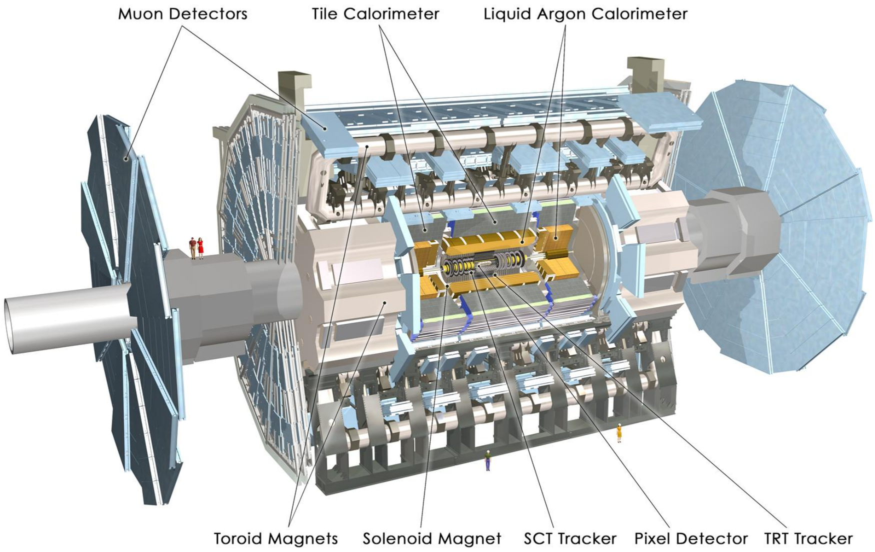

Figure 3.2: Cut-away view of the complete ATLAS Detector [60]

3.2.1 Inner Tracking Detector

The ATLAS Inner Detector (ID), shown in Figure 3.3, provides position measurements of charged particles passing through the fiducial region $|\eta| < 2.5$ by combining information from three separate tracking systems; the Pixel detector, the Semi-Conductor Tracker (SCT), and the Transition Radiation Tracker (TRT). The ID is made of a central cylindrical barrel that covers the region $|\eta| < 1.5$, and two end-caps that complete the ID range $1.5 < |\eta| < 2.5$. The layout of the separate tracking layers in $|\eta|$ is illustrated in Figure 3.4. The ID is surrounded by a superconducting solenoid that encases the entire ID in a 2 T magnetic field. The magnetic field bends the charged particles traveling through the tracker and the induced curvature depends

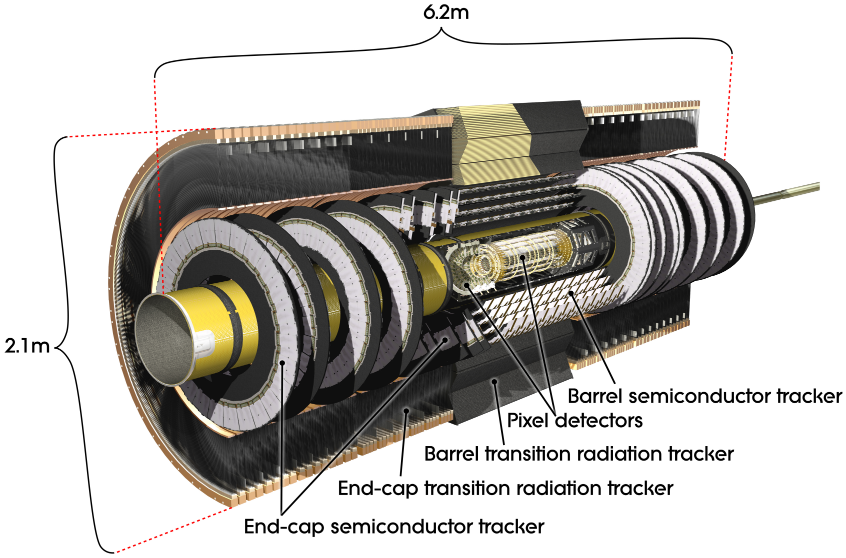

Figure 3.3: Layout of the ALTAS Inner Detector

on the momentum of the particle.

The Pixel detector is the inner most pixelated tracker and has the finest granularity sensors in the ID. There are four pixel layers in the central barrel and the end caps, providing up to four space-points per track. The inner-most layer, called the Insertable B-Layer (IBL), was added during the ATLAS Run-2 upgrade [72]. Planar IBL sensors cover the central region of the barrel, and 3D sensors cover the outer regions. The Pixel detector has approximately 92 million readout channels bonded to pixel sensors segmented in the $r-\phi$ and z directions. The first three layers of Pixel sensors have dimensions 50 μm $\times$ 400 μm in $r-\phi \times z$, and provide an intrinsic resolution of 10 μm in $r-\phi$ and 115 μm along z. The IBL has pixel dimensions 50 μm $\times$ 250 μm with intrinsic

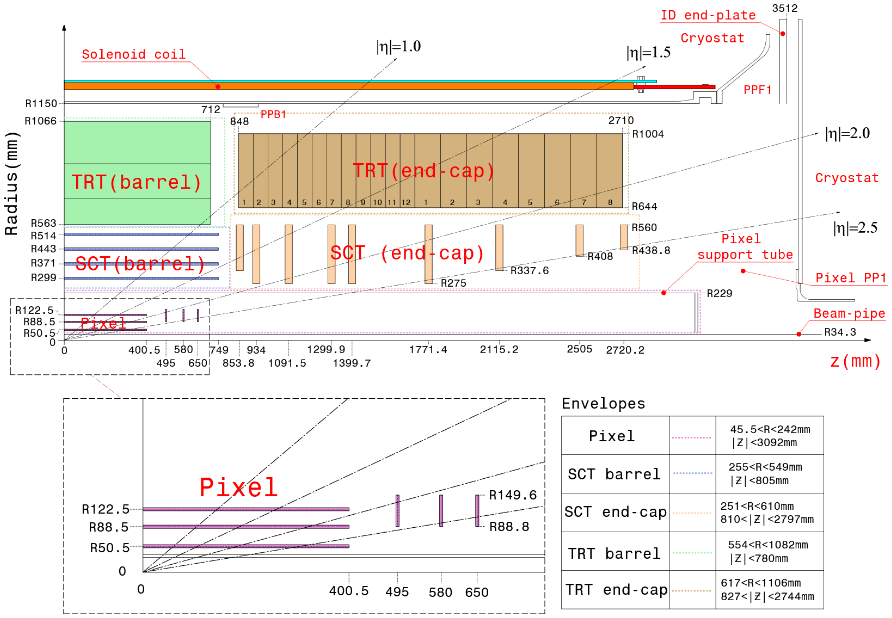

Figure 3.4: Layout of the ALTAS Inner Detector

resolutions 9 μm and 60 μm in the azimuthal and z directions. One benefit of the fine granularity of the Pixel detector is the discrimination between prompt and non-prompt leptons. The added layer closer to the beam pipe helps recover late decays from heavy hadrons and τ-leptons, and the rich granularity helps resolve secondary vertices formed by the charged decay products.

The Semi-Conductor Tracker (SCT) is a silicon micro-strip tracker just outside of the the Pixel detector, with an overall radial extension of 255 mm $< r <$ 549 mm in the barrel and 251 mm $< r <$ 610 mm in the end-caps. It has eight paired strip layers that provide four space points per track. In the barrel (end-cap), one set of strips is aligned parallel (perpendicular) to the beam axis and is daisy chained to a second set of strips, each misaligned with the its partner by a 40 mrad stereo angle[9]. The strip pitch is 80 μm. The resulting intrinsic resolution in both the barrel and the end-caps is 17 μm in $r - \phi$, and in the barrel (end-caps) it is 580 μm in z (r). There are approximately 6.3 million readout channels. The Pixel and SCT layers are are subject to the adverse conditions of event pileup from the large number of interactions at each bunch crossing. Pileup is predominantly produced by the soft scattering of hadrons, which blurs the spacial reconstruction of the interaction point of a hard-scattering collision. The interaction point, called the *primary vertex*, is reconstructed from tracks in the Pixel and SCT layers, and is a critical reference point for events with tracks. This is described more in Chapter 5.

The Transition Radiation Tracker (TRT) is the outermost detector in the ID. It is comprised of straw tubes filled with diluted xenon gas [59], some of which ionizes as charged particles pass through. The outer shell of each straw is held at a negative potential while an anode wire running down the center of the tube is held at ground. As some of the gas ionizes during the charged particle passage, an avalanche of ionization electrons forms on the wire, amplifying the signal by an order of 10^4. Each straw tube in the TRT is 4 mm in diameter but can vary in length between the barrels and the end-caps. In the barrel, the straw tubes are 144 cm long and positioned parallel to the beam axis; in the end-caps, the tubes are 37 cm long and arranged transverse to the beam axis in the radial direction. In both the barrel and the end-caps, the readout electronics have two discriminating thresholds, a low threshold at 300 eV and a high threshold at 6 keV. The high threshold is used to determine the presence of transition radiation photons

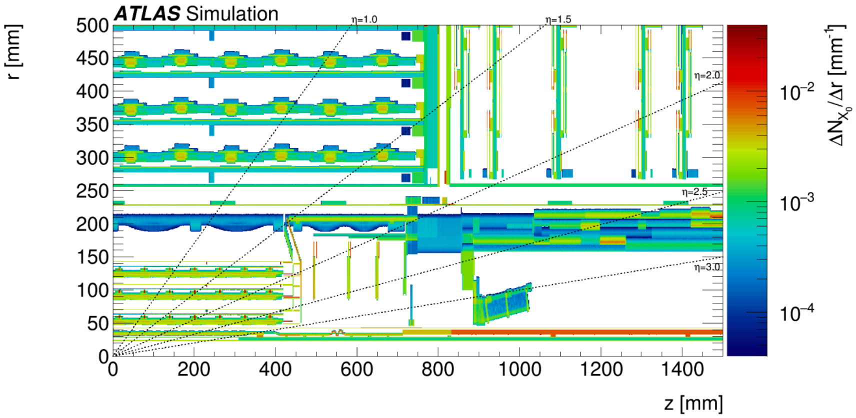

Figure 3.5: ATLAS simulation of material in the Pixel and SCT detectors in terms of the differential radiation length projected on the $r-z$ plane [4].

from the electrons traversing the xenon gas. This gives the TRT special discrimination power between electrons and charged pions with energy in the range 1 GeV $-$ 100 GeV. Scattering effects of low-p_{T} electrons in the ID strains electron/pion discrimination and degrades electron identification efficiency [58].

The material in the ID is on average 2.3 radiation lengths at $\eta = 0$ and increases with pseudorapidity in the barrel. A radiation length (X_0) is the distance over which an electron's energy is reduced by a factor $\frac{1}{e}$ due to bremsstrahlung and $\frac{7}{9}$ of the mean free path λ needed for photon pair production by a high energy photon. Figure 3.5 shows the simulation of material in the Pixel and SCT detectors in differential radiation lengths $\Delta N_{X_0}/\Delta r$ [mm^{-1}].

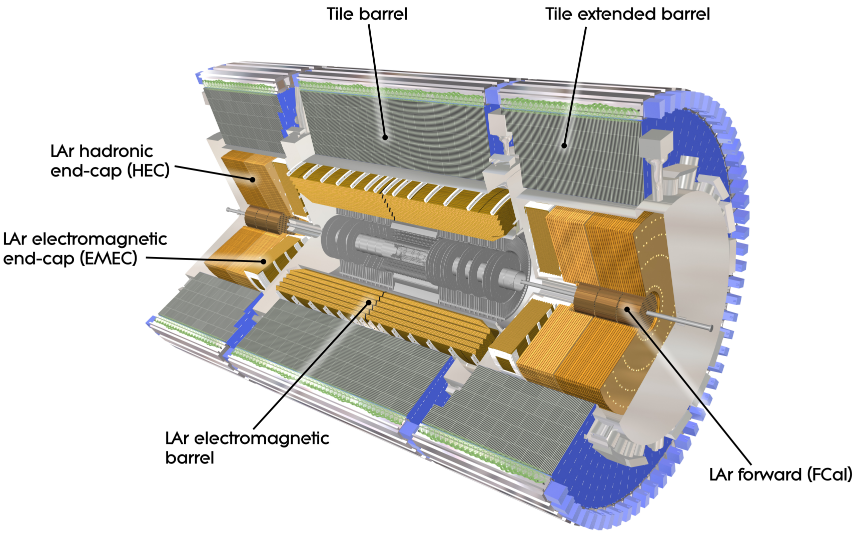

Figure 3.6: Picture of the ATLAS Calorimeters

3.2.2 Calorimeters

Just outside of the ID and the solenoid magnet is the ATLAS calorimeter system. The electromagnetic and hadronic calorimeters, extending to $|\eta| < 4.9$, measure the energy of electromagnetic and hadronic objects as it dissipates inside the calorimeter material. These calorimeters are samplers, meaning they only directly measure a fraction of the absorbed energy, and from this, infer the shape and strength of the full shower.

The electromagnetic calorimeter (LAr)[1] measures the energy of electrons and photons by inducing electromagnetic showering inside the LAr layers through continuous

---

[1] *LAr* stands for Liquid Argon.

photon conversions and Bremsstrahlung, spreading out among calorimeter cells until all the energy of the incident particle has been absorbed. The LAr is composed of electrodes submerged in liquid argon that induce the electromagnetic shower, layered in an accordion shape with lead absorber plates in between. It is divided into a central barrel with $|\eta| < 1.475$ and two end-caps enclosing each side of the barrel. The end-cap regions have an inner wheel corresponding to $1.375 < |\eta| < 2.5$, and an outer wheel for $2.5 < |\eta| < 3.2$. The total thickness is > 24 X_0 in the barrel and > 26 X_0 in the end caps [78].

The LAr is split into three layers. The first layer is the most finely segmented in η to aid the discrimination between true photons and neutral pions that have decayed to a pair of photons. Both objects are trackless in flight and undetectable until they interact with the LAr. Two closely-spaced photons from a boosted neutral pion decay are difficult to resolve as separate photons without the extremely fine grain of this first layer. The fine grain also helps improve the resolution of the shower position, shape and direction. The second layer is more coarsely grained and is also the thickest layer where the majority of the electromagnetic showering occurs. The third layer has the largest granularity layer and it samples from the tail of the shower. The LAr is preceded by a pre-sampler at $|\eta| < 1.8$ to correct for upstream energy losses.

The hadronic calorimeters, shown in Fig 3.6, capture and measure the energy of jets, hadrons, and hadronically decaying τ-leptons to $|\eta| < 4.9$. The barrel region $|\eta| < 1.7$ is made of iron-scintillator tile and steel absorbers and sits just outside the LAr, extending radially from 2.28 m to 4.25 m. Outside the barrel, in the region

$1.5 < |\eta| < 3.2$ are the LAr hadronic end-cap calorimeters, and in the range $3.1 < |\eta| < 4.9$ are the LAr forward calorimeters that measure both electromagnetic and hadronic showers [49]. The thickness of the TileCal and the hadronic LAr is about 10 interaction lengths, with an added 1 λ of outside material to prevent punch-through into the muon system. The nuclear interaction length (λ_n) gives the mean free path over which a strongly-interacting particle loses energy by a factor $\frac{1}{e}$. There is also about 1.2 λ_n of material in the LAr before the TileCal.

3.2.3 Muon System

The muon spectrometer, a tracking detector dedicated entirely to tracking muons, is the outermost sub-detector in ATLAS. It is designed to track muons in the pseudorapidity region $|\eta| < 2.7$ with a central barrel covering $|\eta| < 1.05$ and two end-caps at $1.05 < |\eta| < 2.7$. A network of three large super-conducting toroidal magnets, each with eight coils, supplies a magnetic field to the muon spectrometer with am integral bending power in the barrel of around 2.5 T-m and up to 6 T-m in the end caps. Resistive plate chambers in the central region $|\eta| < 1.05$ and end gap chambers in the forward-backward region $1.05 < |\eta| < 2.7$ impart triggering capabilities to the MS as well as position measurements in η and ϕ with a spacial resolution of 5-10 mm. Monitored drift tube chambers provide precision tracking out to $|\eta| < 2.7$ where each chamber provides 6-8 hits in η along the muon flight path.

3.2.4 Trigger System

Originally a three-level trigger system in Run-1, the trigger was restructured in Run-2 into a two-level system with only a hardware level-1 (L1) trigger and a software-based high-level (HL) trigger. The LHC collision rate is about 40 MHz. The L1 trigger reduces this to $\sim$ 100 kHz, and the HLT further decreases the event rates to $\sim$ 1 kHz. In each event, the L1 trigger identifies Regions-of-Interest (ROIs), which are detector regions where interesting activity is identified. The geographical (η, ϕ) coordinates, the basic characteristics of the detector response in that region, and the set of criteria that triggered the L1 are passed to the HLT for further discrimination. RoI candidates are muons, electromagnetic clusters, jets, or taus. Also, comprehensive sums of missing transverse energy and total energy are assembled. HLT decisions are more sophisticated and can trigger on physics objects such as muons, electrons, photons, jets, b-jets, missing transverse energy, taus and b-hadrons.

Part II

Method

Chapter 4

Data Collection and Simulated Events

The chapter will describe the actual and simulated data used for this analysis and the types of events selected from those datasets. First, Section 4.1 illuminates the LHC *pp* collision data accumulated by ATLAS and analyzed in this search for compressed electroweak SUSY. Next, the simulated signal samples are detailed in Section 4.2, and finally, simulated SM backgrounds are summarized in Section 4.3. All event simulation is performed with Monte Carlo techniques and processed with the same reconstruction software as ATLAS data.

4.1 Data

In June of 2015, the LHC began *pp* collisions at $\sqrt{s} = 13$ TeV in a run campaign called "Run 2," that is scheduled to continue through the end of 2018. The center of mass energy in Run 2 collisions is almost a factor of 2 higher than in the previous LHC Run 1 $\sqrt{s} = 8$ TeV campaign that lasted from 2010 through 2012. The analysis

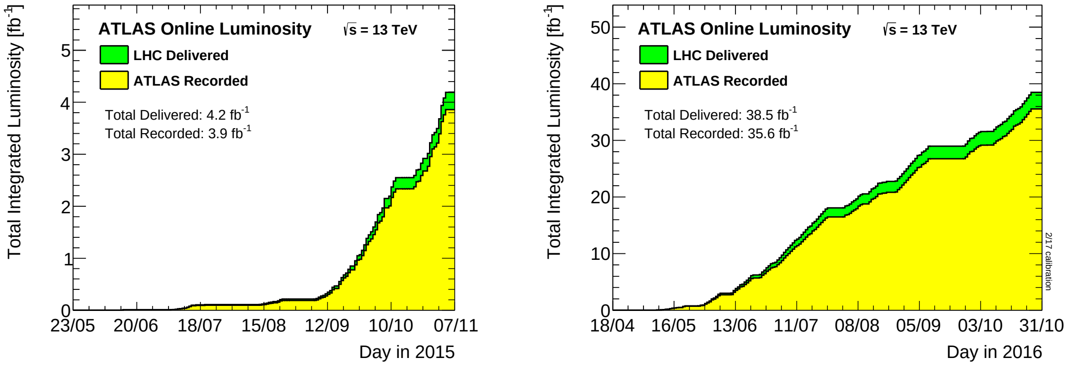

Figure 4.1: Cumulative luminosity versus time delivered to (green) and recorded by (yellow) ATLAS during stable beams for pp collisions at 13 TeV in 2015 (left) and 2016 (right).

described in this thesis uses pp collision data at $\sqrt{s} = 13$ TeV created at the LHC and recorded by ATLAS in 2015 and 2016. In those two years, the peak instantaneous luminosity progressed from 5×10^{33} cm^{-2} s^{-1} in 2015, to 13.8×10^{33} cm^{-2} s^{-1} in 2016, corresponding to a combined 36.1 fb^{-1} of total integrated luminosity, 90% of which comes from 2016 data-taking. The cumulative luminosity versus day in 2015 and 2016 are separately shown in Figure 4.1.

Events in data are initially selected using different inclusive $E_{\mathrm{T}}^{\mathrm{miss}}$ triggers according to the lowest $E_{\mathrm{T}}^{\mathrm{miss}}$ threshold available that is not prescaled. A trigger prescale refers to the fraction of data passing the trigger that gets stored, so having an unprescaled trigger means that every event passing the trigger is kept. The $E_{\mathrm{T}}^{\mathrm{miss}}$ threshold of the lowest unprescaled trigger can increase as data taking progresses if the increasing luminosity makes the trigger rate too large. Table 4.1 shows the evolution of the threshold and the corresponding cumulative integrated luminosity collected from the lowest unprescaled $E_{\mathrm{T}}^{\mathrm{miss}}$ trigger during 2015+2016 data taking. The lowest unprescaled $E_{\mathrm{T}}^{\mathrm{miss}}$ trigger threshold throughout 2015 was 70 GeV and grew to 110 GeV towards the middle of 2016.

Data Period	$E_{\mathrm{T}}^{\mathrm{miss}}$ Threshold	Total Integrated Lumi
2015	70 GeV	3.2 fb^{-1}
2016		
April-June	90 GeV	7.5 fb^{-1}
July-Oct	110 GeV	25.4 fb^{-1}

Table 4.1: Evolution of lowest unprescaled $E_{\mathrm{T}}^{\mathrm{miss}}$ trigger threshold and corresponding total integrated luminosity from the start of 2015 to the end of 2016. All through 2015 the lowest unprescaled $E_{\mathrm{T}}^{\mathrm{miss}}$ trigger threshold was 70 GeV, and it increased to 90 GeV at the start of 2016. By July of 2016, the threshold rose to 110 GeV.

4.2 Simulated Signal Samples

This analysis is designed around two types of signal processes, for which simulated samples were generated using SUSY Higgsino and slepton simplified models [16, 17, 14]. To help interpret the results, another simplified model assuming the direct production of wino-like electroweakinos is considered. Each of these simplified models incorporate the structure and kinematics of the full MSSM with the majority of the mass parameters decoupled, leaving only μ, M_1, and M_2 to float at low scales. The production cross-sections in these simplified models, shown in Fig. 4.2, are SUSY MSSM cross-sections calculated in terms of μ, M_1, and M_2.

The Higgsino simplified model assumes direct production of Higgsino-like elec-

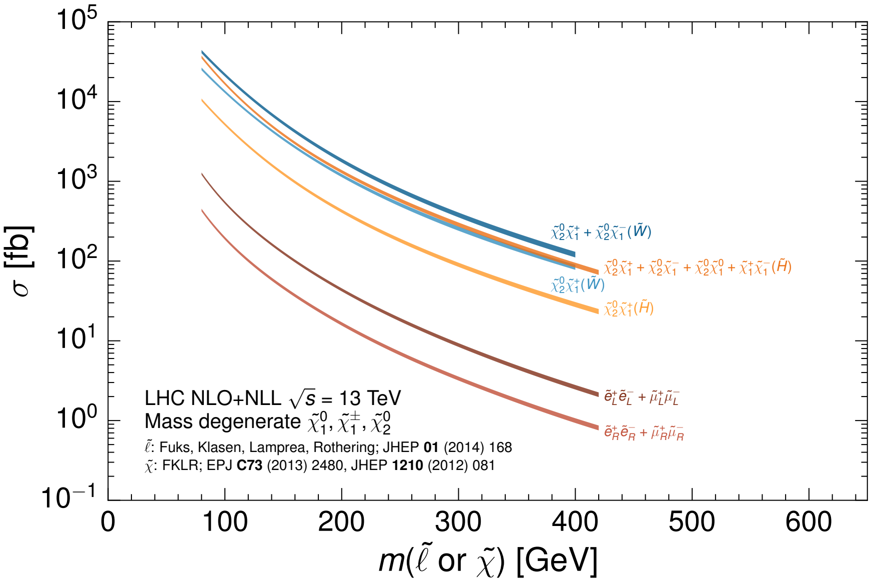

Figure 4.2: Cross-sections for electroweakino $\tilde{\chi}$ and slepton $\tilde{\ell}$ pair production in LHC pp collisions at $\sqrt{s} = 13$ TeV from LHC SUSY Cross-sections Working Group and Refs. [40, 41]. Total cross-sections are exhibited according to production process, with electroweakinos labelled as either being wino $\tilde{W}$ or Higgsino $\tilde{H}$ and slepton by their right- and left-handed chirality.

troweakino pairs that decay to W and Z bosons and a Higgsino-like LSP. The complete set of Higgsino signal samples include the production of $\tilde{\chi}_2^0\tilde{\chi}_1^+$ (N2C1p), $\tilde{\chi}_2^0\tilde{\chi}_1^-$ (N2C1m), $\tilde{\chi}_2^0\tilde{\chi}_1^0$(N2N1), and $\tilde{\chi}_1^+\tilde{\chi}_1^-$ (C1C1) on a grid of $\tilde{\chi}_1^0$ and $\tilde{\chi}_2^0$ masses. The chargino mass is set in terms of $m(\tilde{\chi}_1^0)$ and $m(\tilde{\chi}_2^0)$ as $m(\tilde{\chi}_1^\pm) = \frac{1}{2}[m(\tilde{\chi}_1^0) + m(\tilde{\chi}_2^0)]$. The signal cross-sections are calculated at next-to-leading order in the strong coupling, and next-to-leading-logarithm order for soft gluon corrections with Resummino v1.0.7 [40].

This analysis targets $\tilde{\chi}_2^0 - \tilde{\chi}_1^0$ mass splittings of $1 - 10$ GeV, which is not a natural spectrum in pure Higgsino models. Radiative corrections give rise to mass splittings of pure Higgsino states of order 200 MeV, and some level of wino or bino mixing is needed for larger mass splittings. Nevertheless, the models used to generate Higgsino signal samples assume pure Higgsinos. This choice mainly affects the signal cross-sections, which are be higher when wino/bino mixing is introduced. Higgsino signal samples use cross-sections according to electroweak mixing matrices that assume pure Higgsino states for all mass combinations of $\tilde{\chi}_2^0, \chi_1^0$, $\tilde{\chi}_1^+$, and $\tilde{\chi}_1^-$. Branching ratios for $\tilde{\chi}_2^0 \to Z^*\tilde{\chi}_1^0$ and $\tilde{\chi}_1^\pm \to W^*\tilde{\chi}_1^0$ are fixed at 100%. $Z^* \to \ell^+\ell^-$ branching fractions are modeled with SUSY-HIT v1.5b [36], which correctly treats the finite b-hadron and τ-lepton masses [36]. The branching ratio $Z^* \to \ell^+\ell^-$ depends on the invariant mass of the Z^*, which is driven by the mass splitting between $\tilde{\chi}_2^0$ and $\tilde{\chi}_1^0$. For example, the $Z^* \to \ell^+\ell^-$ branching ratio for a 60 GeV mass splitting is lower than for a mass splitting of 2 GeV by 46% in $Z^* \to e^+e^-$ and by 40% for $Z^* \to \mu^+\mu^-$. This happens as the Z^* mass falls below the threshold needed to produce a pair of heavy quarks or τ leptons. Branching ratio for $W^* \to \bar{\nu}_\ell\ell$ also increases as the mass splitting becomes sufficiently low to suppress decay widths to heavy quarks and τ-leptons.

Events are generated at leading order with up to two extra partons in the matrix element using MadGraph5_aMC@NLO v2.4.2 event generator [15] and the NNPDF23LO parton distribution function (PDF) set [21]. A PDF is a description of the parton momentum distribution inside a proton or other hadron in terms of the parton momentum fraction x for a given squared four-momentum scale Q^2. Electroweakinos are decayed via MadSpin [39, 18] with a two-lepton event filter. This means that events stored in the signal samples contained at least two final state leptons, even if one or more of the leptons came from a leptonic τ decay. The resulting events are interfaced with PYTHIA v8.186 [70] using the A14 [1] set of PDF tune parameters to model the parton shower, hadronization, and underlying event. The A14 set tune parameters correspond to the leading tune parameters in the CTEQ6L1 [64], MSTW2008LO [76], NNPDF23LO [21], and HERAPDF15LO PDF sets. Matrix element parton shower (ME-PS) jet matching is done with CKKW-L scheme [54], with the merging scale set to 15 GeV.

Figure 4.3 shows kinematic distributions in direct electroweakino production samples with masses ($m_{\tilde{\chi}_2^0}$, $m_{\tilde{\chi}_1^\pm}$, $m_{\tilde{\chi}_1^0}$) set to (120 GeV, 110 GeV, 100 GeV). Decays and parton showing are simulated the same as described above, and events are selected with at least two *signal* leptons with $p_{\mathrm{T}} > 3$ GeV, at least one *signal* jet with $p_{\mathrm{T}} > 20$ GeV, and $E_{\mathrm{T}}^{\mathrm{miss}} > 50$. In these plots, all four production mechanisms are shown: $\tilde{\chi}_2^0\tilde{\chi}_1^0$ in green, $\tilde{\chi}_2^0\tilde{\chi}_1^+$ in red, $\tilde{\chi}_2^0\tilde{\chi}_1^-$ in blue, and $\tilde{\chi}_1^\pm\tilde{\chi}_1^\mp$ in magenta. One distinct feature is that the dilepton invariant mass $m_{\ell\ell}$ in Figure 4.3 falls off sharply at the mass-difference $m_{\tilde{\chi}_2^0} - m_{\tilde{\chi}_1^0} = 20$ GeV. Other important characteristics are that the distance between the leading lepton pair $\Delta R_{\ell_1 \ell_2}$ is generally less than 1, and the angular distance between the leading jet and $E_{\mathrm{T}}^{\mathrm{miss}}$ $\Delta\phi_{j_1 - E_{\mathrm{T}}^{\mathrm{miss}}}$ is concentrated near π, which means they are mostly back-to-back. These kinematic variables and features will be explained more in Chapter 6.

Slepton simplified models exploit the direct pair production of selectrons $\tilde{e}_{L,R}$ and smuons $\tilde{\mu}_{L,R}$, where the L and R subscripts denote the left and right chirality. All four sleptons are assumed to be mass degenerate and decay to their Standard Model lepton partner and a $\tilde{\chi}_1^0$ 100% of the time [12]. Simulated slepton events were generated at tree level with MadGraph5_aMC@NLO v2.2.3 with the NNPDF23LO PDF set, with up to two additional partons in the mixing matrix. The MadGraph generation was interfaced with PYTHIA v8.186. ME-PS jet matching is done with the CKKW-L prescription with the merging scale set to one quarter the slepton mass.

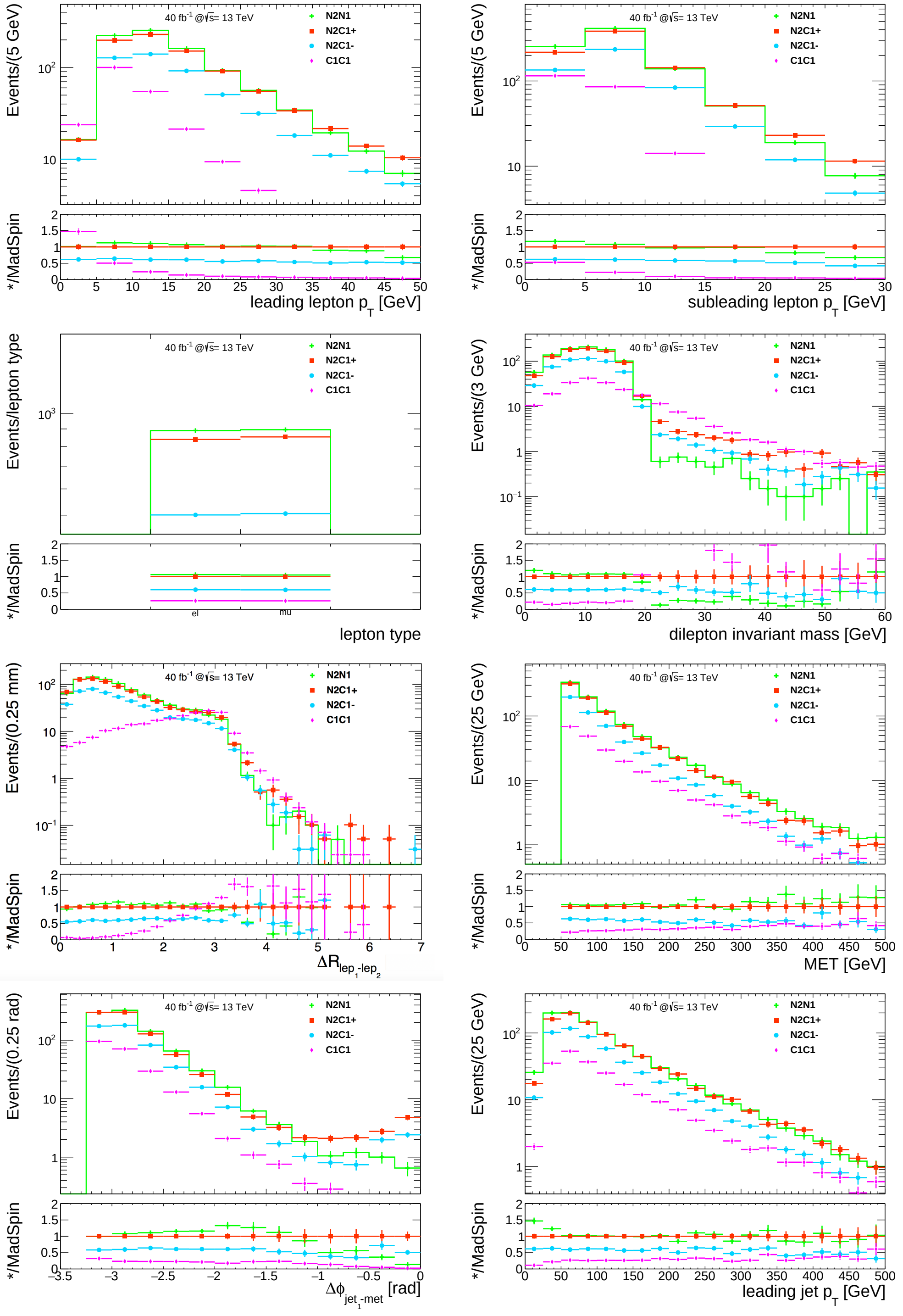

Figure 4.3: Kinematics distributions in electroweakino signal samples, with decays simulated with MadSpin and parton showing performed by PYTHIA v8.186.

4.3 Simulated SM Background Samples

Standard Model background processes were generated with different generators, summarized in Table 4.2. These processes include: W/Z + jets, $W/Z\gamma$, diboson, triboson $t\bar{t}$, single-top, Higgs, and rare three- and four-top production.

Modeling of leptonically decaying W or Z bosons in Z+jets processes is done with SHERPA 2.2.1 and NNPDF30NNLO PDF set. The matrix element is calculated with COMIX [45] and OpenLoops [33] with up to four additional partons at leading order, and jet merging is performed with SHERPA parton showers according to ME-PS @ NLO prescription. Samples are sliced according to the maximum energy sum of the jets (maxHTPTV) and quark flavor content. The dilepton invariant mass of the on shell Z+jets samples is required to be above 50 GeV, and the Z^*+jets samples are restricted to dilepton invariant mass between 10 GeV and 40 GeV with the leading and subleading leptons having p_{T} above 5 GeV. Low mass Drell-Yan samples extend down to invariant masses of 0.5 GeV for $Z(*)/\gamma^* \rightarrow e^+e^-/\mu^+\mu^-$, and down to 3.8 GeV for $Z(*)/\gamma^* \rightarrow \tau^+\tau^-$. The samples are inclusive in quark flavor and only available for maxHTPTV $>$ 280 GeV slice. W and Z production in association with an energetic photon is modeled with SHERPA and CT10 PDF set.

Diboson (WW, WZ, ZZ) and triboson (WWW, WWZ, etc.) samples are generated with SHERPA 2.2.1 and 2.2.2 and NNPDF30NNLO and CT10 PDF sets. Like in the W/Z+jets samples, the matrix element is calculated with COMIX and OpenLoops with up to two additional partons at next-to-leading order, and up to four

Process	Matrix Element	Parton Shower	PDF Sets
$Z^{(*)}/\gamma$+jets	SHERPA 2.2.1		NNPDF 3.0 NNLO
Diboson	SHERPA 2.1.1 / 2.2.1 / 2.2.2		NNPDF 3.0 NNLO
Triboson	SHERPA 2.2.1		NNPDF 3.0 NNLO
$t\bar{t}$	POWHEG-BOX v2	PYTHIA 6.428	NLO CT10
Singletop	POWHEG-BOX v1	PYTHIA 6.428	NLO CT10
$t+W$	POWHEG-BOX v1	PYTHIA 6.428	NLO CT10
$t\bar{t}+W/Z/\gamma^*$	MG5_aMC@NLO 2.3.3	PYTHIA 8.186	NNPDF 3.0 LO
$t\bar{t}+WW/t\bar{t}$	MG5_aMC@NLO 2.2.2	PYTHIA 8.186	NNPDF 2.3 LO
$t+Z$	MG5_aMC@NLO 2.2.1	PYTHIA 6.428	NNPDF 2.3 LO
$t+WZ$	MG5_aMC@NLO 2.3.2	PYTHIA 8.186	NNPDF 2.3 LO
$t+t\bar{t}$	MG5_aMC@NLO 2.2.2	PYTHIA 8.186	NNPDF 2.3 LO
$h(\rightarrow \ell\ell WW$	POWHEG-BOX v2	PYTHIA 8.186	NLO CTEQ6L1
$h+W/Z$	MG5_aMC@NLO 2.2.2	PYTHIA 8.186	NNPDF 2.3 LO

Table 4.2: Summary of the Monte Carlo generators used for each SM background sample production.

additional partons at leading order for some processes. In events with two leptons, the dilepton invariant mass is required to be above 4 GeV, with leading and subleading leptons masses above 5 GeV. Extended diboson samples have coverage in dilepton invariant mass down to 0.5 GeV.

Single top production (t- and s- channel), tW, and $t\bar{t}$ events were generated with POWHEG and interfaced with PYTHIA 6 for parton showering. The tZ process is filtered to have at least one lepton. Matrix elements were calculated with MadGraph5_aMC@NLO and parton showering was handled by PYTHIA 6. Rare events with three and four top quarks or $t\bar{t}$ in association with a Z, W, or WW bosons have matrix elements calculated with MadGraph5_aMC@NLO and showered with PYTHIA8 according to PDF set NNPDF30NNLO.

Single Higgs production through gluon-gluon fusion (ggF) and vector boson fusion (VBF) processes with fully leptonic decays are modeled using POWHEG and NLOCTEQ6L1 PDF set, and interfaced with PYTHIA 8 for parton showing. Processes involving a single Higgs in association with W or Z boson are modeled with PYTHIA 8 only, and using the NNPDF23LO PDF set.

Chapter 5

Physics Object Reconstruction and Identification

The term *reconstruction* describes the process of interpreting signal output from the detector and using that information to make measurements associated with actual physics objects. The ATLAS detector and its reconstruction algorithms are designed for efficient particle identification and precise energy and momentum measurement. Reliable tracking and vertexing are the building blocks for efficient reconstruction and identification of most objects. In this chapter, the assembly of tracks and vertices will first be described in Section 5.1. Next, reconstruction and identification variables are defined for directly and indirectly observable objects in Section 5.2. In ATLAS, these objects are; electrons, muons, jets, photons, and missing transverse energy and momentum. Lastly, Section 5.3 describes the techniques of overlap removal and isolation correction of closely-spaced leptons as subsequent treatment of reconstructed objects before analysis.

5.1 The Building Blocks

Track reconstruction, also called *tracking*, provides the important information needed for primary and secondary vertex reconstruction, charged particle reconstruction, jet flavor tagging, and photon conversions; therefore, track reconstruction algorithms must be swift, concise, and perform with high efficiency, low fake rates and with proper resolution on tracking parameters. In 2015, at the start of Run 2, the LHC extended the center-of-mass energy in proton-proton collisions to 13 TeV, and over the duration of Run 2, ramped up the instantaneous luminosity, pushing the average interactions per bunch crossing (μ) to above 40 by the end of Run 2. This extension of center-of-mass energy and instantaneous luminosity enhances the outlook of discovery while simultaneously slowing down track reconstruction and degrading its efficiency. Events with jet showers in the TeV range and τ leptons and b-hadrons that traverse multiple ID layers before decaying, occur at rates high enough to be considered in optimizing track and cluster reconstruction in Run 2 [3]. In the core of boosted hadronic jets and τ lepton decays, particles in flight are not very separated as they traverse the inner tracking layers, making separate energy deposits in the discrete sensors hard to resolve and near-by tracks hard to distinguish from each other. If tracking efficiency is low in events with high track density, mismeasurements are expected in identifying long-lived b-hadron and hadron τ decays and in calibrating the energy and mass of jets.

These mismeasurements will also cause induced $E_{\mathrm{T}}^{\mathrm{miss}}$, which is an important quantity for this search and many other Beyond Standard Model (BSM) searches.

The first step in track reconstruction involves preprocessing Pixel, SCT, and TRT information. Event-by-event charged track reconstruction in the pixel and SCT detectors starts with clustering groups of pixels and strips in each sensor that respond to an energy deposition above a set threshold and share a common edge or corner. These clusters form three-dimensional space-points that measure where a particle intersects the active material in the ID. In the pixel detector, each particle corresponds to one space-point, while in the SCT, clusters must be combined from both sides of a strip layer to obtain a three-dimensional position measurement.

The next step in tracking is called track finding. This involves combining Pixel and SCT hits into tracks seeds. Three consecutive hits are required for a track seed, and seeds with an additional compatible cluster are sent to a Kalman filter. In the last step, hits from all three of the tracking detectors are fit to make tracks using a global χ^2 function. These tracks are then given a score based on the fit quality and the number of holes and shared clusters. Tracks that fall below the minimum allowable score are rejected.

Reconstructed tracks are characterized using five *perigee* parameters at the point of closest approach to the beam axis.

- ***transverse impact parameter*** d_0 - track distance to the z-axis at the point of closest approach in the $x - y$ plane.

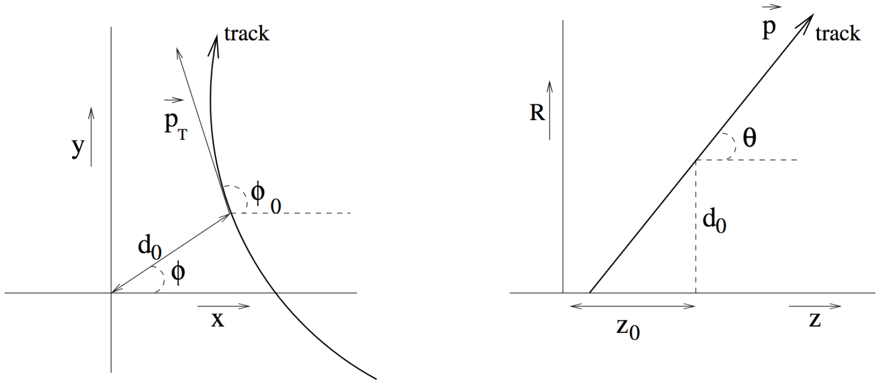

Figure 5.1: Sketch of ATLAS tracking parameters at the perigee in the $x - y$ plane (left) and the $r - z$ plane (right) [55]. In this diagram, the $r - z$ plane is denoted as $R - z$.

- ***longitudinal impact parameter*** z_0 - track coordinate along z at the point of closest approach.
- ***azimuthal angle*** $\phi_0 \equiv \tan^{-1} p_y/p_x$ - track angle to the x-axis in the x-y plane.
- ***polar angle*** θ_0 - track angle to the z-axis in the $r - z$ plane.
- ***charge over momentum*** q/p - electric charge divided by the track momentum.

The primary vertex is defined as space position in the detector of the initial pp interaction. Primary vertices are identified using inner detector tracks that satisfy a set of requirements. For a track to be considered in the construction of a primary vertex, it must have $p_{\mathrm{T}} > 400$ MeV, $|\eta| < 2.5$, between 9 ($|\eta| \leq 1.65$) and 11 ($|\eta| > 1.65$) silicon hits, at least 1 hit in the IBL or B-Layer, a maximum of one shared pixel hit or two shared SCT hits, no holes in the pixel layers, and no more that one hole in the SCT layers.

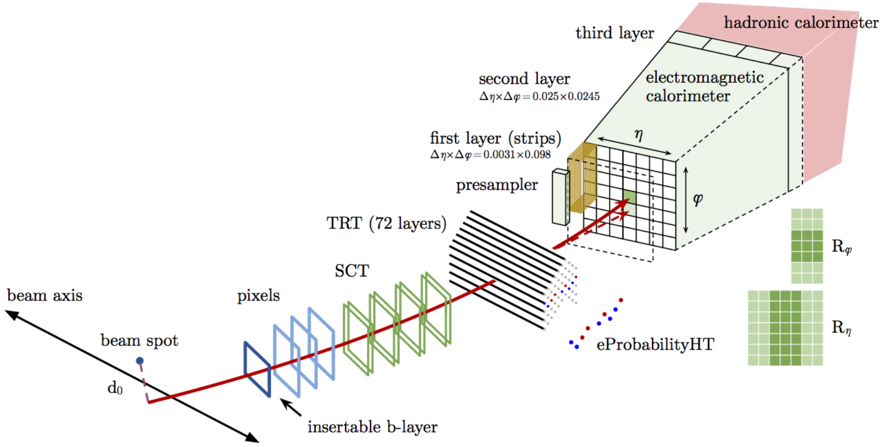

Figure 5.2: Schematic of an electron's flight in the ATLAS [73]

Any primary vertex must have at least two associated tracks for reconstruction [28].

5.2 Particle Identification and Reconstruction

Reconstructed and identified particles in ATLAS are leptons(e, μ, τ), photons, hadronic jets, which can further be identified as b-jets, and missing transverse momentum $E_{\mathrm{T}}^{\mathrm{miss}}$. This analysis does not use τ reconstruction. There are two categories of reconstructed objects: *baseline*, which is the most inclusive definition of an object and is typically used for preliminary event selection and background modeling, and *signal*, a more exclusive object definition that is a subset of *baseline* and is typically used in defining signal events. A summary of all the signal and baseline object definitions is given in Table 5.1.

Electron likelihood identification is a multivariate technique that uses signal and background probability density functions of discriminating variables to give an overall likelihood of being signal or background. Figure 5.2 depicts an electron in ATLAS moving through the ID detectors and into the calorimeters. Likelihood variables related to tracking include: number of hits on the inner-most pixel layer, hits in the Pixel detector, hits in the SCT+Pixel detectors, transverse impact parameter d_0, transverse impact parameter significance ($|d_0/\sigma_{d_0}|$), and fractional momentum lost in the detector, likelihood probability based on the transition radiation in the TRT, and track-cluster matching variables. Likelihood variables that discriminate on calorimeter measurements include: the ratio of transverse energy in the TileCal to the energy in the LAr, the ratio of energy in the last LAr layer to the energy in the full LAr[1], the lateral electromagnetic shower shape in the second LAr layer, shower width in the LAr strip layers. Signal and background probabilities combine into a single discriminant on which a cut is applied to define a likelihood-based operating point. Operating points in the electron likelihood identification menu are *VeryLoose, Loose, LooseAndBLayer, Medium*, *Tight*. *LooseAndBLayer* uses the same likelihood as *Loose* and also requires a hit in the inner-most Pixel layer. All operating points use the same discriminating variables to ensure tighter operating points are subsets of the more loose operating points. The electron efficiencies for the *Loose*, *Medium*, and *Tight* LH working points are compared in Figure 5.3.

Muons in this analysis use a cut-based identification technique that first identifies muon tracks in the ID and MS and combines them to form complete muon tracks. Identification working points are provided based on the muon reconstruction efficiency

---

[1] This variable is only used for electrons with $p_{\mathrm{T}} < 80$ GeV.

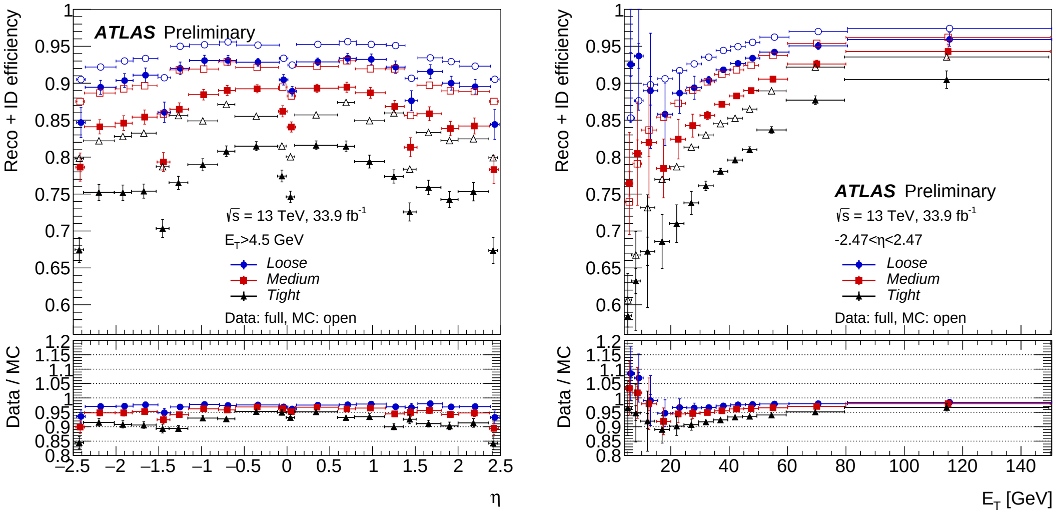

Figure 5.3: Electron efficiency as a function of η (left) and E_{T} (right) in the *Loose*, *Medium*, and *Tight* LH identification algorithms

and background rejection they provide. Muon ID *Medium* is the default working point used by physics analyses in ATLAS [8]. The *Medium* ID achieves over 95% muon efficiency for muons 4 GeV $< p_{\mathrm{T}} <$ 20 GeV, and over 60% background rejection. Muon identification efficiencies measured versus muon p_{T} by the Muon Combined Performance Group in ATLAS are shown in Figure 5.4.

Lepton isolation is quantified by two main variables, track isolation and calorimeter isolation. Track isolation is determined by the transverse momenta of tracks in some cone around the track with a radius determined by the lepton p_{T}. Calorimeter isolation is dictated by the sum of the transverse energy in the topological clusters (topo clusters), which are cell clusters seeded by calorimeter cells with energy more than four times greater than the noise threshold in the cell. Topo clusters are then expanded to neighboring cells with energy more than twice above the noise threshold, and finally a

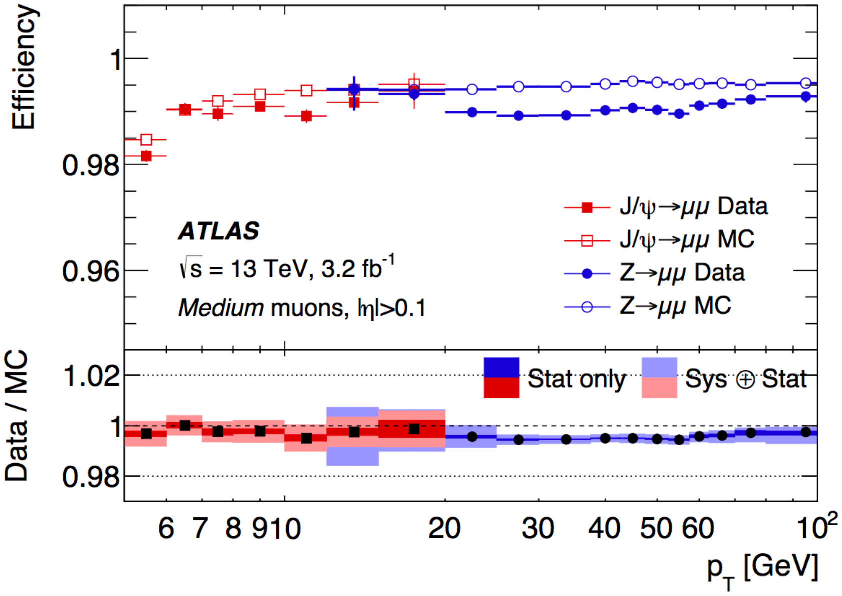

Figure 5.4: Reconstruction efficiency for *Medium* muon identification working point as a function of muon p_{T}, in the region $0.1 < |\eta| < 2.5$ [8].

last layer of calorimeter cells with energy above zero are added to the cluster. To measure the isolation energy, the lepton energy in the isolation topo cluster is removed and the topo cluster is corrected for pileup and any lepton energy that was not subtracted away. Final isolation cuts using the track- and calorimeter-based isolation variables are are classified as either *fixed cut* or *gradient*. Fixed cut means the working point provides fixed efficiencies across the $\eta - p_{\mathrm{T}}$ plane. Gradient means the efficiencies are p_{T}-dependent, but still flat in η. Isolation working points are provided for for three grades of isolation: *Loose, Medium,* and *Tight*, and can be based on track isolation, calorimeter isolation, or both. The *Tight* working points will provide the best rejection of backgrounds, but the lowest efficiencies.

Baseline electrons are seeded from energy deposits in the EM calorimeter and reconstructed with algorithms using EM calorimeter clusters that are matched to inner detector tracks. Baseline electrons must pass a p_{T} threshold of 4.5 GeV and exclusively travel through the central detector region $|\eta| < 2.47$. A longitudinal impact parameter requirement of $|z_0 \sin\theta| < 0.5$ mm is also applied. This analysis uses likelihood based identification criteria only. Baseline electrons are required to satisfy *VeryLooseLLH* identification while signal electrons must pass *Tight* identification plus *GradientLoose* isolation criteria. Signal electrons also require transverse impact parameter significance $|d_0/\sigma(d_0)| < 5$. Electron energy deposits in the LAr are generally narrow in η and ϕ and mostly concentrated in the first two sampling layers.

Muon information primarily comes from tracks in the muon spectrometer that are often matched charged tracks in the inner detector. Baseline muons are reconstructed with algorithms that combine tracks from the inner detector and muon spectrometer to form muon candidates. They must pass a p_{T} threshold of 4 GeV and be in fiducial region $|\eta| < 2.5$. Like with electrons, muon likelihood identification is used, and the discriminating variables are extended to include information from tracks in the muon spectrometer. Baseline muons are also expected to satisfy *Medium* identification standards and have a transverse impact parameter $|z_0 \sin\theta| < 0.5$ mm. Signal muons must also satisfy *FixedCutTightTrackOnly* isolation criteria and a transverse impact parameter significance of $|d_0/\sigma(d_0)| < 3$.

Lepton identification, isolation, impact parameter cuts, fiducial acceptance and p_{T} threshold all effect the lepton efficiencies and result in the efficiencies shown in

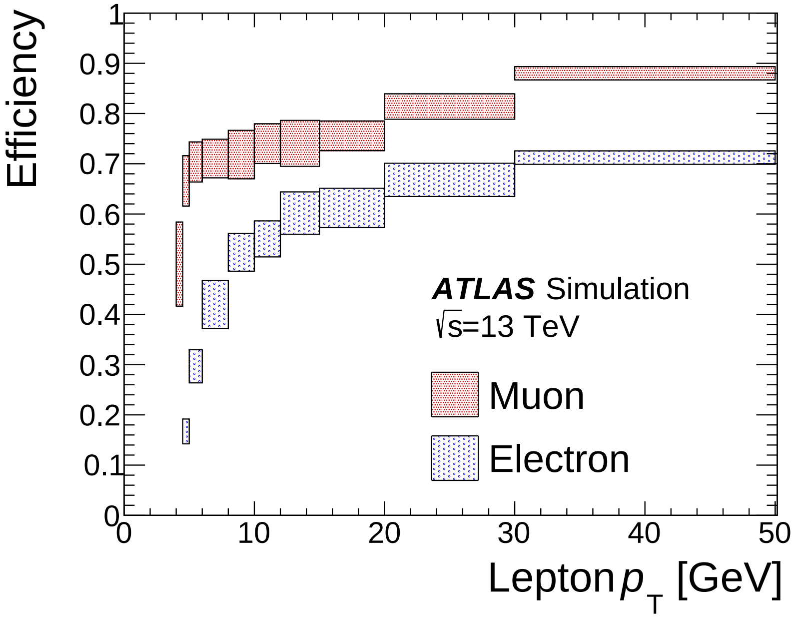

Figure 5.5: Signal lepton efficiencies for electrons and muons, averaged over all Higgsino and slepton samples. Efficiencies are shown for leptons within detector acceptance, and with lepton p_{T} within a factor of 3 of $\Delta\ m(\tilde{l}\tilde{\chi}_1^0)$ for slepton samples or within a factor of 3 of $\Delta\ m(\tilde{\chi}_2^0\tilde{\chi}_1^0)/2$ for Higgsino samples. Uncertainty bands represent the range of efficiencies observed across all signal samples for the given p_{T} bin. The η dependence is consistent with values reported in ATLAS combined performance papers, shown in Figures 5.3 and 5.4.

Figure 5.5 that range from roughly 50% for low-p_{T} muons and up to 90% for higher p_{T}. For electrons the efficiencies are roughly 20% for low p_{T} electrons, and increase up to $\sim$ 65%. This is the average over signal samples that fall within some range, where the most compressed signal samples used to evaluate the low p_{T} leptons and so on.

Baseline jets are built from locally-calibrated three-dimensional topologically clustered calorimeter cells. Topological clustering here is the same as described in

Selection Criteria	**Electrons**	**Muons**	**Jets**
Baseline			
Reco Algorithm	*author 16 veto*		
Kinematic	$p_{\mathrm{T}} > 4.5$ GeV, $\lvert\eta\rvert < 2.47$	$p_{\mathrm{T}} > 4$ GeV, $\lvert\eta\rvert < 2.5$	$p_{\mathrm{T}} > 20$ GeV, $\lvert\eta\rvert < 4.5$
Impact Parameter	$\lvert z_0 \sin\theta\rvert < 0.5$ mm –	$\lvert z_0 \sin\theta\rvert < 0.5$ mm –	
Identification	*VeryLooseLLH*	*Medium*	
Isolation	–	–	
Clustering			Anti-k_t R = 0.4 EMTopo
Jet Vertex Tagging			–
b-tagging			–
Signal			
Reco Algorithm	*author 16 veto*		
Kinematic	$p_{\mathrm{T}} > 4.5$ GeV, $\lvert\eta\rvert < 2.47$	$p_{\mathrm{T}} > 4$ GeV, $\lvert\eta\rvert < 2.5$	$p_{\mathrm{T}} > 30$ GeV, $\lvert\eta\rvert < 2.8$
Impact Parameter	$\lvert z_0 \sin\theta\rvert < 0.5\ mm$, $\lvert d_0/\sigma(d_0)\rvert < 5$	$\lvert z_0 \sin\theta\rvert < 0.5\ mm$, $\lvert d_0/\sigma(d_0)\rvert < 3$	
Identification	*Tight*	*Medium*	
Isolation	*GradientLoose*	*FixedCutTightTrackOnly*	
Clustering			Anti-k_t R = 0.4 EMTopo
Jet Vertex Tagging			*JVT Medium*
b-tagging			$p_{\mathrm{T}} > 20$, $\lvert\eta\rvert < 2.5$ MV2c10 FixedCutBeff 85%

Table 5.1: Summary of object definitions

the discussion of lepton isolation. Jets are constructed using anti-k_t clustering algorithms [31] with radius parameter R = 0.4. Baseline jets must pass a p_{T} threshold of 20 GeVand be in fiducial region $|\eta| < 4.5$. Also, jets within $|\eta| < 2.5$ originating from b-hadrons are tagged with the 2-dimensional multivariate b-tagging algorithm MV2c10 with an 85% working point. Signal jets are further restricted to fiducial region $|\eta| < 2.8$, and pileup jets are removed using the jet vertex tagger (JVT) with *Medium* working point efficiency applied to jets with $p_{\mathrm{T}} > 60$ GeV and $|\eta| < 2.4$.

Well calibrated energy and momentum measurements of the directly observable objects is important for construction of the particles that traverse the detector without interacting. These "missing" particles carry away energy and momentum which is recovered by requiring momentum conservation in the plane transverse to the beam pipe. The vector quantity missing transverse momentum $\vec{p}_{\mathrm{T}}$ is the negative vector sum of the transverse momentum of all the identified physics objects (electrons, muons, jets, photons) plus an additional soft term. The scalar magnitude of the missing transverse momentum vector gives the missing transverse energy $E_{\mathrm{T}}^{\mathrm{miss}}$. The soft term is constructed from all the tracks not associated with any physics object, but are associated with the primary vertex. Therefore, $E_{\mathrm{T}}^{\mathrm{miss}}$ is adjusted for the best possible calibration of the jets and other identified physics objects and still independent of pileup in the soft term. Pileup jets are removed with a jet vertexing technique that matches jets to primary vertices with track-vertex tagging.

5.3 Special Treatment of Reconstructed Objects

Once objects are reconstructed and identified, special algorithms often need to be run before these objects can be used. For this analysis, these final steps were the removal of overlapping objects and the isolation correction of closely-spaced leptons.

Overlap removal is performed to prevent double counting of physics objects by removing objects based in their separation ΔR in detector coordinates η and ϕ, given by:

$$\Delta R_{p_1p_2} = \sqrt{(\eta_{p_1} - \eta_{p_2})^2 + (\phi_{p_1} - \phi_{p_2})^2} \tag{5.1}$$

First, jet-electron overlap removal is performed. If $\Delta R_{\text{jet,electron}}$ is less than 0.2 and the the jet is not tagged as a b-jet, the jet is removed and the electron is kept. If the jet is identified as a b-jet, then the jet is kept and the electron object is removed since the electron is most likely from the semi-leptonic decay of a b-hadron. If $\Delta R_{\text{jet,electron}}$ is less than 0.4, we remove the electron and keep the jet. Similarly, if the $\Delta R_{\text{jet,muon}}$ is less than 0.4, we remove the muon and keep the jet unless the jet has less than three tracks; in which case the muon will be kept and the jet is discarded. Lastly, we perform overlap removal on photons and other objects. It is common that electron and muon objects will also be included in the photon container since they pass the LAr shower requirements, so overlapping photons and leptons will typically result in the photon object being removed from the photon container. If $\Delta R_{\text{photon,electron}}$ is less than 0.4 we remove the photon and keep the electron. If $\Delta R_{\text{photon,muon}}$ is less than 0.4, we remove the photon and keep the muon. If $\Delta R_{\text{photon,jet}}$ is less than 0.4, we keep the photon and remove the jet.

Soft leptons in a boosted system often have small angular separation, especially when they are products of a low-mass Z^* decay. These boosted leptons often lie within each other's isolation cones, leading to efficiency loss for very small mass splittings. The top rows of Figures 5.6 and 5.7 illustrate the efficiency loss for nearby leptons within $\Delta R < 0.4$ and dilepton invariant mass ($m_{\ell\ell}$) < 5 GeV using an electroweakino signal sample with $m_{\tilde{\chi}_2^0} - m_{\tilde{\chi}_1^0} = 10$ GeV. This loss is corrected by using a dedicated tool that checks for baseline leptons that fail the isolation criteria due to another nearby lepton within its isolation cone and removes tracks associated with the nearby lepton from the track isolation sum. If the nearby lepton is an electron, the topocluster E_T is also removed from the calorimeter isolation sum. The corrected isolation variables are then reanalyzed using the original isolation working point. The bottom rows of Figures 5.6 and 5.7 exhibit the recovered dilepton efficiency in simulation after applying the isolation correction tool. Figure 5.8 shows the effect of this correction on low invariant mass dilepton pairs in data. The data are chosen such that $\Delta\phi(E_{\mathrm{T}}^{\mathrm{miss}}, p_t^{j_1}) < 1.5$ to avoid the signal region, which selects $\Delta\phi(E_{\mathrm{T}}^{\mathrm{miss}}, p_t^{j_1}) > 2.0$, as explained in Chapter 6.

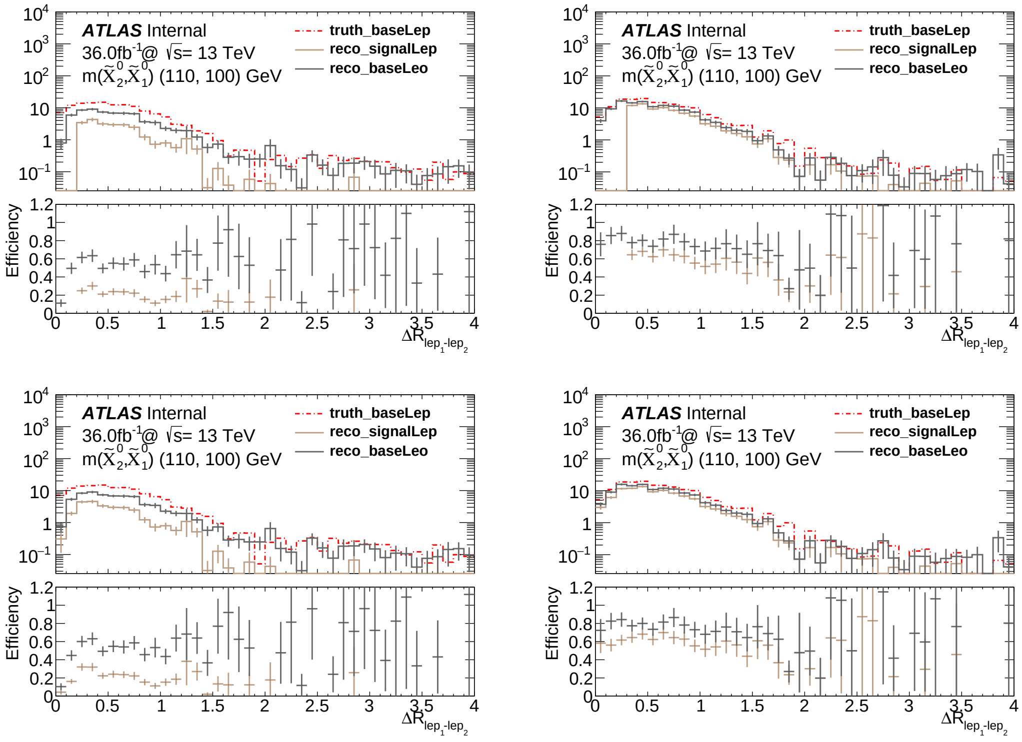

Figure 5.6: Dilepton Δ R distribution before LepIsoCorrection (top) and after LepIsoCorrection (bottom) for the *ee*-channel (left) and $\mu\mu$-channel (right), using electroweakino signal samples with m$(\tilde{\chi}_2^0, \tilde{\chi}_1^0) = (110, 100)$ GeV.

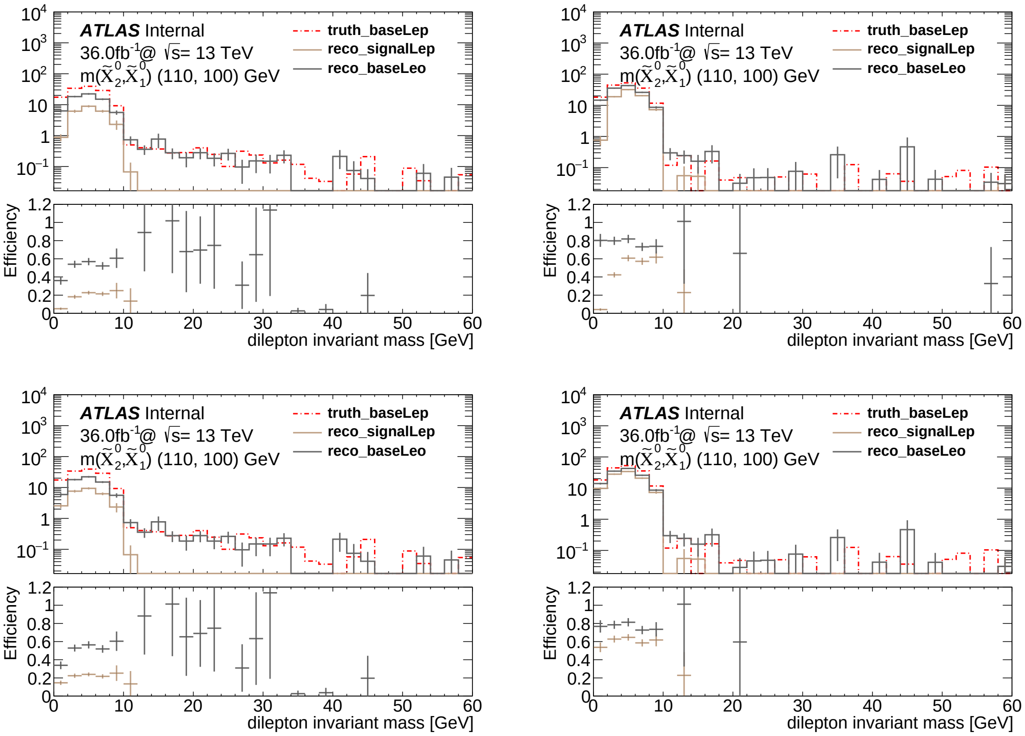

Figure 5.7: Dilepton invariant mass distribution before LepIsoCorrection (top) and after LepIsoCorrection (bottom) for the ee-channel (left) and $\mu\mu$-channel (right), using electroweakino signal samples with m($\tilde{\chi}^0_2\tilde{\chi}^0_1$) $(110, 100)$ GeV.

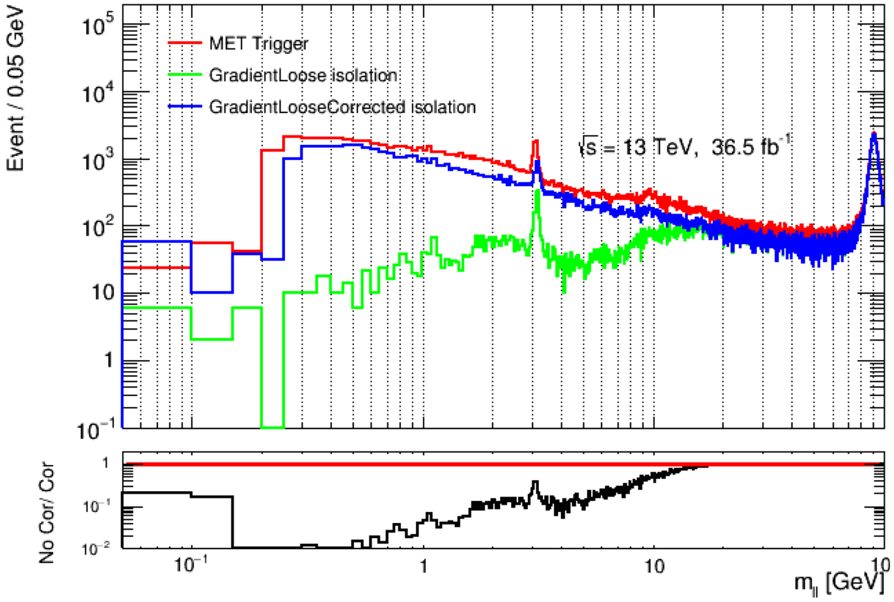

Figure 5.8: Impact of the `NearbyLepIsoCorrection` tool on the efficiency of low-mass dilepton pairs in data. The data are shown in a region with $\Delta\phi(E_{\mathrm{T}}^{\mathrm{miss}}, p_t^{j1}) < 1.5$ to avoid the signal region. Events are triggered with the inclusive-$E_{\mathrm{T}}^{\mathrm{miss}}$ trigger. The red trend shows events with two baseline leptons without applying any isolation; the green shows the impact of applying `GradientLoose` isolation; the blue shows the result of the `NearbyLepIsoCorrection` applied to the `GradientLoose` sample.

Chapter 6

Signal Region Optimization

This analysis relies on external predictions of signal and background processes in data to help interpret observations, and for observations to be meaningful, it is imperative to search for new physics where its presence is not excessively drowned out by SM backgrounds. To achieve this, a signal enriched region in phase space, called a *signal region* (SR), is defined through a series of selection cuts on kinematic variables, targeting events where predicted signal yields display a significant excess over the estimated backgrounds, which are discussed in Chapter 7.

In the chapter, the discriminating variables that define the Higgsino and slepton signal regions are expounded first in Section 6.1, then the signal regions are defined in Section 6.2. To exploit the Higgsino and sleptons models fully, they are treated by separate analyses in independent signal regions, but the compressed nature of these models makes many of their SR cuts overlap. Section 6.2 is broken into two sections, first detailing the common SR selection cuts in Section 6.2.1, then the signal region cuts applied to the Higgsino and slepton SRs individually in Section 6.2.2.

6.1 Discriminating Variables

This section will define all the discriminating variables used to define the signal regions, and the next section will detail how they are applied to the SRs, and what benefits or limitations they present. These discriminating variables are presented in terms of three classifications, those that exploit the lepton information, those that exploit the topology of the jets and the $E_{\mathrm{T}}^{\mathrm{miss}}$, and those that exploit both.

The variables that depend only on lepton information are: lepton flavor, lepton charge, the distance between a lepton pair ($\Delta R_{\ell\ell}$), and the invariant mass of a lepton pair ($m_{\ell\ell}$). Lepton flavor refers to it being an electron or a muon, and the lepton charge is its positive or negative electric charge. The distance between leptons $\Delta R_{\ell\ell}$ is defined in terms of detector coordinates η and ϕ, as:

$$\Delta R_{\ell\ell} = \sqrt{(\eta_{\ell_1} - \eta_{\ell_2})^2 + (\phi_{\ell_1} - \phi_{\ell_2})^2} \tag{6.1}$$

The invariant mass is taken from the energy-momentum 4-vector in Equation 6.2, and the invariant mass of two leptons is the magnitude of the summed lepton energy-momentum vectors, as in Equation 6.3.

$$m^2 = E^2 - \mathbf{p}^2 \tag{6.2}$$

$$m_{\ell\ell} = \sqrt{(E_{\ell_1} + E_{\ell_2})^2 - (\mathbf{p}_{\ell_1} + \mathbf{p}_{\ell_2})^2} \tag{6.3}$$

The variables that exploit the jet and $E_{\mathrm{T}}^{\mathrm{miss}}$ topology are: $E_{\mathrm{T}}^{\mathrm{miss}}$, the p_{T} of the leading[1] jet ($p_{\mathrm{T}}(j_1)$), the number of b-tagged jets ($N_{b-\mathrm{jets}}$), the angular separation between missing transverse momentum and the leading jet ($|\Delta\phi(j_1, p_{\mathrm{T}}^{\mathrm{miss}})|$), and the minimum angular separation between missing transverse momentum and the nearest reconstructed jet ($\min|\Delta\phi(jets, p_{\mathrm{T}}^{\mathrm{miss}})|$). The angular separation between two objects in ATLAS is measured in terms of the azimuthal ϕ, so $|\Delta\phi(j_1, p_{\mathrm{T}}^{\mathrm{miss}})|$ is simply the difference in the ϕ coordinates of the leading jet and $E_{\mathrm{T}}^{\mathrm{miss}}$ in the interval [-π, π]. Similarly, to calculate the minimum separation between the $E_{\mathrm{T}}^{\mathrm{miss}}$ and the reconstructed jets, $|\Delta\phi(j, p_{\mathrm{T}}^{\mathrm{miss}})|$ is measured for each jet and the minimum value is selected.

The variables that use combined information from the leptons, jets, and $E_{\mathrm{T}}^{\mathrm{miss}}$ are described below. The transverse mass of the combined leading lepton and missing transverse momentum ($m_{\mathrm{T}}^{\ell_1}$) is defined by the energy-momentum 4-vector using the transverse quantities:

$$m_{\mathrm{T}}^{\ell_1} = \sqrt{2p_{\mathrm{T}}^{\ell_1} E_T^{\mathrm{miss}}(1 - \cos\Delta\phi(\ell_1, p_{\mathrm{T}}^{\mathrm{miss}})} \tag{6.4}$$

The di-tau invariant mass ($m_{\tau\tau}$), expressed in Equations 6.5 - 6.7, is used by this analysis to veto the $Z \to \tau\tau$ background. This analysis follows the procedure of approximating $m_{\tau\tau}$ in References [48, 20].

$$m_{\tau\tau}^2\left(p_{\ell_1}, p_{\ell_2}, \mathbf{p}_{\mathrm{T}}^{\mathrm{miss}}\right) \equiv 2p_{\ell_1} \cdot p_{\ell_2}(1+\xi_1)(1+\xi_2) \tag{6.5}$$

The parameters ξ_1 and ξ_2 are determined by solving Eq 6.6, and the sign of $m_{\tau\tau}^2$ is given by Eq 6.7.

$$\mathbf{p}_{\mathrm{T}}^{\mathrm{miss}} = \xi_1 \mathbf{p}_{\mathrm{T}}^{\ell_1} + \xi_2 \mathbf{p}_{\mathrm{T}}^{\ell_2} \tag{6.6}$$

---

[1] In reference to particle objects, the term *leading* always refers that type of object in an event with the highest measured p_{T}. *Subleading* always refers to the second-highest p_{T} object in the event.

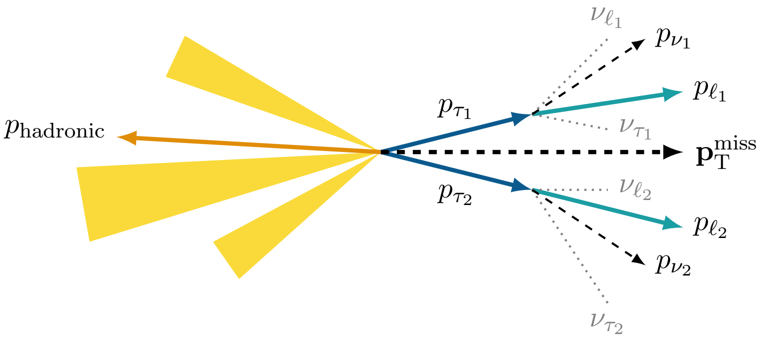

Figure 6.1: Schematic illustrating the fully leptonic $(Z \to \tau\tau)$ + jets system motivating the construction of $m_{\tau\tau}$.

$$m_{\tau\tau}\left(p_{\ell_1}, p_{\ell_2}, \mathbf{p}_{\mathrm{T}}^{\mathrm{miss}}\right) = \begin{cases} \sqrt{m_{\tau\tau}^2}\ ; & m_{\tau\tau}^2 \geq 0, \\ -\sqrt{|m_{\tau\tau}^2|}\ ; & m_{\tau\tau}^2 < 0. \end{cases} \tag{6.7}$$

The purpose of this variable is to reconstruct the di-tau invariant mass of the fully leptonic $Z \to \tau\tau$ process from the measurable quantities in the event, which are the 4-momenta of the two leptons and the missing transverse momentum. A $(Z \to \tau\tau)$ + jets event within the signal region relies on the Z boson recoiling off the jet activity, boosting the decaying di-tau system oppositely along the jet axis. A schematic of this process is displayed in Figure 6.1. This kick from the jets causes the leptons and neutrinos to remain close to a single axis, so the 4-momentum of the invisible neutrino system p_{ν_i}, for the i^{th} τ in the event, can be well approximated by a simple rescaling of the lepton 4-momentum.

Lastly, the stransverse mass $(m_{T2}^{m_\chi})$, detailed in Equations 6.8 - 6.10, is similar to $m_{\mathrm{T}}^{\ell_1}$ in that it relates lepton transverse momentum and $E_{\mathrm{T}}^{\mathrm{miss}}$ [**?**].

$$m_{T2}^{m_\chi}(p_{\mathrm{T}}^{\ell_1}, p_{\mathrm{T}}^{\ell_2}, p_{\mathrm{T}}^{\mathrm{miss}}) = \min_{\mathbf{q}_T}\Big(\max[m_T(p_{\mathrm{T}}^{\ell_1}, q_T; m_\chi), m_T(p_{\mathrm{T}}^{\ell_2}, p_{\mathrm{T}}^{\mathrm{miss}} - q_T; m_\chi)]\Big) \tag{6.8}$$

Here, q_T is the sum of the transverse momentum vectors of each of the invisible particles, as in Eq 6.9. The transverse mass of the leptons and invisible particles is shown explicitly in Eq 6.10.

$$q_T = p_{\mathrm{T}}^{\chi,1} + p_{\mathrm{T}}^{\chi,2} \tag{6.9}$$

$$m_T\left(\mathbf{p}_T^{\ell}, \mathbf{q}_T, m_\chi\right) = \sqrt{m_\ell^2 + m_\chi^2 + 2\left(E_T^{\ell} E_T^{q} - \mathbf{p}_T \cdot \mathbf{q}_T\right)} \tag{6.10}$$

To understand the $m_{T2}^{m_\chi}$ variable, one must consider a process like in Figure 2.2 where a *pp* collision produces a pair of sleptons that immediately decay to visible leptons and invisible LSPs. The stransverse mass essentially determines a bound on the masses of the invisible particles as a function of the p_{T} of the two leading leptons and the measured missing transverse momentum. It is mathematically defined by the minimum value of q_T for the maximum of the transverse mass of the leptons and invisible particles for some set value of m_χ. For the remainder of this text, we arbitrarily choose $m_\chi = 100$ GeV, and so m_{T2}^{100} is the variable used in the signal regions. This choice reflects the absence of any strong dependence in signal sensitivity for the other choices that we considered, which are reviewed in Appendix B.

6.2 Signal Region Definitions

Two types of signal region are defined to optimize signal sensitivity for electroweakino models and slepton models separately used in this analysis. Higgsino and

Variable	Requirement
N_{leptons}	Exactly two signal leptons
Lepton charge and flavor	$e^{\pm}e^{\mp}$ or $\mu^{\pm}\mu^{\mp}$
Leading electron (muon) $p_{\text{T}}^{\ell_1}$	$> 5(5)$ GeV
Subleading electron (muon) $p_{\text{T}}^{\ell_2}$	$> 4.5(4)$ GeV
$m_{\ell\ell}$	[1, 3] or [3.2, 60] GeV
$\Delta R_{\ell\ell}$	> 0.05
$E_{\text{T}}^{\text{miss}}$	> 200 GeV
Leading jet $p_{\text{T}}(j_1)$	> 100 GeV
$\lvert\Delta\phi(j_1, E_{\text{T}}^{\text{miss}})\rvert$	> 2.0
$\min\lvert\Delta\phi(all\ jets, E_{\text{T}}^{\text{miss}})\rvert$	> 0.4
$N_{b-\text{jet}}^{20}$, 85% WP	Exactly zero
$m_{\tau\tau}$	< 0 or > 160 GeV

Table 6.1: Summary of common Higgsino and slepton SR cuts

slepton SRs are uniquely specified using $m_{\ell\ell}$ and m_{T2}^{100}, as detailed in Sections 6.2.2.1 and 6.2.2.2. Many of the Higgsino and slepton SR cuts overlap. These will be described first in Section 6.2.1.

6.2.1 Common Preselection

Common SR selection cuts are summarized in Table 6.1. SR events are required to contain two signal leptons, an intermediate amount of $E_{\text{T}}^{\text{miss}}$, and at least one jet. Figure 6.2 shows the leading lepton p_{T}, subleading lepton p_{T}, and $\Delta R_{\ell\ell}$ distributions after the background-only fit, with all common preselection cuts applied, excluding the variable being displayed, in which case a blue arrow marks the intended cut value. The leading lepton is required to have $p_{\text{T}} > 5$ GeV and the subleading lepton is required to have $p_{\text{T}} > 4.5$ GeV if it is an electron, or $p_{\text{T}} > 4$ GeV if it is a muon. This is chosen because electron and muon calibrations only go as low as 4.5 GeV and 4 GeV.

Below this energy there are large inefficiencies from cluster reconstruction and the fake backgrounds blowup. Furthermore, the two leptons are required to make a same-flavor-opposite-sign[2] (SFOS) pair. For Higgsino signals, this prefers the dominant leptonic decay mode of the Higgsino, via an off-shell Z^*. In slepton signals, light flavor sleptons always decay to two oppositely-charged leptons of the same flavor. Also, selecting OSSF pairs allows the SR to target the decays of this analysis and leaves different flavor or same-signed lepton pairs to be exploited in the control and validation regions. Collinear leptons from photon conversions are filtered out with a restriction on the minimum $\Delta R_{\ell\ell}$ between the leptons of 0.05 and an invariant mass cut of $m_{\ell\ell} > 1$ GeV.

When heavy invisible particles are present in the final state, $E_{\mathrm{T}}^{\mathrm{miss}}$ becomes an important discriminating variable. This analysis uses inclusive $E_{\mathrm{T}}^{\mathrm{miss}}$ triggers to collect data, which imposes its own lower limit. A selection of $E_{\mathrm{T}}^{\mathrm{miss}} > 200$ GeV is made to be fully efficient in the $E_{\mathrm{T}}^{\mathrm{miss}}$ trigger, even though the optimal cut to achieve the best signal over background discrimination might be lower. In signal events, the $E_{\mathrm{T}}^{\mathrm{miss}}$ is correlated with the p_{T} of the leading jet. Since the leptons are so light compared to the mass of the LSP, the boost from the hadronic recoil is mostly given to the $E_{\mathrm{T}}^{\mathrm{miss}}$. If the $p_{\mathrm{T}}(j_1)$ threshold is too high, it will reduce the sensitivity in $E_{\mathrm{T}}^{\mathrm{miss}}$, but if it is too low, other subleading jets may contribute significantly to the recoil of the system. For these reasons, the leading jet p_{T} threshold is set to 100 GeV. Figure 6.3 shows $E_{\mathrm{T}}^{\mathrm{miss}}$, $p_{\mathrm{T}}(j_1)$, $\Delta\phi(j_1, p_{\mathrm{T}}^{\mathrm{miss}})$ distributions after the background-only fit with all common preselection cuts applied. In the plot of leading jet p_{T}, the signal distributions

---

[2] *Sign* is another term for positive or negative electric charge

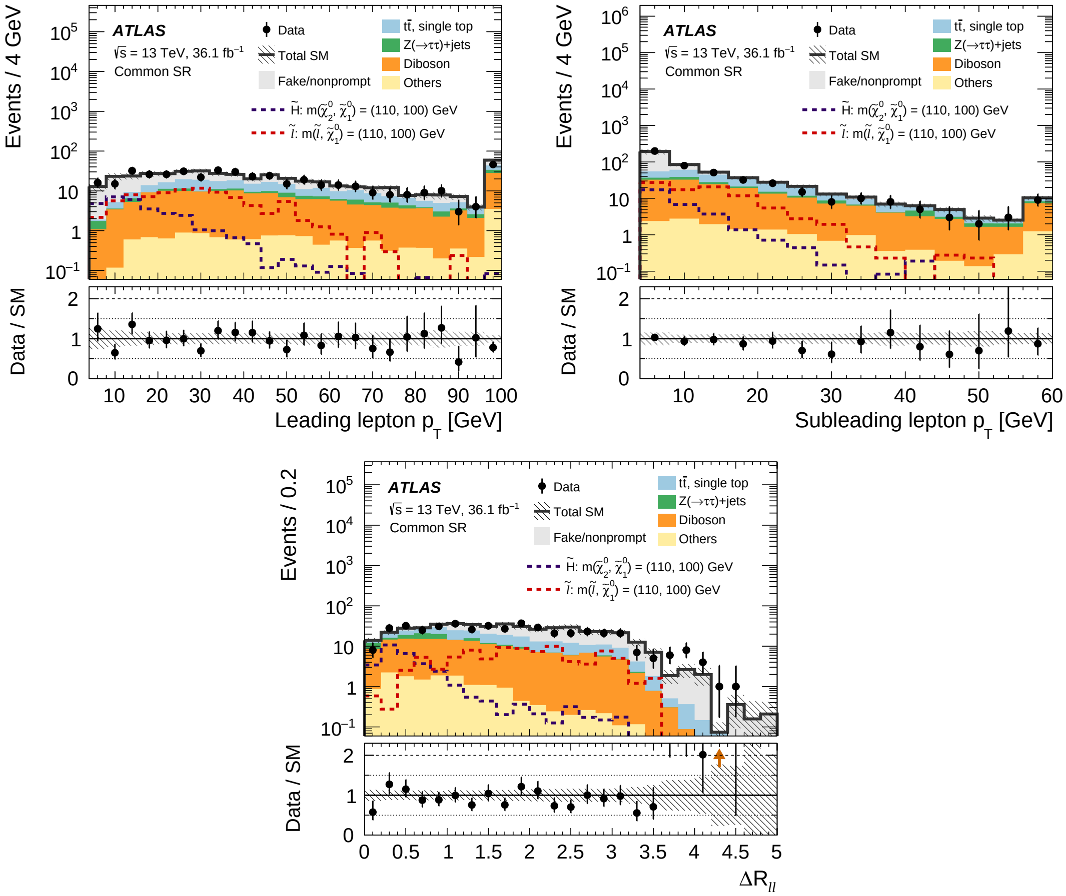

Figure 6.2: Leading lepton p_{T}, subleading lepton p_{T}, and $\Delta R_{\ell\ell}$ distributions after the background-only fit with all common preselection cuts applied. The category 'Others' contains rare backgrounds from triboson, Higgs boson, and three or four top-quark production processes. The first (last) bin includes underflow (overflow). Benchmark Higgsino $\tilde{H}$ and slepton $\tilde{\ell}$ signals are overlaid as dashed lines. Orange arrows in the Data/SM panel indicate values that are beyond the y-axis range.

peak around 200 GeV. In $\Delta\phi(j_1, p_{\mathrm{T}}^{\mathrm{miss}})$, both Higgsino and slepton signals are highly concentrated in events with a large angular separation between the jets and $E_{\mathrm{T}}^{\mathrm{miss}}$. The intermediate $E_{\mathrm{T}}^{\mathrm{miss}}$ requirement sculpts the topology of the signal to prefer events where the direction of the $E_{\mathrm{T}}^{\mathrm{miss}}$ and the direction of the leading jet are opposite each other in the transverse plane. Because of the small mass-splittings between the electroweakinos or the sleptons and the LSP, the LSPs will typically only produce significant enough $E_{\mathrm{T}}^{\mathrm{miss}}$ to pass the $E_{\mathrm{T}}^{\mathrm{miss}} > 200$ GeV cut when they are aligned opposite to the hadronic initial state radiation in the transverse plane. A cut on $\Delta\phi(j_1, p_{\mathrm{T}}^{\mathrm{miss}}) > 2.0$ is established to take advantage of this topology and cut away backgrounds that are more agnostic to it.

Figure 6.4 displays $\min \Delta\phi(jets, p_{\mathrm{T}}^{\mathrm{miss}})$, $N_{b-\mathrm{jets}}$, and $m_{\tau\tau}$ distributions after the background-only fit with all common preselection cuts applied. The variable $\min \Delta\phi(jets, p_{\mathrm{T}}^{\mathrm{miss}})$ considers the minimum angular separation between $p_{\mathrm{T}}^{\mathrm{miss}}$ and the nearest reconstructed jet. In the top left plot in Figure 6.4, low values of $\min \Delta\phi(jets, p_{\mathrm{T}}^{\mathrm{miss}})$, where the $E_{\mathrm{T}}^{\mathrm{miss}}$ is more aligned with the jet, are dominated by background events. Jet mismeasurements tends to align the the $p_{\mathrm{T}}^{\mathrm{miss}}$ with some of the jets, leading to a small $\Delta\phi$ between them. This mostly occurs in QCD and Z+jets events. To reduce $E_{\mathrm{T}}^{\mathrm{miss}}$ induced by jet mismeasurements, a minimum requirement is set at $\min \Delta\phi(jets, p_{\mathrm{T}}^{\mathrm{miss}}) > 0.4$, which cuts away only a small portion of signal events. The $N_{b-\mathrm{jets}}$ distribution of Figure 6.4 shows a noticeable enhancement in top-quark backgrounds in events with at least one b-tagged jet, while the Higgsino and slepton signals do not. Vetoing on events with b-jets effectively discriminates against top-quark backgrounds. Lastly, the variable $m_{\tau\tau}$

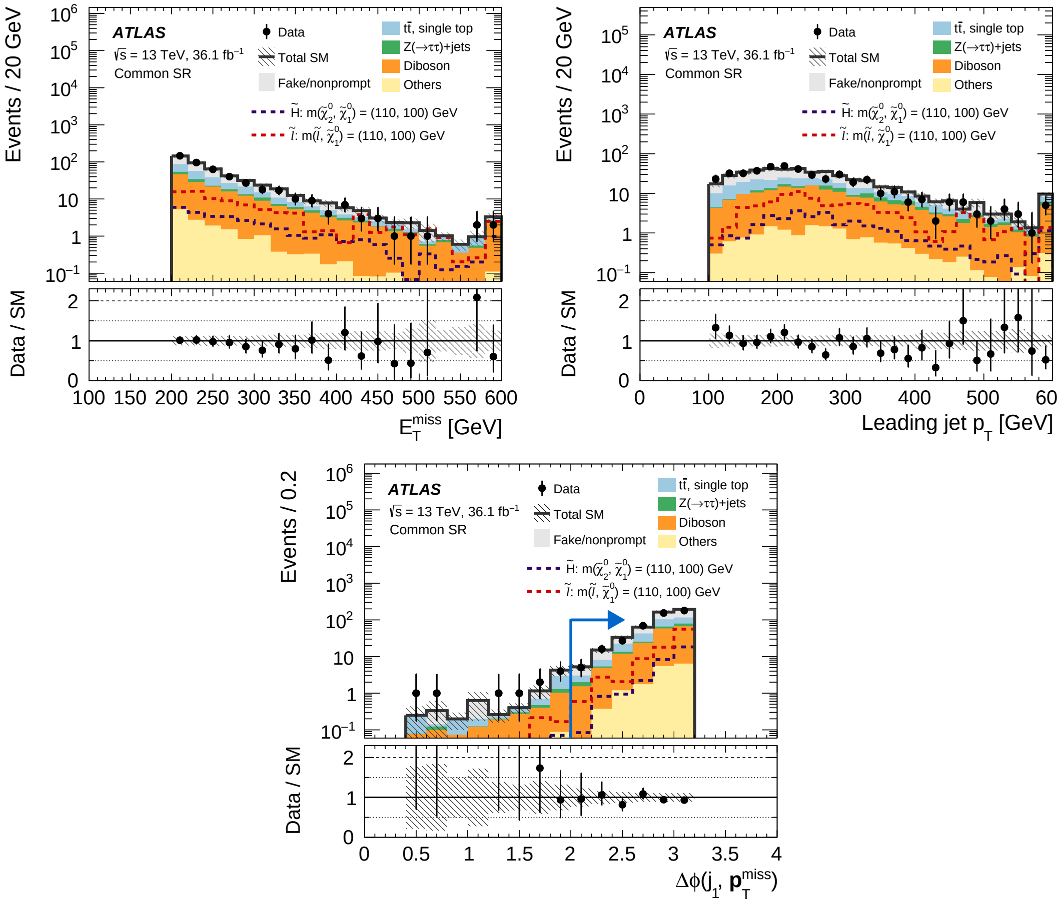

Figure 6.3: Distributions of $E_{\mathrm{T}}^{\mathrm{miss}}$, $p_{\mathrm{T}}(j_1)$, and $\Delta\phi(j_1), p_{\mathrm{T}}^{\mathrm{miss}}$ after the background-only fit with all common preselection cuts applied. Blue arrows in the upper panel denote the final requirement used to define the common SR, otherwise all selections are applied. The category 'Others' contains rare backgrounds from triboson, Higgs boson, and three or four top-quark production processes. The first (last) bin includes underflow (overflow). Benchmark Higgsino $\tilde{H}$ and slepton $\tilde{\ell}$ signals are overlaid as dashed lines. Orange arrows in the Data/SM panel indicate values that are beyond the y-axis range.

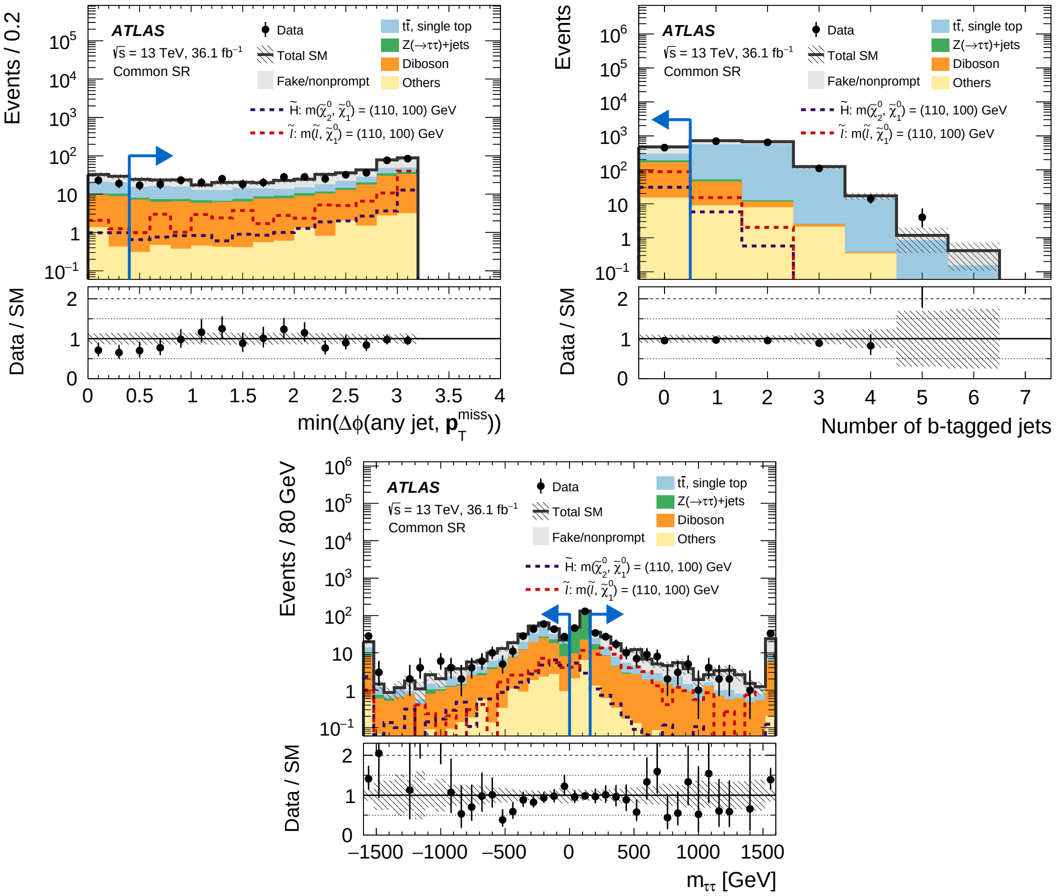

Figure 6.4: Distributions of $\min \Delta\phi(jets, p_{\mathrm{T}}^{\mathrm{miss}})$, number of b-jets, and $m_{\tau\tau}$ after the background-only fit with all common preselection cuts applied. Blue arrows in the upper panel denote the final requirement used to define the common SR, otherwise all selections are applied. The category 'Others' contains rare backgrounds from triboson, Higgs boson, and three or four top-quark production processes. The first (last) bin includes underflow (overflow). Benchmark Higgsino $\tilde{H}$ and slepton $\tilde{\ell}$ signals are overlaid as dashed lines.

reconstructs the invariant mass of an assumed ditau event, and, like in Figure 6.4, is dominated by $Z(\to \tau\tau)$+jets events in the region around the Z-mass. To reduce this background, $m_{\tau\tau} = [0, 160]$ GeV is excluded from the signal regions.

6.2.2 Model-Specific Signal Regions

Before jumping into a description of the individual signal regions, let's recall the differences between the Higgsino and slepton processes, shown again in Figure 6.5. Both processes include an ISR jet, and produce an SFOS lepton pair and invisible LSPs. These common threads lead to the common selection cuts discussed above. The main difference between Higgsino and slepton production is the source of the lepton pair. In electroweakino production, the leptons both come from the decay of the Z^*, and therefore, are kinematically limited by its mass. In slepton production, the leptons arise from separate slepton decays with an associated LSP. The next section dissects the signal region cuts specific to the two types of model due to nature of the leptons in the events.

6.2.2.1 Higgsino Signal Regions

In electroweakino signals, the boosted decay of the $\tilde{\chi}_2^0$ tends to align the leading lepton with a sizable fraction of the $p_{\mathrm{T}}^{\mathrm{miss}}$, resulting in smaller $m_T^{\ell_1}$ values. In background events with W bosons, the $m_T^{\ell_1}$ variable can reconstruct the leptonically decaying W, so cutting on $m_T^{\ell_1} < 70$ GeV can reduce the contribution from $t\bar{t}$, WW/WZ, and $W(\to \ell\nu)$+jets backgrounds. The $m_T^{\ell_1}$ distribution in Figure 6.6 illustrates these fea-

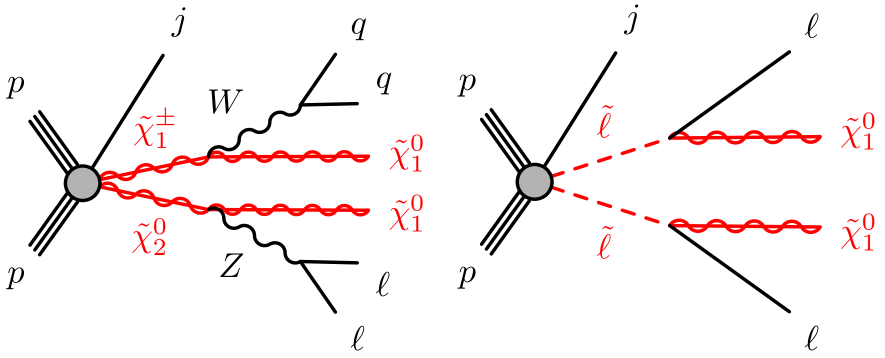

Figure 6.5: Feynman diagram of direct Higgsino (left), and direct slepton (right) production.

tures. The fake background contribution, which is dominantly from $W(\rightarrow \ell\nu)$+jets, is clearly enlarged around the W-mass peak. Also, the Higgsino signal acceptance quickly depreciates below 70 GeV while the slepton acceptance remains fairly flat, making this cut effective for improving signal/background for electroweakinos, and not so much for the sleptons.

The leptons in compressed electroweakino signals are also likely to have small separation, while most backgrounds do not. For this reason, $\Delta R_{\ell\ell}$ tends to be a powerful discriminator for Higgsinos and a cut of $\Delta R_{\ell\ell} < 2.0$ is added to Higgsino SR selection. Slepton SRs do not include this cut because the lepton topology is quite different. In a non-boosted system, the sleptons will decay nearly back-to-back. Including an ISR jet kick can align the decays and subsequent leptons a bit, but the majority pf slepton event have $\Delta R_{\ell\ell} > 1.0$ The $\Delta R_{\ell\ell}$ distributions in Figure 6.2 illustate this difference between the Higgsino and slepton processes.

For intermediate values of $E_{\mathrm{T}}^{\mathrm{miss}}$, SM diboson and $t\bar{t}$ background processes

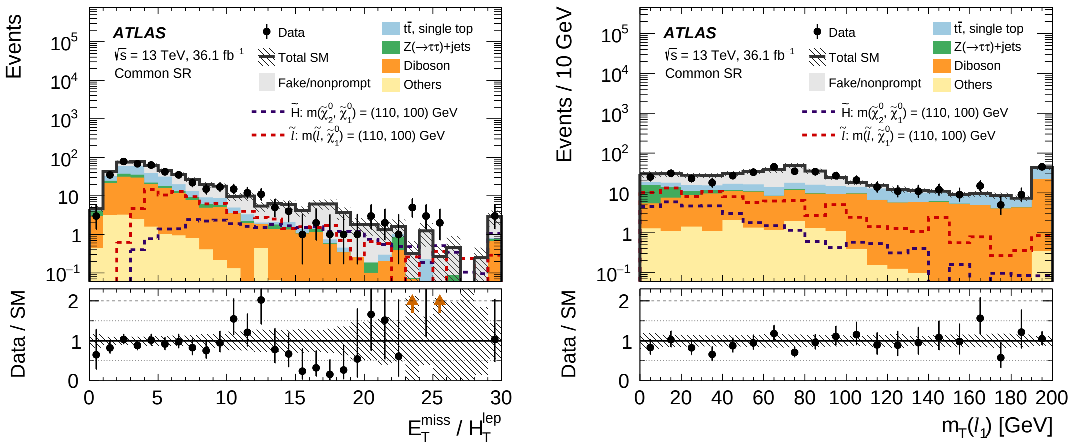

Figure 6.6: Distributions after the background-only fit of kinematic variables used to define selections common to all signal regions, i.e. not including requirements specific to the electroweakino or slepton SR definitions. Benchmark Higgsino $\tilde{H}$ and slepton $\tilde{\ell}$ signals are overlaid as dashed lines. Orange arrows in the Data/SM panel indicate values that are beyond the y-axis range.

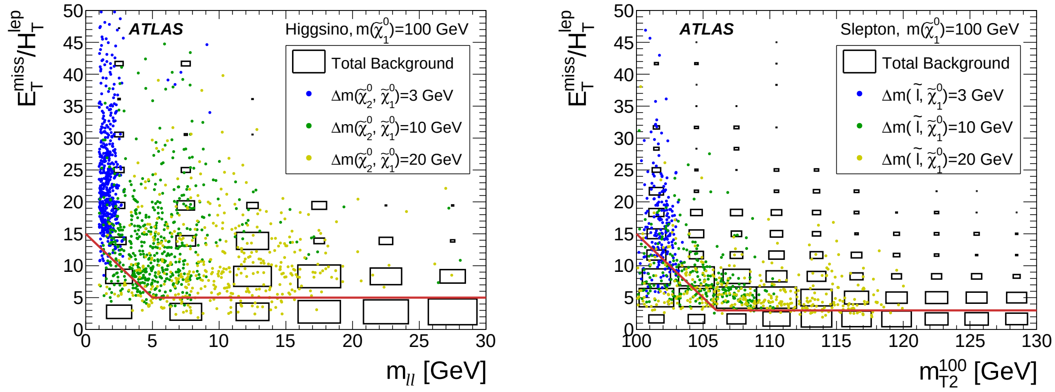

Figure 6.7: Distributions of $E_{\mathrm{T}}^{\mathrm{miss}}/H_{\mathrm{T}}^{\mathrm{lep}}$ for the Higgsino (left) and slepton (right) selections, after applying all signal region cuts except those on the $E_{\mathrm{T}}^{\mathrm{miss}}/H_{\mathrm{T}}^{\mathrm{lep}}$, $m_{\ell\ell}$, or m_{T2}^{100}. The red solid line indicates the cut applied in the signal region; events in the region below the red line are rejected.

produce hard leptons, likewise diminishing the values of $E_{\mathrm{T}}^{\mathrm{miss}}/H_{\mathrm{T}}^{\mathrm{lep}}$. In compressed electroweakino and slepton events, the $E_{\mathrm{T}}^{\mathrm{miss}}$ is mostly from the boost of the hadronic recoil. The recoiling jet affects the heavier invisible particle much more than it effects the lighter leptons; therefore, these signal events prefer larger values of $E_{\mathrm{T}}^{\mathrm{miss}}/H_{\mathrm{T}}^{\mathrm{lep}}$. Figure 6.7 shows the $E_{\mathrm{T}}^{\mathrm{miss}}/H_{\mathrm{T}}^{\mathrm{lep}}$ distribution for Higgsino samples after applying all the signal region cuts except $E_{\mathrm{T}}^{\mathrm{miss}}/H_{\mathrm{T}}^{\mathrm{lep}}$, $m_{\ell\ell}$, or m_{T2}^{100}.

The dilepton invariant mass can both suppress backgrounds as well as exploit special features of the Higgsino model. In compressed $\tilde{\chi}_2^0 \to Z^* \tilde{\chi}_1^0$ decays, the Z^* is produced very far from its mass peak because the only kinematic phase space available to produce the Z comes from the mass-difference $M_{\tilde{\chi}_2^0} - M_{\tilde{\chi}_1^0}$. The invariant mass of the SFOS lepton pair reconstructs the $Z*$, and therefore bound by the $\tilde{\chi}_2^0, \tilde{\chi}_1^0$ mass-splitting. For this reason, the inclusive and exclusive Higgsino SRs are binned in $m_{\ell\ell}$.

Variable	Selection Cut
$E_{\mathrm{T}}^{\mathrm{miss}}/H_{\mathrm{T}}^{\mathrm{leptons}}$	$> \mathrm{Max}\,(5.0, 15 - 2 \cdot m_{\ell\ell}/\text{ GeV})$
$\Delta R_{\ell\ell}$	< 2.0
$m_{\mathrm{T}}^{\ell_1}$	< 70 GeV

Electroweakino SRs [GeV]							
Exclusive							
$SRee - m_{\ell\ell}$, $SR\mu\mu - m_{\ell\ell}$	$[1, 3]$	$[3.2, 5]$	$[5, 10]$	$[10, 20]$	$[20, 30]$	$[30, 40]$	$[40, 60]$
Inclusive							
$SR\ell\ell - m_{\ell\ell}$	$[1, 3]$	$[1, 5]$	$[1, 10]$	$[1, 20]$	$[1, 30]$	$[1, 40]$	$[1, 60]$

Table 6.2: Higgsino specific SR cuts and definitions. SR definitions are expressed as bins in $m_{\ell\ell}$.

The largest value of $m_{\ell\ell}$ included in any Higgsino SR bin is 60 GeV, which is the maximum electroweakino mass-splitting that is relevant for this analysis. The inclusive SRs are defined by a maximum $m_{\ell\ell}$, below which all events are selected. The exclusive SRs are orthogonal in $m_{\ell\ell}$ selection and are define by a min and max bin value. All Higgsino specific cuts and the inclusive and exclusive SR definitions are summarized in Table 6.2.

6.2.2.2 Slepton Signal Regions

Much like dilepton invariant mass discriminant for electroweakino signals, slepton events are subject to a kinematic endpoint defined by the 'stransverse' mass $m_{T2}^{m_\chi}$, which is a function of the measures momentum of the leading two leptons p_{ℓ_1}, p_{ℓ_2}, the measured p_{T}, and the hypothesized invisible particle mass m_χ. For the pair of semi-invisible particles in the slepton signal, $m_{T2}^{m_\chi}$ is always less than the parent slepton mass $m_{\tilde{\ell}}$ when the hypothesized m_χ mass is set to the neutralino mass in the underlying process, but this adds a level of complexity to the signal regions that does gain much signal

Variable	Selection Cut
$E_{\mathrm{T}}^{\mathrm{miss}}/H_{\mathrm{T}}^{\mathrm{leptons}}$	$> \mathrm{Max}\left(3.0, 15 - 2 \cdot \left[m_{\mathrm{T2}}^{100}/\ \mathrm{GeV} - 100\right]\right)$

	Slepton SRs [GeV]					
Exclusive						
$SRee - m_{T2}^{100}$, $SR\mu\mu - m_{T2}^{100}$	$[100, 102]$	$[102, 105]$	$[105, 110]$	$[110, 120]$	$[120, 130]$	$[130, \infty]$
Inclusive						
$SR\ell\ell - m_{T2}^{100}$	$[100, 102]$	$[100, 105]$	$[100, 110]$	$[100, 120]$	$[100, 130]$	$[100, \infty]$

Table 6.3: Slepton specific signal region cuts

sensitivity. There is negligible change in signal acceptance when m_χ is set to the exact LSP hypothesized mass, as detailed in Appendix B, so m_χ is fixed at 100 GeV. This defines the lower kinematic endpoint in m_{T2}^{100} for slepton signals. Requiring $m_{T2}^{100} < m_{\tilde{\ell}}$, various mass scenarios can be probed in the slepton-neutrino mass plane. Standard Model backgrounds do not display this kind of feature since the invisible particles are massless neutrinos, therefore there is no such enhancement in background when making this requirement. In fact, in the compressed region of the slepton-neutrino mass plane, events populate an even narrower region in m_{T2}^{100}, giving this variable more discriminating power. Inclusive and exclusive slepton SRs are binned in m_{T2}^{100}. The inclusive SRs are defined by a maximum m_{T2}^{100}, below which all events are selected. The exclusive SRs are orthogonal in m_{T2}^{100} selection and are defined by a min and max bin value.

6.2.3 SR Acceptance and Efficiency

With the signal regions fully defined, sample acceptance and efficiency plots are shown in Figure 6.8 for the most inclusive Higgsino and slepton signal regions. Signal acceptance α is defined as the ratio of truth events that pass all signal region cuts over the total number of truth events:

$$\alpha = \frac{N_{\text{truth,selected}} \times BR_{Z\to ll} \times \epsilon_{\text{filter}}}{N_{\text{truth,total}}} \tag{6.11}$$

This quantity measures the impact of signal region cuts on signal yields and does not take into account detector effects. Signal efficiency ϵ is defined as the ratio of reconstructed events that pass all signal region cuts to the total number of truth events that pass all signal region cuts:

$$\epsilon = \frac{N_{\text{reco,selected}}}{N_{\text{truth,selected}}} \tag{6.12}$$

This quantity measures the impact of detector inefficiencies on signal. Other interesting versions of these plots are efficiency within acceptance and signal leakage. Appendix A includes acceptance, efficiency, efficiency within acceptance, and signal leakage for each inclusive Higgsino and slepton signal region.

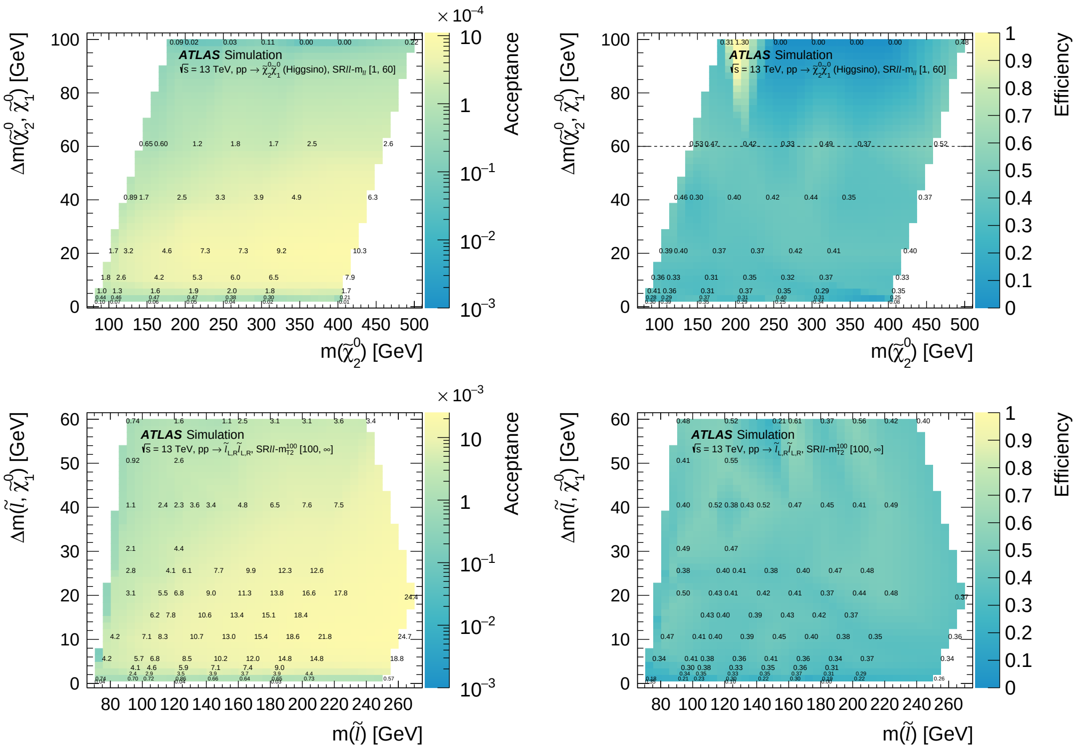

Figure 6.8: Signal acceptance (left) and efficiency (right) for electroweakino $\tilde{\chi}_2^0$, $\tilde{\chi}_1^0$ production in the most inclusive Higgsino signal region SR-$m_{\ell\ell}$ $[1, 60]$ GeV (top) and for slepton pair production in the most inclusive slepton signal region SR-m_{T2}^{100} $[100, \infty]$ GeV (bottom)

Chapter 7

Background Estimation

Signal regions are specifically designed to be enriched in a signal process of interest, but SM backgrounds can still be present and need to be understood. This chapter will detail how the SM backgrounds are evaluated for this analysis. The general background estimation strategy is first discussed in Section 7.1. Next, Section 7.2 focuses on the estimation of irreducible ($t\bar{t}$, $Z(\rightarrow \tau\tau)+\text{jets}$, $VV \rightarrow \ell\nu\ell\nu$) backgrounds, and the last Section 7.3 describes the estimate of backgrounds from instrumental $E_{\mathrm{T}}^{\mathrm{miss}}$. The fake and non-prompt lepton background estimates are discussed in Chapter 8.

7.1 Summary of estimation strategy

The vast majority, and possibly all, LHC *pp* collisions interact only through Standard Model processes, some of which lead to final states that look the same as Higgsino or slepton signals and pass the signal region cuts. We classify two types of backgrounds, irreducible and reducible. Irreducible backgrounds are Standard Model processes that produce the same particle final state (two soft leptons, $E_{\mathrm{T}}^{\mathrm{miss}}$, and jets) as our BSM final state. In this case, Monte Carlo simulation is robust enough to model these background processes so their rates can be estimated in the data. Reducible backgrounds arise from Standard Model events that in theory should not produce the same final state as signal events; and yet, because of mismeasurements inside the detector, can still pass signal selection cuts. Table 7.1 succinctly summarizes, from greatest to least contribution, the processes that constitute the SM background in the SRs and the methods used to estimate them.

For a two soft-lepton, $E_{\mathrm{T}}^{\mathrm{miss}}$, and hard jet analysis, the dominant irreducible backgrounds come from diboson, $t\bar{t}$, tW, and $Z(\rightarrow \tau\tau)$+jets processes. Diboson events are WW, ZZ, and WZ. These backgrounds are evaluated with Monte Carlo and tested in a validation region that exploits $E_{\mathrm{T}}^{\mathrm{miss}}/H_T$. Fully leptonic WW production is the most prominent diboson background in the two lepton plus $E_{\mathrm{T}}^{\mathrm{miss}}$ signal region. The fully leptonic WW decays lead to two real leptons that likely have opposite charge, but are not necessarily of the same flavor. The real $E_{\mathrm{T}}^{\mathrm{miss}}$ in the event comes from the neutrinos, and an additional hard jet must be present. Fully leptonic WZ events can also make their way into the SRs since there is certainly an oppositely signed same flavor lepton pair from the Z, and real $E_{\mathrm{T}}^{\mathrm{miss}}$ from the neutrino in the W decay, but since the SRs require exactly two leptons, the third lepton must either fall outside of acceptance or fail p_{T}, identification, or isolation cuts for this kind of event be selected. Semi-leptonic ZZ and WZ processes can pass SR selection if one Z decays into a proper lepton pair and the quarks from the other vector boson induce enough $E_{\mathrm{T}}^{\mathrm{miss}}$ from mismeasured jet energies to pass the $E_{\mathrm{T}}^{\mathrm{miss}}$ trigger. Lastly, in the fully hadronic cases, there are four jets, two of which must be misidentified as leptons, leaving the others to induce a significant amount of $E_{\mathrm{T}}^{\mathrm{miss}}$. Fully hadronic contributions are negligible.

The top and $Z(\rightarrow \tau\tau)$+jets backgrounds are estimated with a semi-data-driven approach where the estimate is done in dedicated control regions enriched in the particular process. A top quark decays to a b-quark and a W-boson nearly 100% of the time. In the event that a b-jet fails the b-tagging algorithm, each $t\bar{t}$ event can look like a diboson event with additional jets and some special topological features. If both the W-bosons decay leptonically, the event has two real leptons and $E_{\mathrm{T}}^{\mathrm{miss}}$ from the neutrinos. Similarly, insufficiently b-tagged tW events with leptonically decaying W-bosons also supply two real leptons, jets, and real $E_{\mathrm{T}}^{\mathrm{miss}}$ from neutrinos. Even when one or both of the W-bosons decay hadronically, the tW and $t\bar{t}$ processes can still produce backgrounds in the SRs. This happens when one or two of the signal leptons arise from jets faking leptons in the detector. These contributions are accounted for in the data-driven fake estimates. In $Z(\rightarrow \tau\tau)$+jets, each leptonically decaying τ-lepton produces one charged lepton and two neutrinos. Together with the hadronic ISR radiation, that combination produces a final state with two leptons, real $E_{\mathrm{T}}^{\mathrm{miss}}$ from the four neutrinos, and additional jets. On the occasion that these leptons form an SFOS pair, this process will mimic signal events.

Drell-Yan events, in which a quark and an antiquark annihilate into a lepton/antilepton pair through the virtual exchange of a γ^{*}/Z, contribute to the SM backgrounds in Higgsino and slepton samples when enough $E_{\mathrm{T}}^{\mathrm{miss}}$ is generated through jet energy

Background Process	Origin in Signal Region	Estimation Strategy
Fakes (W+jets, $VV(1\ell)$, $t\bar{t}(1\ell)$)	Reducible, jet fakes 2^{nd} ℓ	Fake factor, same sign VR
$t\bar{t}$, $tW(2\ell)$	Irreducible, b-jet fails ID	CR using b-tagging
$Z \rightarrow (\tau\tau)$+jets	Irreducible ($\tau\tau \rightarrow \ell\nu\ell\nu$)	CR using $m_{\tau\tau}$
VV	Irreducible ($\ell\ell\ell$), missed 3^{rd} ℓ	MC, VR using $E_{\mathrm{T}}^{\mathrm{miss}}/H_T$
$Z \rightarrow (ee, \mu\mu)$+jets	Instrumental $E_{\mathrm{T}}^{\mathrm{miss}}$	Monte Carlo (MC)
Low mass Drell-Yan	Instrumental $E_{\mathrm{T}}^{\mathrm{miss}}$	MC, data-driven cross check
Other rare	Irreducible leptonic decays	MC

Table 7.1: Background estimation summary

mismeasurements. Requiring $E_{\mathrm{T}}^{\mathrm{miss}}$ above 200 GeV in the SRs reduces the rate of this process; therefore, Monte Carlo techniques are sufficient for estimating Drell-Yan backgrounds. Other contributions estimated with pure Monte Carlo techniques are rare processes from: Higgs, triboson, and multi-top[1] production. While detector effects that result in the misidentification of physics objects are not well modeled in simulation, misidentification still occurs during reconstruction. Reducible fake lepton backgrounds are estimated with a data-driven method and therefore are already accounted for. Background estimates done with Monte Carlo use only truth-matched leptons to prevent overlap in the MC and data-driven estimates.

7.2 Irreducible Backgrounds

This section describes the semi-data-driven techniques used to evaluate irreducible $t\bar{t}$, tW, $Z(\rightarrow \tau\tau)$+jets, and diboson backgrounds. The approach to the $t\bar{t}$, tW, and $Z(\rightarrow \tau\tau)$+jets estimates requires defining new kinematic regions, called *control regions* (CRs), that are enriched in these backgrounds. Monte Carlo simulated events

---

[1] Multi-top refers to the production of three or more top quarks in an event.

for these backgrounds in the SRs are then normalized in a simultaneous fit with their corresponding CR to constrain their contribution to the SR. This fitting procedure is described in Chapter 10. For this method to be valid, a CR must select events that are orthogonal to the SR to eliminate statistical correlations with the SRs, and yet are kinematically similar enough for a meaningful extrapolation. To validate the extrapolation of Monte Carlo events in the SR to data events in the CR, a third region is defined called a *validation region* (VR) that lies kinematically between the CR and SR and is orthogonal to both.

7.2.1 Top Control Region (CR-top)

The control region designed for the $t\bar{t}$ and tW estimates (CR-top) is defined in this section. One of the most unique aspects of the top-quark signature is the presence of b-jets. To enrich a dilepton sample in top quarks, at least one b-tagged jet is required in each event. CR-top is centered around this requirement. The dilepton invariant mass is restricted to $m_{\ell\ell} < 60$ GeV to stay kinematically consistent with the dilepton SRs. Also, $E_{\mathrm{T}}^{\mathrm{miss}}/H_T$ is constrained to the region $[4, 8]$ to reduce contamination from signal events with a fake b-tagged jet. All leptons in $t\bar{t}$ and tW decays are from leptonically decaying Ws, and the electron and muon branching fractions are identical; so to increase statistics, different-flavor lepton pairs are also accepted in the CR-top selection. Other than the selection criteria just described, CR-top includes all the common preselection cuts in Table 6.1. Figures 7.1 and 7.2 show pre-fit distributions in CR-top. The purity of $t\bar{t}$ and tW events is 72% with a signal contamination of less than 3%.

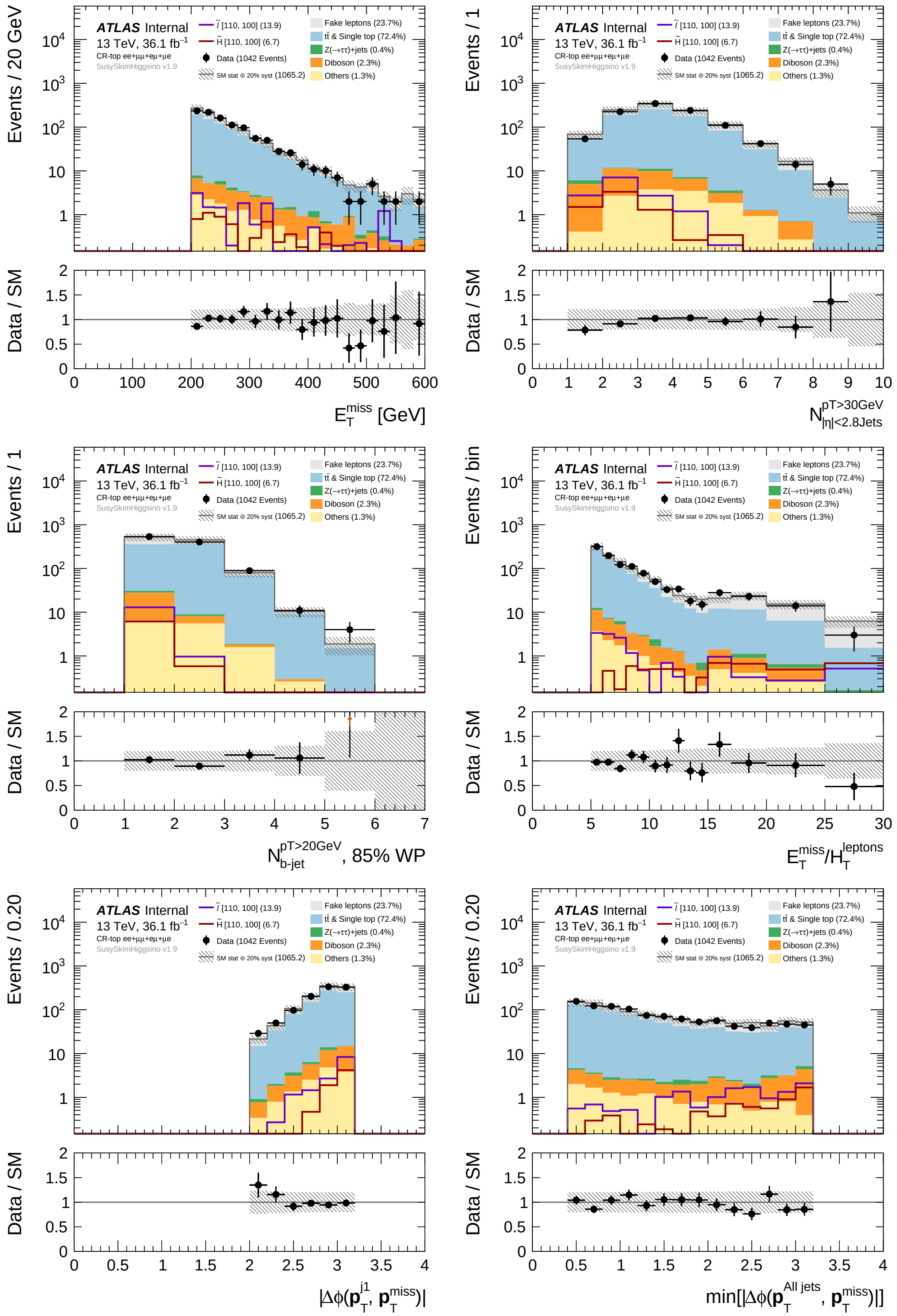

Figure 7.1: CR-top $ee + \mu\mu + e\mu + \mu e$ channel, pre-fit distributions.

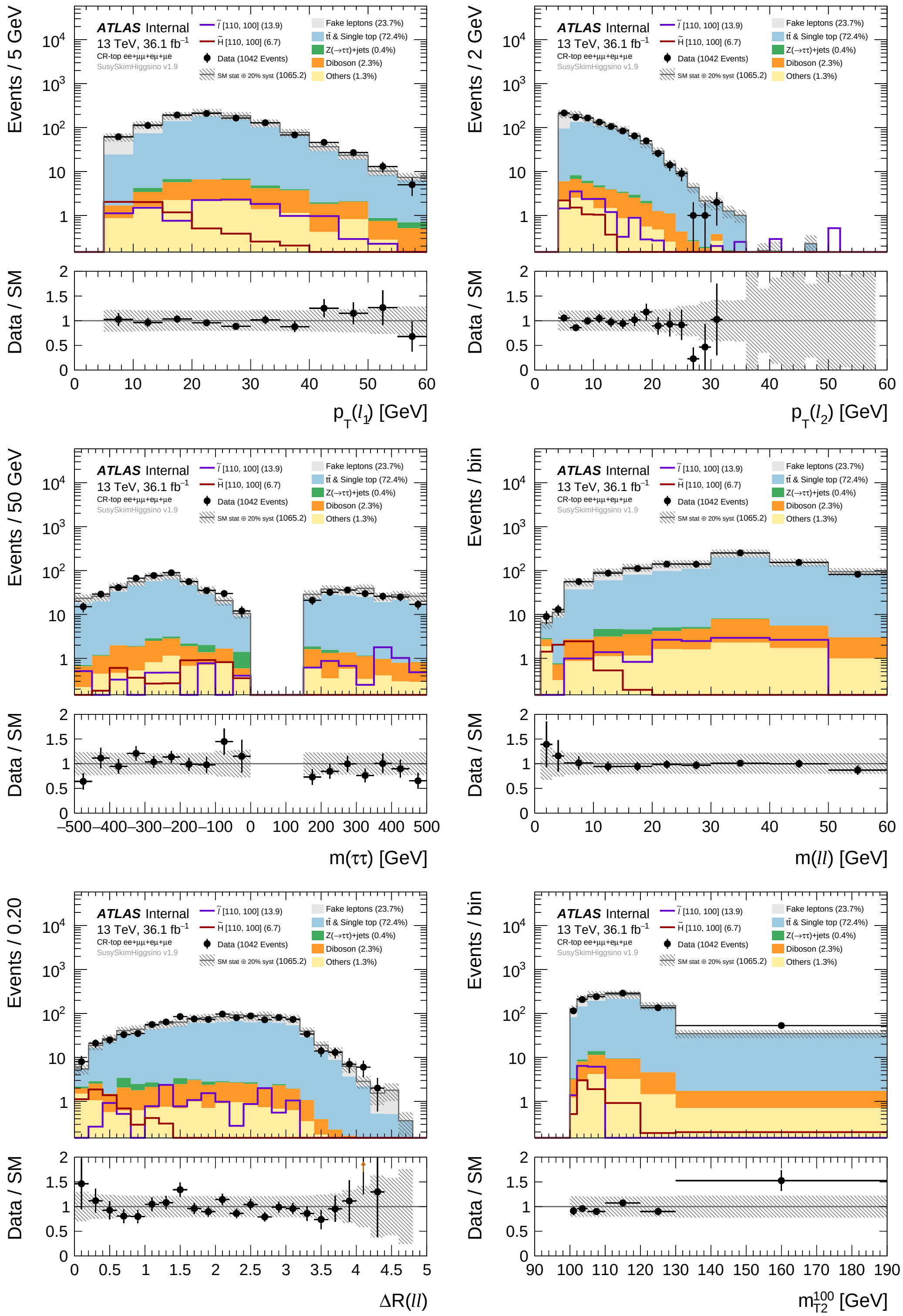

Figure 7.2: CR-top $ee + \mu\mu + e\mu + \mu e$ channel, pre-fit distributions.

7.2.2 Ditau Control Region (CR-tau)

The control region used to estimate $Z \to \tau\tau$ + jets backgrounds (CR-tau) is defined in this section. Getting a handle on the invariant mass of a ditau system is the clearest approach to constructing a dilepton sample enriched in $Z \to \tau\tau$ + jets events, and the $m_{\tau\tau}$ variable, described in section 6.1, is a good proxy for this. Events in CR-tau are required to have an $m_{\tau\tau}$ between 60 GeV and 120 GeV as a way to “bracket” the Z mass. There are also upper and lower bounds on $E_{\mathrm{T}}^{\mathrm{miss}}/H_T$. Just as with CR-top, lepton universality makes different-flavor lepton pairs probabilistically equivalent to same-flavor pairs, so they are also accepted in the CR-tau selection. Figures 7.3 and 7.4 show pre-fit distributions of the some of the variables used to define the Higgsino and slepton signal regions as show above for CR-top. The purity of $Z \to \tau\tau$ + jets events in CR-tau is 80% with a signal contamination of less than 3%.

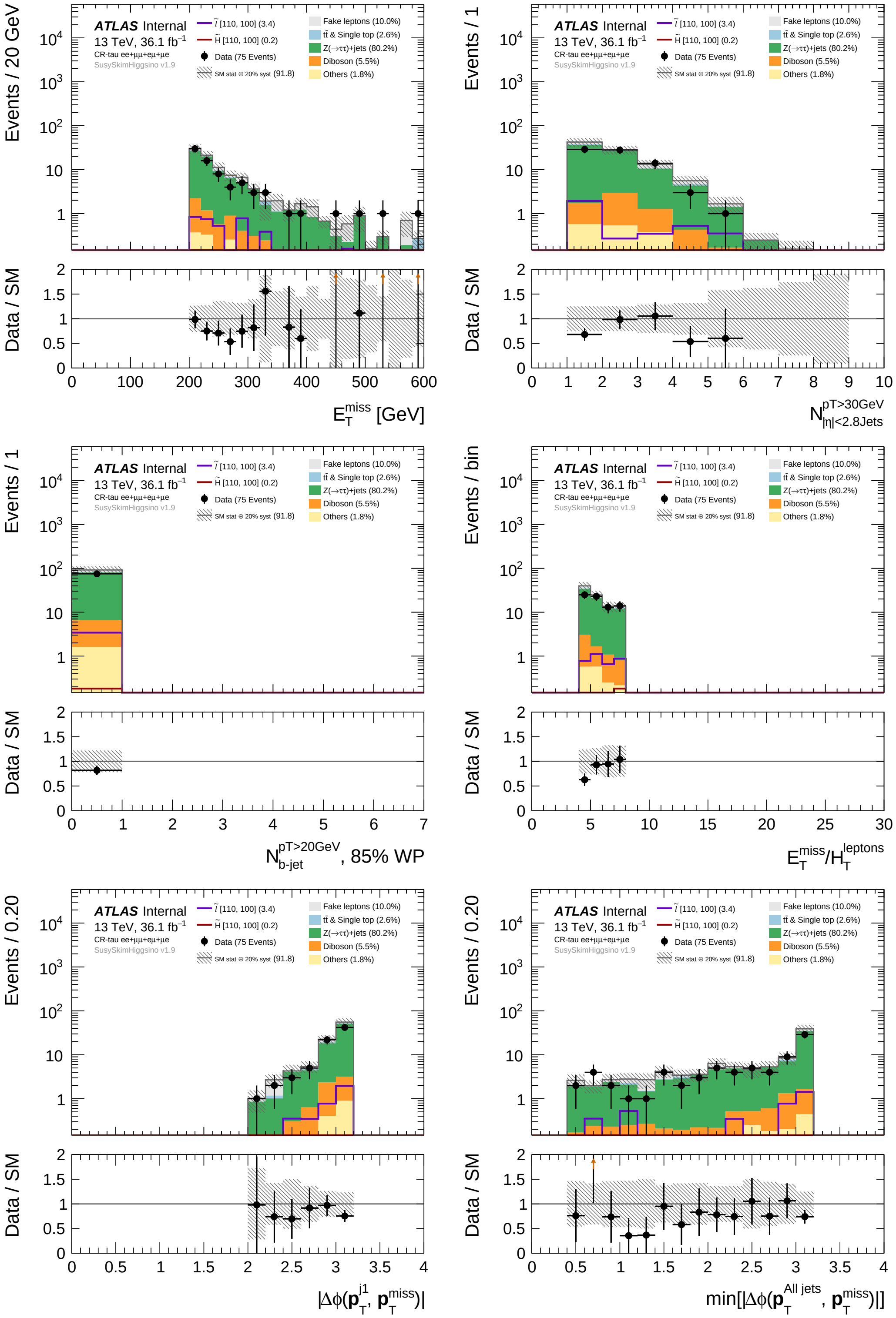

Figure 7.3: CR-tau $ee + \mu\mu + e\mu + \mu e$ channel, pre-fit distributions.

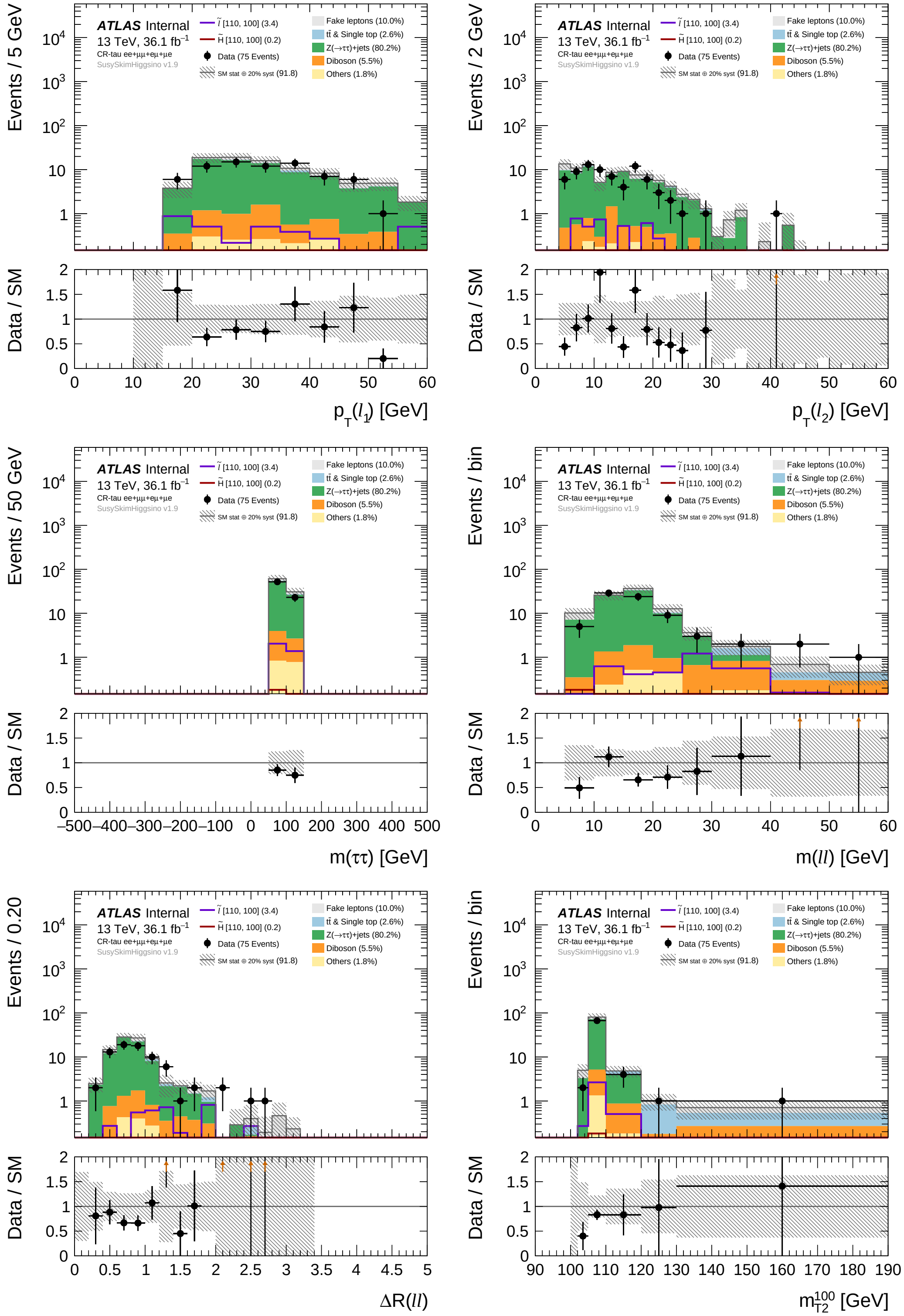

Figure 7.4: CR-tau $ee + \mu\mu + e\mu + \mu e$ channel, pre-fit distributions.

7.2.3 Diboson Validation Region (VR-VV)

Constructing a diboson CR that is free of signal contamination and pure enough in diboson events to allow for confident normalization of Monte Carlo simulation to data is not easy. Therefore, diboson backgrounds are estimated with Monte Carlo samples. The background estimate and the associated uncertainties are validated in a dedicated kinematic region called the *diboson validation region* (VR-VV). This region uses all the same selection cuts as the common signal region in Table 6.1 with an additional $E_{\mathrm{T}}^{\mathrm{miss}}/H_T < 3.0$ requirement to reduce signal events that typically will populate high H_T. Figures 7.5 and 7.6 show VR-VV distributions of some of the variables used to define the Higgsino and slepton signal regions. The VR-VV composition is approximately 40% diboson events, 25% fake/non-prompt leptons events, 23% $t\bar{t}$ and tW events, about 5% $Z \to \tau\tau$ + jets events, and not more than 8% signal events.

7.2.4 Different Flavor Validation Regions (VR-DF)

Additional validation regions are established to check the extrapolation of the fitted Monte Carlo predictions of the irreducible top and ditau backgrounds in the inclusive and exclusive Higgsino and slepton SR, defined in Chapter 6. These VRs take advantage of the flavor symmetry of the $t\bar{t}$, tW, $Z(\to \tau\tau)$+jets processes by selecting only events with different-flavor same-sign lepton pairs in concert with all the other signal region cuts. This includes the inclusive and exclusive binning in $m_{\ell\ell}$ and m_{T2}^{100} that define the Higgsino and slepton signal regions.

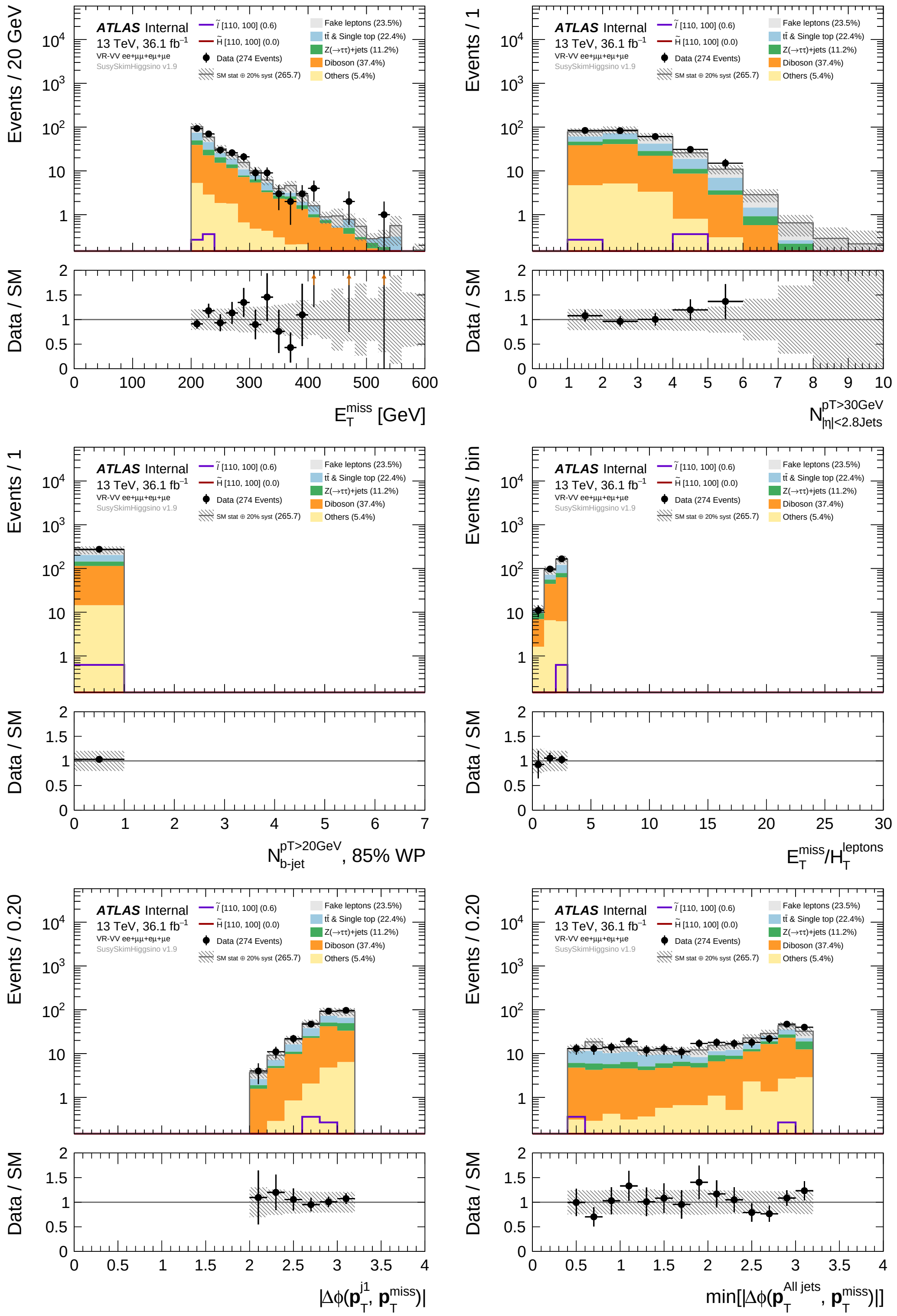

Figure 7.5: VR-VV $ee + \mu\mu + e\mu + \mu e$ channel, pre-fit distributions.

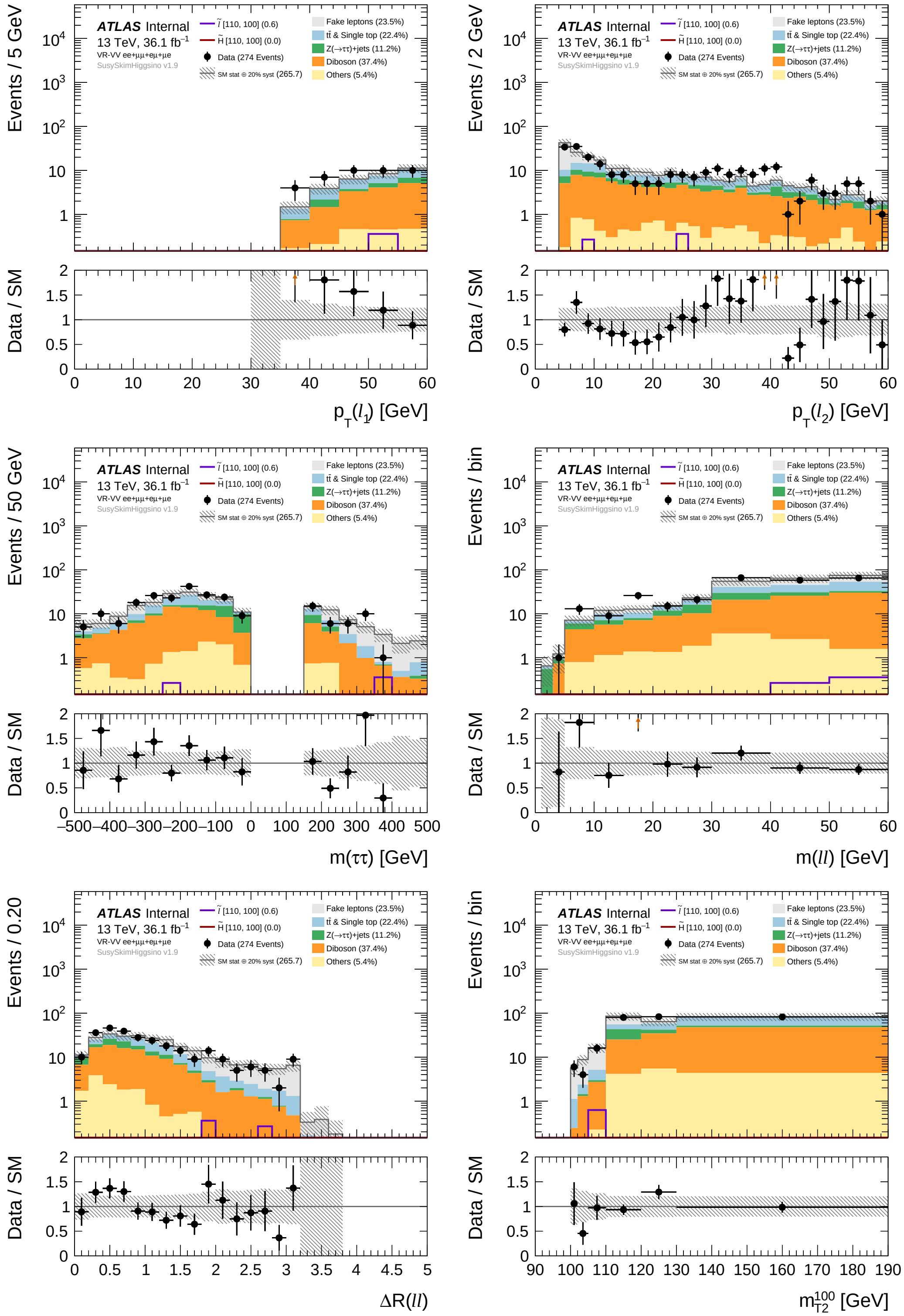

Figure 7.6: VR-VV $ee + \mu\mu + e\mu + \mu e$ channel, pre-fit distributions.

7.3 Drell-Yan Background

Drell-Yan (DY) occurs when two quarks annihilate to produce a lepton pair through the exchange of a virtual Z^*/γ. The invariant mass of the two leptons from this process shows a smooth off-resonance distribution marked by on-resonance peaks at the J/ψ, Υ, and Z masses near 3, 10, and 100 GeV. Figure 7.7 shows the strong presence of DY in data events with two same-sign electrons or muons that pass the inclusive $E_{\mathrm{T}}^{\mathrm{miss}}$ triggers. These events can have sizable jet activity, but there is no source of real $E_{\mathrm{T}}^{\mathrm{miss}}$, so to pass the $E_{\mathrm{T}}^{\mathrm{miss}}$ trigger and signal region selection, a large amount of instrumental $E_{\mathrm{T}}^{\mathrm{miss}}$ from calorimeter jet mismeasurements must be present. A cut on $m_{\ell\ell}$ between 3 and 3.2 GeV removes contributions in the J/ψ peak. Secondly, the signal region cut $\min|\Delta\phi(\text{alljets}, p_{\mathrm{T}}^{\mathrm{miss}})| > 0.4$ removes events where the $E_{\mathrm{T}}^{\mathrm{miss}}$ is very aligned with a single jet, which reduces the occasion of high instrumental $E_{\mathrm{T}}^{\mathrm{miss}}$ from a single mismeasured jet in the detector. DY background contribution in the SRs is insignificant, making it small enough to estimate reliably with Monte Carlo.

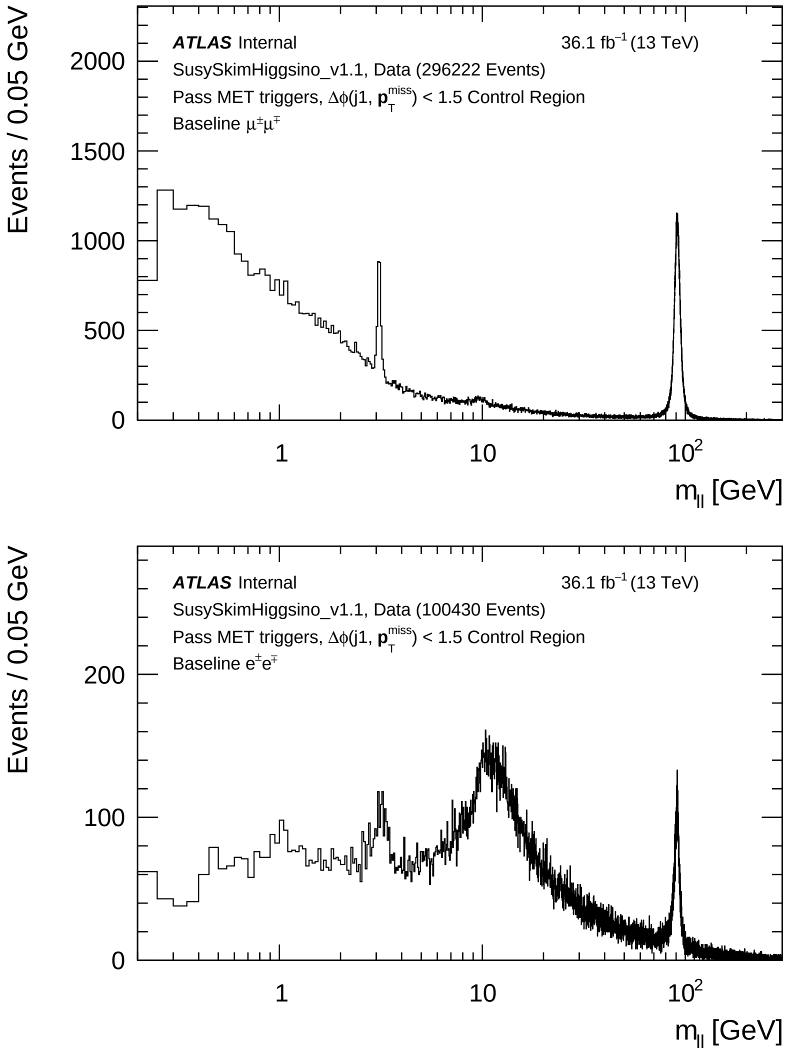

Figure 7.7: Data events passing inclusive $E_{\mathrm{T}}^{\mathrm{miss}}$ triggers with opposite sign baseline leptons in the dilepton invariant mass $m_{\ell\ell}$ spectrum. The $\Delta\phi(j_1, \mathbf{p}_{\mathrm{T}}^{\mathrm{miss}})$ variable is inverted to ensure this is orthogonal to the signal region.

Chapter 8

Fake Factor Method

For low p_{T} dilepton signals, the primary reducible backgrounds are from fake leptons in $W(\rightarrow \ell\nu)$+jets events where one jets is misidentified as a lepton. Monte Carlo techniques can not model the various sources of fake leptons very well, and so a data-driven approach is employed. The rest of this chapter goes as follows: Fake leptons backgrounds are introduced in Section 8.1, then a general overview of the method used to estimate the fake lepton backgrounds for this analysis is given in Section 8.2. Next, the fake factor method applied to low p_{T} di-electron and di-muon events is explained in Section 8.3. Finally, the validation of the fake background estimates is discussed in Section 8.4.

8.1 Introduction

Efficient lepton identification techniques make leptons powerful discriminators in ATLAS physics searches with large background rejection and heavily suppressed

QCD multi-jets. Jet suppression is very high in the range of lepton $p_{\mathrm{T}} > 20$ GeV but degrades at lower lepton p_{T}. Misidentified electrons can be true but non-prompt in photon conversions and heavy-flavor decays, where the real electron in the event does not originate from the primary vertex like true, prompt electrons. Fake electrons can also arise from charged hadrons when the hadronic jet activity in the calorimeters fakes an electron. Muons, on the other hand, are primarily reconstructed using tracks in the ID and the MS, and fakes are mostly from semi-leptonic heavy flavor hadron and meson decays that produce real, non-prompt muons. Electron and muon fake rates are suppressed by strict identification and isolation criteria and track impact parameter cuts, and although electron and muon misidentification rates are low in ATLAS, the $W(\rightarrow \ell\nu)$+jets cross-sections at the LHC are about $10^4 - 10^5$ times higher than compressed Higgsino and slepton cross-sections, as seen in Figure 8.1, comparing the $W(\rightarrow \ell\nu)$+jets and SUSY production cross-sections using ATLAS in Run 1 data and simulated data. The large $W(\rightarrow \ell\nu)$+jets cross-sections provide ample opportunity for jets mismeasurements, and the background contribution from fakes can be significant. A precise Monte Carlo estimate of lepton misidentification would require detailed modeling of jets in non-Gaussian tails of the calorimeter response. This is likely to introduce huge systematic uncertainties and make any prediction unreliable. The fake factor method is a data-driven technique for modeling fake backgrounds in a signal region through measurements of fake lepton yields and their kinematic dependence. The rest of this chapter will describe the general fake factor method and how it is applied to low-p_{T} dilepton events.

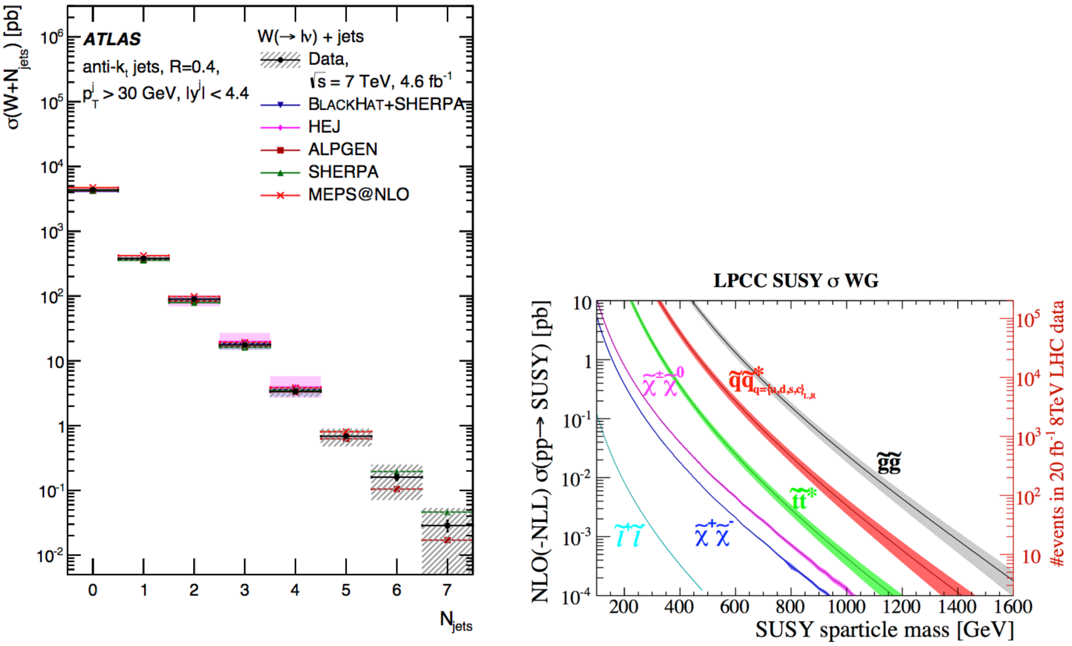

Figure 8.1: Cross-section of $W(\to \ell\nu)$+jets binned in exclusive jet-multiplicity [7] (left), and SUSY cross-sections [25] (right) in LHC pp collisions

8.2 Description of Fake Factor Method

The fake factor method is a data-driven technique for modeling fake rates in data. The general approach is to estimate the number of fake events in a control region, then apply it to the signal regions through a measured transfer factor. To measure the fake factor, two classes of particle are defined: *numerator* or *ID* particles, which have the same definition as those accepted in the signal region, and *denominator* or *anti-ID* particles, which are required to fail certain identification and isolation criteria imposed on the particles in the signal region. An important feature of the numerator definition is that it mimics the fake composition from the primary source; in this analysis, W(→

$\ell\nu$)+jets. A fake factor is measured in a *measurement* region of kinematic phase space contrived to be enriched in fakes as the ratio of ID numerators to anti-ID denominators, binned in terms of the correlated kinematics, as in Equation 8.1

$$F(i) = \frac{\mathrm{N}_{\mathrm{ID}}(i)}{\mathrm{N}_{\mathrm{anti-ID}}(i)} \tag{8.1}$$

Both the ID and anti-ID particles in data should be dominated by fakes, but there is still some contamination from true particles. In practice, these "prompt" contributions are estimated with Monte Carlo simulation in the measurement region and are subtracted from data.

$$F(i) = \frac{\mathrm{N}_{\mathrm{ID}_{\mathrm{data}}}(i) - \mathrm{N}_{\mathrm{ID}_{\mathrm{MC}}}(i)}{\mathrm{N}_{\mathrm{Anti-ID}_{\mathrm{data}}}(i) - \mathrm{N}_{\mathrm{Anti-ID}_{\mathrm{MC}}}(i)} \tag{8.2}$$

Once the fake factor is measured, it can be used to estimate the fake contribution in the signal region. To do this, a control region is constructed to select events with anti-ID objects in a region otherwise identical to the signal region, essentially creating a signal region enriched with fakes. The fake backgrounds in the signal region are estimated by scaling the number of selected events in the control region by the fake factor. The calculation of the total reducible background in the simplest case of having no more than one fake per event is shown in Equation 8.3.

$$N^{\mathrm{SR}}_{\mathrm{reducible}}(i) = \sum_{i} N^{i}_{\mathrm{anti-ID\ CR}} \cdot F(i) \tag{8.3}$$

In cases where two fakes are possible in each event, as in the case with a two-lepton analysis, contributions from both the leading and subleading objects must be considered, and special care taken to not double count events with two fakes. The estimate of

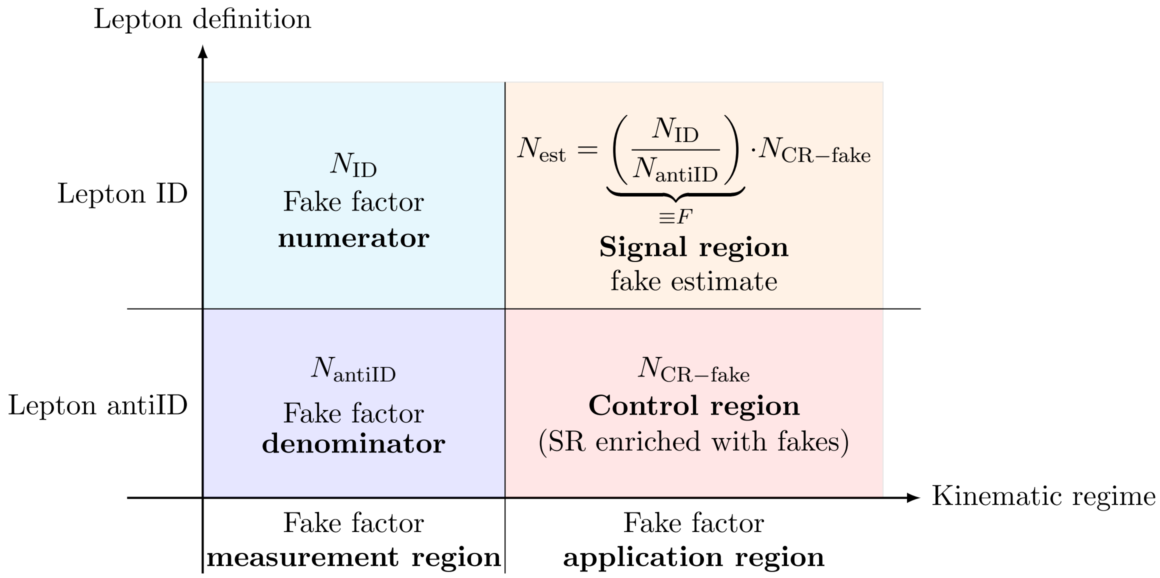

Figure 8.2: Schematic illustrating the fake factor method to estimate the fake lepton contribution in the signal region.

reducible backgrounds in events with two possible fakes is given by:

$$N^{\mathrm{SR}}_{\mathrm{reducible}} = N_{LT} f_1 + N_{TL} f_2 - N_{LL} f_1 f_2 \ , \tag{8.4}$$

where the subscripts "T" and "L" stand for "tagged" and "loose" in place of ID and anti-ID. In Equation 8.4, the minus sign on the last term is to correct for the double counting of events with two fakes, which are included in each of the first two terms. This correction was measured to be very small in the two lepton fake background estimate. Figure 8.2 shows a schematic of the fake factor method.

8.3 Fake Factor Method Applied to Low-p_{T} Di-lepton Events

As described in the previous section, the fake background contribution is estimated in a control region, then scaled to the signal regions by a fake factor. The fake factor is measured in a region of data that is selected to be enriched with fake lepton events. In this region, two classes of lepton – ID and anti-ID – are defined, and the fake factor is equal to the ratio between the occurrence of these leptons in the measurement region. The measurement regions and control regions, along with the ID and anti-ID leptons definitions used to measure the electron and muon fake factors, are detailed in this section.

Electron and muon fake factors are measured using 2015+2016 LHC pp data taken by the ATLAS detector with single electron and muon triggers, called the *fake factor measurement sample* or *FF sample.* The lepton trigger thresholds are chosen to accept the lowest p_{T} leptons possible and still maximize the event statistics. The triggers used for this dataset are summarized in Table 8.1. In ATLAS, single electron and muon triggers with thresholds below 24 GeV are subject to prescales[1] because their true rates are too high for every event to be kept. To resolve the different prescales applied to each trigger, they are unfolded to normalize the entire 2015+2016 dataset arbitrarily to 10 pb^{-1}. For this, and the rest of the discussion of fake factors, the electron and muon samples are treated separately. FF samples are subject to an offline preselection of events with at least two baseline jets according to the jet object definitions summarized

---

[1] The lowest unprescaled electron and muon trigger threshold evolved to 26 GeV by the end of 2016 data-taking.

Trigger Threshold	Prescaled Luminosity [pb^{-1}]	
	2015	2016
Single Electron Trigger		
5 GeV	0.1	0.1
10 GeV	0.5	0.8
15 GeV	5.5	9
20 GeV	10	17
Single Muon Trigger		
4 GeV	0.5	0.5
10 GeV	2.3	2.5
14 GeV	25	14
18 GeV	26	48

Table 8.1: Pre-scaled single-lepton triggers from 2015+2016 used to compute lepton fake factors.

in Table 5.1.

The fake estimate control regions are constructed using 2015+2016 ATLAS data triggered by the lowest unprescaled inclusive $E_{\mathrm{T}}^{\mathrm{miss}}$ triggers, as described in Chapter 4.1. Control region events are selected with all the same cuts as the signal region, but instead of selecting two signal leptons to form the SFOS pair, one signal lepton and one anti-ID lepton are selected to make the SFOS lepton pair.

8.3.1 ID & Anti-ID Lepton Definitions

For both electron and muon fake factors, ID leptons are defined by the same signal lepton criteria as for the lepton pairs in the signal regions. Anti-ID lepton definitions are chosen so that this category is mostly populated with fakes and depleted in real prompt leptons. This fake lepton enhancement is achieved by inverting the cuts used to suppress lepton misidentification. Having an anti-ID definition that is close to the ID definition reduces the systematic uncertainties on the fake background prediction.

Adversely, tighter anti-ID cuts will decrease the acceptance of fakes, which increases the statistical uncertainty on the fake background prediction. This section will detail the anti-ID lepton selections.

8.3.1.1 Electron Definitions

ID electrons are constructed with the same definition as signal electrons, summarized in Table 5.1. These are baseline electrons that also pass *TightLLH* identification, *GradientLoose* isolation, and $|d_0/\sigma(d_0)| < 5.0$ requirements. Anti-ID electrons start as baseline electrons, but are required to pass a slightly tighter PID, *LooseAndBLayerLLH*. Additionally, anti-ID electrons are required to fail at least one of the signal electron criteria. This means anti-ID electrons must fail *TightLLH* identification, or *GradientLoose* isolation, or $|d_0/\sigma(d_0)| < 5.0$, or some combination of these. All ID and anti-ID electrons are required to pass the $|z_0 \sin\theta| < 0.5$ mm requirement to reduce the impact of pileup. The ID and anti-ID electron definitions are summarized in Table 8.2. The fractional composition of anti-ID electrons in the fake factor measurement region,

<table>
<tr><th>Signal Electron Definition</th><th>Anti-ID Electron Definition</th></tr>
<tr><td colspan="2">$p_{\mathrm{T}} > 4.5$ GeV</td></tr>
<tr><td colspan="2">$|\eta| < 2.47$</td></tr>
<tr><td colspan="2">$|z_0 \sin\theta| < 0.5$ mm</td></tr>
<tr><td colspan="2">Electron *author* $! = 16$</td></tr>
<tr><td>Pass *Tight* Identification</td><td>Pass *LooseAndBLayer* Identification</td></tr>
<tr><td></td><td>(Fail *Tight* Identification ***or***</td></tr>
<tr><td>Pass *GradientLoose* Isolation</td><td>Fail *GradientLoose* Isolation ***or***</td></tr>
<tr><td>$|d_0/\sigma(d_0)| < 5$</td><td>$|d_0/\sigma(d_0)| > 5$)</td></tr>
</table>

Table 8.2: Summary of electron definitions.

according to the set of failed signal electron criteria, is shown in Figure 8.3. Here, the m_{T} distribution is plotted over the entire m_{T} spectrum, while the $E_{\mathrm{T}}^{\mathrm{miss}}$, p_{T} and η distributions are all shown for $m_{\mathrm{T}} < 40$ GeV. The motivation behind the m_{T} cut is explained in Section 8.3.2.1. From Fig 8.3, we learn that the anti-ID electrons are 40-50% electrons that fail both the *TightLLH* identification and *GradientLoose* isolation, 25% electrons that only fail identification, 25% electrons that only fail isolation, and a tiny fraction of electrons that fail $|d_0/\sigma(d_0)| < 5.0$.

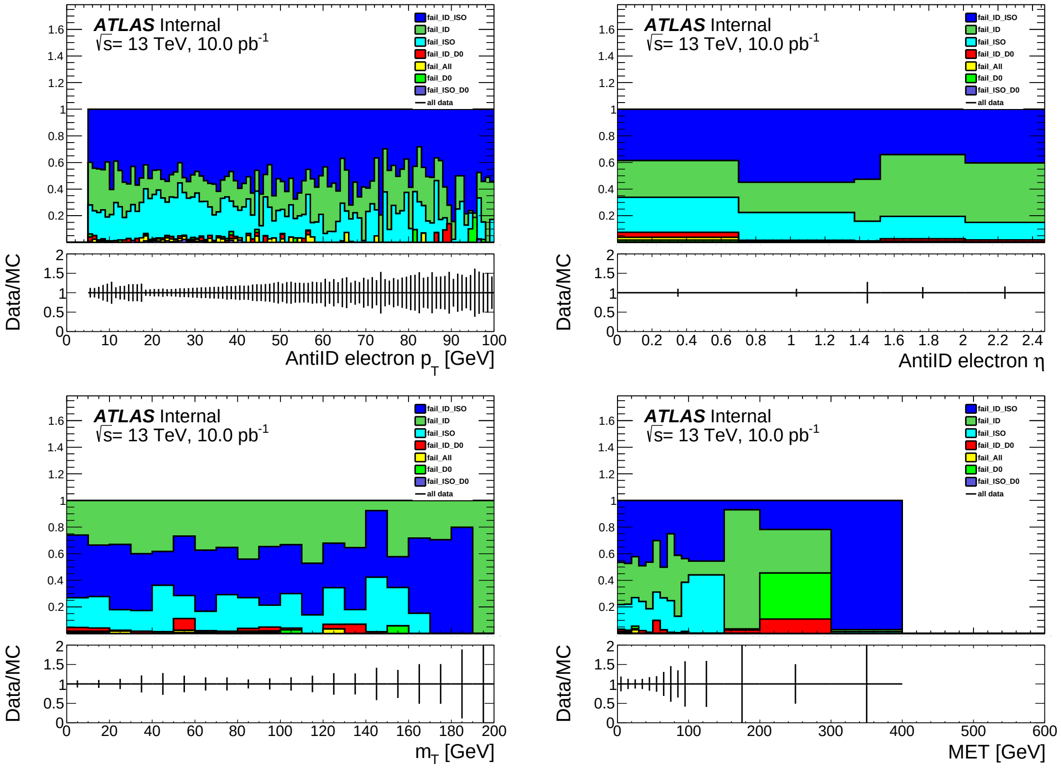

Figure 8.3: Fake electron composition as a function of electron p_{T} (top left), electron η (top right), m_{T}, (bottom left) and $E_{\mathrm{T}}^{\mathrm{miss}}$ (bottom right). All distributions correspond to events in the m_{T} measurement region, except the m_{T} distribution itself.

In choosing the best anti-ID definition to use, there is a trade-off between systematic and statistical uncertainties. A dedicated study of different anti-ID electron definitions was performed to determine which best models the source of fake electron backgrounds and relatively minimizes the statistical uncertainties in the fake background estimate . It was observed that requiring a tighter electron identification working-point enhances the fraction of heavy flavor decays. Requiring tracks to have a hit in the b-layer reduces the fraction of fakes from conversions. A Loose or Medium isolation requirement narrows the source of fakes towards heavy and light hadronic decays. Lastly, requiring a large d_0/σ_{d_0} can increase the fraction of heavy flavor decays and conversions. Unfortunately, the Medium isolation and the large d_0/σ_{d_0} requirements starkly decrease the number of electrons that pass the anti-ID requirements.

8.3.1.2 Muon Definitions

ID muons are defined with the same selection criteria as signal muons, summarized in Table 5.1. These are baseline muons that also satisfy the *FixedCutTightTrackOnly* isolation requirements and the impact parameter significance requirement $|d_0/\sigma(d_0)| < 3.0$. Anti-ID muons are also baseline muons, but instead of requiring they pass the isolation and d_0 significance requirements of the ID muons, they instead must fail the *FixedCutTightTrackOnly* isolation or $|d_0/\sigma(d_0)| < 3.0$ criteria[2]. Both the ID and anti-ID muons are required to pass the $|z_0 \sin\theta| < 0.5$ mm requirement to reduce the impact of pileup. One notable difference with respect to the signal muon require-

---

[2] Failing both the isolation and the d_0 significance cut still satisfies the anti-ID definition.

ments is that the muon-jet overlap removal is relaxed when performing the fake factor measurement. This enhances the statistics used for deriving the fake factors, and is motivated by the observation that the muon-jet overlap removal is primarily designed to reduce the number of heavy flavor decays which are mistakenly being classified as prompt muons. A summary of the ID and anti-ID muon definitions are summarized in Table 8.3

Signal Muon Definition	Anti-ID Muon Definition
$p_{\mathrm{T}} > 4$ GeV	
$\lvert\eta\rvert < 2.5$	
$\lvert z_0 \sin\theta\rvert < 0.5$ mm	
Pass *Medium* Identification	
$\lvert d_0/\sigma(d_0)\rvert < 3$ Pass *FixedCutTightTrackOnly* Isolation	($\lvert d_0/\sigma(d_0)\rvert > 3$ ***or*** Fail *FixedCutTightTrackOnly* Isolation)

Table 8.3: Summary of muon definitions.

The anti-ID muons decomposition, according to which set of ID criteria failed, is shown in Fig 8.4. The m_{T} distribution is plotted over the entire m_{T} range, while the $E_{\mathrm{T}}^{\mathrm{miss}}$, p_{T} and η distributions are all shown for $m_{\mathrm{T}} < 40$ GeV, corresponding to the fake enriched region where the fake factors are measured. Note that these distributions are separated into categories: events with exactly zero b-jets, events with one or more b-jets. In studying the fake factor dependence on different kinematic variables, which is discussed later, b-jet multiplicity was found to have a large variation. In events with exactly zero b-jets, the anti-ID muon composition is approximately 50-65% muons that fail only the *FixedCutTightTrackOnly* isolation, and 20-40% muons that fail both isolation and d_0 significance at low p_{T}. In events with one or more b-jets, the fraction of anti-ID muons that fail only isolation is reduced, but they are still the majority, and the fraction that fail both isolation and d_0 significance is a bit higher.

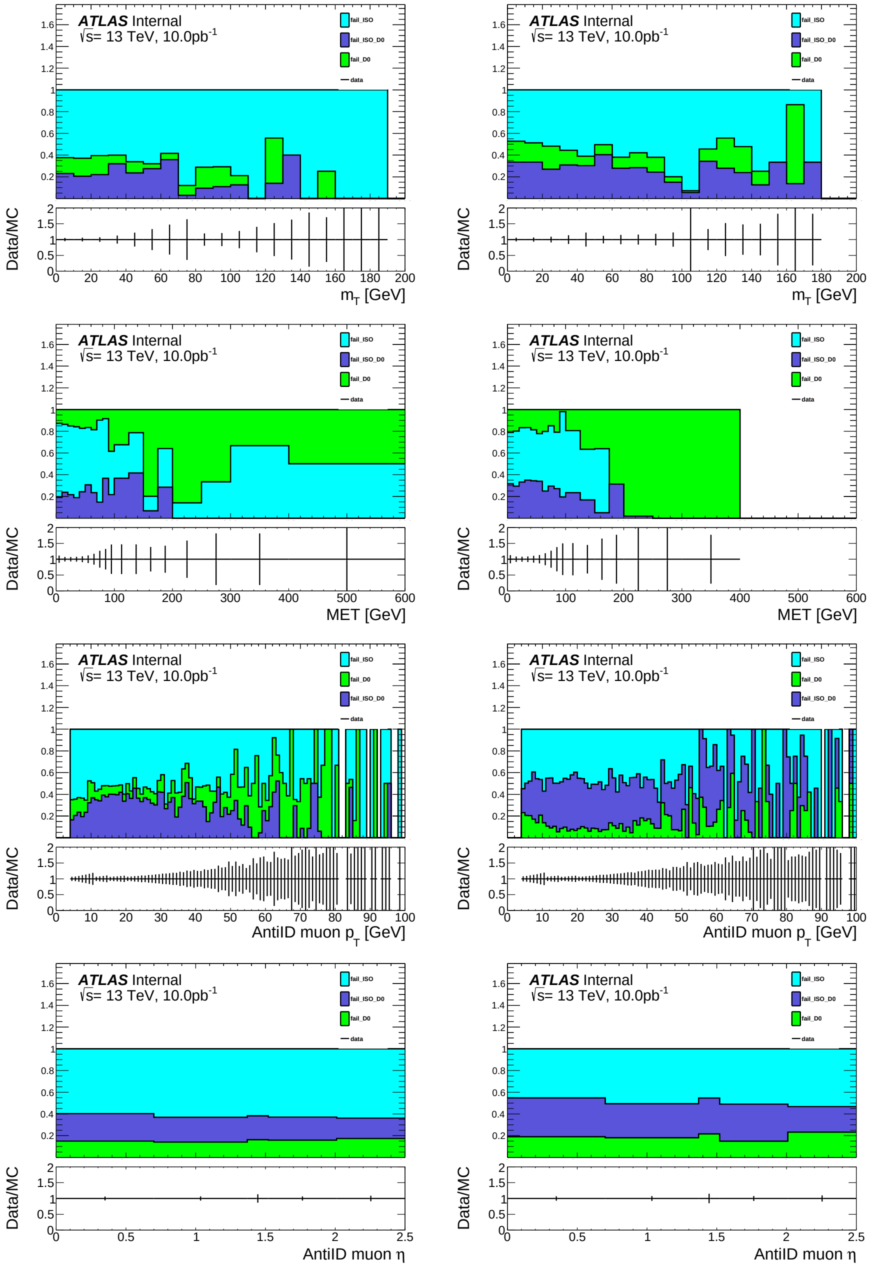

Figure 8.4: Anti-ID muon composition in events with exactly zero b-jets(left) and one or more b-jets(right) as a function of m_{T}, $E_{\mathrm{T}}^{\mathrm{miss}}$, muon p_{T}, and muon η. All but the m_{T} distribution correspond to events with $m_{\mathrm{T}} < 40$ GeV.

8.3.2 Fake Factor Measurement

Data samples are used to select events that have at least one ID or anti-ID lepton within fiducial acceptance of the detector. Monte Carlo samples of SM W+jets, Z+jets, $t\bar{t}$, single-top, and diboson processes are used to represent the contribution from prompt leptons in the fake factor measurement region. We plot all the kinematics of the ID and anti-ID lepton events. The fake factors are measured in the region $m_{\mathrm{T}} < 40$ GeV because this region is dominated by fake leptons. This is shown in the m_{T} plots in data overlaid with the stacked Monte Carlo. The prompt lepton contamination in the measurement region is subtracted off, but first it is normalized to the data in the $E_{\mathrm{T}}^{\mathrm{miss}} > 200$ GeV region that should be dominated by real prompt leptons. The fake factors are expected to depend almost exclusively on lepton p_{T}.

8.3.2.1 Electron Fake Factors

Events in the electron FF samples generally contain just one lepton, and through ID and anti-ID electron selection, these events get separated into ID and anti-ID electron samples. Besides the two baseline jets requirement, the only selection requirement for the ID and anti-ID samples is that the electron p_{T} fall within some p_{T} range set by the highest single-electron trigger that fired. Restricting the electrons in this way alleviates the effect of having overlapping trigger prescales to unfold. The most efficient p_{T} range associated with each trigger is determined from the electron distributions for each trigger, displayed in Figure 8.5. The 5 GeV electron trigger in blue is used to select electrons with p_{T} 5-11 GeV, the 10 GeV electron trigger in red selects electrons with

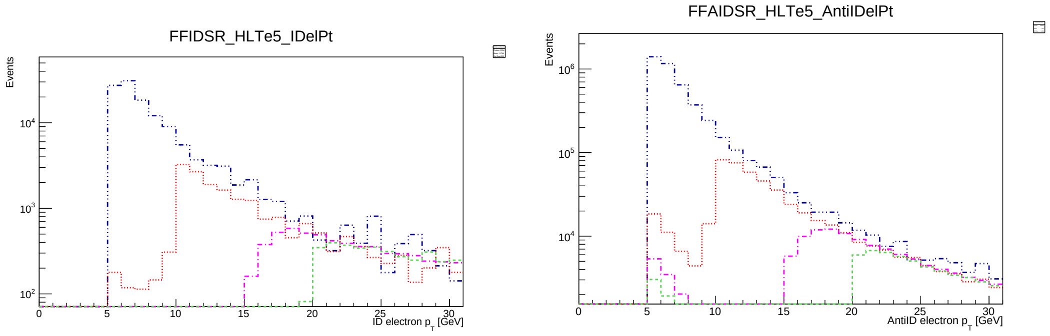

Figure 8.5: The ID electron (left) and anti-ID electron (right) p_{T} distributions for pre-scaled single-lepton-trigger, normalized to 1 pb^{-1}. Blue curve: 5 GeV trigger threshold, red curve: 10 GeV threshold, magenta curve: 15 GeV threshold, green curve: 20 GeV threshold.

Trigger Name	Trigger Threshold	$e^{\pm}$ p_{T} range [GeV]
HLT_e5_lvhloose	5 GeV	5–11
HLT_e10_lvhloose_L1EM7	10 GeV	11–18
HLT_e15_lvhloose_L1EM13VH	15 GeV	18–23
HLT_e20_lvhloose	20 GeV	> 23

Table 8.4: Single-Electron triggers and their corresponding p_{T} range.

p_{T} 11-18 GeV, the 15 GeV electron trigger in magenta selects electrons with p_{T} 18-23 GeV, and the 20 GeV electron trigger is used to select electrons with p_{T} above 23 GeV. The p_{T} range corresponding to each single-electron trigger is shown in Table 8.4.

To calculate fake factors, two kinematic regions are established: one region dominated by fake leptons and used to measure the fake factors, and another region dominated by real leptons and used to normalize the total Monte Carlo yield to the data. In Figure 8.6, the $E_{\mathrm{T}}^{\mathrm{miss}}$ distributions in data for ID and anti-ID electrons display a unique shape at low $E_{\mathrm{T}}^{\mathrm{miss}}$ compared to Monte Carlo, but at high $E_{\mathrm{T}}^{\mathrm{miss}}$ the data and Monte Carlo distributions follow the same trend. This is because there are many more

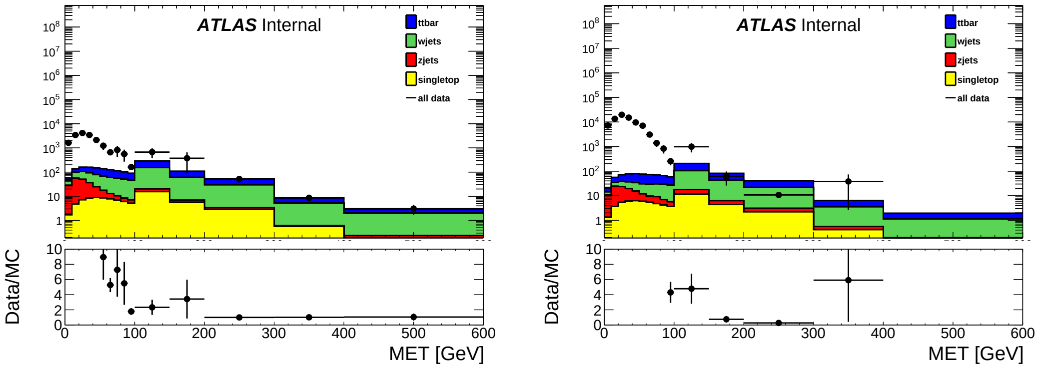

Figure 8.6: The $E_{\mathrm{T}}^{\mathrm{miss}}$ distributions for ID (left) and anti-ID (right) electrons in FF sample. MC is rescaled to match data in the $E_{\mathrm{T}}^{\mathrm{miss}} > 200$ GeV region.

ID Electron Scale Factor	Anti-ID Electron Scale Factor
1.42 ± 0.39	5.07 ± 3.82

Table 8.5: ID and anti-ID normalization scale factors calculated in $E_{\mathrm{T}}^{\mathrm{miss}} > 200$ GeV..

fake lepton events occupying the low $E_{\mathrm{T}}^{\mathrm{miss}}$ region and Monte Carlo can not simulate this in the data very well. Oppositely, real leptons mostly occupy the high $E_{\mathrm{T}}^{\mathrm{miss}}$, and up to some scale-factor, this is well modeled by simulation. Therefore, Monte Carlo is normalized to the data in region $E_{\mathrm{T}}^{\mathrm{miss}} > 200$ GeV with a separate scale-factor for the ID electrons and for the anti-ID events. These scale factors are presented in Table 8.5. If instead, the MC is re-scaled to match the data for events with $m_{\mathrm{T}} > 100$GeV, a region that should also be pure in prompt leptons, the scale factors are 2.39 ± 0.10 for ID electrons and 10.69 ± 0.81 for anti-ID muons. Variations in the re-scaling factors produce only small changes in the fake factors. The difference between the two methods is used as a systematic uncertainty.

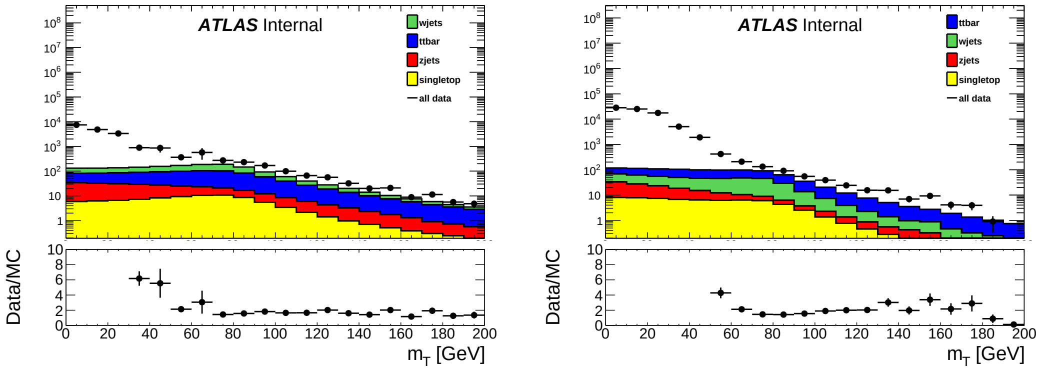

Figure 8.7: $\mathrm{m_T}$ distributions for ID (left) and anti-ID (right) electrons in the FF sample. MC has been scaled to the data in the $E_{\mathrm{T}}^{\mathrm{miss}} > 200$ GeV region.

Figure 8.7 shows the m_{T} distributions for ID and anti-ID electrons in data and Monte Carlo. Just like with the $E_{\mathrm{T}}^{\mathrm{miss}}$, the data points at low m_{T} display a different shape than simulation, but in high m_{T}, data and Monte Carlo progress in more or less the same way. In the case where a hadronic jets fakes a lepton, the difference in the jet and electron electron energy scales affects the calibration of the object. The leptons will typically be measured as a lower energy object than if it were correctly identified as a jet, and this loss of energy reappears as $E_{\mathrm{T}}^{\mathrm{miss}}$ aligned with the lepton. This alignment results in a diminished m_{T} calculation; therefore, fake lepton events are understood to occupy low values of m_{T}. The fake factor measurement region is defined as $m_{\mathrm{T}} < 40$ GeV.

Electron fake factors are assumed to depend almost exclusively on lepton p_{T}. Figure 8.8 shows the ID and anti-ID electron p_{T} distributions in the measurement region after the Monte Carlo normalization factors are applied. The discontinuities in the data curves between 10 GeV and 20 GeV are a relic of the trigger prescales, and further

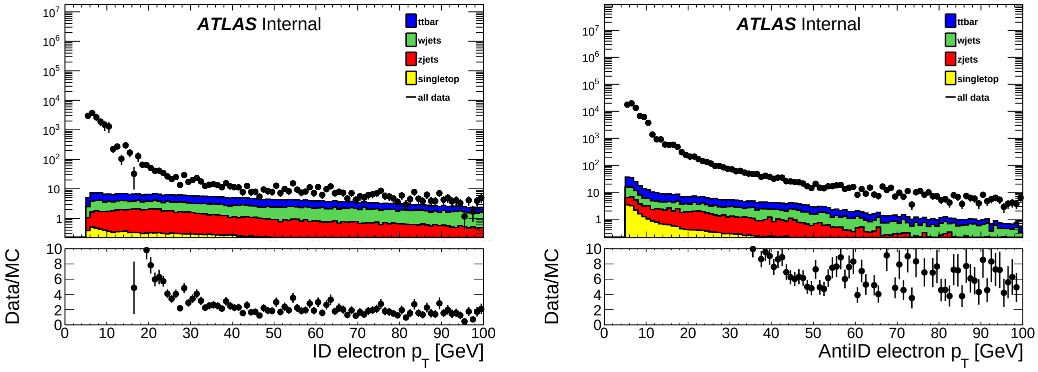

Figure 8.8: p_{T} distributions of ID (left) and anti-ID (right) electrons in FF sample for events with $m_{\mathrm{T}} < 40$ GeV. MC has been rescaled to match data for $E_{\mathrm{T}}^{\mathrm{miss}} > 200$ GeV.

shifting of the associated p_{T} bins does not soften this effect any more without significant losses in statistics. The fake factors are calculated as the ratio of ID electron events to anti-ID electron events bin by bin after the Monte Carlo “prompt lepton”’events have been subtracted out of each p_{T} distribution. While electron fake factors show the largest dependence on electron p_{T}, they also display a dependence on the leading jet p_{T}. Fig. 8.9 shows electron fake factors as a function of electron p_{T} and leading jet p_{T} separately. Given this trend, and the fact that all signal regions used in this analysis require a hard jet with p_{T} greater than 100 GeV, the fake factor measurement region is augmented to also require a jet with $p_{\mathrm{T}} < 100$ GeV.

Final fake factors computed as a function of electron p_{T} are shown in Fig. 8.10a. In addition, fake factors are computed in terms of other kinematic variables to check any unforeseen fake factor dependence in one of these variables. Small correlations compared to the electron p_{T} are folded into the systematic uncertainties. Fake factors binned in $|\eta|$,

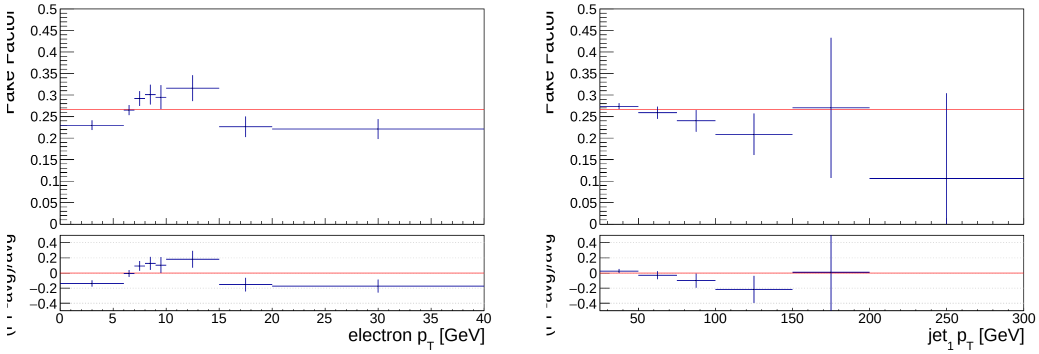

Figure 8.9: Electron fake factors *before* requiring a jet with $p_{\mathrm{T}} > 100$ GeV, as a function of electron p_{T} (left) and leading jet p_{T} (right). The average electron fake factor over all p_{T} is 0.267.

$\Delta\phi_{\mathrm{jet}-E_{\mathrm{T}}^{\mathrm{miss}}}$, jet multiplicity, b-jet multiplicity, average interaction per bunch crossing μ, and number of primary vertices nPV are shown in Figure 8.11. Relative uncertainties on the final electron fake factors versus electron p_{T} are shown in Fig. 8.12. The sources and calculations of the systematic uncertainties are detailed in Chapter 9.1.2.

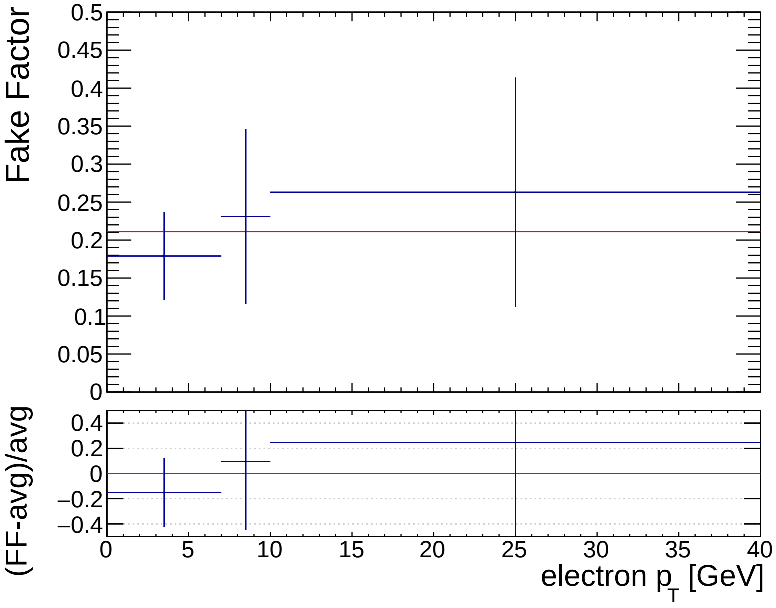

Figure 8.10: Electron fake factors as a function of electron p_{T} in the measurement region $m_{\mathrm{T}} <$ 40 GeV and leading jet $p_{\mathrm{T}} > 100$ GeV. Fake factors for electron p_{T} $4.5 - 5$ GeV are taken to be the same as electron p_{T} $5 - 6$ GeV. A red line marks the average electron fake factor over all electron p_{T}; 0.211.

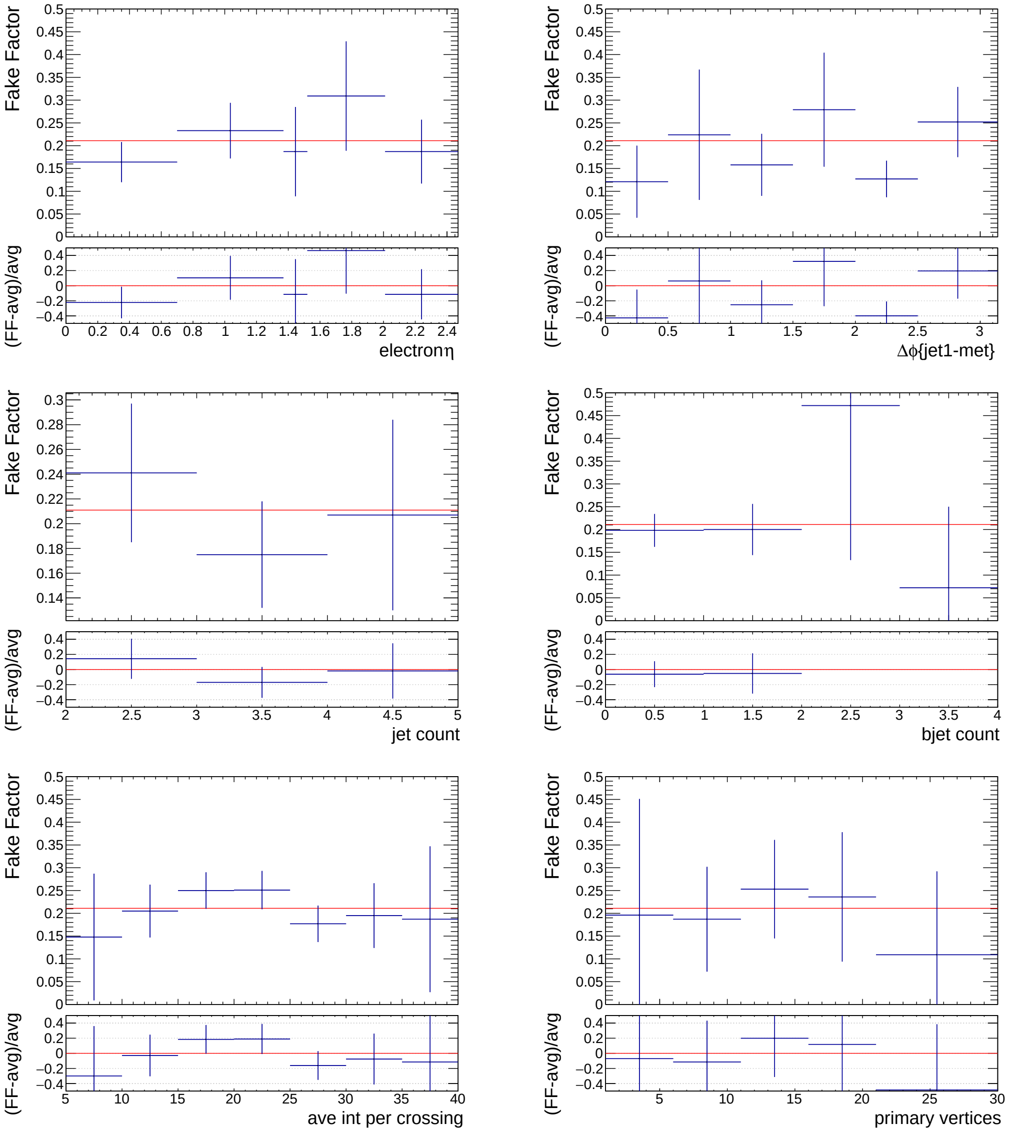

Figure 8.11: Electron fake factors binned in alternative kinematic variable in the measurement region $m_{\mathrm{T}} < 40$ GeV and leading jet $p_{\mathrm{T}} > 100$ GeV. A red line marks the average electron fake factor over all electron p_{T}.

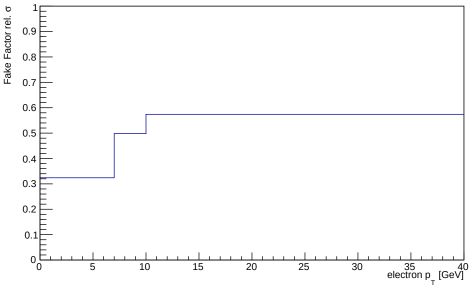

Figure 8.12: Relative uncertainties on electron fake factors binned in electron p_{T}.

8.3.2.2 Muon Fake Factors

The muon fake factors are calculated in nearly the same way as for electrons. Muon FF samples with a requirement of two baseline jets are used and events are selected according to muon definition. ID muon samples give the numerator component of the fake factor, and anti-ID samples give the denominator component. Both data and MC contributions to the ID and anti-ID samples in the single-muon trigger sample are normalized to 10 pb^{-1}, to remove the effects of the prescales in the data. Both the ID and anti-ID samples have the requirement that the muon p_{T} lie within the p_{T} range associated with highest single muon trigger that fired. Just like in the electron case, associating each trigger with an exclusive p_{T} range reduces the complexity of using multiple pre-scaled triggers. The ID and anti-ID muon p_{T} distributions for each trigger are presented in Figure 8.13. The 4 GeV muon trigger in blue is used to select muons with p_{T} 4-11 GeV, the 10 GeV muon trigger in red selects muons with p_{T} 11-15 GeV, the 14 GeV muon trigger in magenta selects muons with p_{T} 15-20 GeV, and the 20 GeV electron trigger is used to select electrons with p_{T} above 23 GeV. The p_{T} range

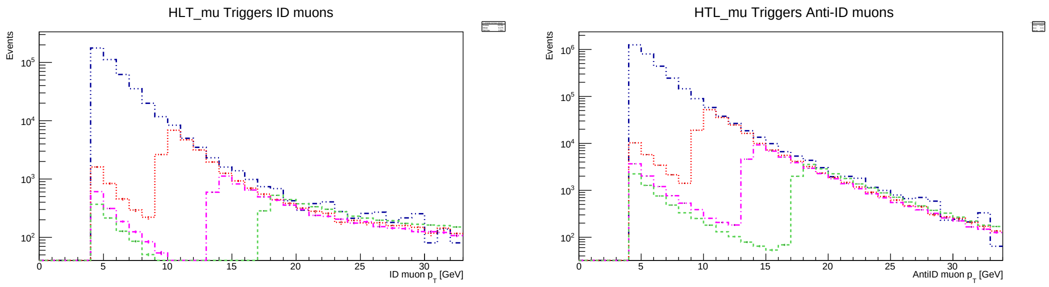

Figure 8.13: The ID (left) and anti-ID (right) muon p_{T} distributions for pre-scaled single-muon triggers, normalized to 1 pb^{-1}. Blue curve: 4 GeV trigger threshold, red curve: 10 GeV threshold, magenta curve: 14 GeV threshold, green curve: 18 GeV trigger threshold.

Trigger Name	Trigger Threshold	μ p_{T} range [GeV]
HLT_mu4	4 GeV	4 –11
HLT_mu10	10 GeV	11–15
HLT_mu14	14 GeV	15–20
HLT_mu18	18 GeV	> 20

Table 8.6: Single-muon triggers used for fake factor computation and their corresponding p_{T} range.

corresponding to each single-muon trigger is displayed in Table 8.6.

For both ID and anti-ID muon samples, the Monte Carlo events are re-scaled to match the data in events with $E_{\mathrm{T}}^{\mathrm{miss}} > 200$ GeV, a kinematic region expected to be pure in prompt leptons. The $E_{\mathrm{T}}^{\mathrm{miss}}$ distributions after applying the rescale factors are displayed in Figure 8.14. The region $E_{\mathrm{T}}^{\mathrm{miss}} < 100$ GeV shows a distinct difference in the shapes for data compared to simulation. This signifies the overwhelming presence of fake muons that are poorly modeled with Monte Carlo. Events with $E_{\mathrm{T}}^{\mathrm{miss}} > 200$ GeV show nice agreement between data and Monte Carlo, as they did in the electron samples.

The scale factors corresponding to each $E_{\mathrm{T}}^{\mathrm{miss}}$ distribution in Figure 8.14 are

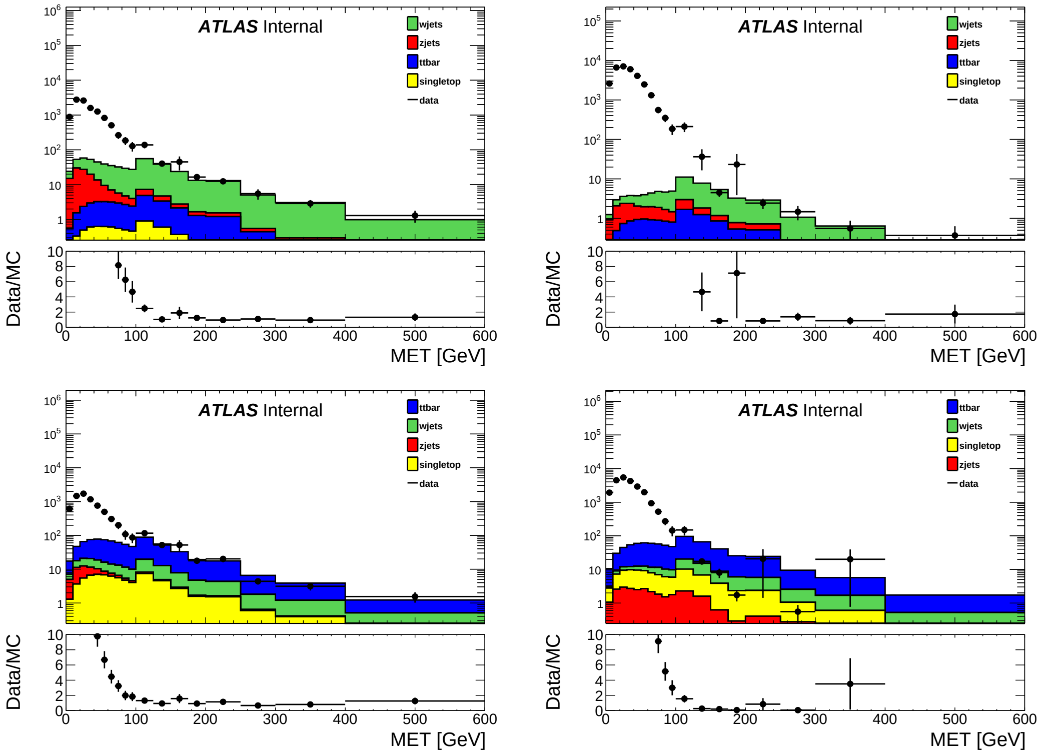

Figure 8.14: The $E_{\mathrm{T}}^{\mathrm{miss}}$ distributions for ID (left) and anti-ID (right) muons in muon FF samples for events with exactly zero b-jets (top), and events with at least one b-jet (bottom). MC is scaled to match the data in the region $E_{\mathrm{T}}^{\mathrm{miss}} > 200$ GeV.

	ID Muon Scale Factor	Anti-ID Muon Scale Factor
0 b-jets	1.01 ± 0.13	1.20 ± 0.29
$>$ 0 b-jets	1.24 ± 0.20	7.34 ± 5.00

Table 8.7: ID and anti-ID muon scale factors calculated in $E_{\mathrm{T}}^{\mathrm{miss}} > 200$ GeV separated by muon definition and

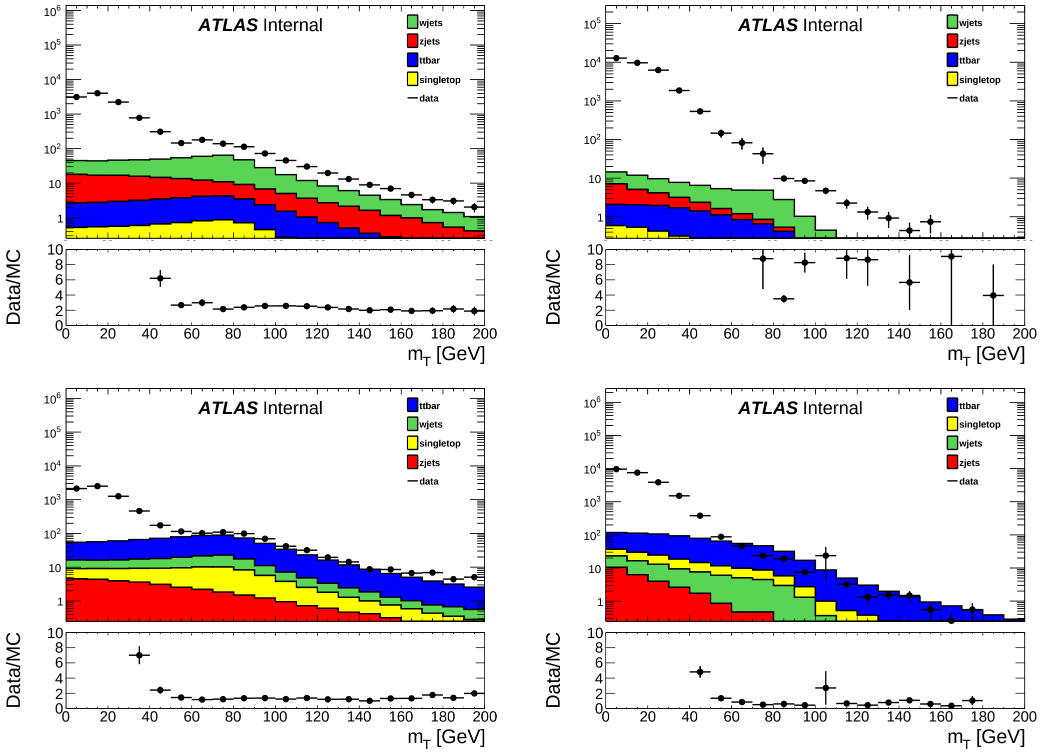

Figure 8.15: The m_{T} distributions for ID (left) and anti-ID (right) muons in muon FF samples for events with exactly zero b-jets (top), and events with one or more b-jets (bottom). MC is scaled to the data in the region $E_{\mathrm{T}}^{\mathrm{miss}} > 200$ GeV.

summarized in Table 8.7. If instead, the MC is re-scaled to match the data for events with $m_{\mathrm{T}} > 100\mathrm{GeV}$, a region that should also be pure in prompt leptons, the re-scaling factors for events with exactly 0 b-jets are 2.37 ± 0.10 for ID muons and 11.68 ± 2.28 for anti-ID muons; events with one or more b-jets have re-scaling factors 1.60 ± 0.06 for ID muons and 10.41 ± 6.34 for anti-ID muons. The re-scaling factors vary significantly between the two methods but the fake factors themselves exhibit small changes between the two methods, and the relative difference can be used as a systematic uncertainty.

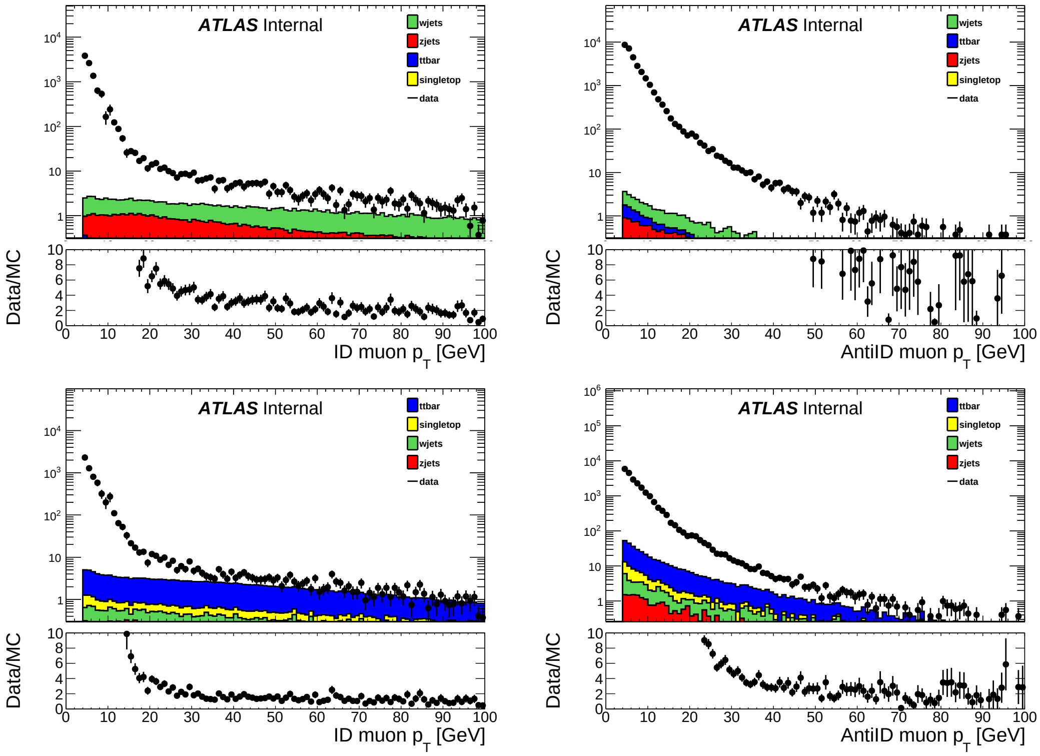

Figure 8.16: ID (left) and anti-ID (right) muon p_{T} in the fake factor measurement region $m_{\mathrm{T}} < 40$ GeV for events with exactly zero b-jets (top), and events with one or more b-jets (bottom). MC has been rescaled to the data in the region $E_{\mathrm{T}}^{\mathrm{miss}} > 200$ GeV.

Figure 8.15 shows the m_{T} distributions for ID and anti-ID muons in data and Monte Carlo events. In the region $m_{\mathrm{T}} > 100$ GeV, the cumulative Monte Carlo trend matches the shape of the data, but in the region $m_{\mathrm{T}} < 40$ GeV, the data is greatly more populated with fake muons. The explanation is the same as described in the previous section and is mostly due to the instrumental $E_{\mathrm{T}}^{\mathrm{miss}}$ that often accompanies mismeasured jets.

Muon fake factors are computed as the ratio of ID electron events to anti-

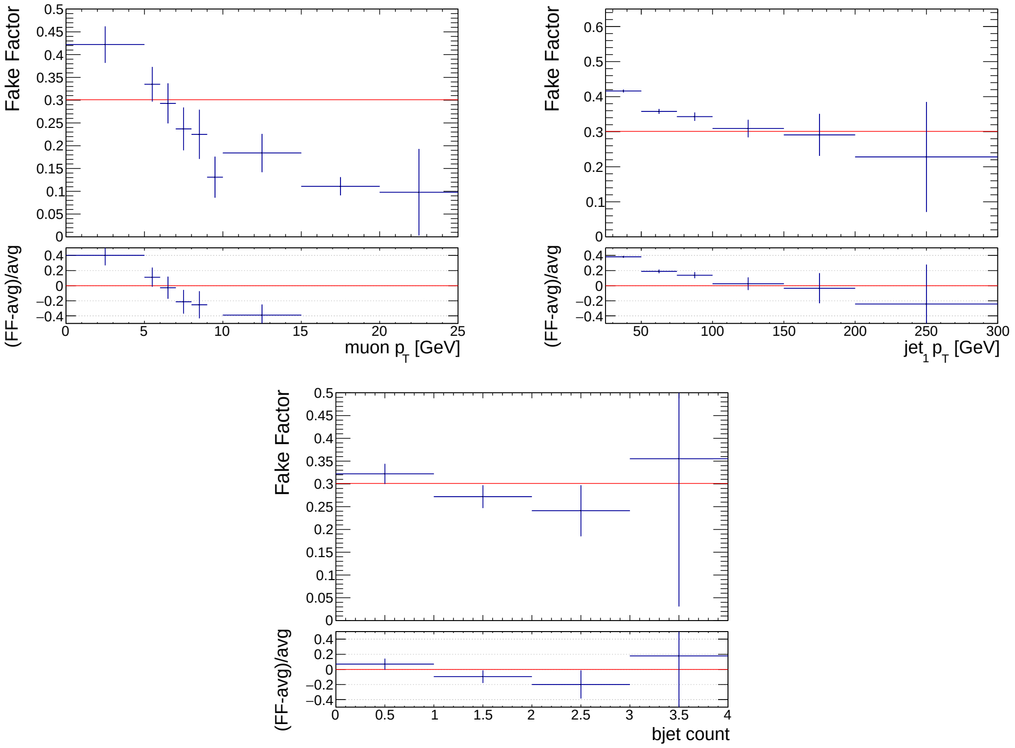

Figure 8.17: Muon fake factors *before* requiring a hard jet of $p_\mathrm{T} > 100$ GeV, computed from muon FF samples as a function of muon p_T (top-left), as a function of leading jet p_T (top-right), and as a function of b-jet multiplicity (bottom). A red line marks the average muon fake factor over all muon p_T.

ID electron events bin by bin after subtracting the Monte Carlo prompt muons in the region $m_\mathrm{T} < 40$ GeV. Like with the electrons, fake factors are initially assumed to depend exclusively on muon p_T, and are calculated bin by bin using the distribution in Figure 8.16. But this assumption does not always work. Muon fake factors display a particular dependence on the presence of b-jets, which is visible in Figure 8.17. The fake factors also show a similar variation in leading jet p_T as did the electrons fake factors.

For the final muon fake factor calculation, the measurement region is modified to require a jet with p_{T} greater than 100 GeV, and the fake factors are binned in muon p_{T} and in number of b-jets. The bin with exactly zero b-jets is used to estimate the fake contribution in the signal region, and the bin with one or more b-jets is used to estimate the fake contribution in the $t\bar{t}$ control region. The final fake factors are shown in Fig. 8.18 as a functions of muon p_{T} for each of the b-jet multiplicity bins. In addition to the final fake factors binned in p_{T}, fake factors binned in other variables are also inspected to check for significant trends:

- Fake factors as a function of muon η are shown in Fig. 8.19,
- Fake factors as a function of $\Delta\phi(j_1 - E_{\mathrm{T}}^{\mathrm{miss}})$ are shown in Fig. 8.20,
- Fake factors as a function of jet multiplicity are shown in Fig. 8.21,
- Fake factors as a function of average interactions per bunch crossing are shown in Fig. 8.22,
- Fake factors as a function of the number of primary vertices are shown in Fig. 8.23.

The relative uncertainties on the muons fake factors versus muon p_{T} for the separate b-jet multiplicity bins are show in Fig. 8.24. The sources and calculations of the systematic uncertainties are detailed in Chapter 9.1.2.

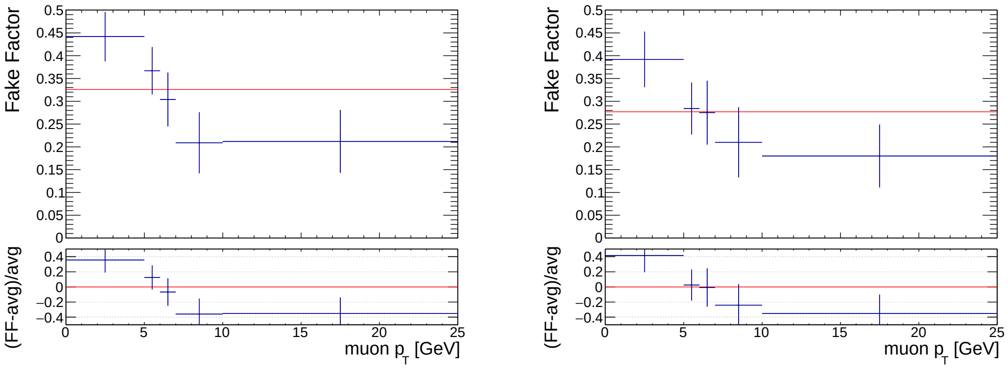

Figure 8.18: Muon fake factors as a function of muon p_{T} in events with exactly zero b-jets (left) and one or more b-jets (right). A red line denotes the average muon fake factor over all muon p_{T}.

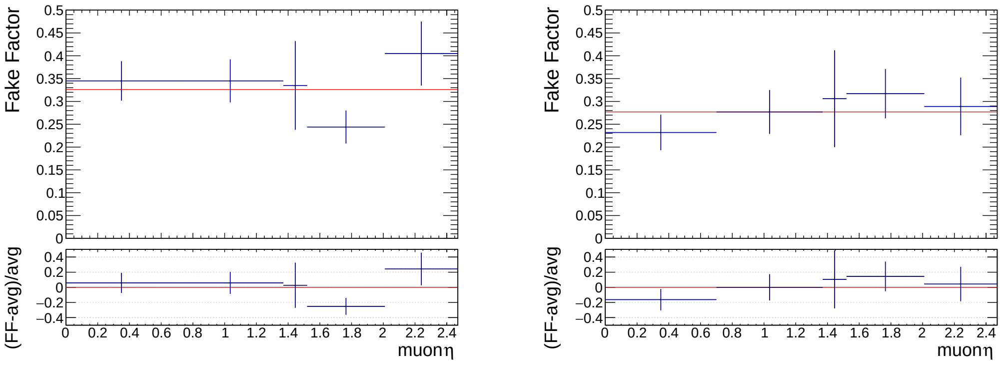

Figure 8.19: Muon fake factors as a function of muon η in events with exactly zero b-jets (left) and one or more b-jets (right).

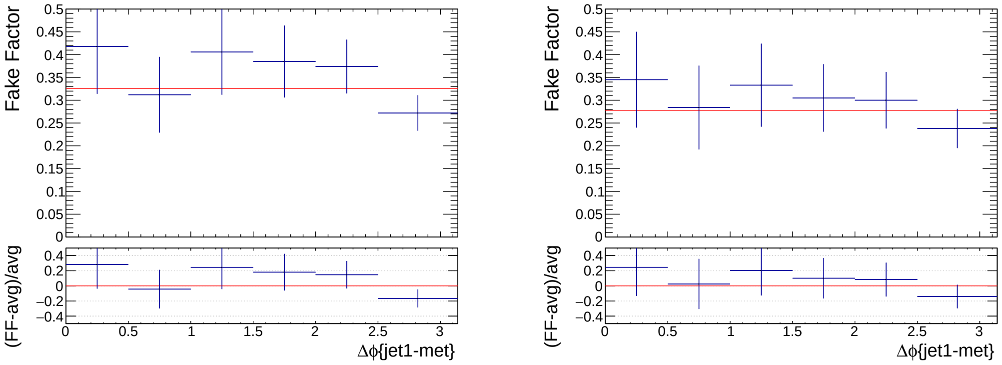

Figure 8.20: Muon fake factors as a function of $\Delta\phi_{jet-E_{\mathrm{T}}^{\mathrm{miss}}}$ in events with exactly zero b-jets (left) and one or more b-jets (right).

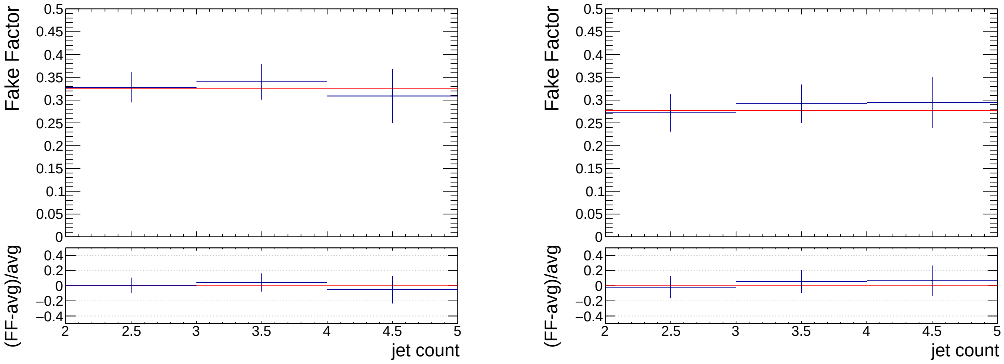

Figure 8.21: Muon fake factors as a function of the jet multiplicity in events with exactly zero b-jets (left) and one or more b-jets (right).

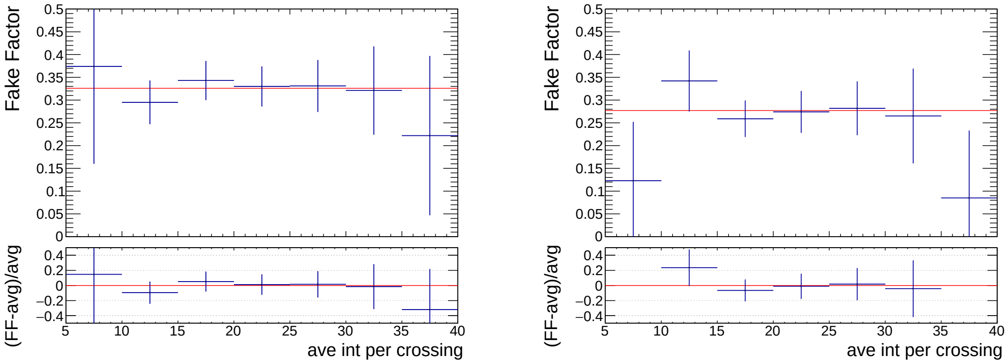

Figure 8.22: Muon fake factors as a function of the average number of interactions per bunch crossing in events with exactly zero *b*-jets (left) and one or more *b*-jets (right).

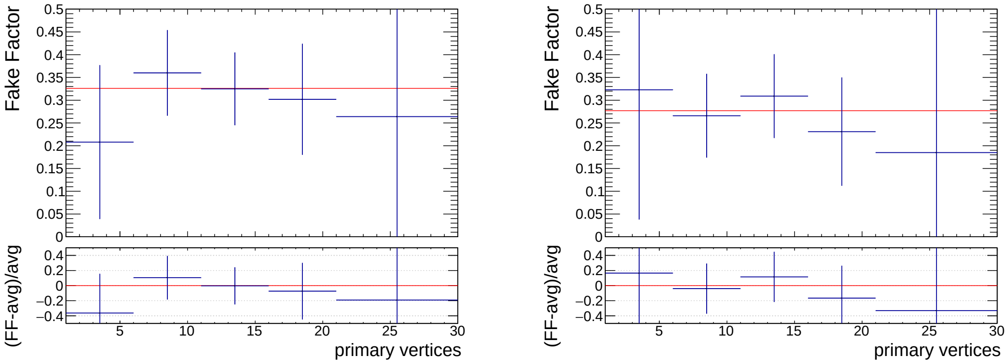

Figure 8.23: Muon fake factors as a function of the number of primary vertices in events with exactly zero *b*-jets (left) and one or more *b*-jets (right).

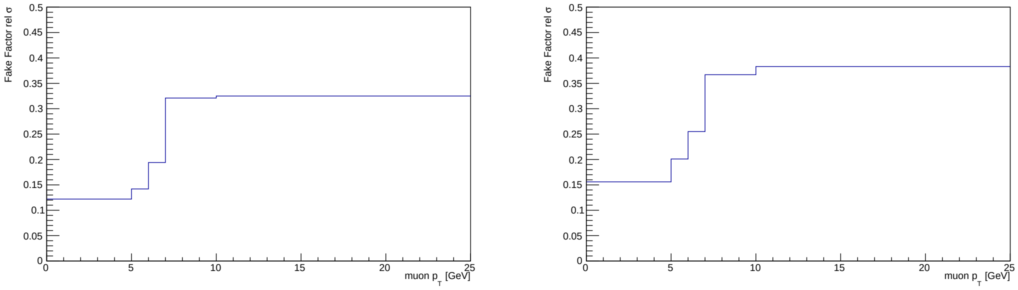

Figure 8.24: Relative uncertainties on muon fake factors versus muon p_{T} in zero b-jets bin (left) and one or more b-jets bin (right).

8.4 Same-Sign Validation Regions (VR-SS)

The same sign validation regions (VR-SS) are defined by the same selection criteria used to define the signal regions in Chapter 6 except that instead of same-flavor opposite-sign lepton pairs, same-flavor same-sign (SFSS) and different-flavor same-sign (DFSS) lepton pairs are selected. $W(\rightarrow \ell\nu)$+jets events are understood to be flavor agnostic since the jet faking a lepton does not depend on the flavor of the W-decay. To motivate the use of same-sign events to construct fake factor validation regions, Monte Carlo W+jets samples are used to compare the composition of lepton fakes between SFOS events and SFSS events. Figure 8.25 illustrates this comparison with same-sign muons in events in the signal region with and without isolation applied. Among the opposite-sign and same-sign distributions, the same general composition is observed.

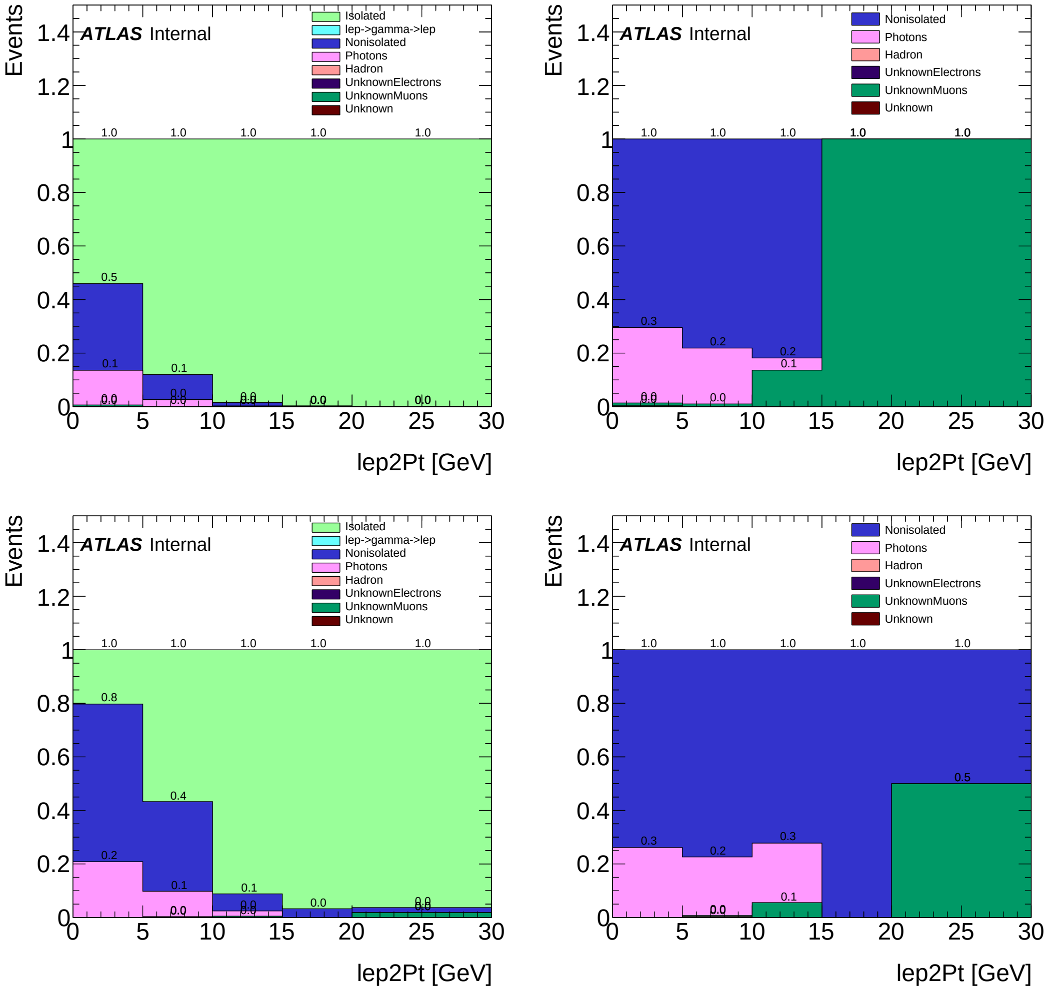

Figure 8.25: Fake lepton composition as a function of subleading lepton p_T, with and without prompt (“Isolated” plus “lep→gamma→lep”) leptons, for opposite sign muon pairs in the signal region. Top left: SR iso, top right: SR no iso, bottom left: ssSR iso, bottom right: ssSR no iso.

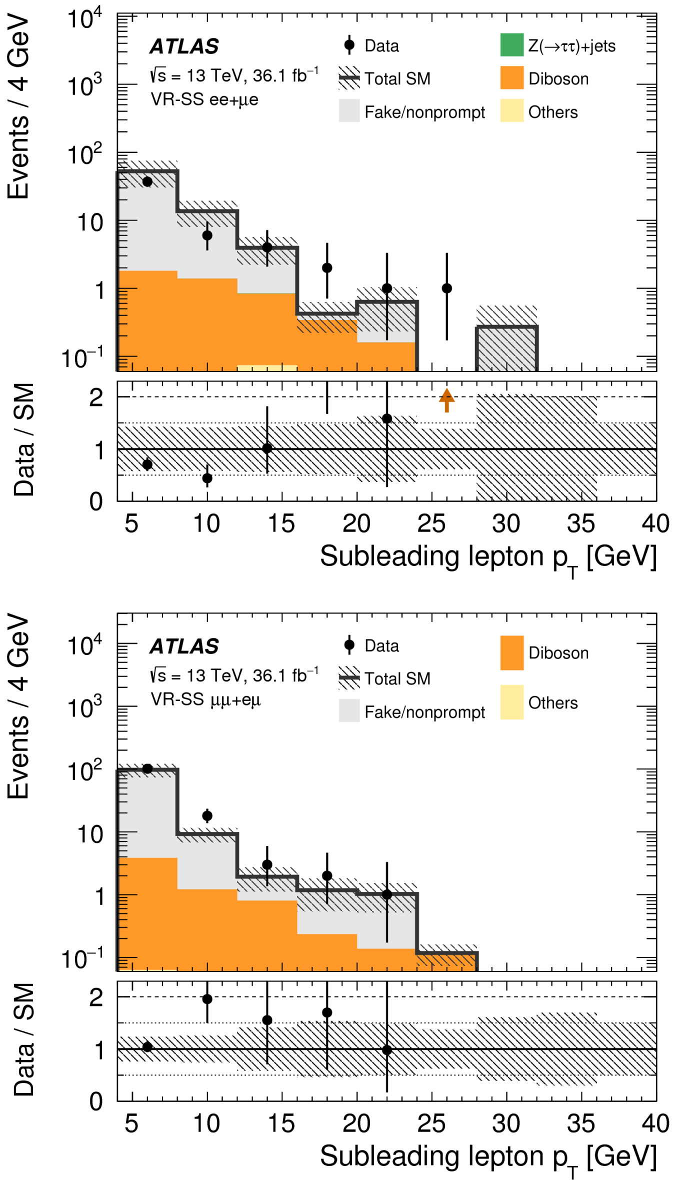

Figure 8.26: Distributions after the background-only fit for the same-sign validation regions, where the subleading lepton is either the electron $ee + \mu e$ (top) or muon $\mu\mu + e\mu$ (bottom). The category "Others" contains rare backgrounds from triboson, Higgs boson, and the multi-top processes. The last bin includes overflow.

Part III

Analysis and Results

Chapter 9

Systematic Uncertianties

Systematic uncertainties are split into two categories: experimental and theoretical. The major sources of experimental uncertainties are the modeling of particle reconstruction in detector simulation, luminosity and pileup measurements, and systematic effects from data-driven estimates. The main theoretical uncertainties emerge from the modeling of Standard Model background processes. Simulation of these processes relies on cross-section measurements, parton distribution functions, and renormalization and factorization scale assumptions. Systematic uncertainties propagate to the final expected yields of signal to background, and limit the resolution of predictions.

This chapter is organized as follows: experimental uncertainties are described in Section 9.1, where first CP Group uncertainties on measurements of pile-up reweighting, luminosity, jets, electrons, muons, and missing transverse energy are summarized in Section 9.1.1, and next fake factor uncertainties are described in Section 9.1.2. Finally, theoretical uncertainties on SM background modeling are dissected in Section 9.2.

9.1 Experimental Uncertainties

This chapter will cover uncertainties from CP group recommendations and fake factor measurements.

9.1.1 CP Group Uncertainties

Combined Performance (CP) groups are dedicated teams in ATLAS that work to optimize the characteristic measurements of certain classes of particle. These groups make recommendations to analysis teams about pile-up re-weighting, luminosity measurements, and which jet, electron, muon, and missing transverse energy definitions to use. The uncertainties associated with these objects and measurements are discussed in this section.

Multiple pile-up interactions need to be modeled well in Monte Carlo so that the simulated detector response and particle reconstruction conditions match the actual data. The distribution of the average number of interactions per bunch crossing applied to Monte Caro events, the μ profile, is based on relevant assumptions and does not always agree with the μ profile observed in data. To resolve these disagreements, the μ profile for Monte Carlo is reweighted to better match the shape in data. This is typically called pile-up reweighting. Studies of the data/MC agreement for the number of primary vertices versus μ suggest an additional rescaling of the μ distribution in data of 1/1.16. A systematic uncertainty for the pile-up reweighting scheme is assigned by varying the scaling factor assigned to data between 1.00 and 1.21 and assessing the change in event yields. An uncertainty on the luminosity measurement is also examined. For the 2015+2016 combined datasets, the luminosity uncertainty is observed to be 3.2%.

Uncertainties on the jet energy scale and jet energy resolution are measured using five parameters varied up and down for the energy uncertainty estimate, and one parameter varied up and down for the uncertainty on the resolution. A separate uncertainty is assigned to account for the differences in the jet-vertex tagging and b-jet tagging efficiencies between Monte Carlo and data. Uncertainties on the electron energy and momentum scale and resolution are also considered, along with uncertainties on the electron and muon scale factors applied to Monte Carlo events that ensure the simulated reconstruction, identification, isolation, and track-to-vertex association efficiencies match the data. Furthermore, uncertainties on the missing transverse energy and momentum arise from the propagation of error in the transverse momentum measurements of hard physics objects. Additional uncertainties on the $E_{\mathrm{T}}^{\mathrm{miss}}$ propagate from the scale and resolution of the track-based soft term, described in Chapter 5.2. The dominant CP group systematic is from the jet energy scale and resolution.

9.1.2 Fake Factor Uncertainties

Fake and non-prompt lepton backgrounds are estimated with a data-driven fake factor method, as described in Chapter 8. Uncertainties arise from several sources, but are mainly from: kinematic dependencies, non-closure in the same-sign validation region, statistical uncertainties on the applied fake factors, and prompt lepton subtraction using Monte Carlo.

The primary fake factor uncertainty comes from kinematic dependancies on variables that are not included in the fake factor binning. Fake factors are measured as a function of electron p_{T} for the electrons, and as a function of muon p_{T} and $N_{b-\mathrm{jet}}$ for the muons. These choices are motivated by the strong correlation of the fake factors and these variables, but other, smaller kinematic dependencies are present. The fake factor vulnerabilities are not large enough to consider binning them in every variable, so they are accounted for as a systematic. Figure 8.11 presents electron fake factors, and Figures 8.19 - 8.23 present muon fake factors binned in alternative variables. We consider the largest, statistically meaningful variation of the fake factors binned in the alternative relevant variables and subtract it from the average fake factor for the electron and muon samples separately. The resulting uncertainty is 25% for each, both driven by the variation in lepton η.

The relationship between the fake lepton estimate and the data in VR-SS is another source of systematic uncertainty. This is quantified by comparing data in a version of the VR-SS that does not require an $E_{\mathrm{T}}^{\mathrm{miss}}/H_T$ cut in the envelope containing the systematic variations described above. The root mean square of the variations is compared with the data and the quadrature difference is interpreted as the closure systematic. This uncertainty is determined to be 38% for electrons with $p_{\mathrm{T}} < 7$ GeV, 97% for muons with p_{T} 7-10 GeV, and 0% everywhere else.

Statistical uncertainties on the fake factors are due to the limited size of the samples used to derive them. These samples use pre-scaled single lepton triggers to select events in data, which are further scrutinized based on the identification, isolation, and impact parameter of the reconstructed leptons to be determined tas either an “ID” or “anti-ID” lepton event. It is possible that there are overlapping events in these two categories, but it is a rare occurrence since less than 10% of the events have more than one lepton, and both the “ID” and the “anti-ID” leptons would need to fall in the p_{T} range associated with highest lepton p_{T} trigger that fired. Figures 8.12 and 8.24 show the relative systematic uncertainties on the electron and muon fake factors per lepton p_{T} bin. For electrons, statistical uncertainties range from about 32% in the lowest p_{T} bin to about 58% in the highest p_{T} bin. For muons, the uncertainties on fake factors used to estimate fake backgrounds in the signal regions vary between 12% in the lowest p_{T} bin to about 32% in the highest p_{T} bin, and uncertainties on fake factors used to estimate fake backgrounds in the $t\bar{t}$ control region vary between 16% and 38%.

Fake factors are measured in regions of data enriched with fake leptons, but prompt lepton contamination is still present. In the measurement region $m_T < 40$ GeV, prompt lepton events are subtracted from the p_{T} distributions using SM Monte Carlo that have been rescaled to match data in the high $E_{\mathrm{T}}^{\mathrm{miss}}$ region. To calculate the systematic uncertainty on this method of prompt subtraction, the change in the binned fake factors is studied as three key parameters are varied. The $E_{\mathrm{T}}^{\mathrm{miss}}$ region, where the scale factor for the prompt subtraction is computed, is varied up and down by 20 GeV from the nominal $E_{\mathrm{T}}^{\mathrm{miss}} > 200$ GeV selection, the region where the fake factors are measured is varied up and down by 10 GeV from the nominal $m_T < 40$ GeV selection, and the scale factor that is applied to the subtracted Monte Carlo is varied up and down by 20%. Uncertainty contributions in the prompt subtraction are assessed further by recomputing the Monte Carlo scale factor in the region $m_T > 100$ GeV and assessing the change in the fake factors. All together, the resulting uncertainties on both electron and muon scale factors are less that 10%, but for one exception in the muon p_{T} bin above 20 GeV, where the uncertainty is 19%. The overall contribution from prompt subtraction is minute compared to the other sources.

9.2 Theoretical Uncertainties

Theoretical uncertainties from signal and background simulation arise from the uncertainties on the underlying parameters in the Monte Carlo generation.

9.2.1 Uncertainty on Simulated Signal Events

Statistical uncertainties on Higgsino and slepton simulated signal events dominantly arise from the next-to-leading order calculations of the hadronic initial state radiation (ISR), factorization and renormalization scale (FSR), and the underlying event. ISR/FSR/EU are all around 20%. PDF uncertainties on signal acceptances are also estimated to be around 10%. Uncertainties on signal cross-section are around 5%.

9.2.2 Uncertainty on Simulated Background Events

Diboson, $Z(\to \tau\tau)$+jets, and $t\bar{t}$ are the dominant background processes estimated with Monte Carlo simulation. There are three main sources of uncertainty: choice of QCD renormalization and factorization scales μ_R and μ_F, choice of strong coupling constant α_s, and choice of PDF set. To calculate the uncertainties, each of these is varied symmetrically around some parameter, or, in the case of the PDF uncertainty, varied by PDF set. The effect of the variations on the predicted yield from each of the dominant background processes is evaluated in the signal, control, and validation regions. μ_R and μ_F are deviated up and down by a factor of 2 and α_s is varied within its uncertainty of 0.001, and the range of impact on the expected yields are evaluated as the uncertainties. PDF uncertainties are obtained from the envelope of symmetrized variations within acceptance of the MMHT2014, CT14, NNPDF PDF sets. Figures 9.1, 9.2, and 9.3 show the assortment of event yields in the Higgsino and slepton SRs for the diboson, $Z(\rightarrow \tau\tau)$+jets, and $t\bar{t}$ predictions. The final uncertainty in each region is calculated as the quadrature sum of all the individual contributions and adds up to $\sim 10\%$ relative uncertainty on the Monte Carlo background prediction.

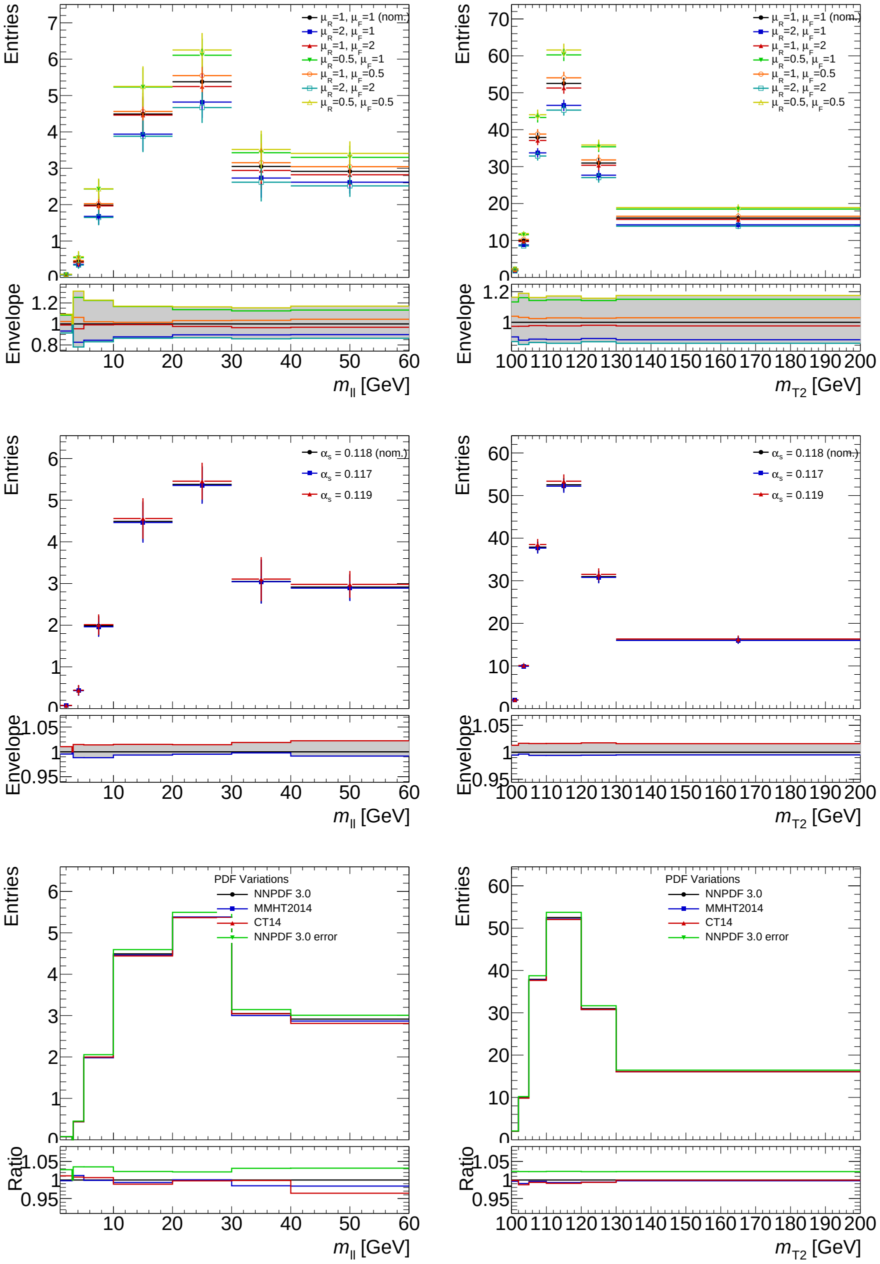

Figure 9.1: QCD scale, α_s and PDF uncertainties on the shape and normalization of the diboson background in the Higgsino (left) and slepton (right) signal regions, but with no lepton flavor requirement.

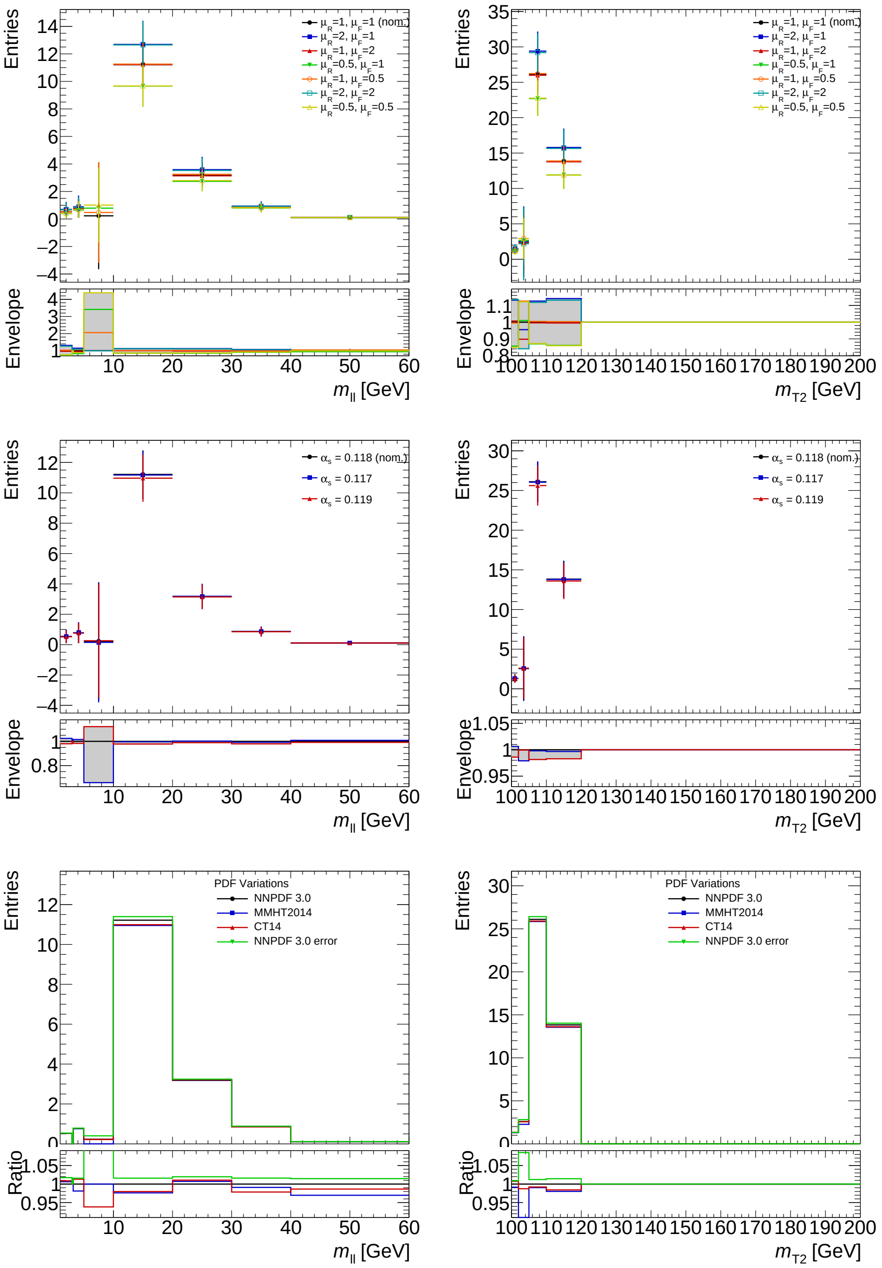

Figure 9.2: QCD scale, α_s and PDF uncertainties on the shape and normalization of the $Z \to \tau\tau$ background in the Higgsino (left) and slepton (right) signal regions, but with no lepton flavor requirement.

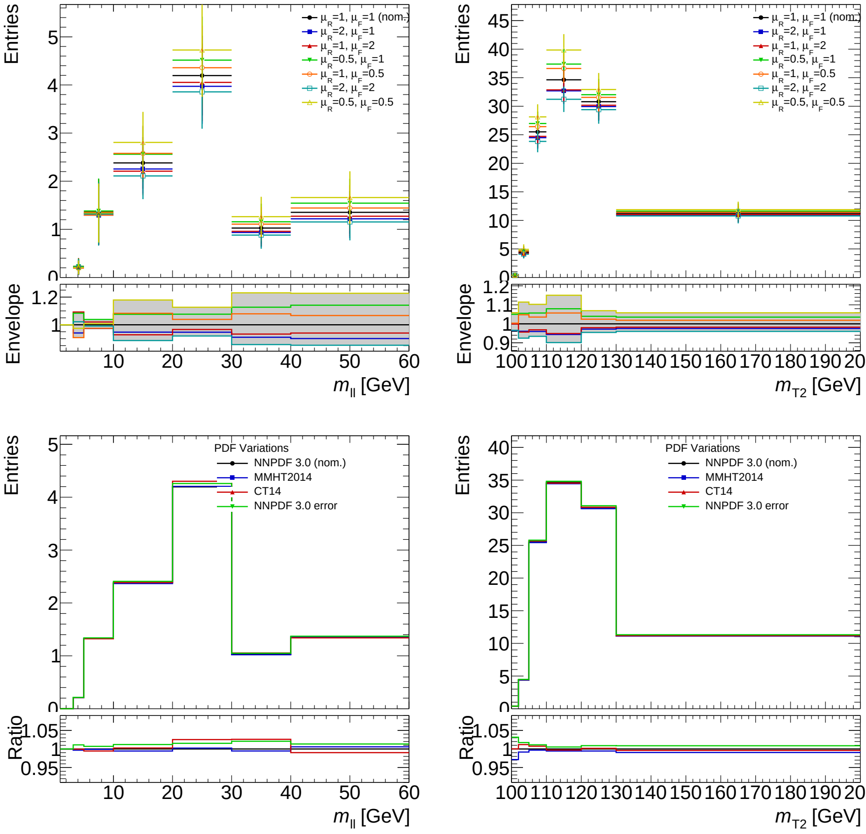

Figure 9.3: QCD scale and PDF uncertainties on the shape and normalization of the $t\bar{t}$ background in the Higgsino (left) and slepton (right) signal regions, but with no lepton flavor requirement.

Chapter 10

Statistical Analysis

The signal, control, and validation regions, defined in Chapter 6 are related through statistical fits in the data. SRs are defined to maximize the statistical significance of signal over background, and CRs are defined to maximize the statistical significance of certain backgrounds related to the SRs while minimizing signal contamination. VRs are kinematically positioned between the CRs and the SRs, and are meant to help mediate the assumptions made in extrapolations between the CRs and SRs. It is important that the CRs and SRs are statistically independent so they can be described by different probability density functions and eventually combined into a simultaneous fit. The statistical combination of multiple regions or bins within them is based on a profile likelihood method implemented in the HistFitter package [19] that builds probability density functions, fits them to data, and interprets them with statistical tests. In this method, a likelihood is constructed as the product of the Poisson probability distributions that describe the total number of events observed in each bin. The mean is taken as the nominal MC yield in a given region and systematic uncertainties are treated as nuisance parameters in the fit.

In this chapter, test statistics and p-values are discussed in Section 10.1, fit strategies are presented in Section 10.2, and nuisance parameter pulls are discussed in Section 10.3.

10.1 Test Statistics and p-values

The test statistic that provides the most powerful test is the likelihood ratio function, given by Equation 10.1.

$$L(\mu,\vec{\theta}) = \prod_{c}\prod_{i} Pois\big(n_{ci}^{obs}|n_{ci}^{sig}(\mu\vec{\theta}) + n_{ci}^{bkg}(\vec{\theta})\big)\prod_{k} f_k(\theta'_k|\theta_k) \tag{10.1}$$

In Equation 10.1, μ and $\vec{\theta}$ represent the signal strength and the set of nuisance parameters. The values of these parameters that maximize $L(\mu,\vec{\theta})$, or equivalently, minimize -$\ln L(\mu,\vec{\theta})$ are called maximum likelihood estimates (MLEs) and are denoted as $\hat{\mu}$ and $\hat{\vec{\theta}}$. There is also a conditional maximum likelihood estimate, $\hat{\hat{\vec{\theta}}}$, which is the value of $\vec{\theta}$ that maximizes $L(\mu,\vec{\theta})$ for a fixed μ. These are all used with the likelihood function $L(\mu,\vec{\theta})$ to construct the profile likelihood ratio:

$$\lambda(\mu) = \left(\frac{L\big(\mu,\hat{\hat{\vec{\theta}}}(\mu)\big)}{L(\hat{\mu},\hat{\vec{\theta}})}\right) \tag{10.2}$$

In a physical theory, the true signal strength μ is a non-negative value, and a negative value of $\hat{\mu}$ implies a shortage of signal-like events in the background. The boundary at $\mu = 0$ convolutes the asymptotic distributions in $\lambda(\mu)$, so μ is free to occupy positive and negative values while the full profile likelihood ratio is defined as:

$$\tilde{\lambda}(\mu) = \begin{cases} \frac{L\left(\mu,\hat{\hat{\vec{\theta}}}(\mu)\right)}{L(\hat{\mu},\hat{\vec{\theta}})} & \hat{\mu} \geq 0 \\ \frac{L\left(\mu,\hat{\hat{\vec{\theta}}}(\mu)\right)}{L(0,\hat{\hat{\vec{\theta}}}(0))} & \hat{\mu} < 0 \end{cases} \tag{10.3}$$

As stated before, maximizing the likelihood is equivalent to minimizing the negative-log likelihood, which is more convenient for visualization. The test statistic $\tilde{q}$ is defined separately for discovery and limit-setting using the negative-log likelihood ratio (NLLR).

For discovery, the test statistic $\tilde{q}_0$ is built to distinguish the background only hypothesis $\mu = 0$ from the alternative hypothesis $\mu > 0$, where there is an excess above background. When the MLE $\hat{\mu}$ is positive, the test statistic is the NLLR, otherwise it is zero, as shown in Equation 10.4.

$$\tilde{q}_0 = \begin{cases} -2\ln\lambda(\mu) & \hat{\mu} > 0 \\ 0 & \hat{\mu} \leq 0 \end{cases} \tag{10.4}$$

When setting limits, the test statistic $\tilde{q}_\mu$ is meant to distinguish the signal hypothesis, where signal events are produced above background at some rate μ, from the alternative hypothesis with signal events produced at some rate less than or equal to μ. In this case, when the MLE $\hat{\mu}$ is less than μ, $\tilde{q}_\mu$ equals the NLLR, otherwise, it is set to zero. This is shown in Equation 10.5

$$\tilde{q}_\mu = \begin{cases} -2\ln\lambda(\mu) & \hat{\mu} \leq \mu \\ 0 & \hat{\mu} > \mu \end{cases} \tag{10.5}$$

Through the test statistic, the data are mapped to a single real-valued number that represents the outcome of the experiment. If the experiment was performed many times, the test profile likelihood ratio function would output a different value each time, making a distribution of real-valued discriminating variables. In practice, Monte Carlo simulation is used to generate numerous pseudo experiments, and while the test statistic $\tilde{q}$ is a function of μ, the distribution of $\tilde{q}$ becomes explicitly a function of the nuisance parameters $\vec{\theta}$, denoted as $f(\tilde{q}|\mu, \vec{\theta})$. The p-value for any given hypothesis represents the probability to observe an equal or more extreme outcome given that hypothesis as the integral of the test statistic distribution from $\tilde{q}_{\mu,obs}$ to ∞.

$$p_{\mu,\vec{\theta}} = \int_{\tilde{q}_{\mu,obs}}^{\infty} f(\tilde{q}_\mu|\mu, \vec{\theta}) d\tilde{q}_\mu \tag{10.6}$$

Conventionally in high energy particle physics experiments, a standard one-sided frequentist confidence interval defines an upper limit on the parameter of interest at 95% confidence level. The p-value can be used to measure how well the data agrees with a signal hypothesis of signal strength μ, given in Equation 10.7, or it can be used to measure how consistent the data are with the background only hypothesis, as in Equation 10.8.

$$p_\mu = \int_{\tilde{q}_{\mu,obs}}^{\infty} f(\tilde{q}_\mu|\mu, \hat{\hat{\vec{\theta}}}(\mu, obs)) d\tilde{q}_\mu \tag{10.7}$$

$$p_b = 1 - \int_{\tilde{q}_{\mu,obs}}^{\infty} f(\tilde{q}_\mu|0, \hat{\hat{\vec{\theta}}}(\mu = 0, obs)) d\tilde{q}_\mu \tag{10.8}$$

The CL_s upper limit on μ comes from solving as a function of μ for $p'_\mu = 0.05$, where p'_μ is the ratio of p-values in Equation 10.9.

$$p'_\mu = \frac{p_\mu}{1 - p_b} \tag{10.9}$$

10.2 Fit Stategies

This analysis relies on three kinds of fit strategies: background-only, model-dependent, and model-independent.

A background-only fit makes no assumptions about any of the signal models, uses background samples exclusively, and assumes there to be no signal contamination in the CRs. The fit is only done in the CRs and the dominant backgrounds sources are normalized to fit the observed data yields. The background-only fit assumes only background processes are present and the background parameters of the Poisson distribution functions should be the same through all the CRs, SRs, and VRs. For these reasons, this fit is used to normalize the predicted backgrounds in the SRs and VRs.

The model-dependent fits are performed in the CRs and the SRs simultaneously. It is common to fit multiple exclusive SR bins simultaneously assuming the same signal model. For each SR simultaneously fit with the CRs, the background samples and a signal sample are assumed. This provides the model dependence in the SRs and accounts for any signal contamination in the CRs. In the absence of any significant excess in the SRs, this fit strategy is used to set model-dependent exclusion limits on the assumed signal models.

The model-independent fits are meant stay general to interpretations so the observations can be used by others who want to check its implied exclusion on other models. The fits are performed in the same way as the model-dependent strategy, but with a single-binned inclusive SR fit simultaneously with the CRs. Also, only background is assumed in the CRs while both the backgrounds and signal are allowed in the SR.

10.3 Nuisance Parameter Pulls

To assess the behavior of the nuisance parameters in a background only fit, relative changes, or pulls, in the nuisance parameters are studied. Any observed upward or downward fluctuations in data above background prediction is inadequately explained by a signal in the exclusion shape fit, and many of the background systematics are pulled and/or constrained to accommodate. An example of the fit and nuisance parameter pulls for the background only fit in the CR, simultaneously in the CR and inclusive SR-$m_{\ell\ell}$, and simultaneously in the CR and inclusive SR-$m_{\mathrm{T2}^{100}}$ are shown in Figure 10.1. The simultaneous fits with the SRs include the shape fits in $m_{\ell\ell}$ and $m_{\mathrm{T2}^{100}}$, which pull on the nuisance parameters to adjust to the fit.

Ranked pull plots how how the uncertainties shown in the last chapter impact signal strength, and can be used to understand what the largest uncertainties are. Instead of looking at the relative change in nuisance parameters from pre-fit to post-fit, we look at the relative impact on μ_{signal}, the expected signal strength. This tells us which uncertainties are actually changing how our confidence in our statement on how much signal there might be in data. Figure 10.2 shows ranked pull plots for the most inclusive Higgsino and slepton signal regions. MC statistics, fake factor systematics, jet resolution, and diboson theory uncertainties are the largest.

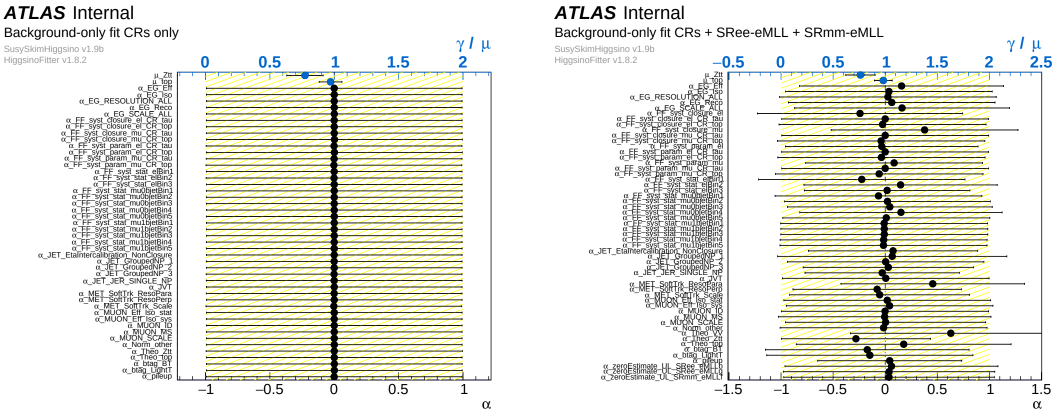

(a) CRs-only

(b) CRs +exclusive SR$\ell\ell$-$m_{\ell\ell}$

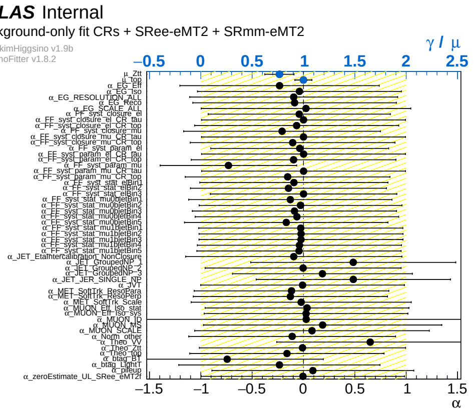

(c) CRs + exclusive SR$\ell\ell$-m_{T2}^{100}

Figure 10.1: Fit parameters for background-only fit in various configurations of the regions allowed to be treated as constraining.

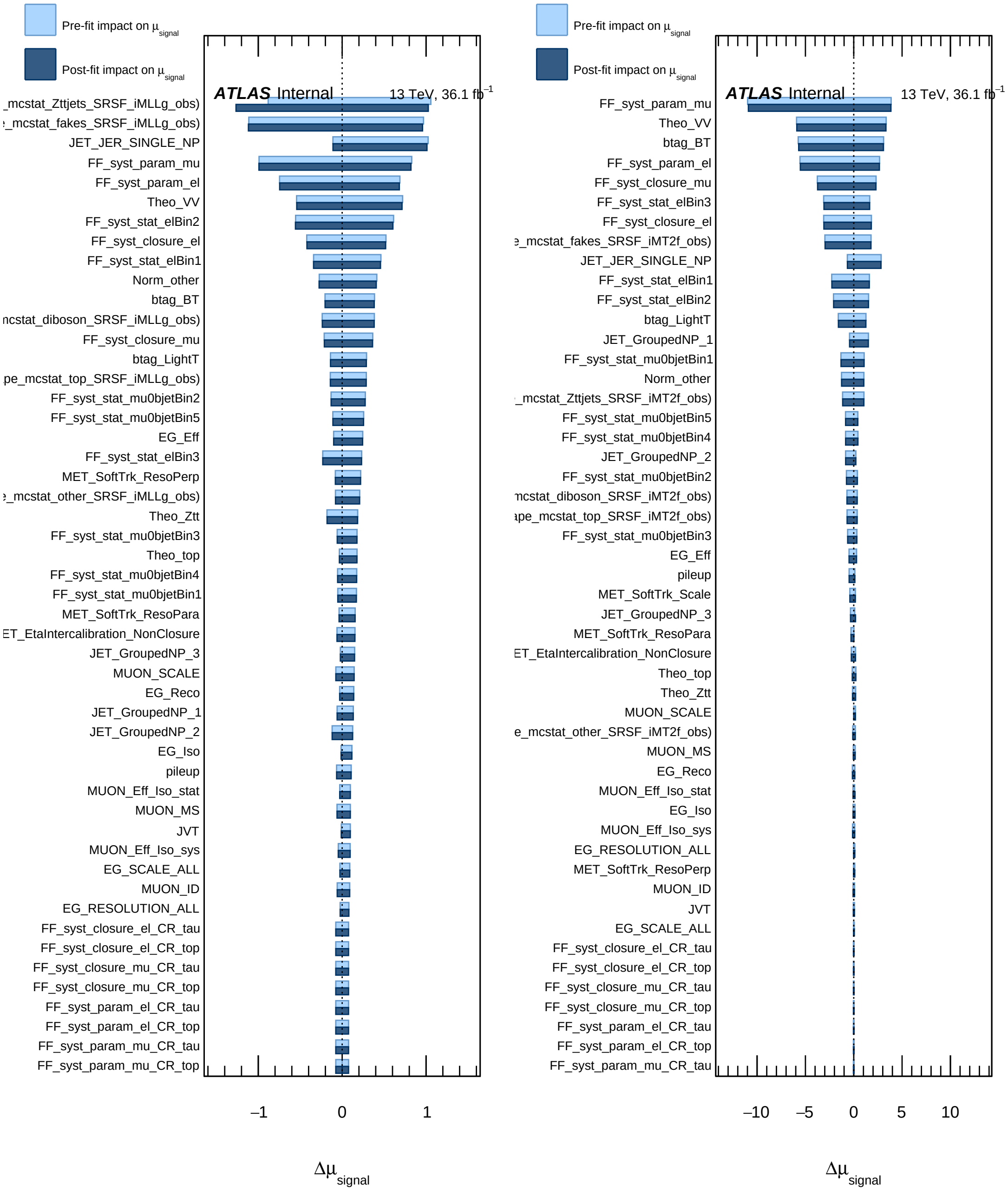

(a) CRs + SR$\ell\ell$-$m_{\ell\ell}$ $[1, 60]$ (b) CRs + SR$\ell\ell$-m_{T2}^{100} $[100, \infty]$

Figure 10.2: Ranking of systematics impact on μ_{signal} in the most inclusive Higgsino (left) and slepton (right) signal regions

Chapter 11

Results

11.1 Background-Only Fit

In the background-only fit, only the CRs are used to constrain the fit parameters by maximizing the likelihood function assuming there are no signal events in the CRs. In this way, the SM background predictions are independent of the signal regions. The factors μ_{top} and $\mu_{\tau\tau}$, used to normalize of the combined t, tW, and $t\bar{t}$ samples and the $Z(\rightarrow \tau\tau)$+jets samples, are obtained in a simultaneous fit to data in CR-top and CR-tau. For exclusion, two simultaneous shape fits are performed across ee and $\mu\mu$ channels, one in the $m_{\ell\ell}$ variable, and the other in the m_{T2}^{100} variable. The normalization parameters μ_{top} and $\mu_{\tau\tau}$ for the background-only fit are $\mu_{\text{top}} = 0.72 \pm 0.13$ and $\mu_{\tau\tau} = 1.02 \pm 0.09$, where the uncertainty is the combination of the statistical and systematic contributions.

Data and background prediction are shown for the diboson, same-sign, and

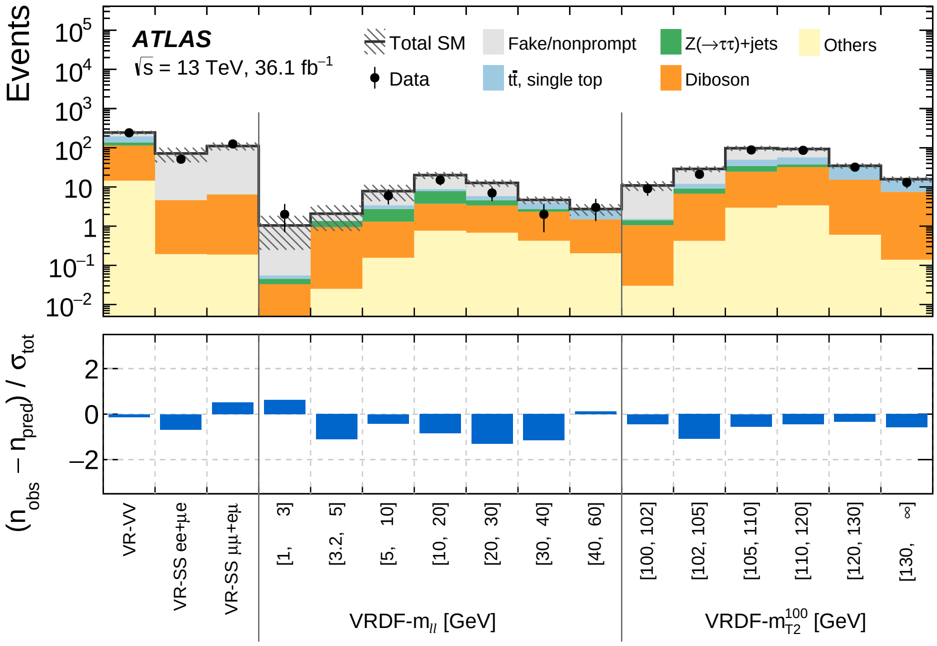

Figure 11.1: Summary of Monte Carlo yields in control, validation and signal regions in a background-only fit using data only in the two CRs to constrain the fit.

different-flavor validation regions in Figure 11.1. The accuracy of the background prediction is tested in each of the validation regions and is consistently within 1.5 standard deviations of the observed data yields. Figure 11.2 shows distributions of the data and expected backgrounds for a selection of VRs and kinematic variables, including the $m_{\ell\ell}$ distribution in VR-VV and the m_{T2} distribution in VR-SS. Similar levels of agreement are observed in other kinematic distributions for VR-SS and VR-VV. Data and background predictions are compatible within uncertainties. Figure 11.3 shows kinematic distributions of data and expected backgrounds in the inclusive Higgsino and slepton signal regions. No significant excesses above expected backgrounds are observed.

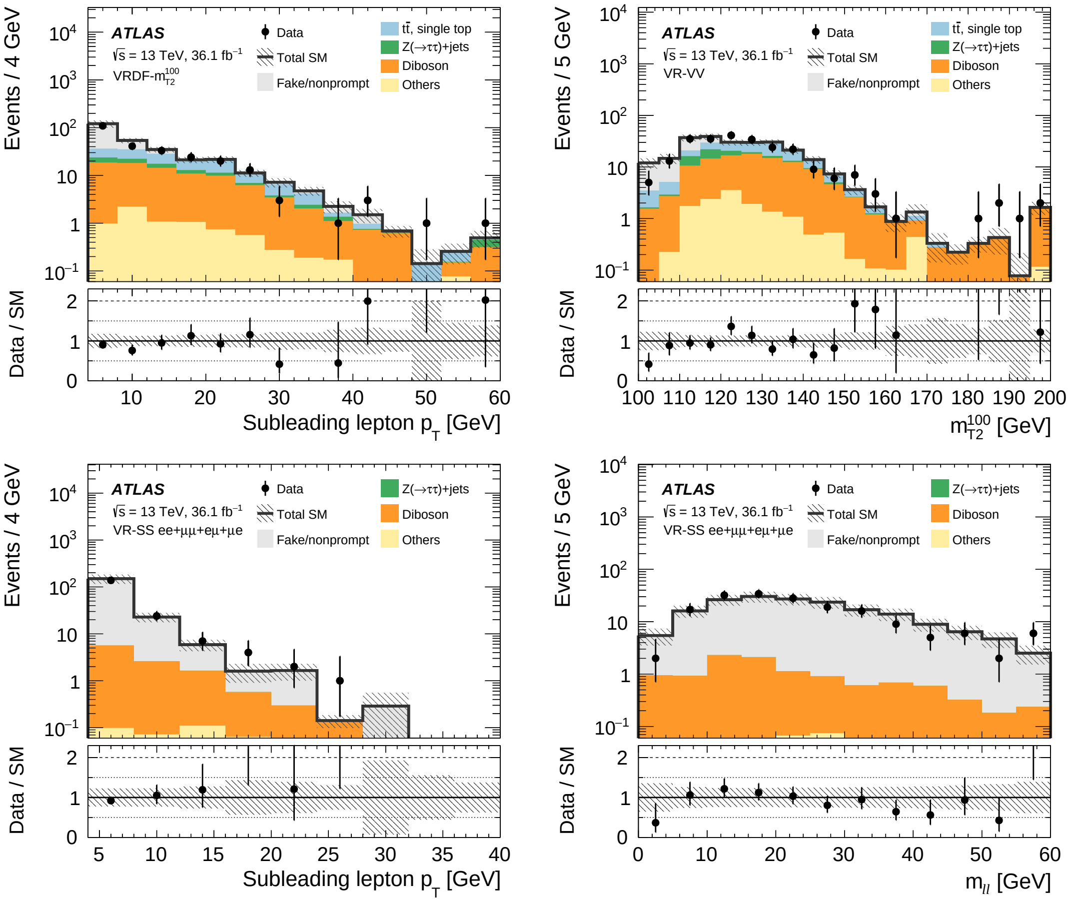

Figure 11.2: Kinematic distributions of data and expected backgrounds after the background-only fit. Top left plot shows the sub-leading lepton p_{T} distribution in the different-flavor validation region VRDF-m_{T2}^{100}; the top right plot shows the m_{T2}^{100} distribution in the diboson validation region VR-VV (top right); the sub-leading lepton p_{T} distribution in the bottom right plot and the $m_{\ell\ell}$ distribution in the bottom left are shown in the same-sign validation region VR-SS inclusive of lepton flavor. Background processes containing fewer than two prompt leptons are categorized as "Fake/nonprompt." The category "Others" contains rare backgrounds from triboson, Higgs boson, and multi-top processes. The last bin includes overflow.

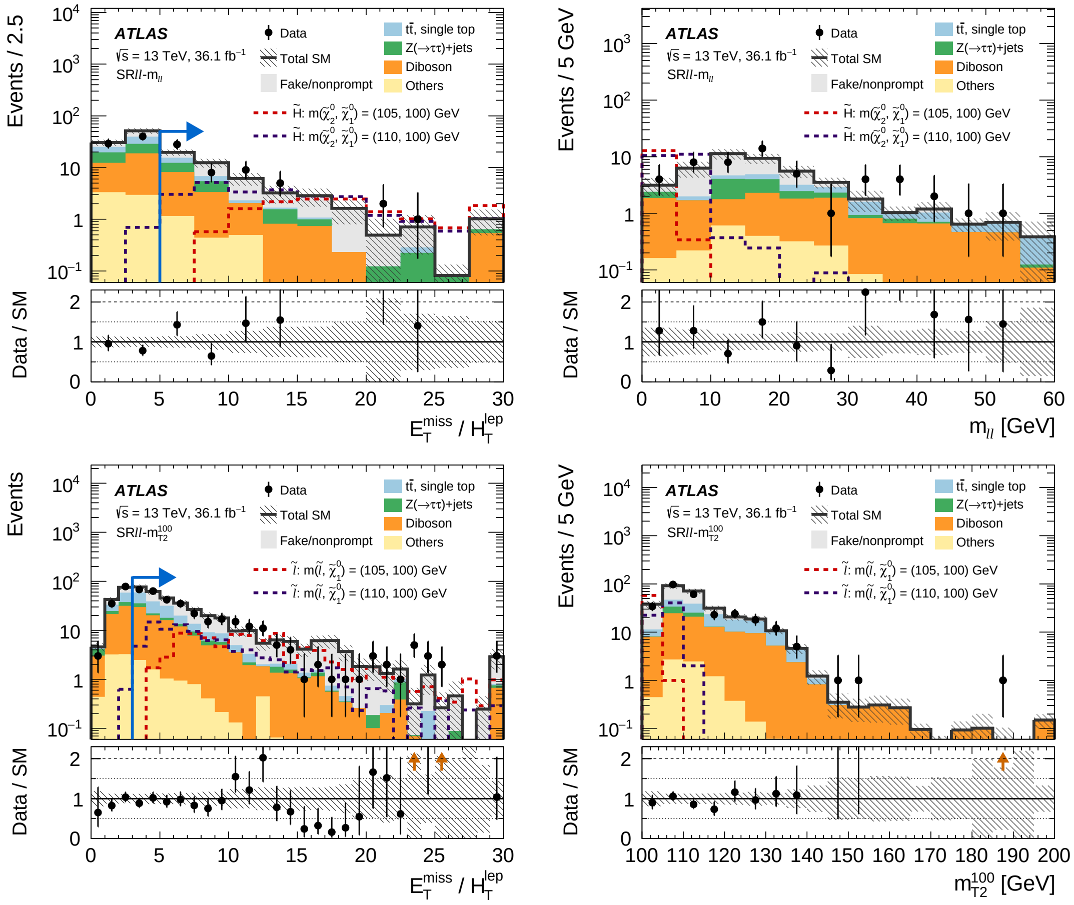

Figure 11.3: Kinematic distributions after the background-only fit showing the data as well as the expected background in the most inclusive electroweakino SR$\ell\ell$-$m_{\ell\ell}$ $[1, 60]$ (top) and slepton m_{T2}^{100} $[100, \infty]$ (bottom) signal regions. The arrow in the $E_{\mathrm{T}}^{\mathrm{miss}}/H_{T}^{lep}$ variables indicates the minimum value of the requirement imposed in the final SR selection. The $m_{\ell\ell}$ and m_{T2}^{100} distributions (right) have all the SR requirements applied. Background processes containing fewer than two prompt leptons are categorized as “Fake/nonprompt.” The category “Others” contains rare backgrounds from triboson, Higgs boson, and multi-top processes. The last bin includes overflow. The dashed lines represent benchmark signal samples corresponding to the Higgsino $\widetilde{H}$ and slepton $\tilde{\ell}$ simplified models. Orange arrows in the Data/SM panel indicate values that are beyond the y-axis range.

11.2 Model-Independent Upper Limits on New Physics

Model-independent limits are useful so that, for any signal model of interest, one can evaluate the number of events predicted in a signal region and check if the model is excluded by current measurements. For this, single-binned inclusive SRs are used, since binning in the SRs requires some model-based assumptions about the distribution of the signal over these bins. Table 11.1 present the observed and expected event yields, the upper limits on the number of observed and expected signal events, and the visible cross-section for new physics in each of the inclusive Higgsino SR$\ell\ell$-$m_{\ell\ell}$ and slepton m_{T2}^{100} signal regions. An upper limit on the number of observed (S_{obs}^{95}) and expected (S_{exp}^{95}) signal events in each SR at 95% CL is procured in the same way as the background-only fit, but now using CRs and SRs and with the observed number of events in a signal region given as inputs to the fit. The observed (N_{obs}) and predicted (N_{exp}) event yields are used to set the upper limits by including one inclusive signal region at a time in a simultaneous fit with the CRs. The profile-likelihood hypothesis test performed to get the upper limits uses the background estimates obtained from the background-only test in the CRs and SRs, and both the expected and observed upper limits use the same background estimates. An upper limit on the visible cross-section for new physics in a given SR, $\langle\epsilon\sigma\rangle_{\mathrm{obs}}^{95}$ [fb], is equal to product of the signal region acceptance, the reconstruction efficiency, and the production cross-section. The discovery p-value, $p(s = 0)$ in the right-most column of the table, represents the significance of an excess of events in a signal region by considering the probability that the backgrounds in a SR

Table 11.1: Left to right: The first two columns present observed (N_{obs}) and expected (N_{exp}) event yields in the inclusive signal regions. The latter are obtained by the background-only fit of the control regions, and the errors include both statistical and systematic uncertainties. The next two columns show the observed 95% CL upper limits on the visible cross-section $\left(\langle\epsilon\sigma\rangle^{95}_{\mathrm{obs}}\right)$ and on the number of signal events $\left(S^{95}_{\mathrm{obs}}\right)$. The fifth column $\left(S^{95}_{\mathrm{exp}}\right)$ shows what the 95% CL upper limit on the number of signal events would be, given an observed number of events equal to the expected number (and $\pm1\sigma$ deviations from the expectation) of background events. The last column indicates the discovery p-value ($p(s=0)$), which is capped at 0.5.

Signal Region	N_{obs}	N_{exp}	$\langle\epsilon\sigma\rangle^{95}_{\mathrm{obs}}$ [fb]	S^{95}_{obs}	S^{95}_{exp}	$p(s=0)$
SR$\ell\ell$-$m_{\ell\ell}$ $[1,3]$	1	1.7 ± 0.9	0.10	3.8	$4.3^{+1.7}_{-0.7}$	0.50
SR$\ell\ell$-$m_{\ell\ell}$ $[1,5]$	4	3.1 ± 1.2	0.18	6.6	$5.6^{+2.3}_{-1.0}$	0.32
SR$\ell\ell$-$m_{\ell\ell}$ $[1,10]$	12	8.9 ± 2.5	0.34	12.3	$9.6^{+3.2}_{-1.9}$	0.21
SR$\ell\ell$-$m_{\ell\ell}$ $[1,20]$	34	29 ± 6	0.61	22	17^{+7}_{-6}	0.25
SR$\ell\ell$-$m_{\ell\ell}$ $[1,30]$	40	38 ± 6	0.59	21	20^{+9}_{-5}	0.38
SR$\ell\ell$-$m_{\ell\ell}$ $[1,40]$	48	41 ± 7	0.72	26	20^{+8}_{-5}	0.20
SR$\ell\ell$-$m_{\ell\ell}$ $[1,60]$	52	43 ± 7	0.80	29	24^{+5}_{-10}	0.18
SR$\ell\ell$-m^{100}_{T2} $[100,102]$	8	12.4 ± 3.1	0.18	7	9^{+4}_{-2}	0.50
SR$\ell\ell$-m^{100}_{T2} $[100,105]$	34	38 ± 7	0.49	18	23^{+7}_{-7}	0.50
SR$\ell\ell$-m^{100}_{T2} $[100,110]$	131	129 ± 18	1.3	48	47^{+13}_{-15}	0.37
SR$\ell\ell$-m^{100}_{T2} $[100,120]$	215	232 ± 29	1.4	52	62^{+21}_{-15}	0.50
SR$\ell\ell$-m^{100}_{T2} $[100,130]$	257	271 ± 32	1.7	61	69^{+22}_{-17}	0.50
SR$\ell\ell$-m^{100}_{T2} $[100,\infty]$	277	289 ± 33	1.8	66	72^{+24}_{-17}	0.50

are more signal-like than observed.

11.3 Model Dependent Sensitivity with Shape Fit

Here we assume the Higgsino and slepton signals give rise to the $m_{\ell\ell}$ and m_{T2}^{100} distributions in our signal regions. This consideration provides better constraining power for these models over the model-independent upper limits of the "Discovery" fit. Like in the model-independent case, the fit is performed on the CRs and SRs simultaneously, but different from the model-independent case, the multi-binned exclusive SRs and considered. Background and signal samples are included in both the CR and SR fits to account for any signal contamination in the CRs.

Table 11.2 summarizes the observed event yields in the exclusive electroweakinio signal regions, and Table 11.3 summarizes the observed event yields in the exclusive slepton signal regions after the fit is performed using an exclusion fit configuration where the signal strength parameter is set to zero. Extending the background-only fit to include the signal regions further constrains the background contributions in the absence of any signal, therefore these predicted yields differ slightly compared to those obtained with the background-only fit. Figure 11.4 demonstrates the harmony between the fitted and observed yields in these signal regions. No significant contrast between the fitted background estimates and the observed event yields are observed in any of the exclusive signal regions.

Table 11.2: Observed event yields and exclusion fit results with the signal strength parameter set to zero for the exclusive electroweakino and slepton signal regions. Background processes containing fewer than two prompt leptons are categorized as “Fake/nonprompt.” The category “Others” contains rare backgrounds from triboson, Higgs boson, and multi-top processes. Uncertainties in the fitted background estimates combine statistical and systematic uncertainties.

SRee-$m_{\ell\ell}$	[1, 3]	[3.2, 5]	[5, 10]	[10, 20]	[20, 30]	[30, 40]	[40, 60]
Obs Evts	0	1	1	10	4	6	2
Exp SM Evts	$0.01^{+0.11}_{-0.01}$	$0.6^{+0.7}_{-0.6}$	$2.4^{+1.0}_{-1.0}$	$8.3^{+1.6}_{-1.6}$	4.0 ± 1.0	2.4 ± 0.6	1.4 ± 0.5
Fakes	$0.00^{+0.08}_{-0.00}$	$0.02^{+0.12}_{-0.02}$	1.4 ± 0.9	4.0 ± 1.5	1.6 ± 0.9	0.7 ± 0.6	$0.02^{+0.11}_{-0.02}$
Diboson	$0.007^{+0.014}_{-0.007}$	$0.28^{+0.29}_{-0.28}$	$0.51^{+0.28}_{-0.28}$	1.9 ± 0.6	$1.36^{+0.31}_{-0.31}$	0.72 ± 0.22	0.80 ± 0.28
$Z(\rightarrow \tau\tau)$+jets	$0.000^{+0.007}_{-0.000}$	$0.3^{+0.8}_{-0.3}$	$0.3^{+0.5}_{-0.3}$	1.7 ± 0.7	$0.25^{+0.26}_{-0.25}$	0.20 ± 0.18	$0.04^{+0.28}_{-0.04}$
$t\bar{t}$, single top	$0.00^{+0.08}_{-0.00}$	$0.02^{+0.12}_{-0.02}$	$0.11^{+0.14}_{-0.11}$	$0.44^{+0.29}_{-0.29}$	0.63 ± 0.35	0.7 ± 0.4	0.6 ± 0.4
Others	$0.002^{+0.015}_{-0.002}$	$0.012^{+0.013}_{-0.012}$	$0.12^{+0.11}_{-0.11}$	$0.25^{+0.16}_{-0.16}$	0.21 ± 0.12	$0.05^{+0.06}_{-0.05}$	$0.0018^{+0.0033}_{-0.0018}$

SR$\mu\mu$-$m_{\ell\ell}$	[1, 3]	[3.2, 5]	[5, 10]	[10, 20]	[20, 30]	[30, 40]	[40, 60]
Obs Evts	1	2	7	12	2	2	2
Exp SM Evts	1.1 ± 0.6	1.3 ± 0.6	4.9 ± 1.3	13.1 ± 2.2	4.2 ± 1.0	1.4 ± 0.6	1.6 ± 0.6
Fakes	$0.00^{+0.33}_{-0.00}$	$0.4^{+0.5}_{-0.4}$	3.0 ± 1.3	7.3 ± 2.1	$0.4^{+0.8}_{-0.4}$	$0.03^{+0.19}_{-0.03}$	$0.0^{+0.5}_{-0.0}$
Diboson	0.9 ± 0.5	0.7 ± 0.4	1.3 ± 0.6	1.4 ± 0.5	1.9 ± 0.4	0.9 ± 0.5	0.97 ± 0.28
$Z(\rightarrow \tau\tau)$+jets	$0.18^{+0.25}_{-0.18}$	0.13 ± 0.12	$0.3^{+0.5}_{-0.3}$	2.4 ± 0.8	0.7 ± 0.4	$0.001^{+0.011}_{-0.001}$	$0.05^{+0.06}_{-0.05}$
$t\bar{t}$, single top	$0.01^{+0.10}_{-0.01}$	$0.02^{+0.12}_{-0.02}$	0.19 ± 0.13	1.4 ± 0.6	0.8 ± 0.4	0.37 ± 0.21	0.51 ± 0.33
Others	0.047 ± 0.030	$0.07^{+0.09}_{-0.07}$	$0.13^{+0.12}_{-0.12}$	$0.7^{+0.5}_{-0.5}$	$0.35^{+0.20}_{-0.20}$	$0.09^{+0.07}_{-0.07}$	$0.020^{+0.020}_{-0.020}$

Table 11.3: Observed event yields and exclusion fit results with the signal strength parameter set to zero for the exclusive electroweakino and slepton signal regions. Background processes containing fewer than two prompt leptons are categorized as “Fake/nonprompt.” The category “Others” contains rare backgrounds from triboson, Higgs boson, and multi-top processes. Uncertainties in the fitted background estimates combine statistical and systematic uncertainties.

$\mathbf{SR}ee\text{-}m_{\mathbf{T2}}^{100}$	[100, 102]	[102, 105]	[105, 110]	[110, 120]	[120, 130]	$[130, \infty]$
Obs Evts	3	10	37	42	10	7
Exp SM Evts	3.5 ± 1.2	11.0 ± 2.0	33 ± 4	42 ± 4	15.7 ± 2.0	7.5 ± 1.1
Fakes	2.9 ± 1.2	6.8 ± 2.0	13 ± 4	14 ± 4	1.9 ± 1.2	$0.01^{+0.10}_{-0.01}$
Diboson	0.33 ± 0.12	2.3 ± 0.6	8.5 ± 1.6	12.7 ± 2.4	7.4 ± 1.4	4.3 ± 0.9
$Z(\to \tau\tau)$+jets	$0.13^{+0.23}_{-0.13}$	0.6 ± 0.4	4.1 ± 1.8	2.9 ± 1.0	$0.00^{+0.08}_{-0.00}$	$0.00^{+0.20}_{-0.00}$
$t\bar{t}$, single top	0.08 ± 0.08	1.2 ± 0.5	6.5 ± 1.6	10.7 ± 2.4	6.3 ± 1.4	3.2 ± 0.9
Others	$0.011^{+0.012}_{-0.011}$	0.17 ± 0.11	0.8 ± 0.4	1.3 ± 0.7	0.14 ± 0.09	0.06 ± 0.04

$\mathbf{SR}\mu\mu\text{-}m_{\mathbf{T2}}^{100}$	[100, 102]	[102, 105]	[105, 110]	[110, 120]	[120, 130]	$[130, \infty]$
Obs Evts	5	16	60	42	32	13
Exp SM Evts	6.8 ± 1.5	15.0 ± 2.1	57 ± 5	53 ± 4	24.9 ± 2.9	11.0 ± 1.4
Fakes	5.1 ± 1.5	8.2 ± 2.1	26 ± 5	18 ± 4	1.2 ± 0.8	$0.02^{+0.17}_{-0.02}$
Diboson	0.89 ± 0.22	4.1 ± 0.9	14.3 ± 2.2	18.0 ± 2.7	12.9 ± 2.2	5.9 ± 1.1
$Z(\to \tau\tau)$+jets	0.31 ± 0.23	$1.0^{+1.3}_{-1.0}$	6.6 ± 1.7	$1.6^{+1.8}_{-1.6}$	$0.03^{+0.25}_{-0.03}$	$0.02^{+0.24}_{-0.02}$
$t\bar{t}$, single top	0.43 ± 0.22	1.4 ± 0.5	8.3 ± 2.2	12.4 ± 2.9	10.5 ± 2.6	5.0 ± 1.3
Others	$0.020^{+0.024}_{-0.020}$	0.24 ± 0.15	1.8 ± 1.0	2.4 ± 1.3	0.35 ± 0.23	0.11 ± 0.07

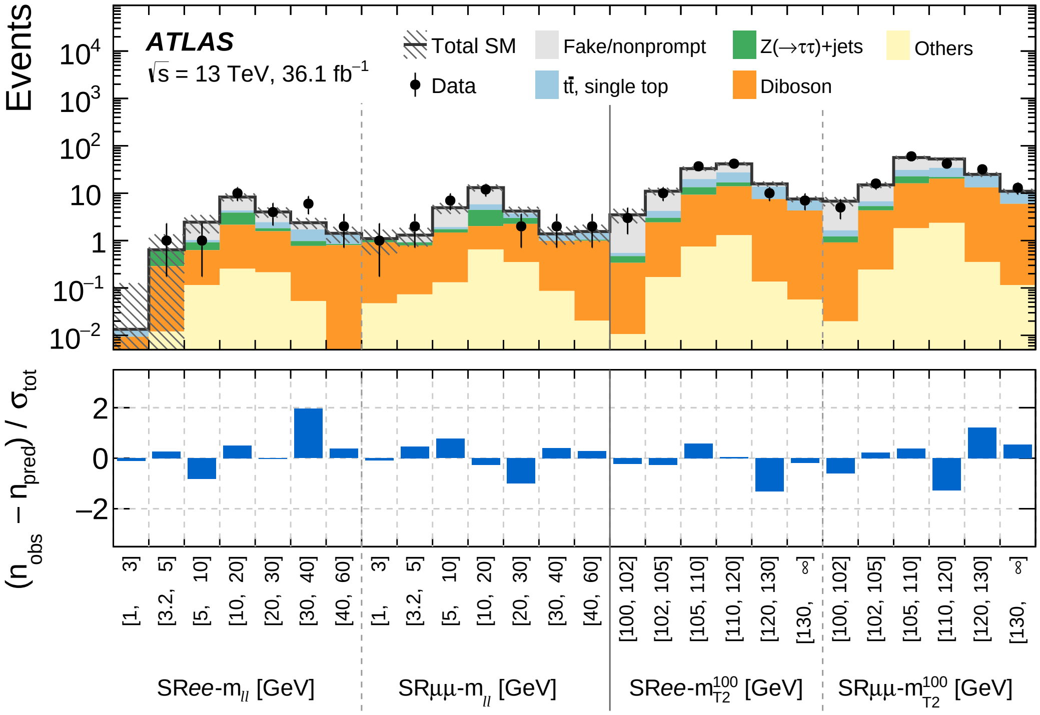

Figure 11.4: Comparison of observed and expected event yields after the exclusion fit. Background processes containing fewer than two prompt leptons are categorized as "Fake/nonprompt." The category "Others" contains rare backgrounds from triboson, Higgs boson, and multi-top processes. Uncertainties in the background estimates include both the statistical and systematic uncertainties, where σ_{tot} denotes the total uncertainty.

Chapter 12

Interpretations

In absence of any significant excesses over backgrounds, the results are interpreted as constraints on the SUSY models presented in Chapter 2 using the exclusive, multi-binned Higgsino and slepton signal regions. The background-only fit is extended to allow for a signal model with a corresponding signal strength parameter in a simultaneous fit of all CRs and relevant SRs, this is referred to as the exclusion fit. In the previous chapter, background-level estimates obtained from a background-only fit in the CRs only were presented. When electroweakino simplified models are assumed, the results are interpreted in the 14 exclusive Higgsino signal regions, binned in $m_{\ell\ell}$ and split evenly between the ee and $\mu\mu$ channels. By statistically combining these signal regions, the signal shape of the $m_{\ell\ell}$ spectrum can be exploited to improve the sensitivity. When slepton simplified models are assumed, the results are interpreted in 12 slepton signal regions, binned in $m_{T2^{100}}$ with 6 SRs the ee-channel and 6 in the $\mu\mu$-channel.

12.1 Compressed Higgsino

Hypothesis tests are performed to set limits on simplified model scenarios using the CL_s prescription. Figure 12.1 shows the 95% confidence level limits set on the Higgsino simplified model projected onto the plane defined by the mass difference between the lightest and next-to-lightest neutralino as a function of the next-to-lightest neutralino mass. These limits are based on an exclusion fit that exploits the shape of the dilepton invariant mass spectrum from the exclusive electroweakino signal regions and exclude next-to-lightest neutralino masses up to 130 GeV for mass splittings between 5 and 10 GeV. For mass splittings down to 3 GeV next-to-lightest neutralino masses are excluded up to 100 GeV.

12.2 Compressed Wino

The 95% confidence level intervals for the wino-bino simplified model are shown in Figure 12.2. Just like in the Higgsino exclusion plot, these limits are based on an exclusion fit that exploits the shape of the dilepton invariant mass spectrum from the exclusive electroweakino signal regions. Exclusion limits are projected onto the mass difference $\Delta m(\tilde{\chi}_2^0, \tilde{\chi}_1^0)$ plane as a function of the $\tilde{\chi}_2^0$ mass. For wino-bino simplified models, next-to-lightest neutralino masses are excluded up to 170 GeV for mass splittings above 10 GeV, and excluded up to 100 GeV for mass splittings down to 2.5 GeV.

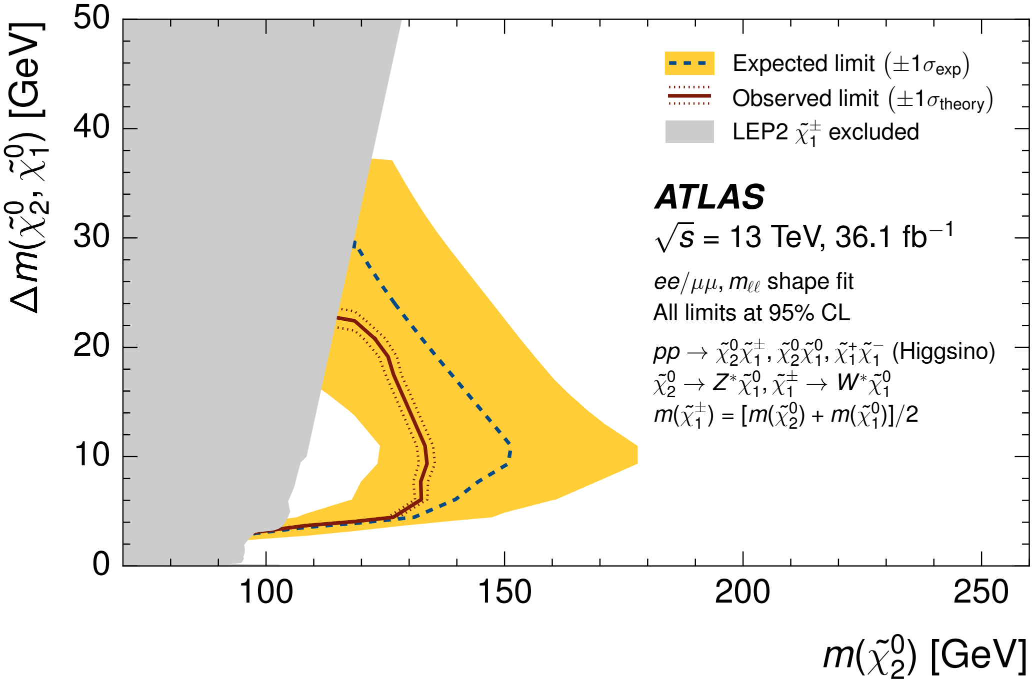

Figure 12.1: Expected 95% CL exclusion sensitivity (blue dashed line) with $\pm 1\sigma_{\text{exp}}$ (yellow band) from experimental systematics and observed limits (red solid) with $\pm 1\sigma_{\text{theory}}$ (dotted red) from signal cross section uncertainties. A shape fit of Higgsino signals to the $m_{\ell\ell}$ spectrum is used to derive the limit is displayed in the $m(\tilde{\chi}_2^0) - m(\tilde{\chi}_1^0)$ vs $m(\tilde{\chi}_2^0)$ plane. The chargino $\tilde{\chi}_1^\pm$ mass is assumed to be half way between the two lightest neutralinos. The gray region denotes the lower chargino mass limit from LEP [13].

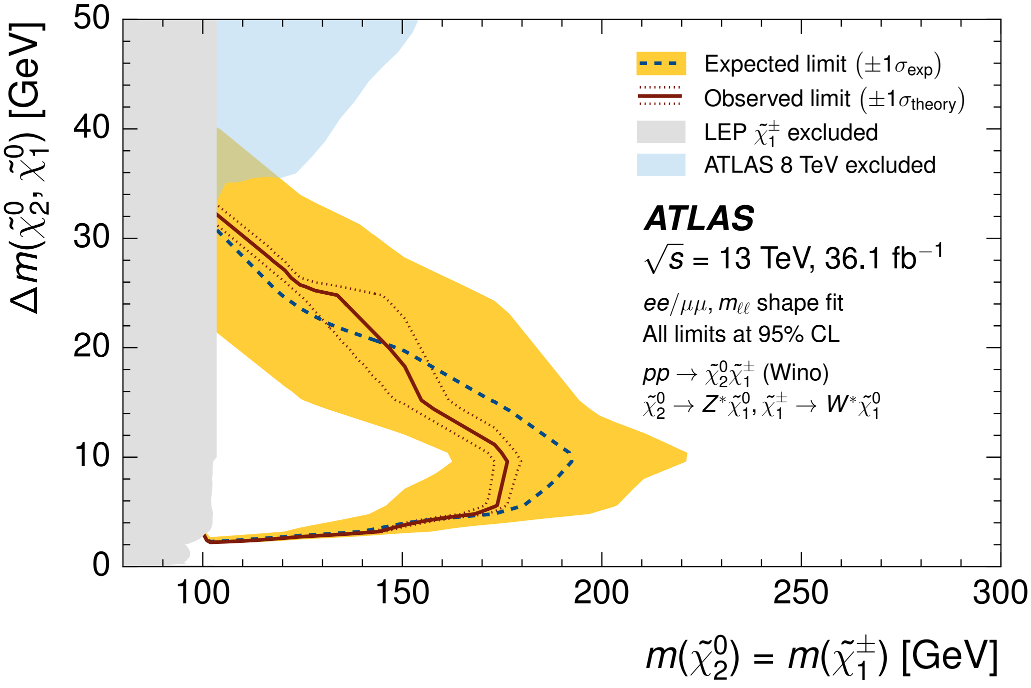

Figure 12.2: Expected 95% CL exclusion sensitivity (blue dashed line) with $\pm1\sigma_{\text{exp}}$ (yellow band) from experimental systematic uncertainties and observed limits (red solid line) with $\pm1\sigma_{\text{theory}}$ (dotted red line) from signal cross-section uncertainties for simplified models direct wino production. A shape fit of wino signals to the $m_{\ell\ell}$ spectrum is used to derive the limit is displayed in the $m(\tilde{\chi}_2^0) - m(\tilde{\chi}_1^0)$ vs $m(\tilde{\chi}_2^0)$ plane. The chargino $\tilde{\chi}_1^\pm$ mass is assumed equal to the $m(\tilde{\chi}_2^0)$ mass. The gray region denotes the lower chargino mass limit from LEP [13], and the blue region in the lower plot indicates the limit from the 2ℓ+3ℓ combination of ATLAS Run 1.

12.3 Compressed Slepton

Figure 12.3 shows the 95% confidence level limits set on the slepton simplified model projected onto the plane defined by the mass difference between the slepton and lightest neutralino as a function of the slepton mass. These limits are based on an exclusion fit that exploits the shape of the m_{T2} spectrum from the exclusive slepton signal regions and exclude slepton masses up to 180 GeV for mass splittings down to 5 GeV. For mass splittings down to 1 GeV slepton masses are excluded up to 70 GeV. In slepton simplified models, a fourfold degeneracy is assumed between the left and right-handed selectrons and smuons: $\tilde{e}_R = \tilde{e}_L = \tilde{\mu}_R = \tilde{\mu}_L$.

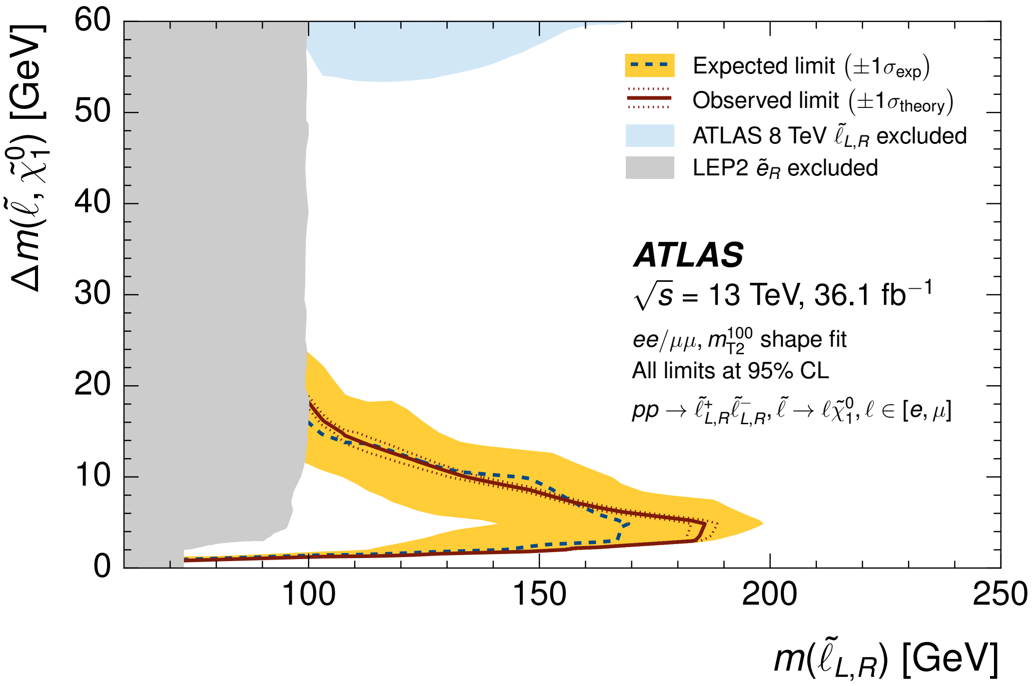

Figure 12.3: Expected 95% CL exclusion sensitivity (blue dashed line) with $\pm1\sigma_{\text{exp}}$ (yellow band) from experimental systematics and observed limits (red solid) with $\pm1\sigma_{\text{theory}}$ (dotted red) from signal cross section uncertainties. A shape fit of slepton signals to the m_{T2}^{100} spectrum is used to derive the limit projected into the $m(\tilde{\ell}) - m(\tilde{\chi}_1^0)$ vs $m(\tilde{\ell})$ plane. The slepton $\tilde{\ell}$ refers to a 4-fold mass degenerate system of left- and right-handed selectron and smuon. The gray region denotes a conservative right-handed smuon $\tilde{\mu}_R$ mass limit from LEP [13], while the blue region is the 4-fold mass degenerate slepton limit from ATLAS Run 1 [6].

Chapter 13

Conclusion

A search for supersymmetry in scenarios with compressed mass spectra was performed using ATLAS data, collected in 2015 and 2016 at $\sqrt(s)$ 13 TeV, corresponding to 36.1 fb^{-1}. We searched for directly-produced electroweakinos and sleptons in events containing two soft, opposite-sign same-flavor leptons with an intermediate amount of missing transverse energy and a hard jet. Signal event characteristics are studied with Higgsino and slepton simplified models. The directly-produced electroweakinos and sleptons subsequently decay to a lightest SUSY particle which is nearly degenerate in mass and their Standard Model partners. The energy of the visible leptons is related to the mass splitting between the neutral electroweakinos $\tilde{\chi}_2^0$ and $\tilde{\chi}_1^0$ or between the sleptons $\tilde{\ell}_{L,R}$ and the lightest neutral electroweakino $\tilde{\chi}_1^0$. The relationship between lepton momentum and the mass splittings provides discriminating variables unique to the electroweakino and slepton decays. Electroweakino signals are sensitive to the invariant mass of the dilepton system, $m_{\ell\ell}$, and slepton signals are sensitive to the stransverse mass of the $E_{\mathrm{T}}^{\mathrm{miss}}$ and leptons, m_{T2}^{100}. Inclusive and exclusive signal regions are binned in $m_{\ell\ell}$ for the searches targeting electroweakino production, and in m_{T2}^{100} for the search targeting sleptons.

The dominant backgrounds to signal event with soft leptons and $E_{\mathrm{T}}^{\mathrm{miss}}$ are from jets faking leptons in the detector. These are estimated with a data-driven fake factor technique and tested in a same-sign validation region that includes $ee+\mu e$ events in the electron channel, and $\mu\mu+e\mu$ events in the muon channel. Irreducible backgrounds from $t\bar{t}$, tW, and $Z(\rightarrow\tau\tau)$+jets processes were estimated with Monte Carlo and normalized in data-driven control regions. Irreducible diboson backgrounds were estimated with Monte Carlo and tested in a dedicated diboson validation region. Low mass Drell-Yan, Higgs, triboson, and multi-top backgrounds were estimated with Monte Carlo only.

Background only fits were performed on CR-top and CR-tau to obtain background normalization parameters $\mu_{\mathrm{top}} = 0.72 \pm 0.13$ and $\mu_{\tau\tau} = 1.02 \pm 0.09$, respectively. The accuracy of the background prediction was tested in each of the validation regions and is consistently within 1.5 σ of the observed data. Model independent upper limits were set at 95% CL on the observed and expected upper limits on the number of signal events in the inclusive SRs were set with simultaneous fits in each SR and the CRs, assuming the background only hypothesis. No significant excess in data over Standard Model background was found; therefore, results were consistent with Standard Model prediction.

For model dependent interpretations, shape fits in $m_{\ell\ell}$ and m_{T2}^{100} were performed. These are full simultaneous fits over the exclusive, multi-binned SRs and the

CRs including both signal and backgrounds predictions. In the absence of significant excesses in data over background, result were interpreted as constraints on SUSY electroweakino and slepton models. Higgsino models are excluded for next-to-lightest neutralino masses up to 130 GeV for mass splittings between 5 and 10 GeV. For mass splittings down to 3 GeV next-to-lightest neutralino masses are excluded up to 100 GeV. For wino-bino simplified models, next-to-lightest neutralino masses are excluded up to 170 GeV for mass splittings above 10 GeV, and excluded up to 100 GeV for mass splittings down to 2.5 GeV. For slepton simplified models, slepton masses are excluded up to 180 GeV for mass splittings down to 5 GeV. For mass splittings down to 1 GeV slepton masses are excluded up to 70 GeV.

Figure 13.1 summarizes the current limits on compressed electroweak SUSY set by LEP in 2001, the ATLAS Run 2 disappearing track analysis, and the two-soft-lepton analysis that is the subject of this thesis. Future versions of the two-soft-lepton analysis will try to extend the reach in the $\Delta m(\tilde{\chi}_1^{\pm}\tilde{\chi}_1^0)$, $m(\tilde{\chi}_1^{\pm})$ phase space, with different techniques designed to extend the limits in different directions. To reach farther in $m(\tilde{\chi}_1^{\pm})$ or $m(\tilde{\chi}_2^0)$ will require more data to overcome the falling cross-sections as the chargino and neutralino masses grow. In 2017 alone, ATLAS doubled the amount of data it took in 2015 and 2016 combined, and data-taking for 2018 is currently underway. Extending the search to target mass-splittings above 10 GeV will require a new optimization of the electroweakino and slepton signal regions. For mass-splittings below 10 GeV, $m_{\ell\ell}$ and m_{T2}^{100} are powerful discriminators for compressed signals, but once the mass-splittings rise, the kinematic end-point still exists, but the distributions begin to flatten, washing out some of the signal shape. Re-optimizing the signal regions with the use of recursive jigsaw variables [50] may help to recover signal over backgrounds for larger mass-splittings by exploiting boosted, compressed systems when the $E_{\mathrm{T}}^{\mathrm{miss}}$ associated with the invisible LSPs gets most of its energy from the kick of an ISR jet. Lastly, the limiting factor on the minimum mass-splittings available to this search is the minimum p_{T} at which leptons are reconstructed. A similar version of this analysis, searching for a single identified lepton and an isolated track, is a possible way to get around the p_{T} limit for reconstructed leptons. Each of these modifications are being studied, and new versions of this search using the full Run 2 data set are under construction.

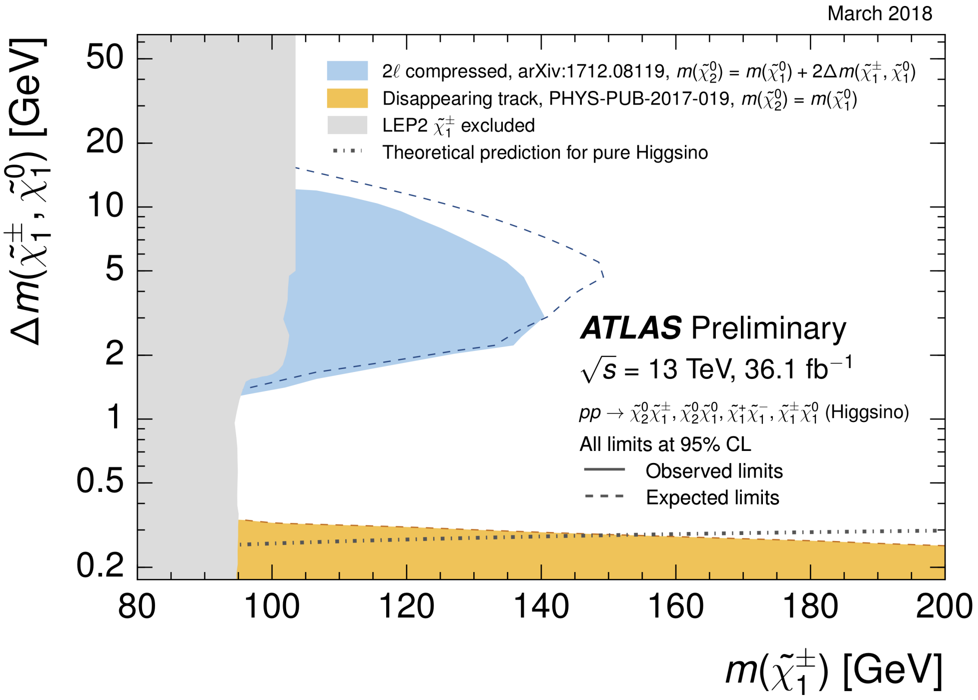

Figure 13.1: Summary plot for compressed electroweak searches, including combined LEP limits in grey. The ATLAS Run 2 disappearing track analysis, which targets mass-splittings $\mathcal{O}(1)$ GeV, is shown in orange. The two-soft-lepton analysis described in this thesis is shown in light blue.

Bibliography

[1] ATLAS Run 1 Pythia8 tunes. Technical Report ATL-PHYS-PUB-2014-021, CERN, Geneva, Nov 2014.

[2] LEP Design Report: Vol.2. The LEP Main Ring. 1984.

[3] M. Aaboud et al. Performance of the ATLAS Track Reconstruction Algorithms in Dense Environments in LHC Run 2. *Eur. Phys. J.*, C77(10):673, 2017.

[4] Morad Aaboud et al. Study of the material of the ATLAS inner detector for Run 2 of the LHC. *JINST*, 12(12):P12009, 2017.

[5] G. Aad et al. The ATLAS Experiment at the CERN Large Hadron Collider. *JINST*, 3:S08003, 2008.

[6] Georges Aad et al. Search for direct production of charginos and neutralinos in events with three leptons and missing transverse momentum in $\sqrt{s} = 8\text{TeV}$ pp collisions with the ATLAS detector. *JHEP*, 04:169, 2014.

[7] Georges Aad et al. Measurements of the W production cross sections in association with jets with the ATLAS detector. *Eur. Phys. J.*, C75(2):82, 2015.

[8] Georges Aad et al. Muon reconstruction performance of the ATLAS detector in pp collision data at $\sqrt{s}$ =13 TeV. *Eur. Phys. J.*, C76(5):292, 2016.

[9] A. Abdesselam et al. The barrel modules of the ATLAS semiconductor tracker. *Nucl. Instrum. Meth.*, A568:642–671, 2006.

[10] Q. R. Ahmad et al. Measurement of the rate of $\nu_e + d \to p + p + e^-$ interactions produced by ^8B solar neutrinos at the Sudbury Neutrino Observatory. *Phys. Rev. Lett.*, 87:071301, 2001.

[11] A. Airapetian et al. ATLAS: Detector and physics performance technical design report. Volume 1. 1999.

[12] M. Adeel Ajaib, Bhaskar Dutta, Tathagata Ghosh, Ilia Gogoladze, and Qaisar Shafi. Neutralinos and sleptons at the LHC in light of muon $(g-2)_\mu$. *Phys. Rev.*, D92(7):075033, 2015.

[13] ALEPH, DELPHI, L3, OPAL Experiments. Combined LEP Chargino Results, up to 208 GeV for low DM. LEPSUSYWG/02-04.1, 2002.

[14] Daniele Alves. Simplified Models for LHC New Physics Searches. *J. Phys.*, G39:105005, 2012.

[15] J. Alwall, R. Frederix, S. Frixione, V. Hirschi, F. Maltoni, O. Mattelaer, H. S. Shao, T. Stelzer, P. Torrielli, and M. Zaro. The automated computation of tree-level and next-to-leading order differential cross sections, and their matching to parton shower simulations. *JHEP*, 07:079, 2014.

[16] Johan Alwall, My-Phuong Le, Mariangela Lisanti, and Jay G. Wacker. Searching for Directly Decaying Gluinos at the Tevatron. *Phys. Lett.*, B666:34–37, 2008.

[17] Johan Alwall, Philip Schuster, and Natalia Toro. Simplified Models for a First Characterization of New Physics at the LHC. *Phys. Rev.*, D79:075020, 2009.

[18] Pierre Artoisenet, Rikkert Frederix, Olivier Mattelaer, and Robbert Rietkerk. Automatic spin-entangled decays of heavy resonances in Monte Carlo simulations. *JHEP*, 03:015, 2013.

[19] M. Baak, G. J. Besjes, D. Cte, A. Koutsman, J. Lorenz, and D. Short. HistFitter software framework for statistical data analysis. *Eur. Phys. J.*, C75:153, 2015.

[20] Howard Baer, Azar Mustafayev, and Xerxes Tata. Monojet plus soft dilepton signal from light higgsino pair production at LHC14. *Phys. Rev.*, D90(11):115007, 2014.

[21] Richard D. Ball et al. Parton distributions with LHC data. *Nucl. Phys.*, B867:244–289, 2013.

[22] Alan Barr and James Scoville. A boost for the EW SUSY hunt: monojet-like search for compressed sleptons at LHC14 with 100 fb^{-1}. *JHEP*, 04:147, 2015.

[23] Giuseppe Battistoni et al. The Application of the Monte Carlo Code FLUKA in Radiation Protection Studies for the Large Hadron Collider. *Prog. Nucl. Sci. Tech.*, 2:358–364, 2011.

[24] Philip Bechtle, Klaus Desch, Werner Porod, and Peter Wienemann. Determination

of MSSM parameters from LHC and ILC observables in a global fit. *Eur. Phys. J.*, C46:533–544, 2006.

[25] Philip Bechtle, Tilman Plehn, and Christian Sander. Supersymmetry. In Thomas Schrner-Sadenius, editor, *The Large Hadron Collider: Harvest of Run 1*, pages 421–462. 2015.

[26] Gianfranco Bertone, Dan Hooper, and Joseph Silk. Particle dark matter: Evidence, candidates and constraints. *Phys. Rept.*, 405:279–390, 2005.

[27] Samoil M. Bilenky and J. Hosek. GLASHOW-WEINBERG-SALAM THEORY OF ELECTROWEAK INTERACTIONS AND THE NEUTRAL CURRENTS. *Phys. Rept.*, 90:73–157, 1982.

[28] S Boutle, D Casper, B Hooberman, and ATLAS Collaboration. Primary vertex reconstruction at the ATLAS experiment. *Journal of Physics: Conference Series*, 898(4):042056, 2017.

[29] Joseph Bramante, Nishita Desai, Patrick Fox, Adam Martin, Bryan Ostdiek, and Tilman Plehn. Towards the final word on neutralino dark matter. *Phys. Rev. D*, 93:063525, Mar 2016.

[30] Giorgio Busoni, Andrea De Simone, Thomas Jacques, Enrico Morgante, and Antonio Riotto. Making the Most of the Relic Density for Dark Matter Searches at the LHC 14 TeV Run. *JCAP*, 1503(03):022, 2015.

[31] Matteo Cacciari, Gavin P. Salam, and Gregory Soyez. The Anti-k(t) jet clustering algorithm. *JHEP*, 04:063, 2008.

[32] Jean-Luc Caron. Overall view of LHC experiments.. Vue d'ensemble des experiences du LHC. AC Collection. Legacy of AC. Pictures from 1992 to 2002., May 1998.

[33] Fabio Cascioli, Philipp Maierhofer, and Stefano Pozzorini. Scattering Amplitudes with Open Loops. *Phys. Rev. Lett.*, 108:111601, 2012.

[34] Gordon Chalmers. Quantum gravity with the standard model. 2002.

[35] C. Chang et al. Dark Energy Survey Year 1 Results: Curved-Sky Weak Lensing Mass Map. *Mon. Not. Roy. Astron. Soc.*, 475(3):3165–3190, 2018.

[36] A. Djouadi, M. M. Muhlleitner, and M. Spira. Decays of supersymmetric particles: The Program SUSY-HIT (SUspect-SdecaY-Hdecay-InTerface). *Acta Phys. Polon.*, B38:635–644, 2007.

[37] Joakim Edsjo and Paolo Gondolo. Neutralino relic density including coannihilations. *Phys. Rev.*, D56:1879–1894, 1997.

[38] Lyndon Evans and Philip Bryant. LHC Machine. *JINST*, 3:S08001, 2008.

[39] Stefano Frixione et al. Angular correlations of lepton pairs from vector boson and top quark decays in Monte Carlo simulations. *Journal of High Energy Physics*, 2007(10):081, 2007.

[40] Benjamin Fuks, Michael Klasen, David R. Lamprea, and Marcel Rothering. Precision predictions for electroweak superpartner production at hadron colliders with Resummino. *Eur. Phys. J.*, C73:2480, 2013.

[41] Benjamin Fuks, Michael Klasen, David R. Lamprea, and Marcel Rothering. Revisiting slepton pair production at the Large Hadron Collider. *JHEP*, 01:168, 2014.

[42] Y. Fukuda et al. Evidence for oscillation of atmospheric neutrinos. *Phys. Rev. Lett.*, 81:1562–1567, 1998.

[43] Katherine Garrett and Gintaras Duda. Dark Matter: A Primer. *Adv. Astron.*, 2011:968283, 2011.

[44] S. L. Glashow. Partial Symmetries of Weak Interactions. *Nucl. Phys.*, 22:579–588, 1961.

[45] Tanju Gleisberg and Stefan Hoeche. Comix, a new matrix element generator. *JHEP*, 12:039, 2008.

[46] Kim Griest and David Seckel. Three exceptions in the calculation of relic abundances. *Phys. Rev. D*, 43:3191–3203, May 1991.

[47] Rudolf Haag, Jan T. Lopuszanski, and Martin Sohnius. All possible generators of supersymmetries of the S-matrix. *Nuclear Physics B*, 88:257 – 274, 1972.

[48] Zhenyu Han, Graham D. Kribs, Adam Martin, and Arjun Menon. Hunting quasidegenerate Higgsinos. *Phys. Rev.*, D89(7):075007, 2014.

[49] A. Henriques and the ATLAS Collaboration. The ATLAS Tile Calorimeter. March 2015.

[50] Paul Jackson, Christopher Rogan, and Marco Santoni. Sparticles in motion: Analyzing compressed SUSY scenarios with a new method of event reconstruction. *Phys. Rev.*, D95(3):035031, 2017.

[51] Can Kilic, Karoline Kopp, and Takemichi Okui. LHC Implications of the WIMP Miracle and Grand Unification. *Phys. Rev.*, D83:015006, 2011.

[52] Stephen F. King, Alexander Merle, Stefano Morisi, Yusuke Shimizu, and Morimitsu Tanimoto. Neutrino Mass and Mixing: from Theory to Experiment. *New J. Phys.*, 16:045018, 2014.

[53] Volker Koch. Introduction to chiral symmetry. In *3rd TAPS Workshop on Electromagnetic and Mesonic Probes of Nuclear Matter Bosen, Germany, September 10-15, 1995*, 1995.

[54] Nils Lavesson and Leif Lonnblad. Merging parton showers and matrix elements: Back to basics. *JHEP*, 04:085, 2008.

[55] M. Limper. *Track and vertex reconstruction in the ATLAS inner detector*. Dissertation, University of Amsterdam, 2009.

[56] Stephen P. Martin. A Supersymmetry primer. pages 1–98, 1997. [Adv. Ser. Direct. High Energy Phys.18,1(1998)].

[57] John McDonald. Generation of WIMP Miracle-like Densities of Baryons and Dark Matter. 2012.

[58] Bartosz Mindur. ATLAS Transition Radiation Tracker (TRT): Straw tubes for tracking and particle identification at the Large Hadron Collider. Technical Report ATL-INDET-PROC-2016-001, CERN, Geneva, Mar 2016.

[59] Vasiliki A. Mitsou. The ATLAS transition radiation tracker. In *Astroparticle, particle and space physics, detectors and medical physics applications. Proceedings, 8th Conference, ICATPP 2003, Como, Italy, October 6-10, 2003*, pages 497–501, 2003.

[60] Tapan K. Nayak. Heavy Ions: Results from the Large Hadron Collider. *Pramana*, 79:719–735, 2012.

[61] Arnold Neumaier and Dennis Westra. Classical and quantum mechanics via lie algebras. *arXiv:0810.1019v2 [quant-ph]*, 2014.

[62] C. Patrignani et al. Review of Particle Physics. *Chin. Phys.*, C40(10):100001, 2016.

[63] Stefano Profumo, Tim Stefaniak, and Laurel Stephenson-Haskins. Not-so-well-tempered neutralino. *Phys. Rev. D*, 96:055018, Sep 2017.

[64] J. Pumplin, D. R. Stump, J. Huston, H. L. Lai, Pavel M. Nadolsky, and W. K. Tung. New generation of parton distributions with uncertainties from global QCD analysis. *JHEP*, 07:012, 2002.

[65] Vera C. Rubin. Dark matter in spiral galaxies. *Scientific American*, 248:96–108, 1983.

[66] Vera C. Rubin, Jr. W. Kent Ford, and Judith S. Rubin. A curious distribution of radial velocities of sci galaxies with $14.0 \leq m \leq 15.0$. *The Astrophysical Journal*, 183:L111–L115, 1973.

[67] A. D. Sakharov. Violation of CP Invariance, C asymmetry, and baryon asymmetry of the universe. *Pisma Zh. Eksp. Teor. Fiz.*, 5:32–35, 1967. [Usp. Fiz. Nauk161,no.5,61(1991)].

[68] Abdus Salam. Weak and Electromagnetic Interactions. *Conf. Proc.*, C680519:367–377, 1968.

[69] Andreas Salzburger. Optimisation of the ATLAS Track Reconstruction Software for Run-2. *J. Phys. Conf. Ser.*, 664(7):072042, 2015.

[70] Torbjorn Sjostrand, Stephen Mrenna, and Peter Z. Skands. A Brief Introduction to PYTHIA 8.1. *Comput. Phys. Commun.*, 178:852–867, 2008.

[71] Gary Steigman, Basudeb Dasgupta, and John F. Beacom. Precise Relic WIMP Abundance and its Impact on Searches for Dark Matter Annihilation. *Phys. Rev.*, D86:023506, 2012.

[72] Y. Takubo. The Pixel Detector of the ATLAS experiment for the Run2 at the Large Hadron Collider. *JINST*, 10(02):C02001, 2015.

[73] Grigore Tarna. Electron identification with the ATLAS detector. Technical Report ATL-PHYS-PROC-2017-173, CERN, Geneva, Sep 2017.

[74] Christopher G. Tully. *Elementary Particle Physics in a Nutshell.* Princeton University Press, 2011.

[75] Vidal and Manzano. *Taking a Closer Look at LHC Beta & Emittance.* https://www.lhc-closer.es/taking_a_closer_look_at_lhc/0.beta___emittance.

[76] G. Watt and R. S. Thorne. Study of Monte Carlo approach to experimental uncertainty propagation with MSTW 2008 PDFs. *JHEP*, 08:052, 2012.

[77] Steven Weinberg. A model of leptons. *Phys. Rev. Lett.*, 19:1264–1266, Nov 1967.

[78] Henric Wilkens and the ATLAS Collaboration. The ATLAS Liquid Argon calorimeter: An overview. *J. Phys.: Conf. Ser.*, 160:012043, 2009.

[79] C. N. Yang and R. L. Mills. Conservation of isotopic spin and isotopic gauge invariance. *Phys. Rev.*, 96:191–195, Oct 1954.

[80] Martin zur Nedden. The Run-2 ATLAS Trigger System: Design, Performance and Plan. Technical Report ATL-DAQ-PROC-2016-039, CERN, Geneva, Dec 2016.

Appendix A

Signal Acceptance and Efficiency

Signal acceptance, efficiency, efficiency within acceptance, and signal leakage plots are all shown in this appendix.

A.1 Acceptance

Signal acceptance α is defined as the ratio of truth events that pass all signal region cuts over the total number of truth events in the TRUTH3 signal sample. Both the numerator and denominator events are weighted by the event weight and the numerator events are also weighted by the $Z \rightarrow ll$ branching ratio and filter efficiency, which is mostly driven by the $E_{\mathrm{T}}^{\mathrm{miss}} > 50$ GeV requirement. Signal acceptance is described in equation A.1.

- Slepton & Higgsino acceptances include branching fraction times filter efficiency

BF × ϵ_{filt} scale factor from SUSYTools.

- Slepton acceptances have stau veto applied to the denominator using a global 1.5 scale factor.
- Ran over p3135 TRUTH3 derivations of Higgsino and slepton samples.
- The z-axis scale is fixed between $[0, 25] \times 10^{-3}$ for sleptons and $[0, 11] \times 10^{-4}$ for Higgsino grids.

$$\alpha = \frac{N_{truth,selected} \times BR_{Z \to ll} \times \epsilon_{filter}}{N_{truth,total}} \tag{A.1}$$

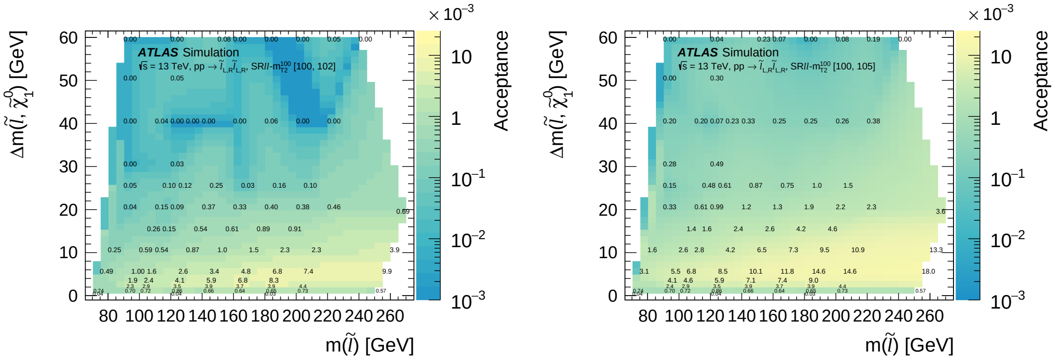

(a) $SR\ell\ell - m_{T2}^{100}[100, 102]$

(b) $SR\ell\ell - m_{T2}^{100}[100, 105]$

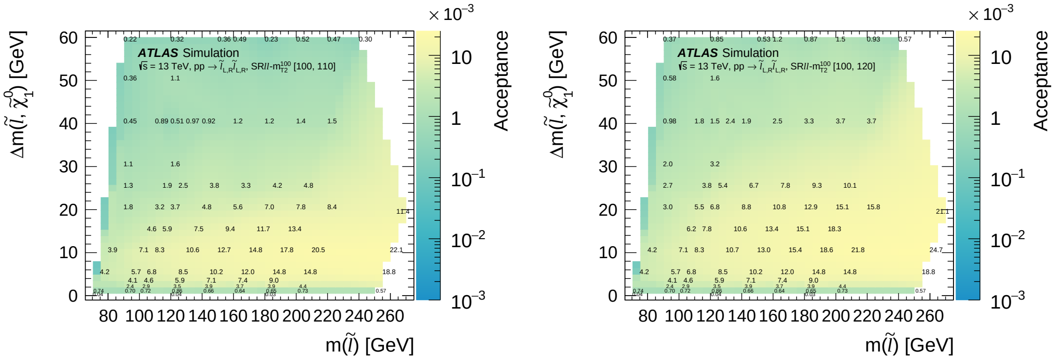

(c) $SR\ell\ell - m_{T2}^{100}[100, 110]$

(d) $SR\ell\ell - m_{T2}^{100}[100, 120]$

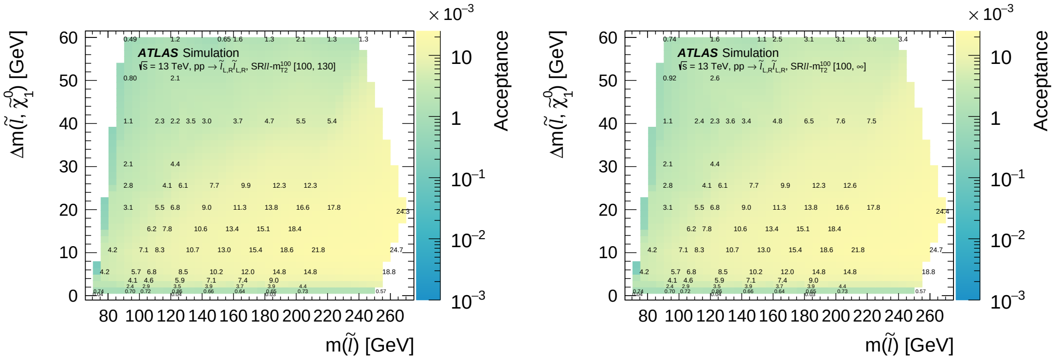

(e) $SR\ell\ell - m_{T2}^{100}[100, 130]$

(f) $SR\ell\ell - m_{T2}^{100}[100, \infty]$

Figure A.1: **Slepton**.

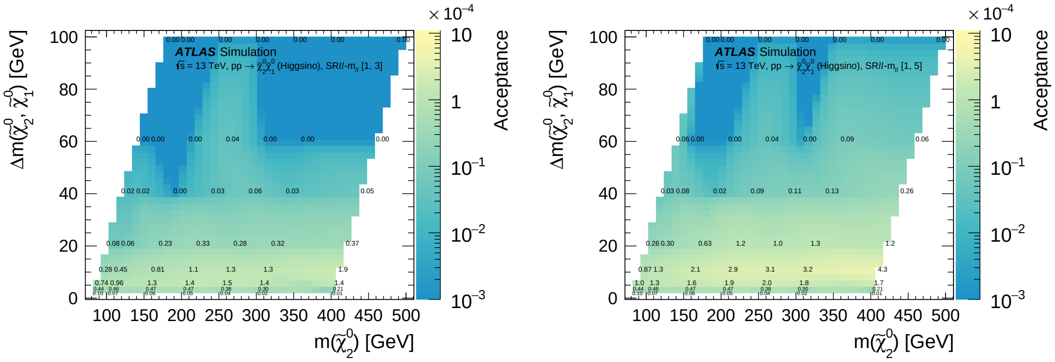

(a) $SR\ell\ell - m_{\ell\ell}[1,3]$

(b) $SR\ell\ell - m_{\ell\ell}[1,5]$

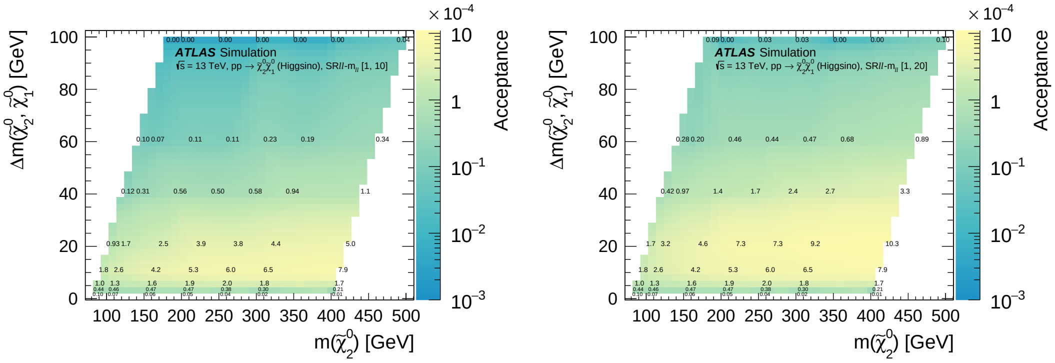

(c) $SR\ell\ell - m_{\ell\ell}[1,10]$

(d) $SR\ell\ell - m_{\ell\ell}[1,20]$

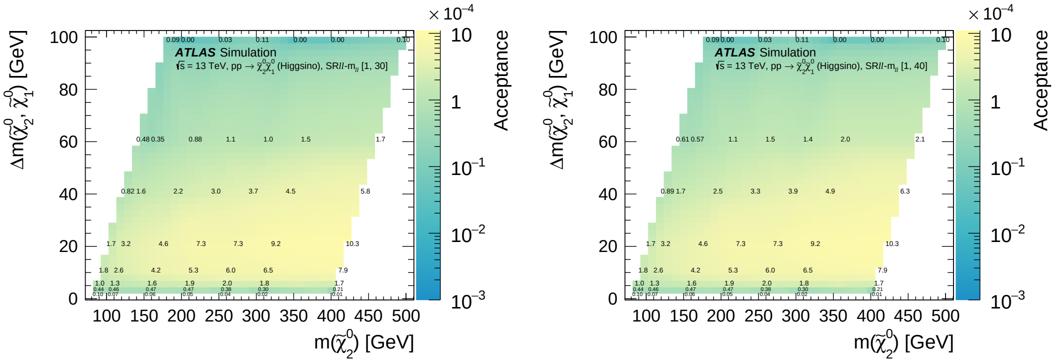

(e) $SR\ell\ell - m_{\ell\ell}[1,30]$

(f) $SR\ell\ell - m_{\ell\ell}[1,40]$

Figure A.2: **N2N1**.

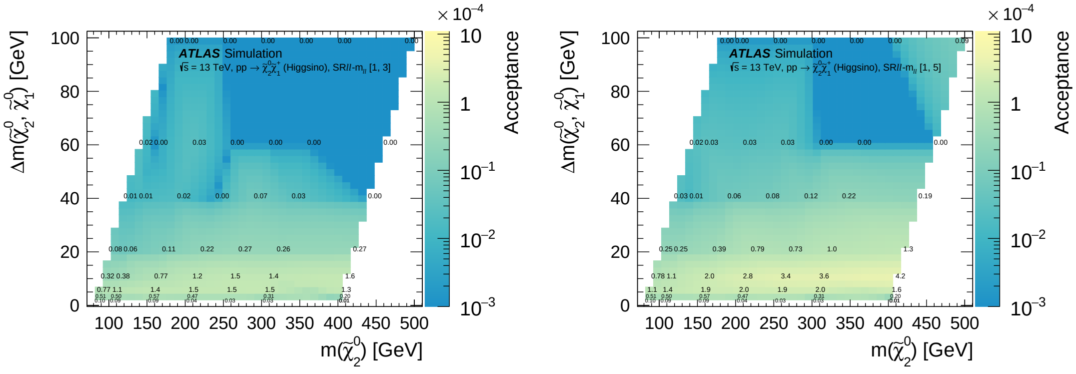

(a) $SR\ell\ell - m_{\ell\ell}[1,3]$ (b) $SR\ell\ell - m_{\ell\ell}[1,5]$

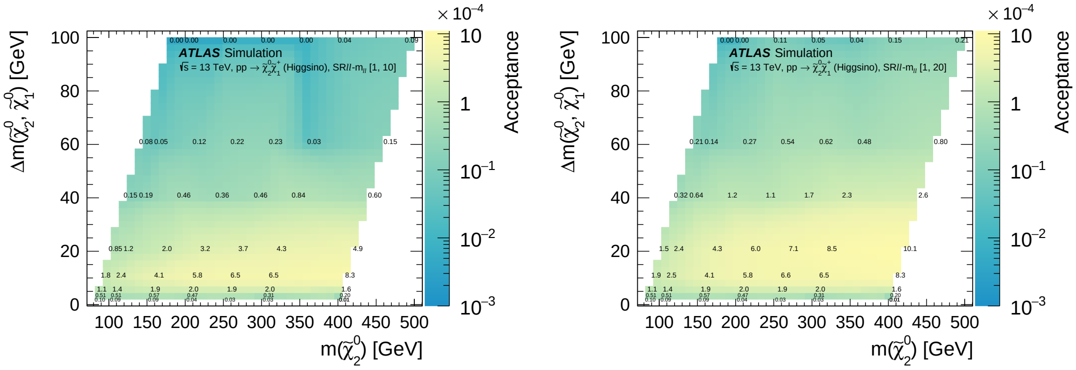

(c) $SR\ell\ell - m_{\ell\ell}[1,10]$ (d) $SR\ell\ell - m_{\ell\ell}[1,20]$

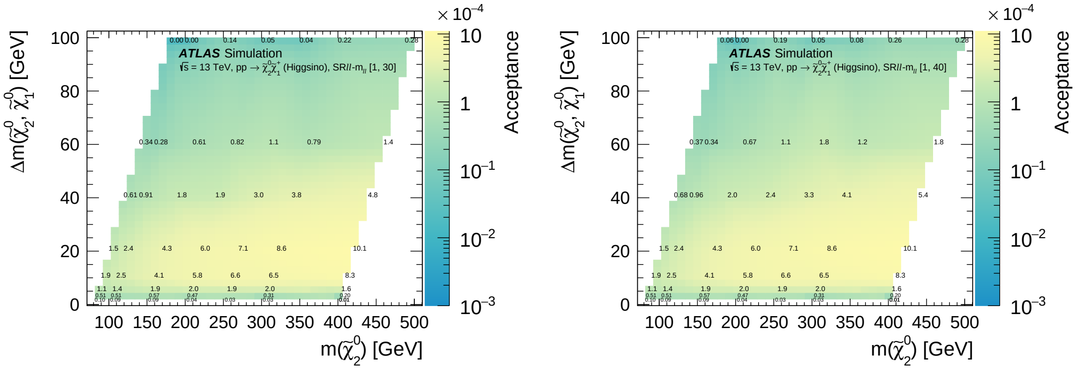

(e) $SR\ell\ell - m_{\ell\ell}[1,30]$ (f) $SR\ell\ell - m_{\ell\ell}[1,40]$

Figure A.3: **N2C1p**.

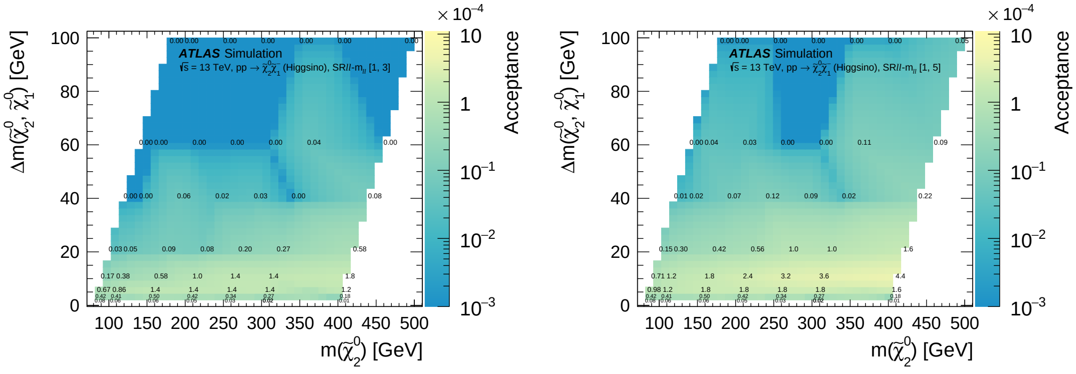

(a) $SR\ell\ell - m_{\ell\ell}[1,3]$ (b) $SR\ell\ell - m_{\ell\ell}[1,5]$

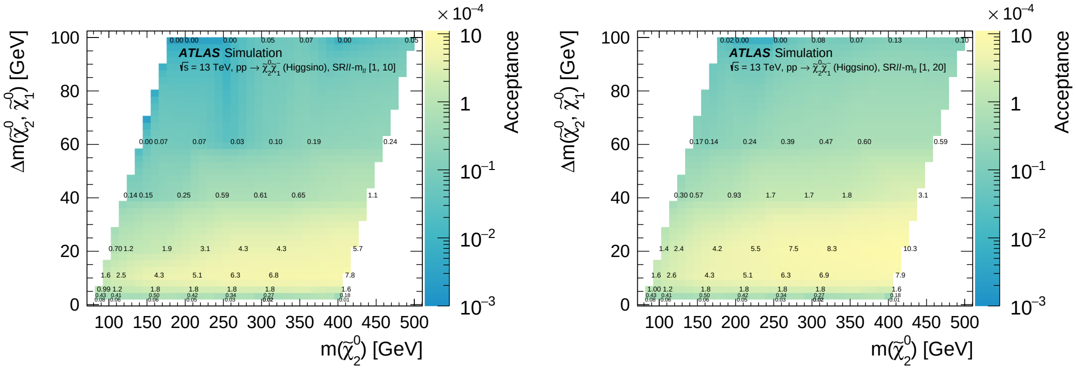

(c) $SR\ell\ell - m_{\ell\ell}[1,10]$ (d) $SR\ell\ell - m_{\ell\ell}[1,20]$

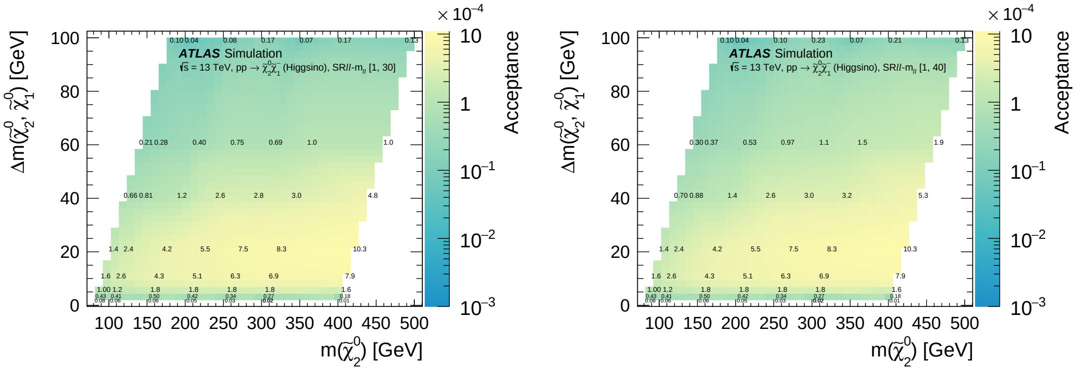

(e) $SR\ell\ell - m_{\ell\ell}[1,30]$ (f) $SR\ell\ell - m_{\ell\ell}[1,40]$

Figure A.4: **N2C1m**.

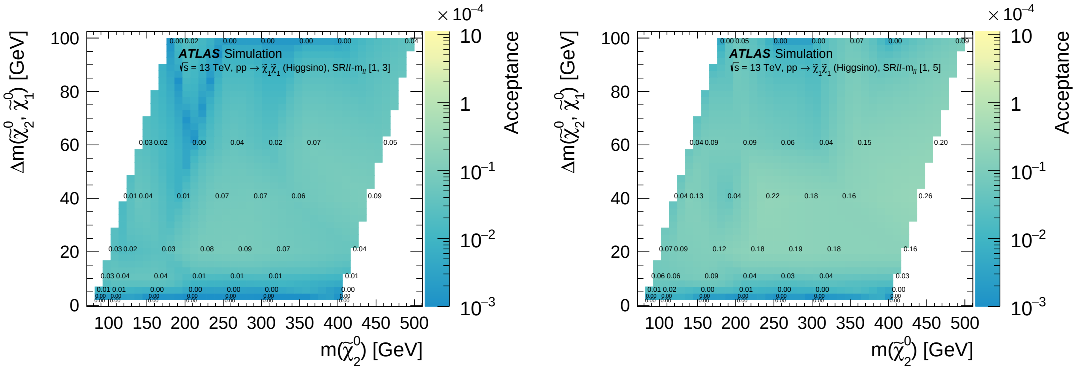

(a) $SR\ell\ell - m_{\ell\ell}[1,3]$

(b) $SR\ell\ell - m_{\ell\ell}[1,5]$

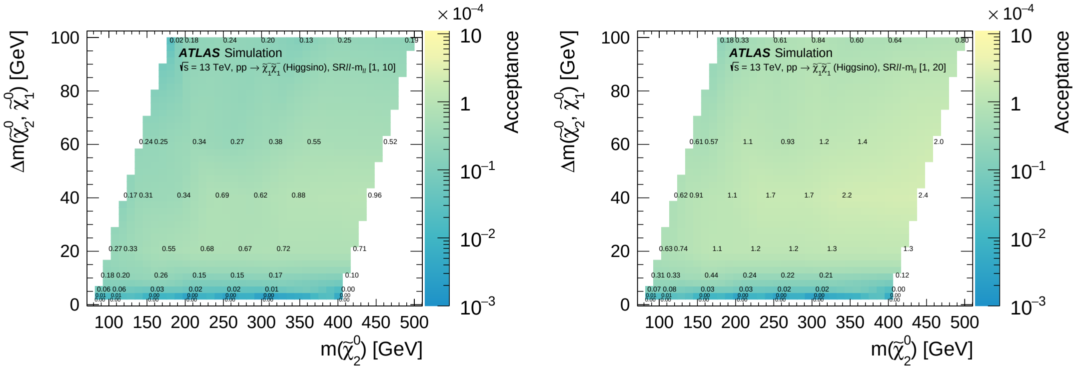

(c) $SR\ell\ell - m_{\ell\ell}[1,10]$

(d) $SR\ell\ell - m_{\ell\ell}[1,20]$

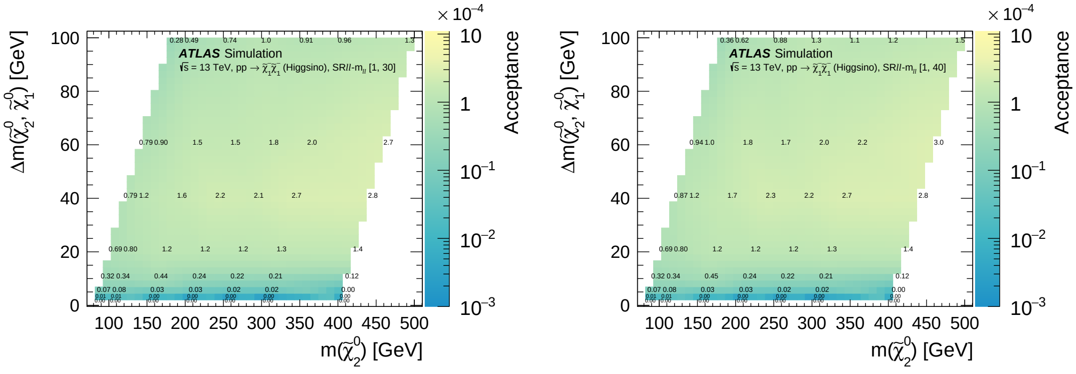

(e) $SR\ell\ell - m_{\ell\ell}[1,30]$

(f) $SR\ell\ell - m_{\ell\ell}[1,40]$

Figure A.5: **C1C1**.

A.1.1 Efficiency

- Slepton & Higgsino efficiencies are derived using reconstructed events passing signal region cuts as the numerator and truth events passing signal region cuts as denominator.
- Slepton efficiencies have stau veto applied to the denominator using a global 1.5 scale factor.
- Ran over p3135 TRUTH3 derivations of Higgsino and slepton samples for truth events passing signal region cuts.
- Ran over p2952 SUSY16 derivations of Higgsino and slepton samples for reconstructed events passing signal region cuts.

Signal efficiency, ϵ, is defined as the ratio of reconstructed events that pass all signal region cuts to the total number of truth events that pass all signal region cuts. Signal efficiency is described in equation A.2.

$$\epsilon = \frac{N_{reco,selected}}{N_{truth,selected}} \tag{A.2}$$

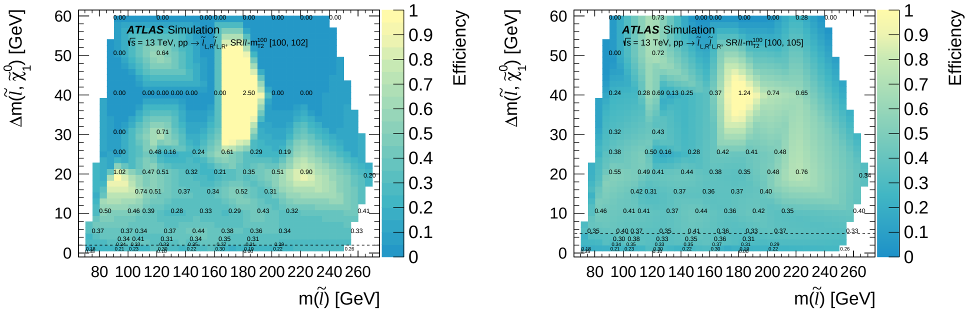

(a) $SR\ell\ell - m_{T2}^{100}[100, 102]$ (b) $SR\ell\ell - m_{T2}^{100}[100, 105]$

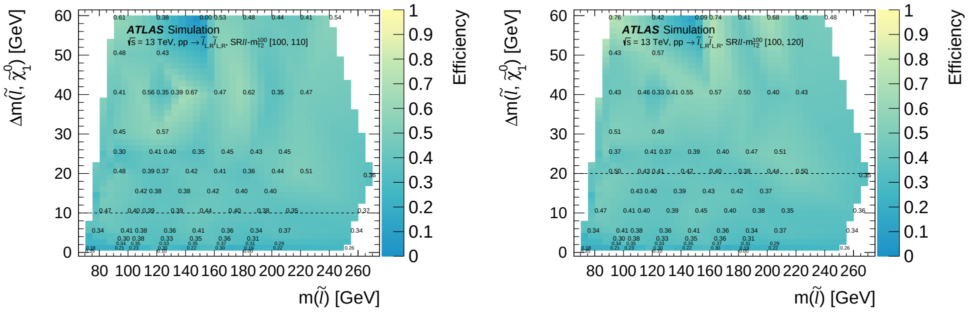

(c) $SR\ell\ell - m_{T2}^{100}[100, 110]$ (d) $SR\ell\ell - m_{T2}^{100}[100, 120]$

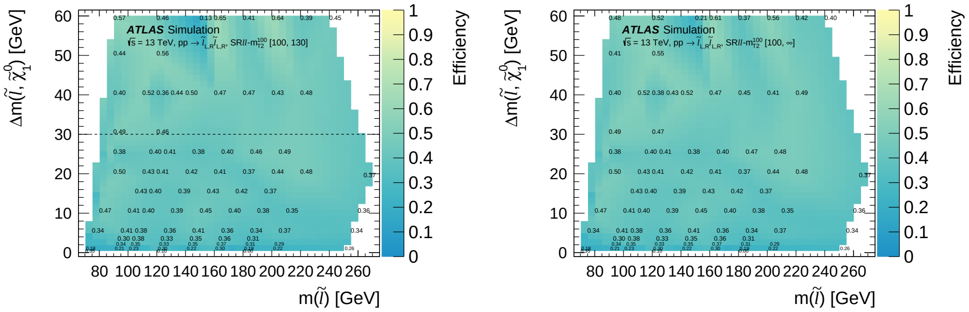

(e) $SR\ell\ell - m_{T2}^{100}[100, 130]$ (f) $SR\ell\ell - m_{T2}^{100}[100, \infty]$

Figure A.6: **Slepton Efficiency**.

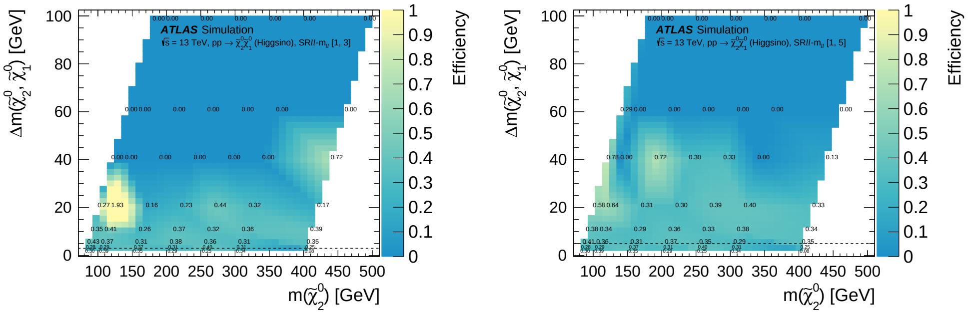

(a) $SR\ell\ell - m_{\ell\ell}[1,3]$

(b) $SR\ell\ell - m_{\ell\ell}[1,5]$

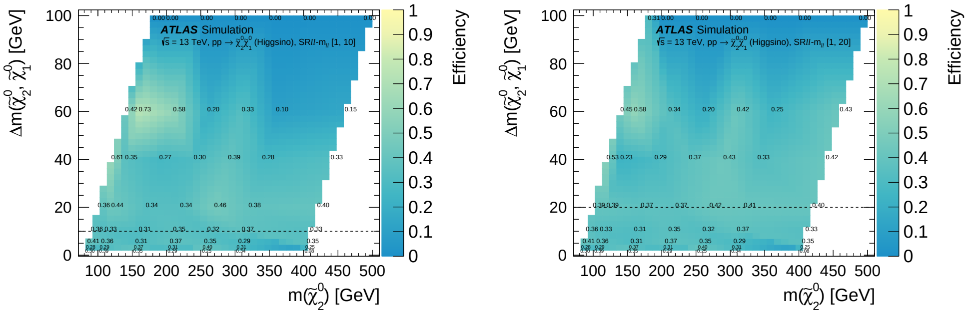

(c) $SR\ell\ell - m_{\ell\ell}[1,10]$

(d) $SR\ell\ell - m_{\ell\ell}[1,20]$

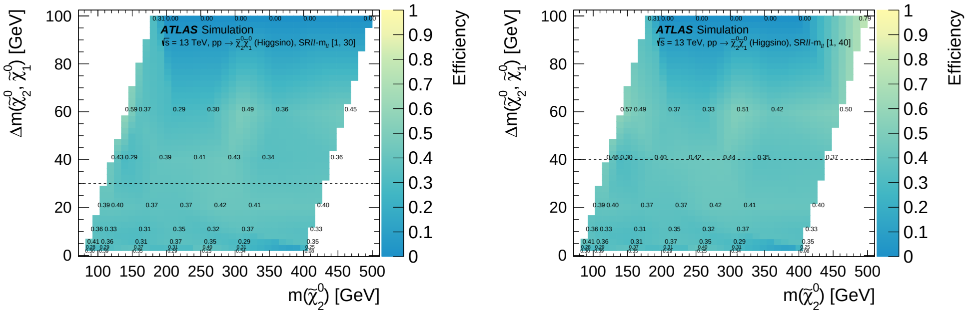

(e) $SR\ell\ell - m_{\ell\ell}[1,30]$

(f) $SR\ell\ell - m_{\ell\ell}[1,40]$

Figure A.7: **N2N1 Efficiency**.

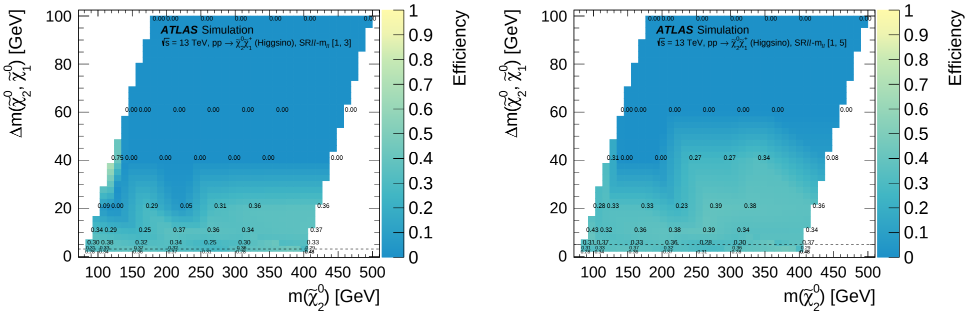

(a) $SR\ell\ell - m_{\ell\ell}[1,3]$ (b) $SR\ell\ell - m_{\ell\ell}[1,5]$

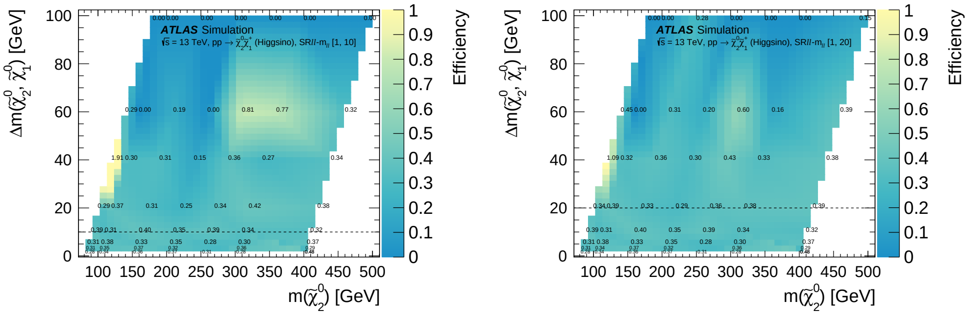

(c) $SR\ell\ell - m_{\ell\ell}[1,10]$ (d) $SR\ell\ell - m_{\ell\ell}[1,20]$

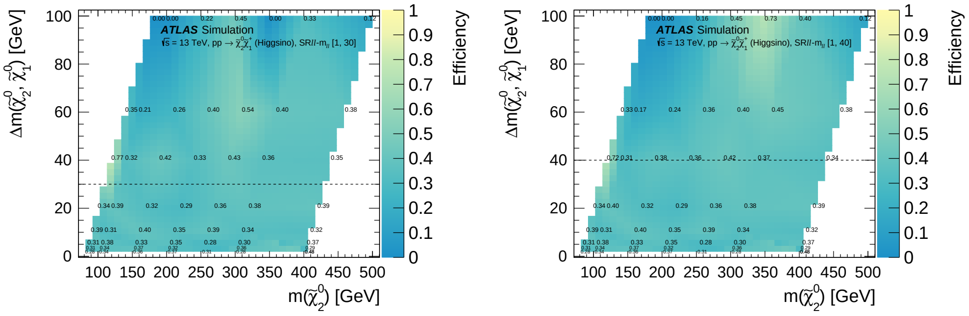

(e) $SR\ell\ell - m_{\ell\ell}[1,30]$ (f) $SR\ell\ell - m_{\ell\ell}[1,40]$

Figure A.8: **N2C1p Efficiency**.

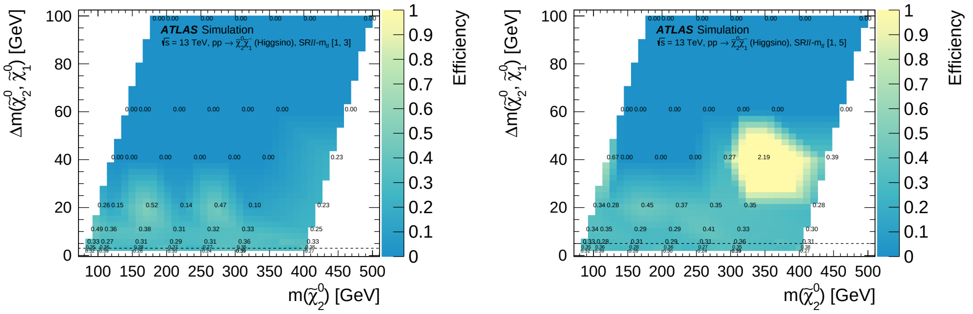

(a) $SR\ell\ell - m_{\ell\ell}[1,3]$ (b) $SR\ell\ell - m_{\ell\ell}[1,5]$

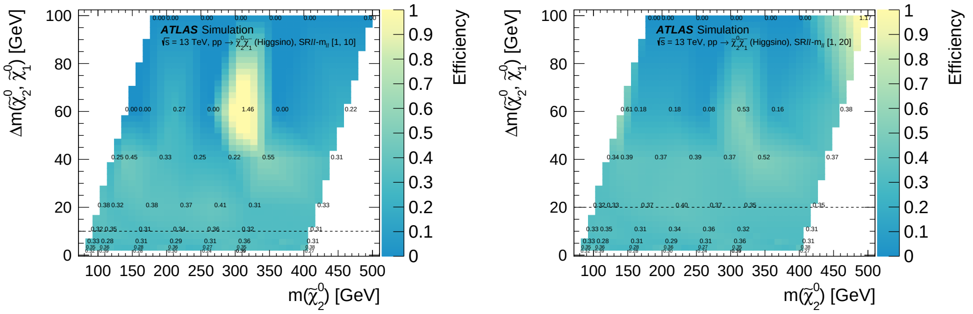

(c) $SR\ell\ell - m_{\ell\ell}[1,10]$ (d) $SR\ell\ell - m_{\ell\ell}[1,20]$

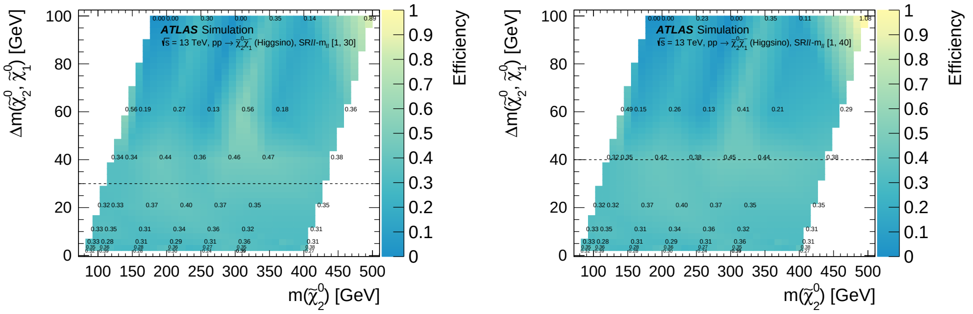

(e) $SR\ell\ell - m_{\ell\ell}[1,30]$ (f) $SR\ell\ell - m_{\ell\ell}[1,40]$

Figure A.9: **N2C1m Efficiency**.

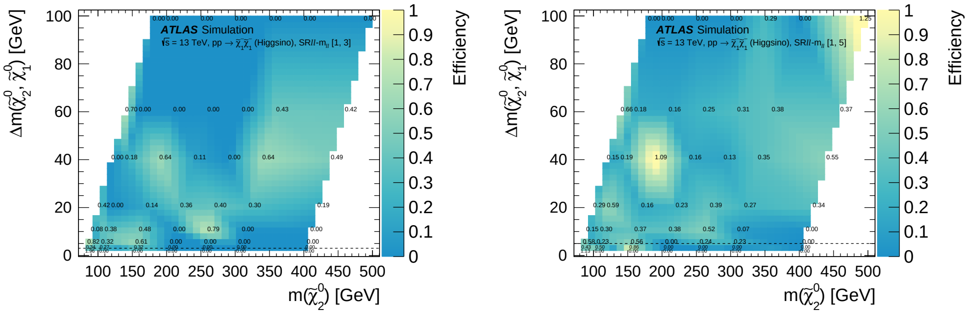

(a) $SR\ell\ell - m_{\ell\ell}[1,3]$

(b) $SR\ell\ell - m_{\ell\ell}[1,5]$

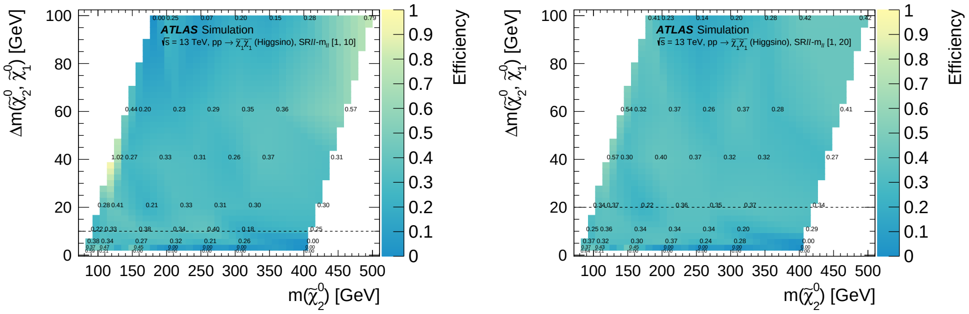

(c) $SR\ell\ell - m_{\ell\ell}[1,10]$

(d) $SR\ell\ell - m_{\ell\ell}[1,20]$

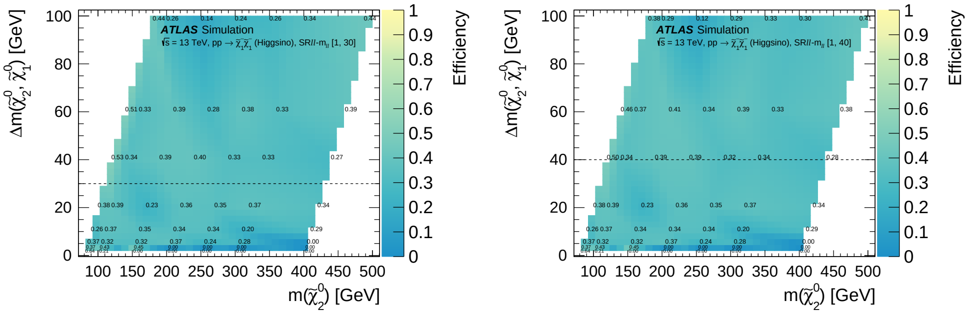

(e) $SR\ell\ell - m_{\ell\ell}[1,30]$

(f) $SR\ell\ell - m_{\ell\ell}[1,40]$

Figure A.10: **C1C1 Efficiency**.

A.1.2 Efficiency within Acceptance

Figures A.21 to A.25 shows the efficiencies for the Higgsino signals split by process and slepton signal.

- Slepton & Higgsino efficiencies within acceptance are derived using truth events passing signal region cuts as the denominator and reconstructed events passing signal region cuts that are matched to denominator events for the numerator.
- Slepton efficiencies have stau veto applied to the denominator using a global 1.5 scale factor.
- Ran over p3135 TRUTH3 derivations of Higgsino and slepton samples for truth events passing signal region cuts.
- Ran over p2952 SUSY16 derivations of Higgsino and slepton samples for reconstructed events passing signal region cuts.

Efficiency within acceptance, denoted ϵ_α, is defined as the ratio of reconstructed events that pass all signal region cuts to the total number of truth events that pass all signal region cuts, but in this case, each reconstructed event in the numerator must match a truth event in the denominator. Efficiency within acceptance is described in equation A.3.

$$\epsilon_\alpha = \frac{N_{reco,selected,matched}}{N_{truth,selected}} \tag{A.3}$$

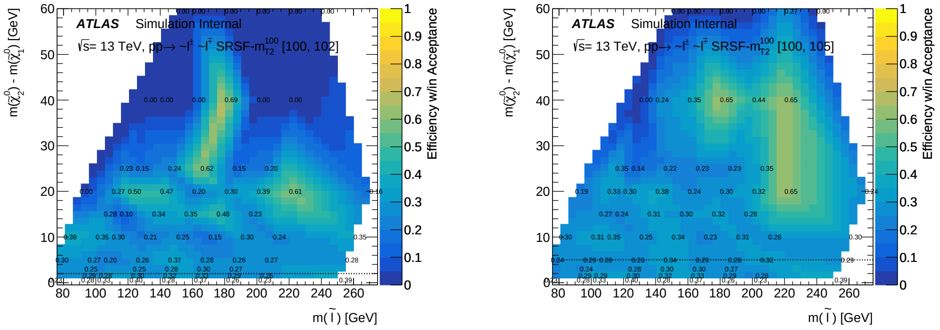

(a) $SR\ell\ell - m_{T2}^{100}[100, 102]$ (b) $SR\ell\ell - m_{T2}^{100}[100, 105]$

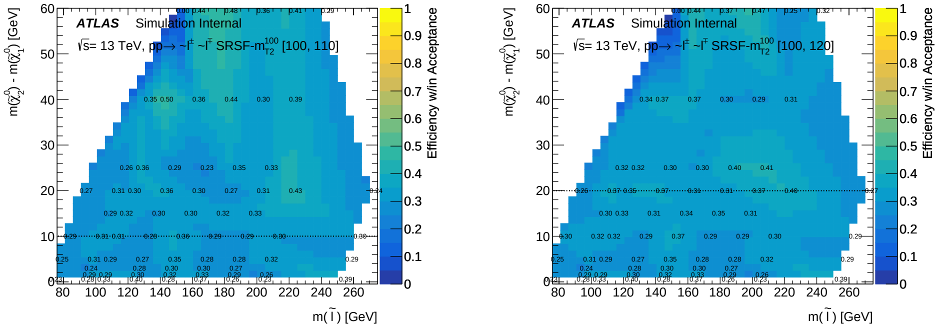

(c) $SR\ell\ell - m_{T2}^{100}[100, 110]$ (d) $SR\ell\ell - m_{T2}^{100}[100, 120]$

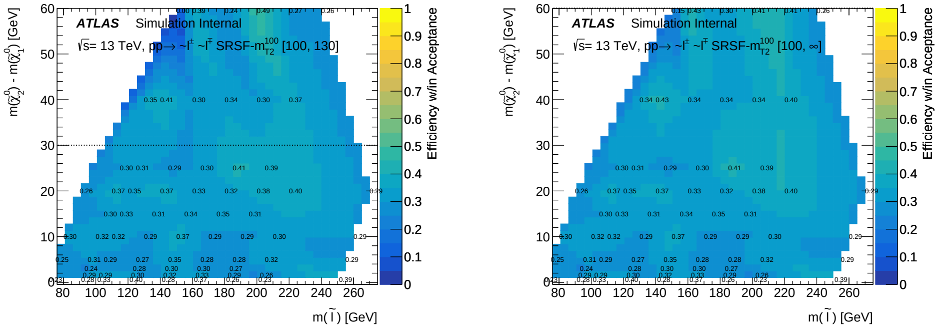

(e) $SR\ell\ell - m_{T2}^{100}[100, 130]$ (f) $SR\ell\ell - m_{T2}^{100}[100, \infty]$

Figure A.11: **Slepton Efficiency within acceptance**.

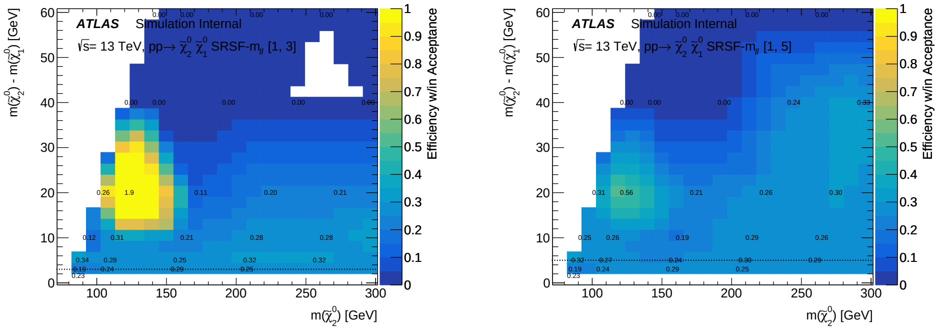

(a) $SR\ell\ell - m_{\ell\ell}[1,3]$ (b) $SR\ell\ell - m_{\ell\ell}[1,5]$

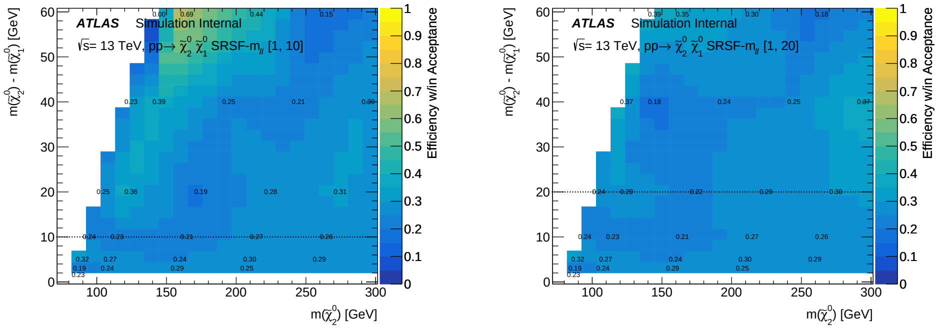

(c) $SR\ell\ell - m_{\ell\ell}[1,10]$ (d) $SR\ell\ell - m_{\ell\ell}[1,20]$

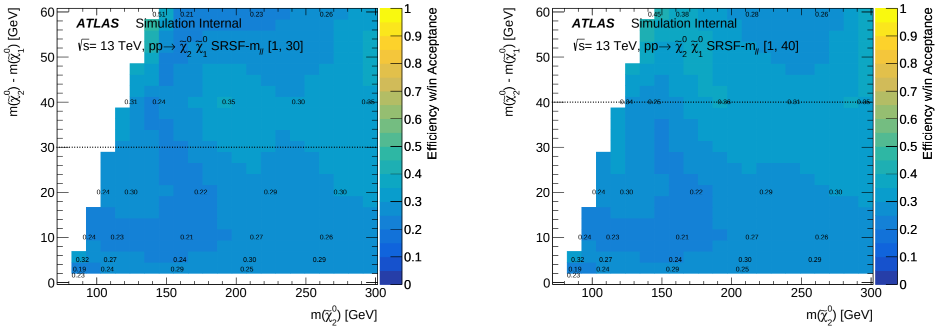

(e) $SR\ell\ell - m_{\ell\ell}[1,30]$ (f) $SR\ell\ell - m_{\ell\ell}[1,40]$

Figure A.12: **N2N1 Efficiency within acceptance**.

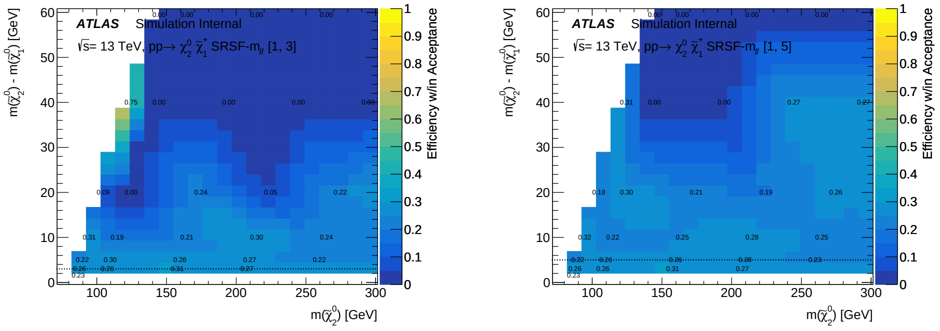

(a) $SR\ell\ell - m_{\ell\ell}[1, 3]$ (b) $SR\ell\ell - m_{\ell\ell}[1, 5]$

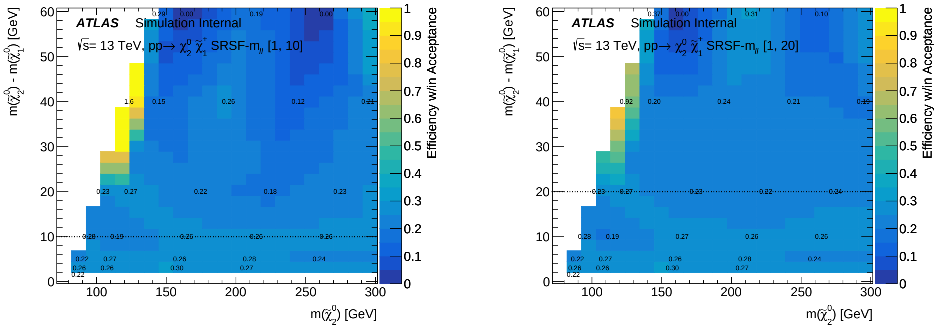

(c) $SR\ell\ell - m_{\ell\ell}[1, 10]$ (d) $SR\ell\ell - m_{\ell\ell}[1, 20]$

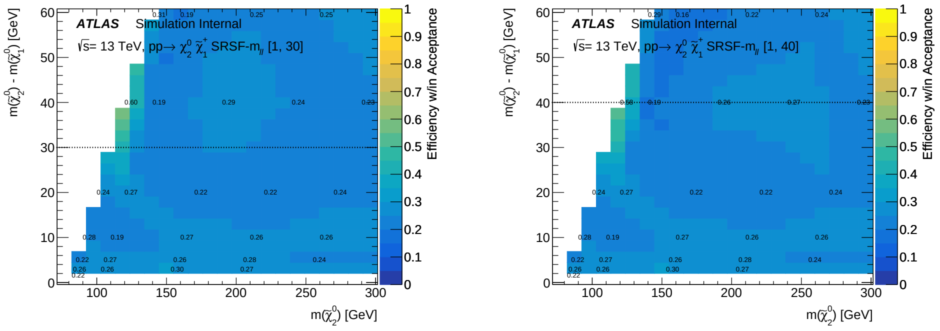

(e) $SR\ell\ell - m_{\ell\ell}[1, 30]$ (f) $SR\ell\ell - m_{\ell\ell}[1, 40]$

Figure A.13: **N2C1p Efficiency within acceptance**.

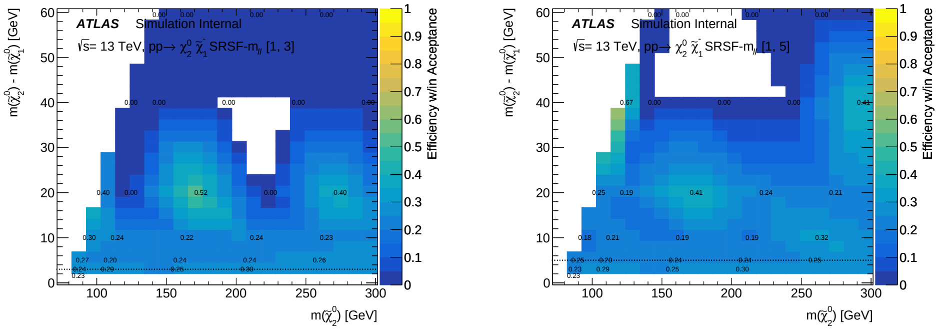

(a) $SR\ell\ell - m_{\ell\ell}[1,3]$

(b) $SR\ell\ell - m_{\ell\ell}[1,5]$

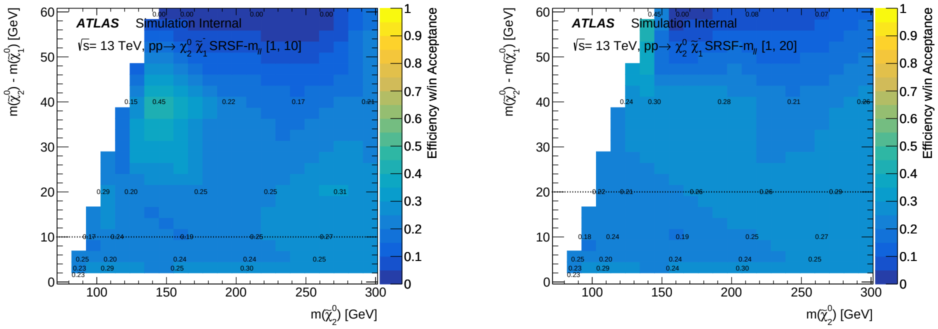

(c) $SR\ell\ell - m_{\ell\ell}[1,10]$

(d) $SR\ell\ell - m_{\ell\ell}[1,20]$

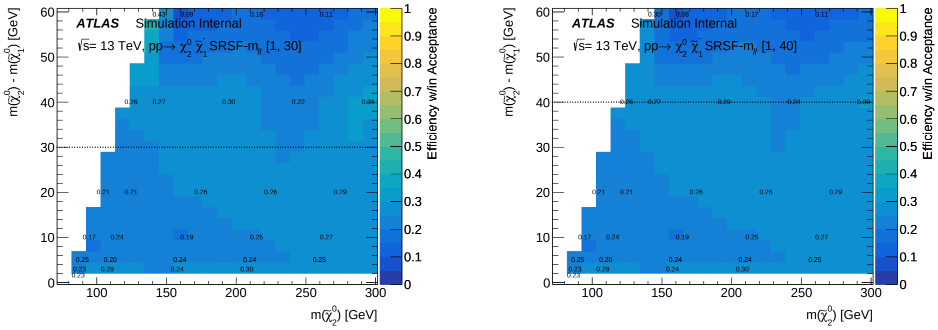

(e) $SR\ell\ell - m_{\ell\ell}[1,30]$

(f) $SR\ell\ell - m_{\ell\ell}[1,40]$

Figure A.14: **N2C1m Efficiency within acceptance**.

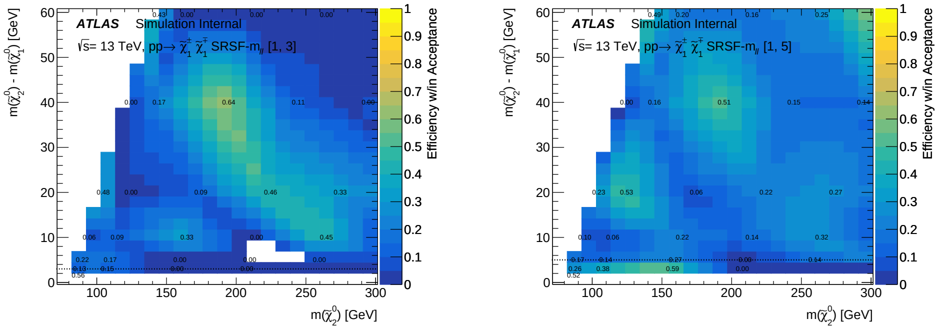

(a) $SR\ell\ell - m_{\ell\ell}[1,3]$

(b) $SR\ell\ell - m_{\ell\ell}[1,5]$

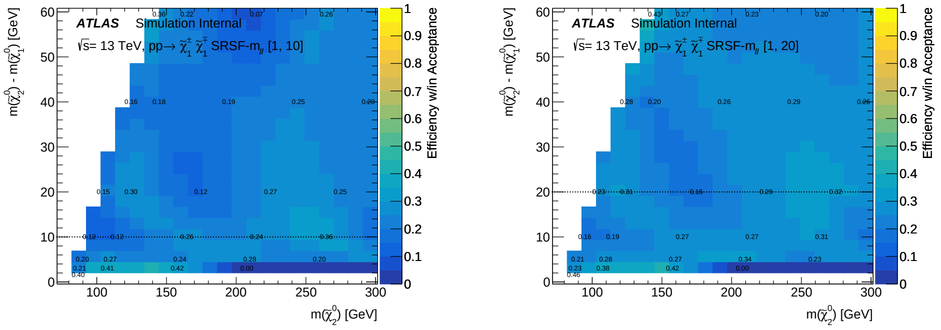

(c) $SR\ell\ell - m_{\ell\ell}[1,10]$

(d) $SR\ell\ell - m_{\ell\ell}[1,20]$

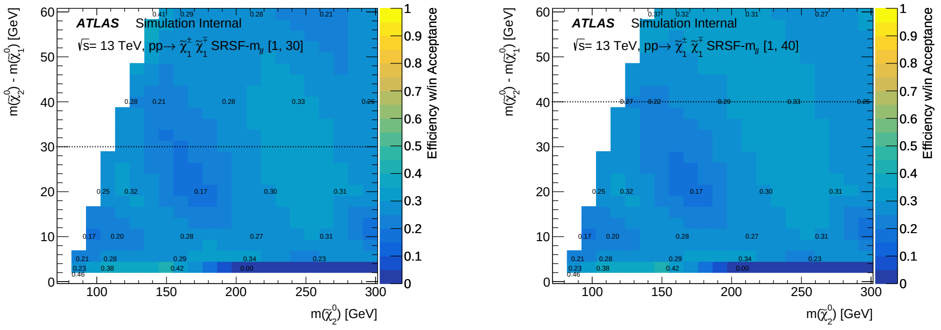

(e) $SR\ell\ell - m_{\ell\ell}[1,30]$

(f) $SR\ell\ell - m_{\ell\ell}[1,40]$

Figure A.15: **C1C1 Efficiency with acceptance**.

A.1.3 Signal Leakage

Figures A.16 to A.20 shows the leakage for the Higgsino signals split by process and slepton signal.

- Slepton & Higgsino signal leakages are derived using truth events passing signal region cuts as the denominator and reconstructed events passing signal region cuts that do not match denominator events as the numerator.
- Slepton efficiencies have stau veto applied to the denominator using a global 1.5 scale factor.
- Ran over p3135 TRUTH3 derivations of Higgsino and slepton samples for truth events passing signal region cuts.
- Ran over p2952 SUSY16 derivations of Higgsino and slepton samples for reconstructed events passing signal region cuts.

Signal leakage, λ, is defined as the ratio of reconstructed events in the signal region that are not matched to a truth event in the signal region divided by the total number of truth events in the signal region. Signal leakage is described in equation A.4. Studies of the migrating truth quantities during recontruction reveal the $E_{\mathrm{T}}^{\mathrm{miss}}$ and $M_{\tau}\tau$ and the two variables responsible for the majority of the leakage events.

$$\lambda = \frac{N_{reco,selected,unmatched}}{N_{truth,selected}} \tag{A.4}$$

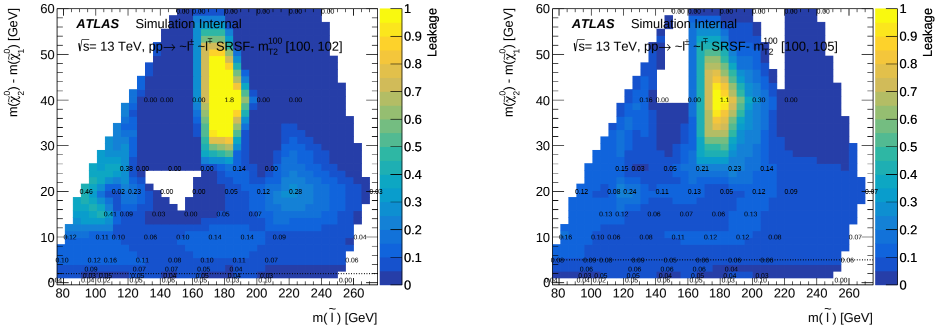

(a) $SR\ell\ell - m_{T2}^{100}[100, 102]$

(b) $SR\ell\ell - m_{T2}^{100}[100, 105]$

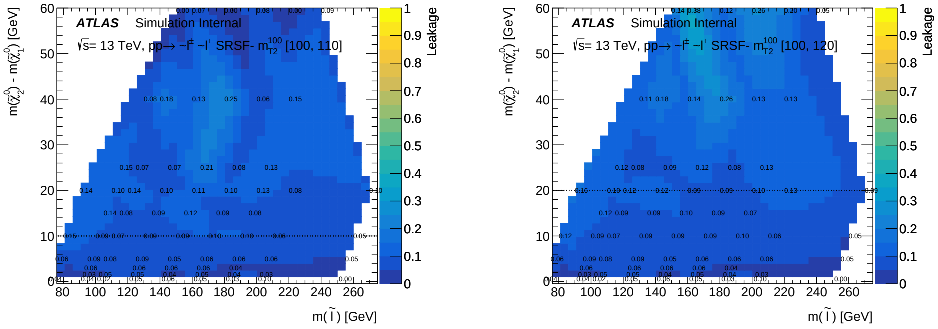

(c) $SR\ell\ell - m_{T2}^{100}[100, 110]$

(d) $SR\ell\ell - m_{T2}^{100}[100, 120]$

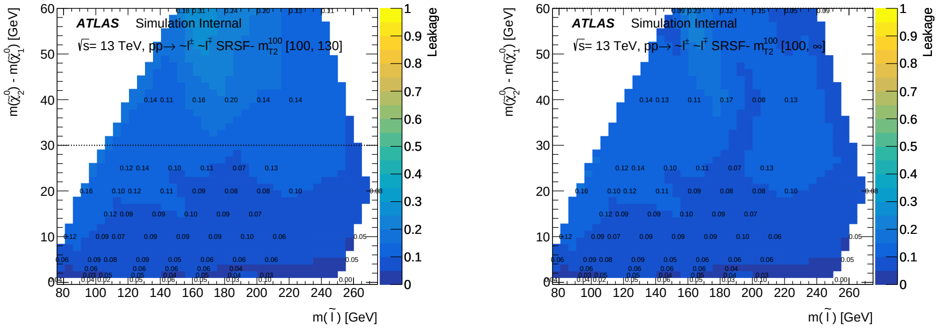

(e) $SR\ell\ell - m_{T2}^{100}[100, 130]$

(f) $SR\ell\ell - m_{T2}^{100}[100, \infty]$

Figure A.16: **Slepton Signal Leakage**.

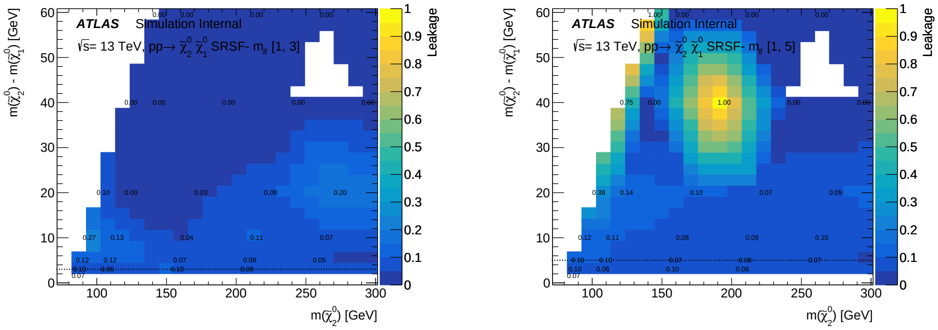

(a) $SR\ell\ell - m_{\ell\ell}[1,3]$ (b) $SR\ell\ell - m_{\ell\ell}[1,5]$

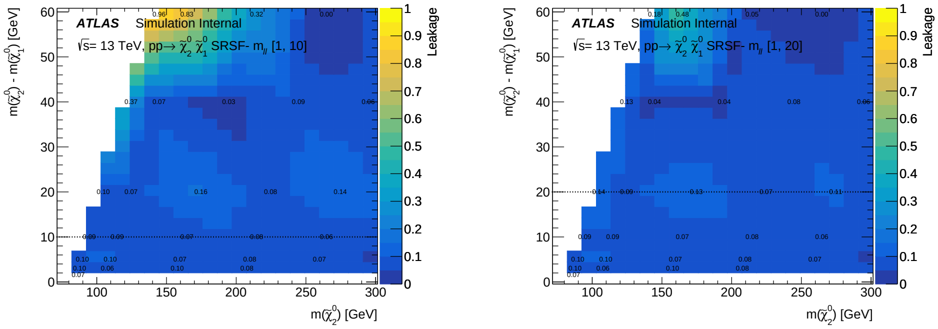

(c) $SR\ell\ell - m_{\ell\ell}[1,10]$ (d) $SR\ell\ell - m_{\ell\ell}[1,20]$

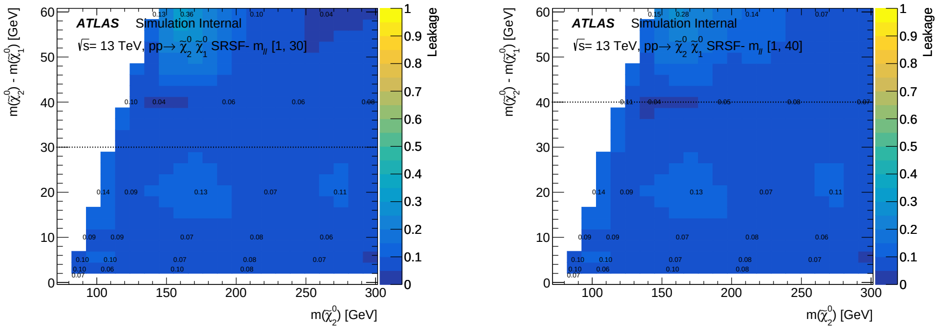

(e) $SR\ell\ell - m_{\ell\ell}[1,30]$ (f) $SR\ell\ell - m_{\ell\ell}[1,40]$

Figure A.17: **N2N1 Signal Leakage**.

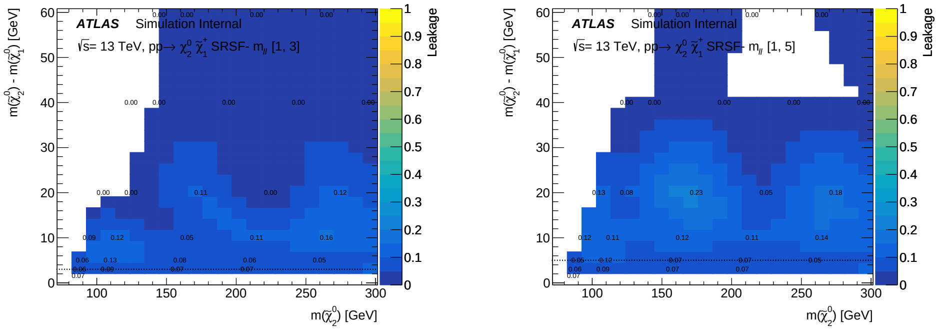

(a) $SR\ell\ell - m_{\ell\ell}[1,3]$ (b) $SR\ell\ell - m_{\ell\ell}[1,5]$

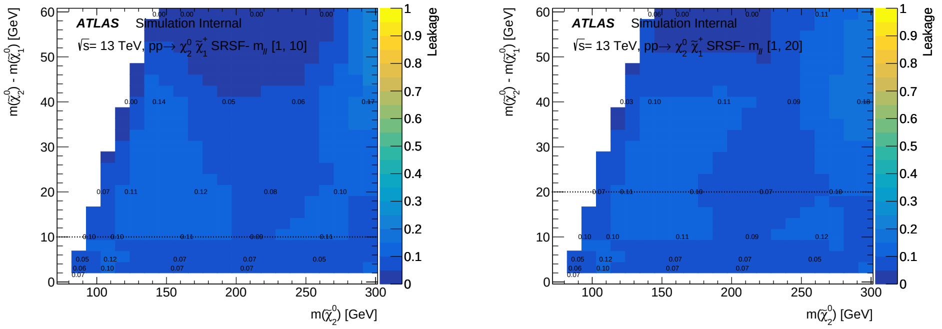

(c) $SR\ell\ell - m_{\ell\ell}[1,10]$ (d) $SR\ell\ell - m_{\ell\ell}[1,20]$

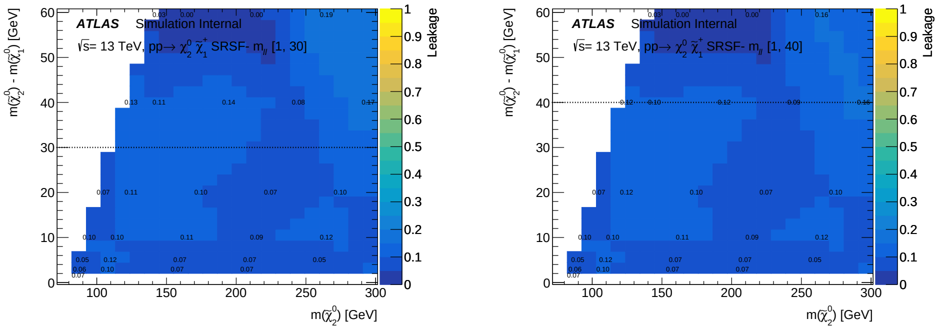

(e) $SR\ell\ell - m_{\ell\ell}[1,30]$ (f) $SR\ell\ell - m_{\ell\ell}[1,40]$

Figure A.18: **N2C1p Signal Leakage**.

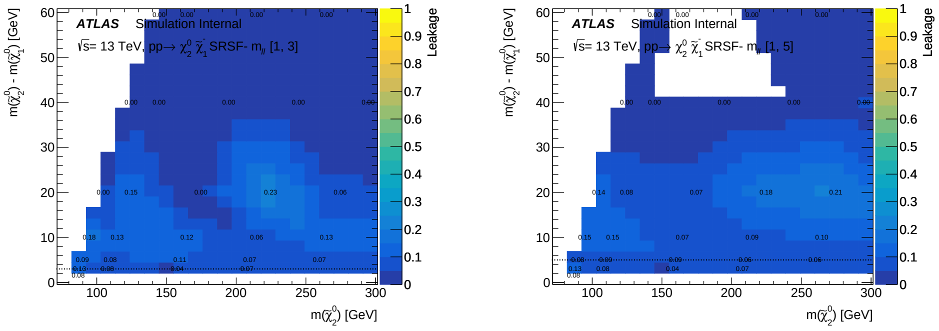

(a) $SR\ell\ell - m_{\ell\ell}[1,3]$ (b) $SR\ell\ell - m_{\ell\ell}[1,5]$

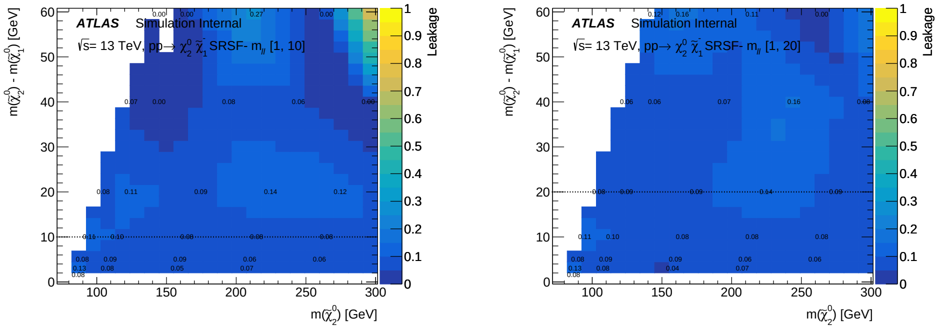

(c) $SR\ell\ell - m_{\ell\ell}[1,10]$ (d) $SR\ell\ell - m_{\ell\ell}[1,20]$

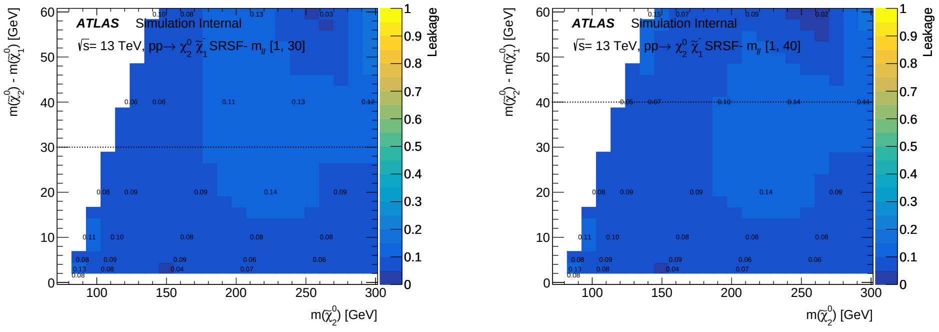

(e) $SR\ell\ell - m_{\ell\ell}[1,30]$ (f) $SR\ell\ell - m_{\ell\ell}[1,40]$

Figure A.19: **N2C1m Signal Leakage**.

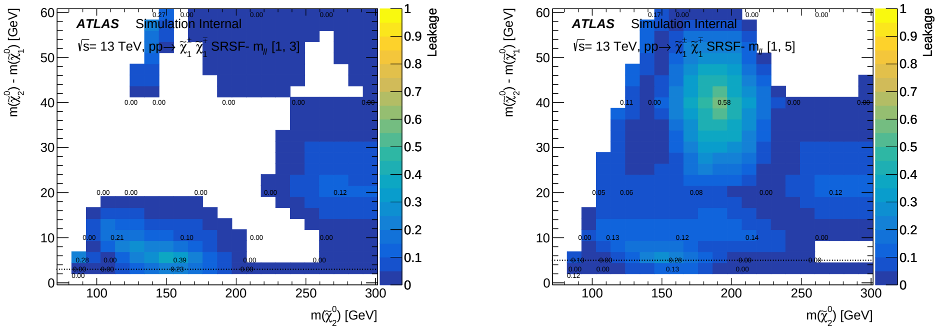

(a) $SR\ell\ell - m_{\ell\ell}[1,3]$ (b) $SR\ell\ell - m_{\ell\ell}[1,5]$

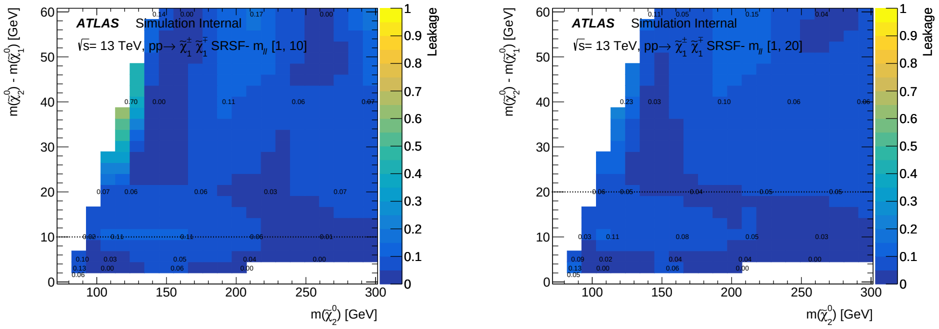

(c) $SR\ell\ell - m_{\ell\ell}[1,10]$ (d) $SR\ell\ell - m_{\ell\ell}[1,20]$

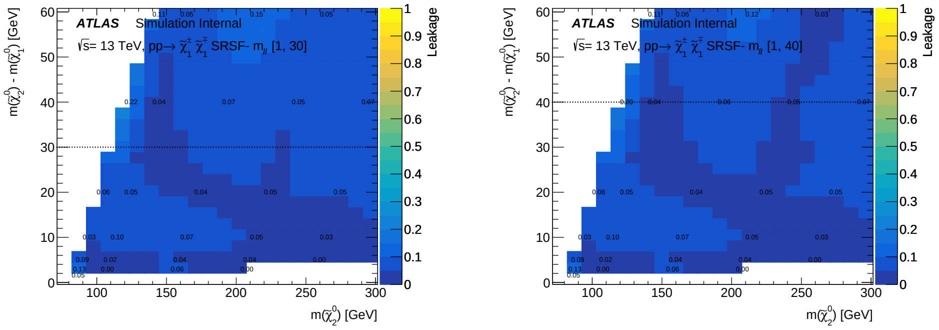

(e) $SR\ell\ell - m_{\ell\ell}[1,30]$ (f) $SR\ell\ell - m_{\ell\ell}[1,40]$

Figure A.20: **C1C1 Signal Leakage**.

A.1.4 Acceptance*Efficiency

Figures A.25 shows the acceptance*efficiencies for the Higgsino signals split by process and slepton signal.

- Slepton & Higgsino acceptance times efficiencies are derived using truth events passing signal region cuts as the denominator and reconstructed events passing signal region cuts that are matched to denominator events for the numerator.
- Slepton efficiencies have stau veto applied to the denominator using a global 1.5 scale factor.
- Ran over p3135 TRUTH3 derivations of Higgsino and slepton samples for truth events passing signal region cuts.
- Ran over p2952 SUSY16 derivations of Higgsino and slepton samples for reconstructed events passing signal region cuts.

Acceptance times efficiency is defined as the ratio of reconstructed events that pass all signal region cuts over the total number of truth events in the TRUTH3 signal sample, but in this case, the denominator events are weighted by the event weight and the numerator events are weighted by the event weight, the detector weights, the filter efficiency, and the $Z \to ll$ branching ratio. Acceptance multiplied by efficiency is described in equation A.5.

$$\alpha \times \epsilon = \frac{\Sigma w_{reco,sel} \times BR_{Z \to ll} \times \epsilon_{filter}}{\Sigma evt\_w_{truth,tot}} \tag{A.5}$$

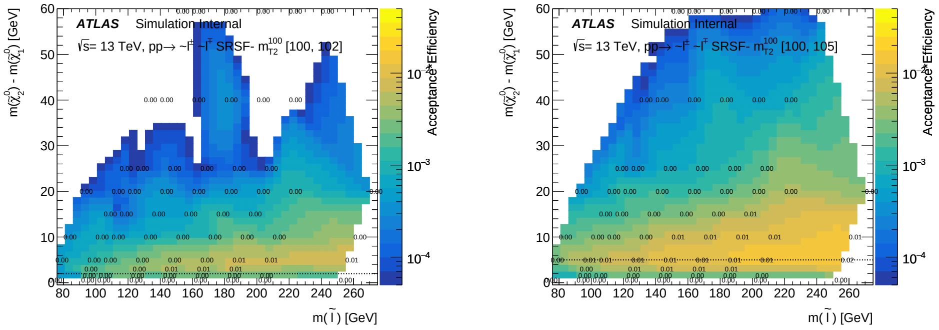

(a) $SR\ell\ell - m_{T2}^{100}[100, 102]$ (b) $SR\ell\ell - m_{T2}^{100}[100, 105]$

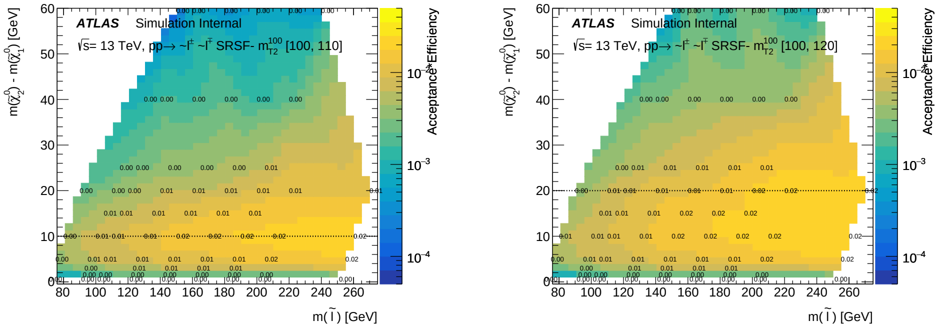

(c) $SR\ell\ell - m_{T2}^{100}[100, 110]$ (d) $SR\ell\ell - m_{T2}^{100}[100, 120]$

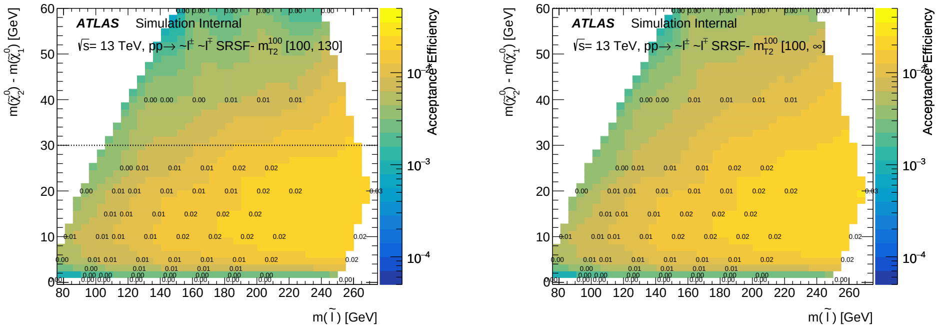

(e) $SR\ell\ell - m_{T2}^{100}[100, 130]$ (f) $SR\ell\ell - m_{T2}^{100}[100, \infty]$

Figure A.21: **Slepton Acceptance*Efficiency**.

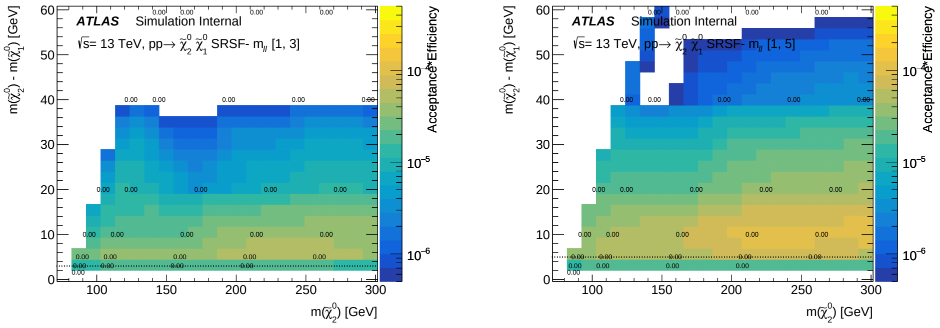

(a) $SR\ell\ell - m_{\ell\ell}[1, 3]$ (b) $SR\ell\ell - m_{\ell\ell}[1, 5]$

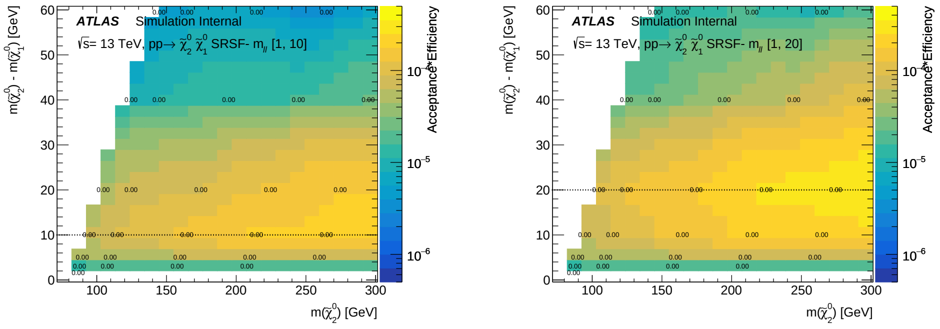

(c) $SR\ell\ell - m_{\ell\ell}[1, 10]$ (d) $SR\ell\ell - m_{\ell\ell}[1, 20]$

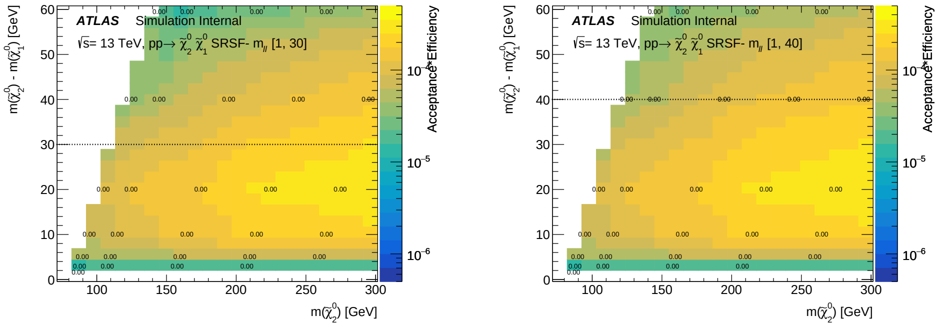

(e) $SR\ell\ell - m_{\ell\ell}[1, 30]$ (f) $SR\ell\ell - m_{\ell\ell}[1, 40]$

Figure A.22: **N2N1 Acceptance*Efficiency**.

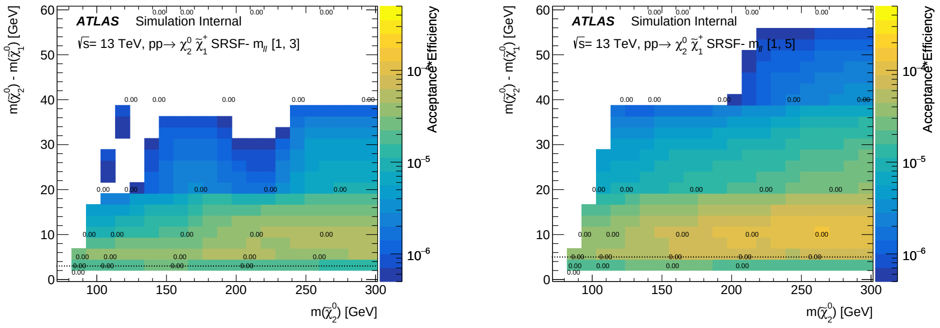

(a) $SR\ell\ell - m_{\ell\ell}[1,3]$ (b) $SR\ell\ell - m_{\ell\ell}[1,5]$

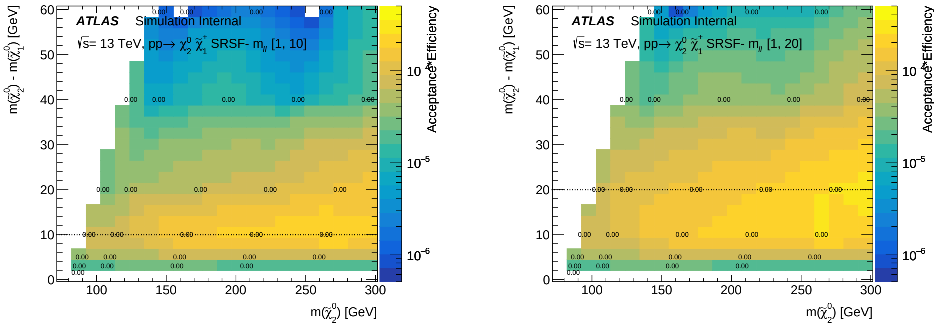

(c) $SR\ell\ell - m_{\ell\ell}[1,10]$ (d) $SR\ell\ell - m_{\ell\ell}[1,20]$

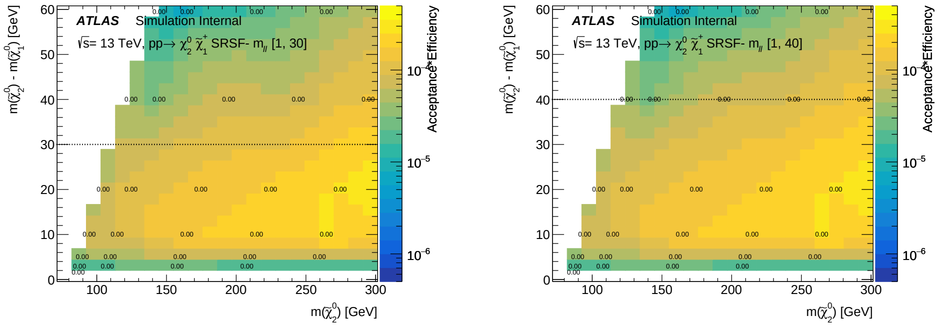

(e) $SR\ell\ell - m_{\ell\ell}[1,30]$ (f) $SR\ell\ell - m_{\ell\ell}[1,40]$

Figure A.23: **N2C1p Acceptance*Efficiency**.

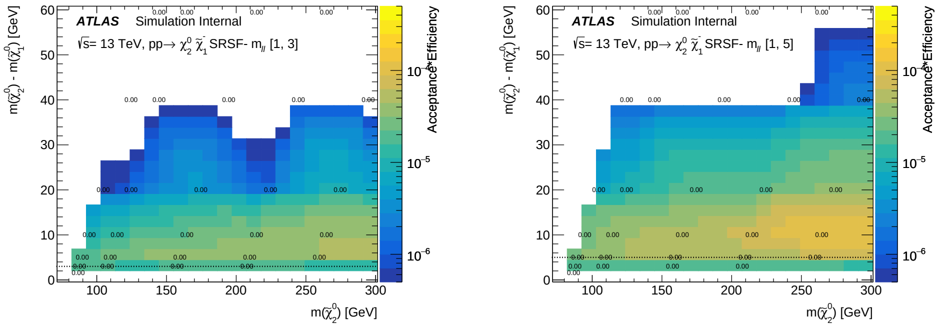

(a) $SR\ell\ell - m_{\ell\ell}[1,3]$ (b) $SR\ell\ell - m_{\ell\ell}[1,5]$

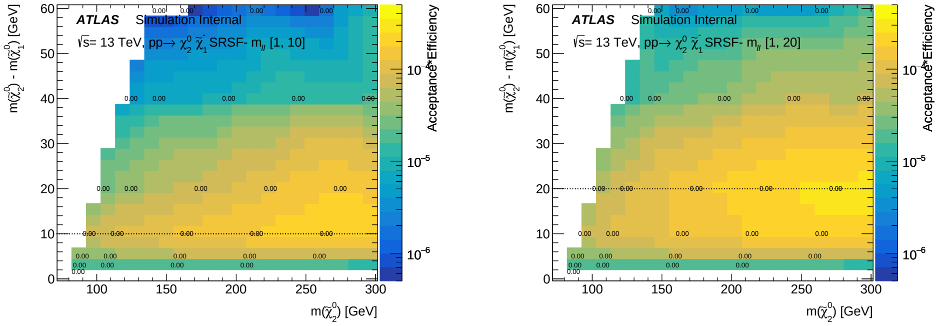

(c) $SR\ell\ell - m_{\ell\ell}[1,10]$ (d) $SR\ell\ell - m_{\ell\ell}[1,20]$

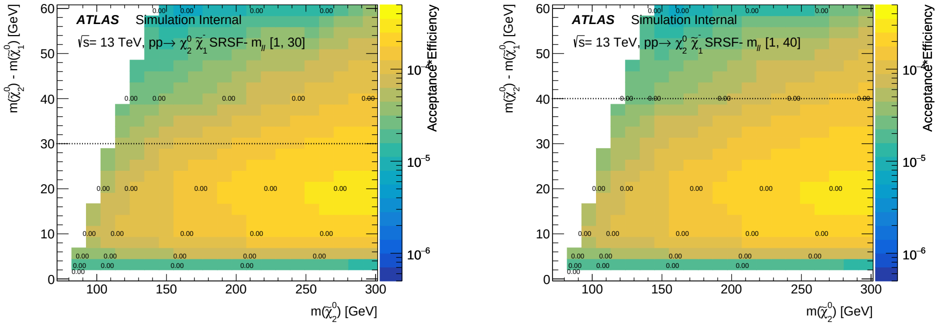

(e) $SR\ell\ell - m_{\ell\ell}[1,30]$ (f) $SR\ell\ell - m_{\ell\ell}[1,40]$

Figure A.24: **N2C1m Acceptance*Efficiency**.

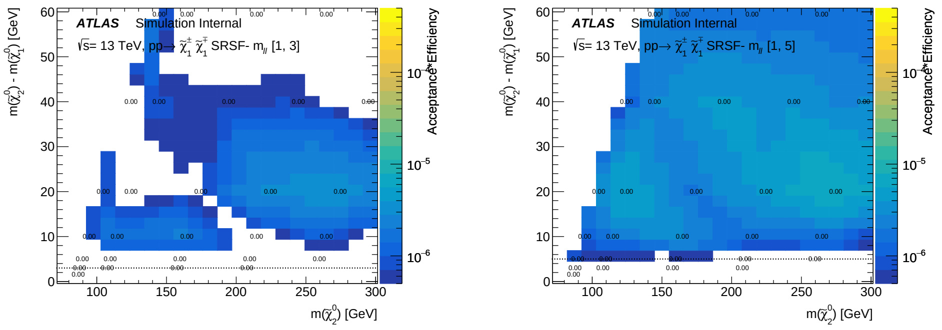

(a) $SR\ell\ell - m_{\ell\ell}[1,3]$ (b) $SR\ell\ell - m_{\ell\ell}[1,5]$

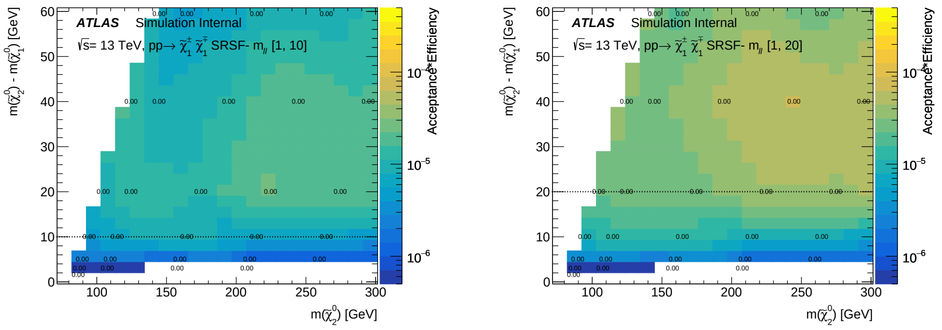

(c) $SR\ell\ell - m_{\ell\ell}[1,10]$ (d) $SR\ell\ell - m_{\ell\ell}[1,20]$

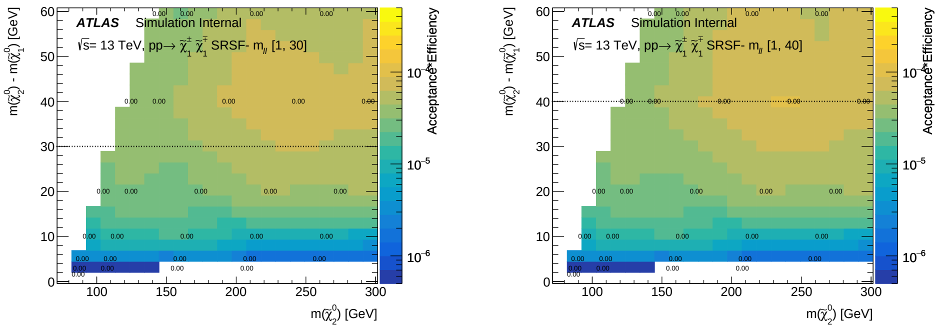

(e) $SR\ell\ell - m_{\ell\ell}[1,30]$ (f) $SR\ell\ell - m_{\ell\ell}[1,40]$

Figure A.25: **C1C1 Acceptance*Efficiency**.

Appendix B

Trial invisible mass m_χ in $m_{\mathbf{T2}}^{m_\chi}$

This appendix studies the impact of varying the trial invisible mass m_χ of the $m_{\mathrm{T2}}^{m_\chi}$ variable, which is relevant for the shape fit to slepton signals.

Ideally, the m_χ value is chosen to match the LSP mass $m(\tilde{\chi}_1^0)$ of the underlying signal. A notable shape in the signal with a kinematic endpoint at the slepton mass can be used to distinguish signal from SM backgrounds. The technical implementation would then involve a two-dimensional shape fit binned both in m_χ and $m_{\mathrm{T2}}^{m_\chi}$, allowing a robust proxy of the LSP and slepton masses. Therefore, both the mass scale and difference of the signal can be exploited to increase search sensitivity and for post-discovery mass measurement.

This analysis uses a one-dimensional shape fit binned in $m_{\mathrm{T2}}^{m_\chi}$ for one value of m_χ. The nominal value chosen for this analysis is $m_\chi = 100$ GeV. The trial invisible mass m_χ is varied between $m_\chi = 0$ to $m_\chi = 300$ GeV, and these distributions are displayed in Figures B.1 to B.11. For simplicity and the purpose of these figures, a fixed

$E_{\mathrm{T}}^{\mathrm{miss}}/H_{\mathrm{T}}^{\mathrm{leptons}} > 5$ selection is used for the signal rewgion SRSF-MT2.

The CR-top (upper left) constructed by requiring $N_{\text{b-jets}}^{20} \geq 1$ and CR-VV (lower left) constructed by requiring $E_{\mathrm{T}}^{\mathrm{miss}}/H_{\mathrm{T}}^{\mathrm{leptons}} < 5$ control regions are used to verify reasonable modelling of backgrounds. The distributions of the slepton signal and backgrounds in a signal region denoted SRSF-MT2 are displayed for various m_χ. For the SR distributions, two classes of signals are displayed:

- In the lower left figures, the LSP mass is fixed $m(\tilde{\chi}_1^0) = 100$ GeV while the slepton–LSP mass splittings are varied $\Delta M = [2, 5, 10, 20]$ GeV.
- In the lower right figures, the slepton–LSP mass splitting is fixed to $\Delta M = 10$ GeV, while the LSP masses are varied $m(\tilde{\chi}_1^0) = [90, 120, 140, 180]$ GeV.

There are three cases of interest for discussion:

- $m_\chi \sim m(\tilde{\chi}_1^0)$: trial invisible mass m_χ *matches* underlying signal LSP $m(\tilde{\chi}_1^0)$. The signal has a kinematic endpoint at the slepton mass and a prominent shape compared to the broad background distributions.
- $m_\chi < m(\tilde{\chi}_1^0)$: trial invisible mass m_χ *underestimates* underlying signal LSP $m(\tilde{\chi}_1^0)$. The signal loses much of its shape, with a broad distribution. The backgrounds also broaden significantly with increasing underestimation.
- $m_\chi > m(\tilde{\chi}_1^0)$: trial invisible mass m_χ *overestimates* underlying signal LSP $m(\tilde{\chi}_1^0)$. The signal distributions tend to broaden, though more slowly with respect to changes in m_χ compared to the underestimation case. The backgrounds also

increasingly occupy lower values of $m_{\mathrm{T2}}^{m_\chi}$. However, these distributions do not account for the rejection of these backgrounds from the $m_{\mathrm{T2}}^{m_\chi}$ dependent $E_{\mathrm{T}}^{\mathrm{miss}}/H_{\mathrm{T}}^{\mathrm{leptons}}$ cut employed in the main analysis such as

$$E_{\mathrm{T}}^{\mathrm{miss}}/H_{\mathrm{T}}^{\mathrm{leptons}} > \max\left(5.0, 15 - 2 \cdot \left[m_{\mathrm{T2}}^{m_\chi}/\ \mathrm{GeV} - m_\chi\right]\right). \tag{B.1}$$

Figures B.12a to B.14 shows the expected sensivity when considering the full shape fit to various m_χ. The sensitivity for larger mass splittings is noticeably reduced when low values of $m_\chi = 0$ and 50 GeV are chosen. The stability of the contour for m_χ around 100 GeV and above is notable. Note that in these figures, the selection

$$E_{\mathrm{T}}^{\mathrm{miss}}/H_{\mathrm{T}}^{\mathrm{leptons}} > \max\left(5.0, 15 - 2 \cdot \left[m_{\mathrm{T2}}^{m_\chi}/\ \mathrm{GeV} - m_\chi\right]\right). \tag{B.2}$$

is allowed to vary dynamically with the mass splitting reconstructed from $m_{\mathrm{T2}}^{m_\chi}$.

Overall, choosing $m_\chi = 100$ is reasonably optimal to ensure stability of the signal shape for higher LSP masses this analysis expects sensitivity.

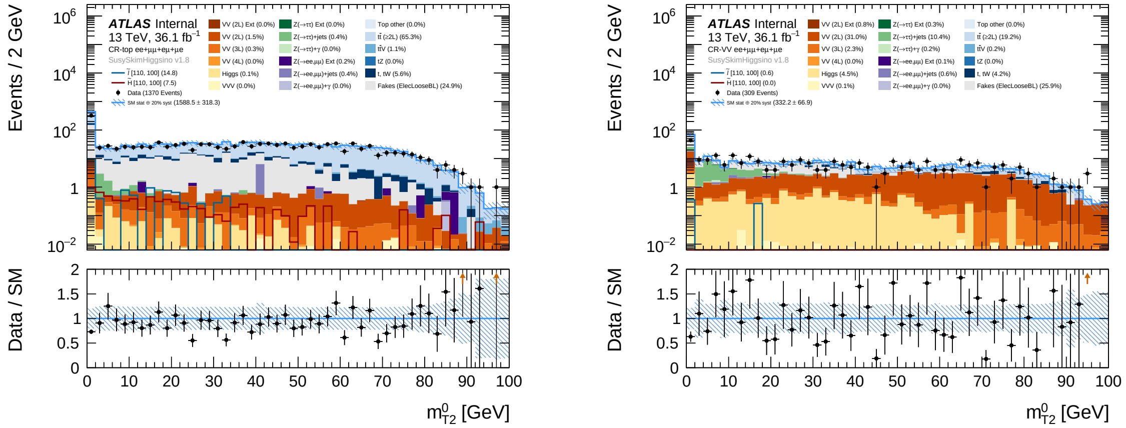

(a) CR-top $ee + \mu\mu + e\mu + \mu e$ (b) CR-VV $ee + \mu\mu + e\mu + \mu e$

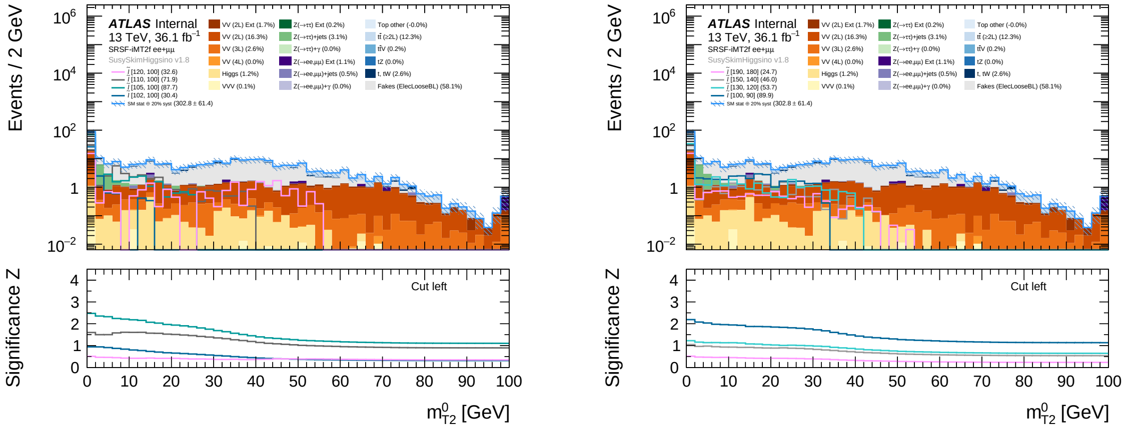

(c) SRSF-MT2, vary ΔM (d) SRSF-MT2, vary $m(\tilde{\chi}_1^0)$

Figure B.1: m^0_{T2}. Using $E_{\mathrm{T}}^{\mathrm{miss}}/H_{\mathrm{T}}^{\mathrm{leptons}} > 5$.

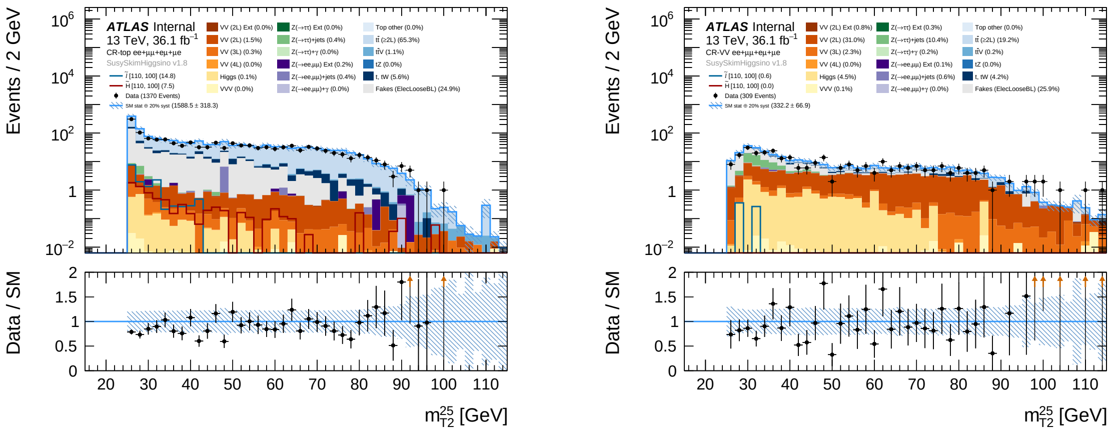

(a) CR-top $ee + \mu\mu + e\mu + \mu e$

(b) CR-VV $ee + \mu\mu + e\mu + \mu e$

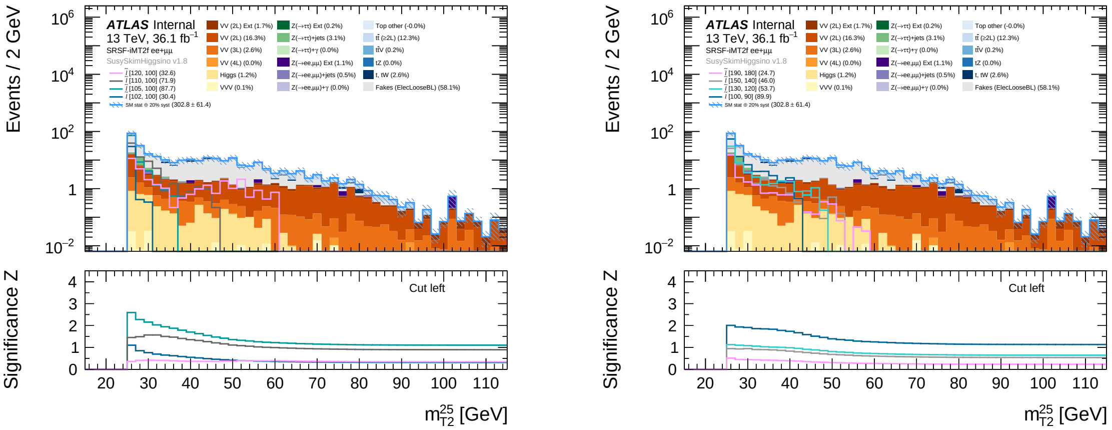

(c) SRSF-MT2, vary ΔM

(d) SRSF-MT2, vary $m(\tilde{\chi}_1^0)$

Figure B.2: m_{T2}^{25}. Using $E_{\mathrm{T}}^{\mathrm{miss}}/H_{\mathrm{T}}^{\mathrm{leptons}} > 5$.

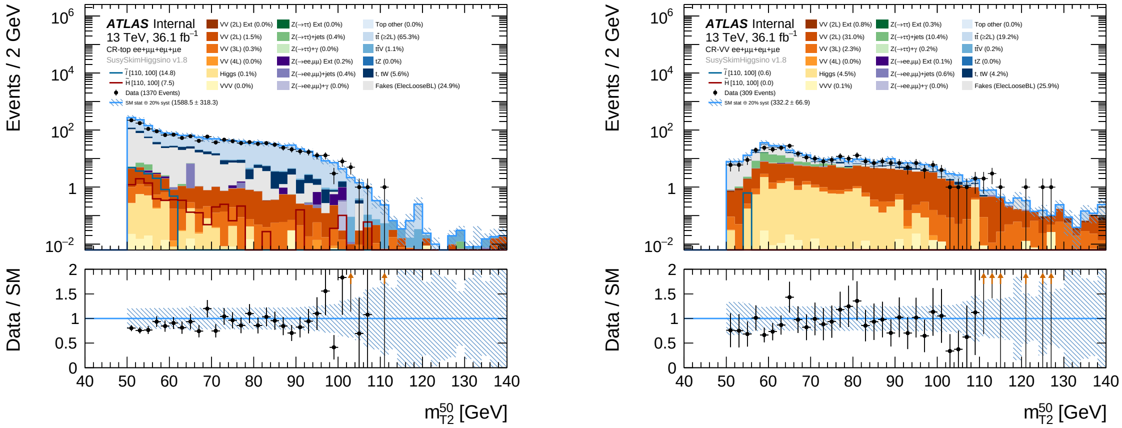

(a) CR-top $ee + \mu\mu + e\mu + \mu e$

(b) CR-VV $ee + \mu\mu + e\mu + \mu e$

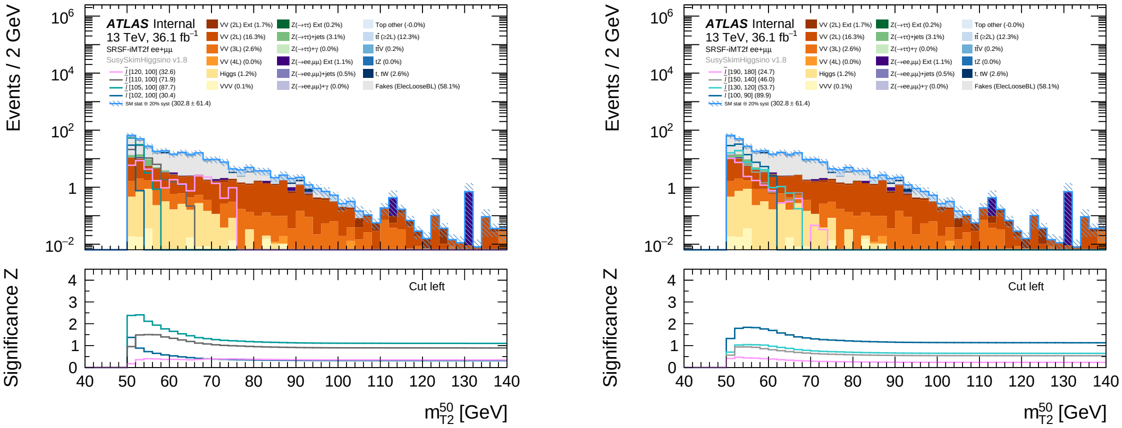

(c) SRSF-MT2, vary ΔM

(d) SRSF-MT2, vary $m(\tilde{\chi}_1^0)$

Figure B.3: m_{T2}^{50}. Using $E_{\mathrm{T}}^{\mathrm{miss}}/H_{\mathrm{T}}^{\mathrm{leptons}} > 5$.

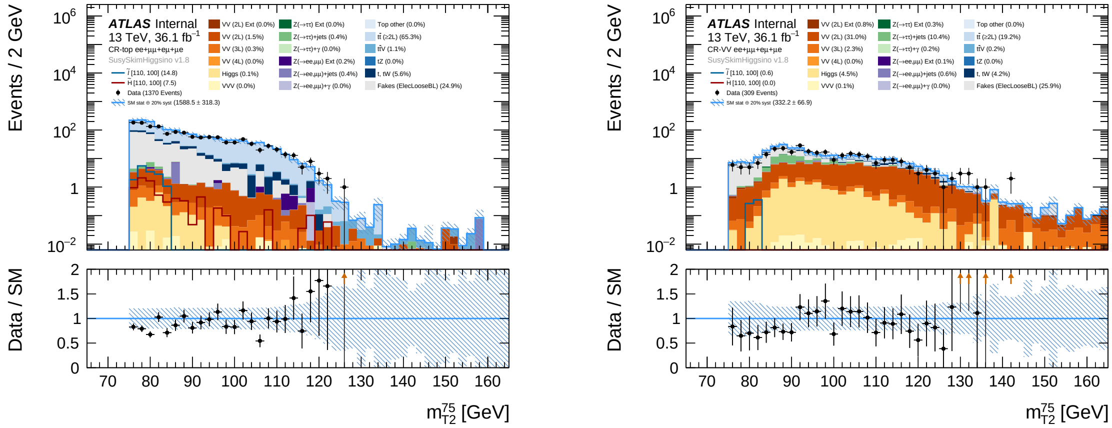

(a) CR-top $ee + \mu\mu + e\mu + \mu e$

(b) CR-VV $ee + \mu\mu + e\mu + \mu e$

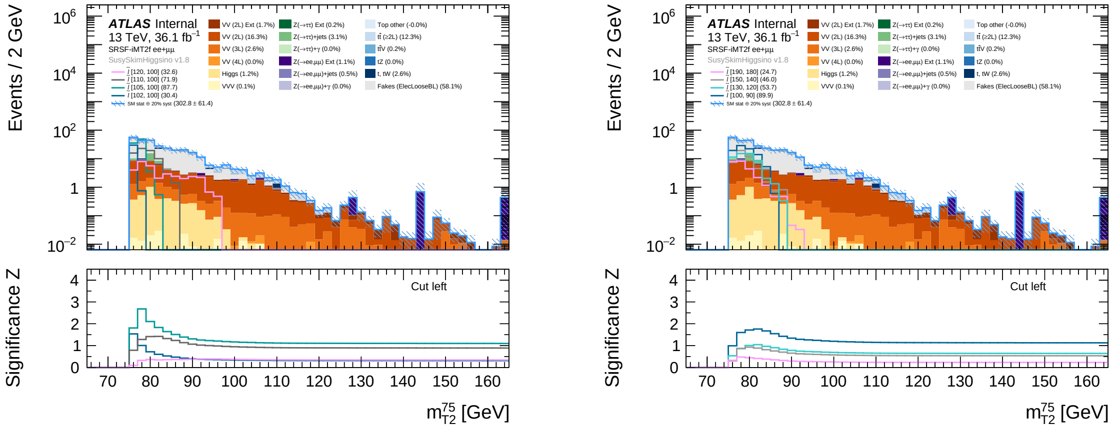

(c) SRSF-MT2, vary ΔM

(d) SRSF-MT2, vary $m(\tilde{\chi}_1^0)$

Figure B.4: m_{T2}^{75}. Using $E_{\mathrm{T}}^{\mathrm{miss}}/H_{\mathrm{T}}^{\mathrm{leptons}} > 5$.

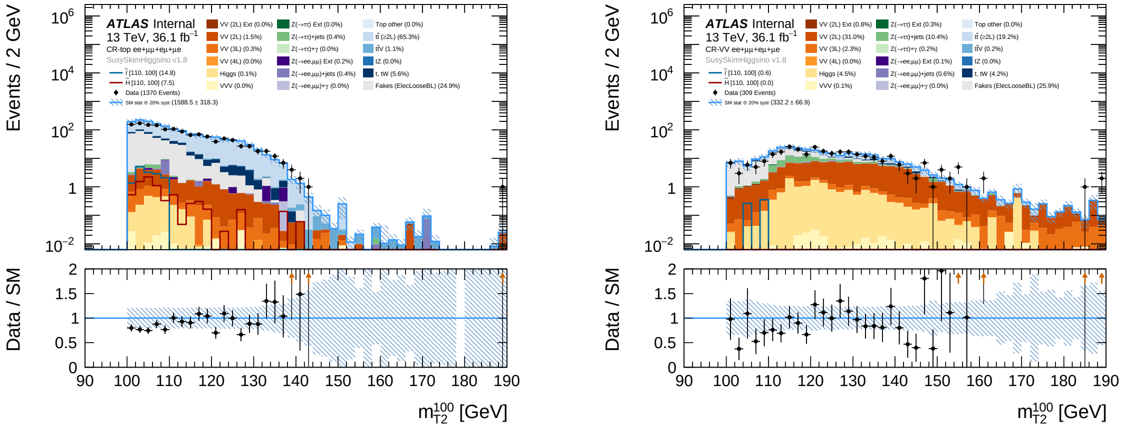

(a) CR-top $ee + \mu\mu + e\mu + \mu e$ (b) CR-VV $ee + \mu\mu + e\mu + \mu e$

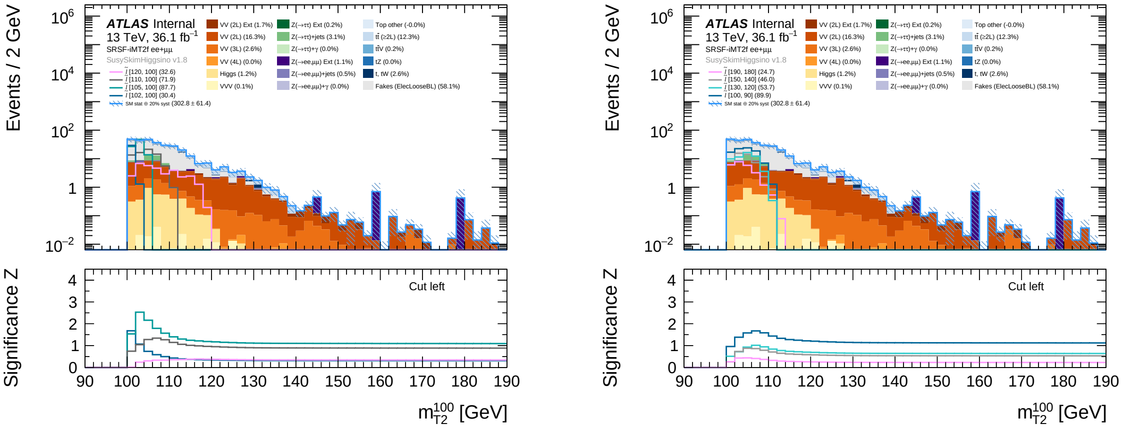

(c) SRSF-MT2, vary ΔM (d) SRSF-MT2, vary $m(\tilde{\chi}_1^0)$

Figure B.5: m_{T2}^{100}. Using $E_{\mathrm{T}}^{\mathrm{miss}}/H_{\mathrm{T}}^{\mathrm{leptons}} > 5$.

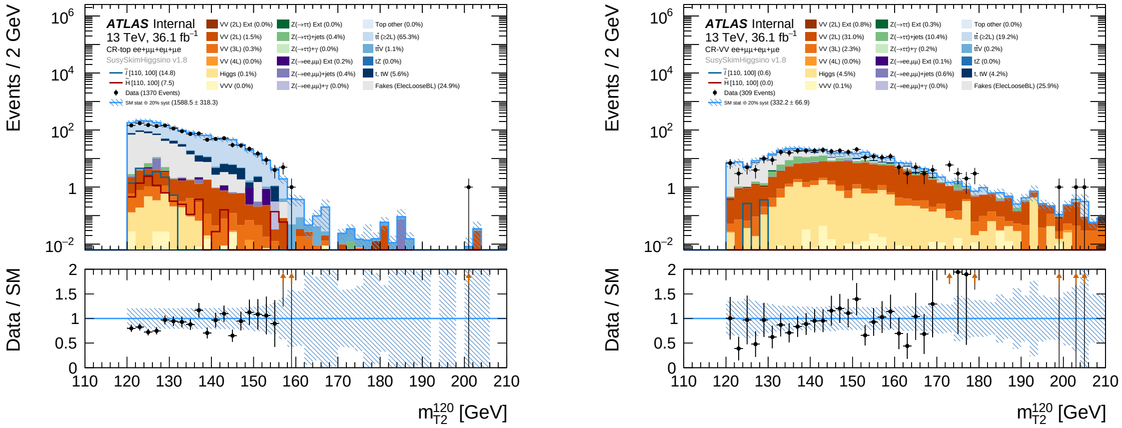

(a) CR-top $ee + \mu\mu + e\mu + \mu e$

(b) CR-VV $ee + \mu\mu + e\mu + \mu e$

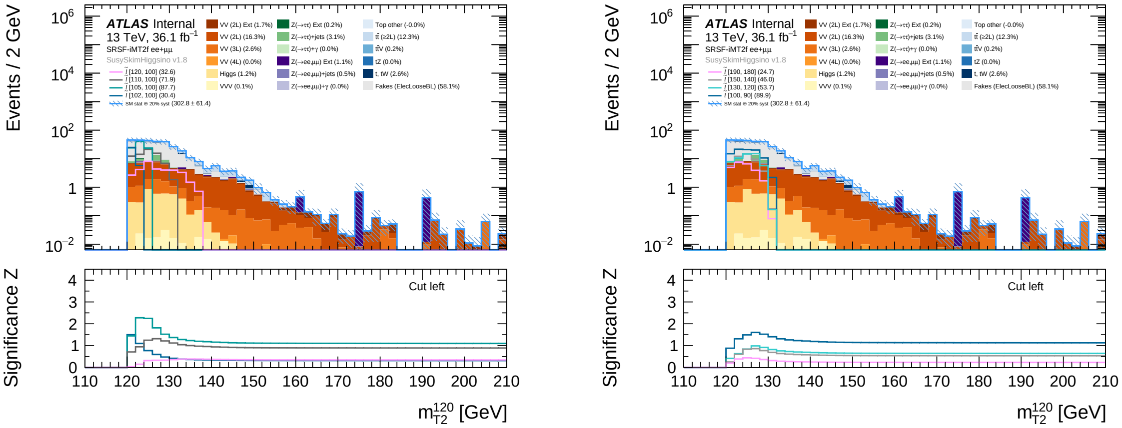

(c) SRSF-MT2, vary ΔM

(d) SRSF-MT2, vary $m(\tilde{\chi}_1^0)$

Figure B.6: m_{T2}^{120}. Using $E_{\mathrm{T}}^{\mathrm{miss}}/H_{\mathrm{T}}^{\mathrm{leptons}} > 5$.

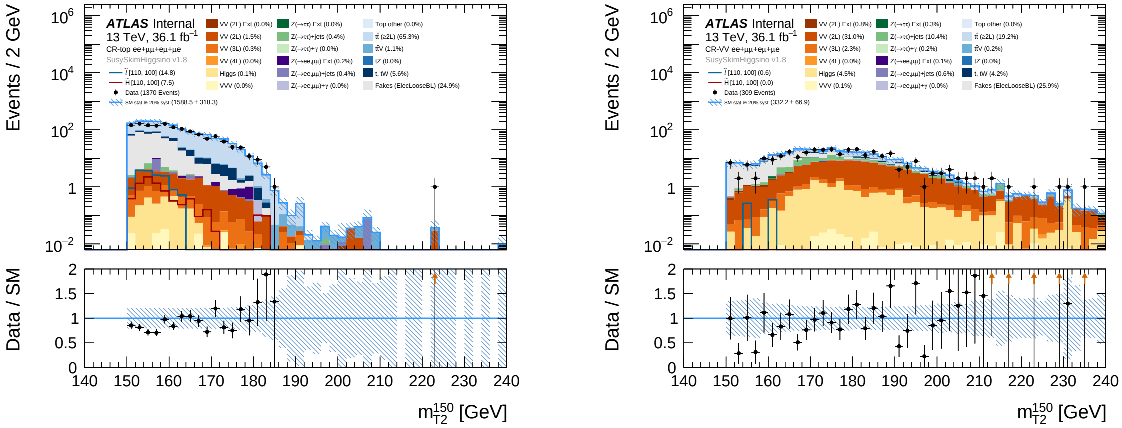

(a) CR-top $ee + \mu\mu + e\mu + \mu e$

(b) CR-VV $ee + \mu\mu + e\mu + \mu e$

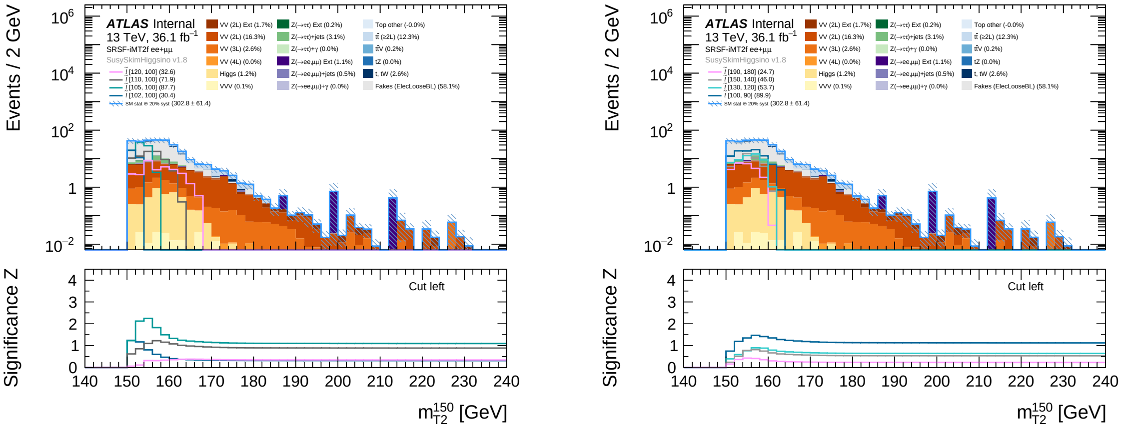

(c) SRSF-MT2, vary ΔM

(d) SRSF-MT2, vary $m(\tilde{\chi}_1^0)$

Figure B.7: m_{T2}^{150}. Using $E_{\mathrm{T}}^{\mathrm{miss}}/H_{\mathrm{T}}^{\mathrm{leptons}} > 5$.

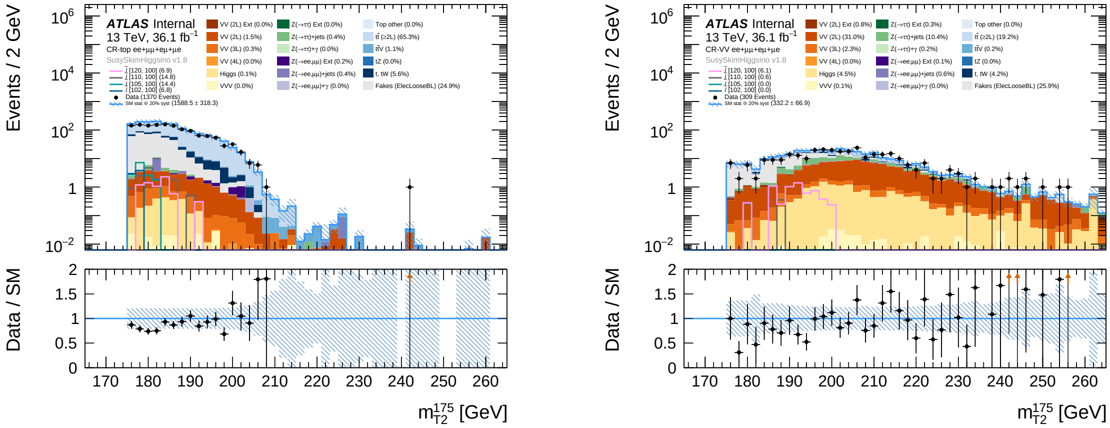

(a) CR-top $ee + \mu\mu + e\mu + \mu e$

(b) CR-VV $ee + \mu\mu + e\mu + \mu e$

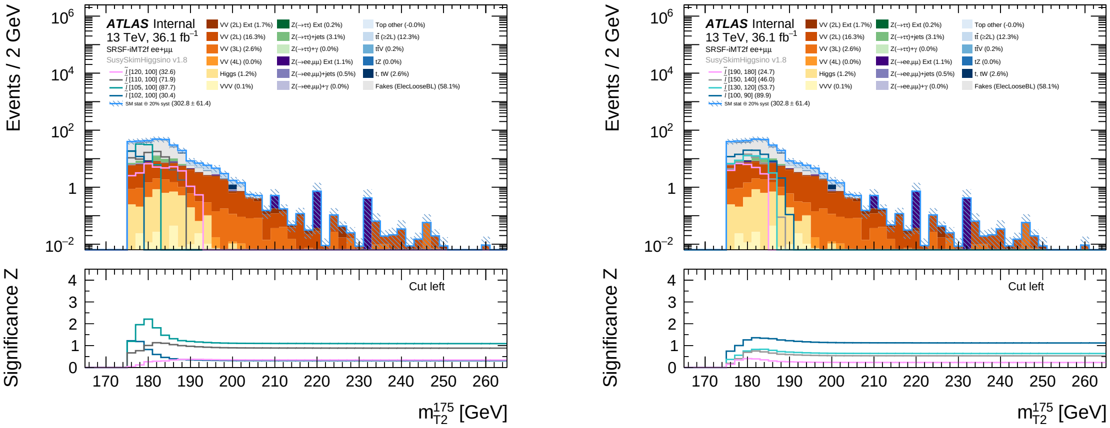

(c) SRSF-MT2, vary ΔM

(d) SRSF-MT2, vary $m(\tilde{\chi}_1^0)$

Figure B.8: m_{T2}^{175}. Using $E_{\mathrm{T}}^{\mathrm{miss}}/H_{\mathrm{T}}^{\mathrm{leptons}} > 5$.

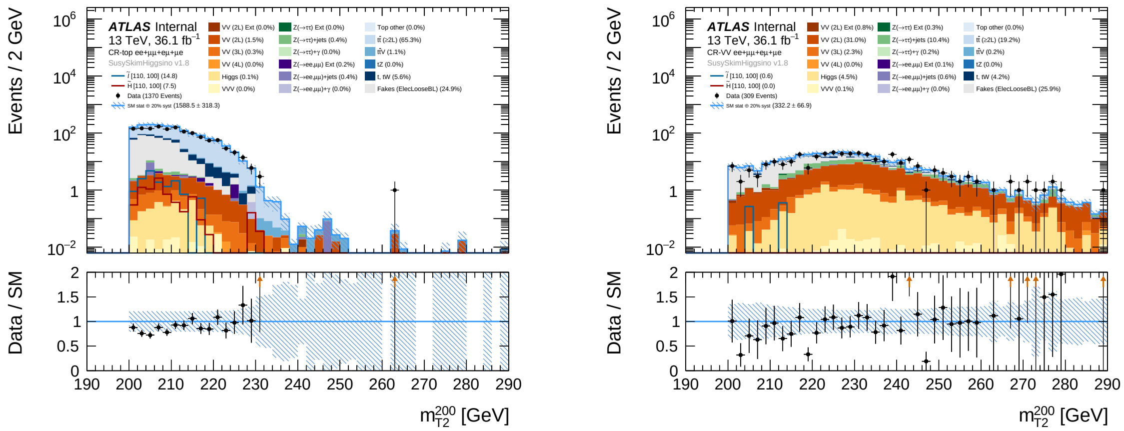

(a) CR-top $ee + \mu\mu + e\mu + \mu e$

(b) CR-VV $ee + \mu\mu + e\mu + \mu e$

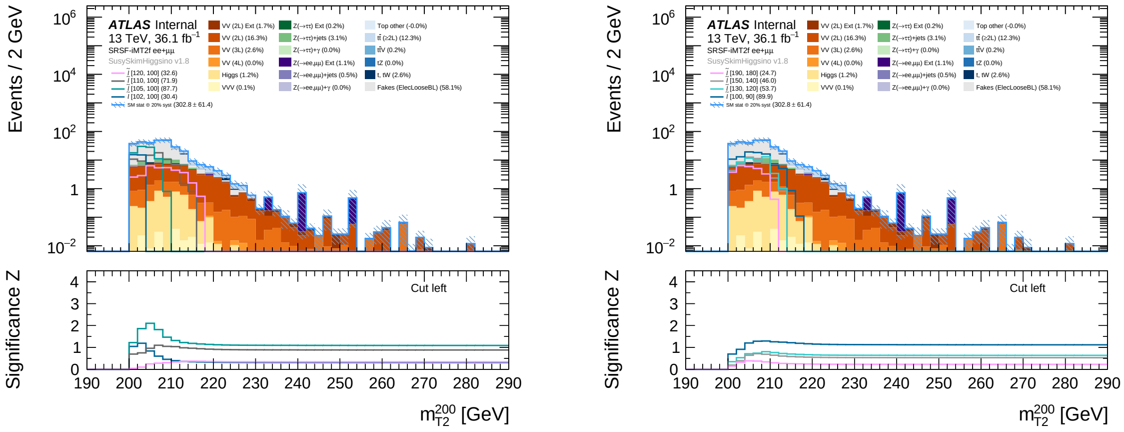

(c) SRSF-MT2, vary ΔM

(d) SRSF-MT2, vary $m(\tilde{\chi}_1^0)$

Figure B.9: m_{T2}^{200}. Using $E_{\mathrm{T}}^{\mathrm{miss}}/H_{\mathrm{T}}^{\mathrm{leptons}} > 5$.

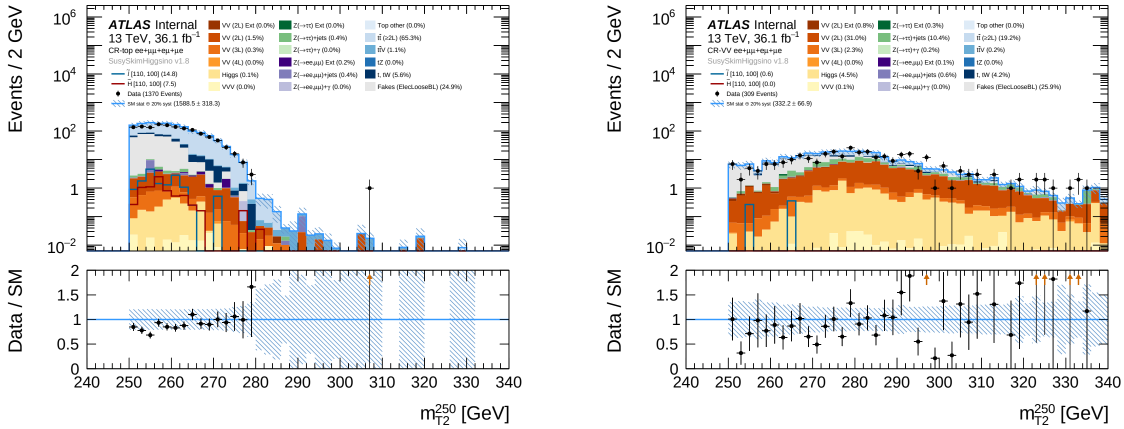

(a) CR-top $ee + \mu\mu + e\mu + \mu e$

(b) CR-VV $ee + \mu\mu + e\mu + \mu e$

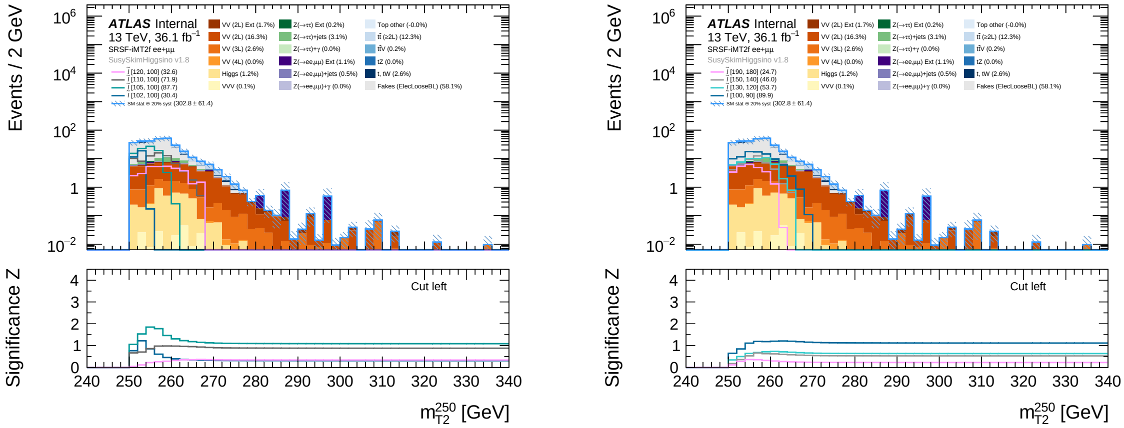

(c) SRSF-MT2, vary ΔM

(d) SRSF-MT2, vary $m(\tilde{\chi}_1^0)$

Figure B.10: m_{T2}^{250}. Using $E_{\mathrm{T}}^{\mathrm{miss}}/H_{\mathrm{T}}^{\mathrm{leptons}} > 5$.

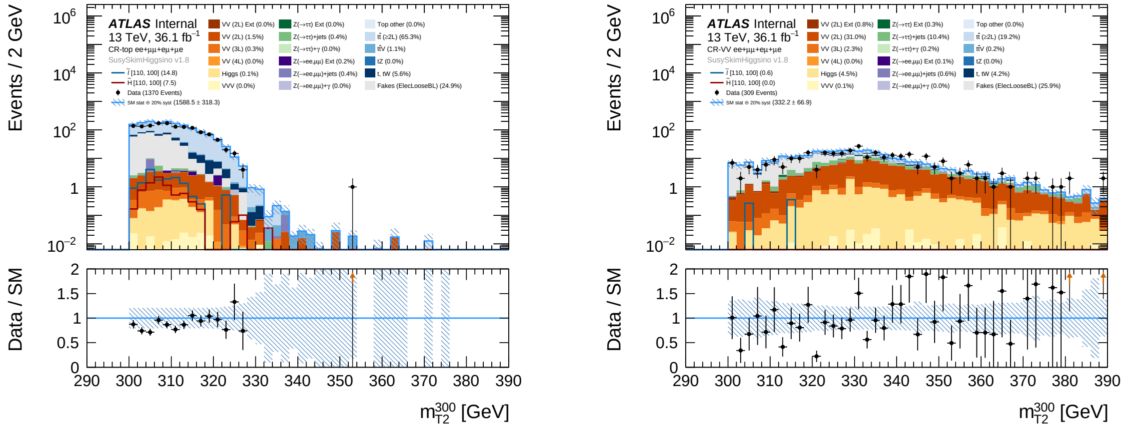

(a) CR-top $ee + \mu\mu + e\mu + \mu e$

(b) CR-VV $ee + \mu\mu + e\mu + \mu e$

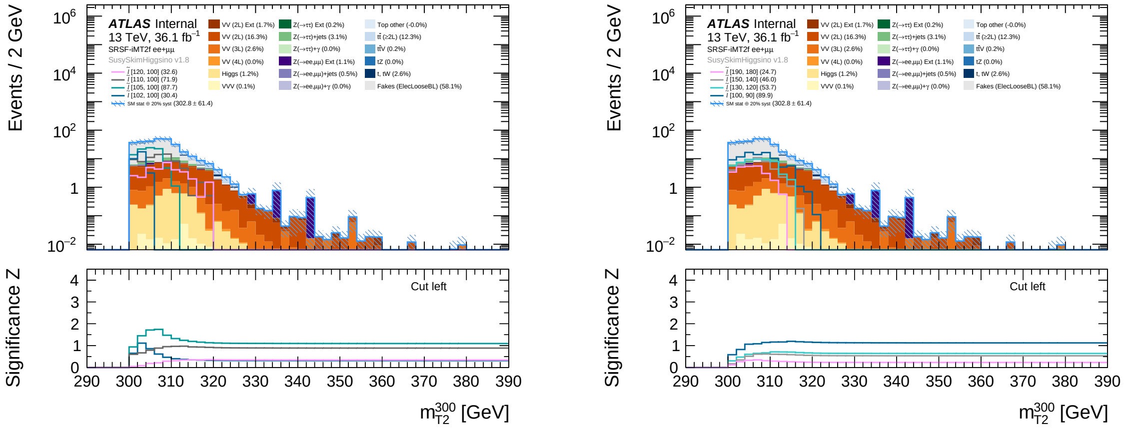

(c) SRSF-MT2, vary ΔM

(d) SRSF-MT2, vary $m(\tilde{\chi}_1^0)$

Figure B.11: m_{T2}^{300}. Using $E_{\mathrm{T}}^{\mathrm{miss}}/H_{\mathrm{T}}^{\mathrm{leptons}} > 5$.

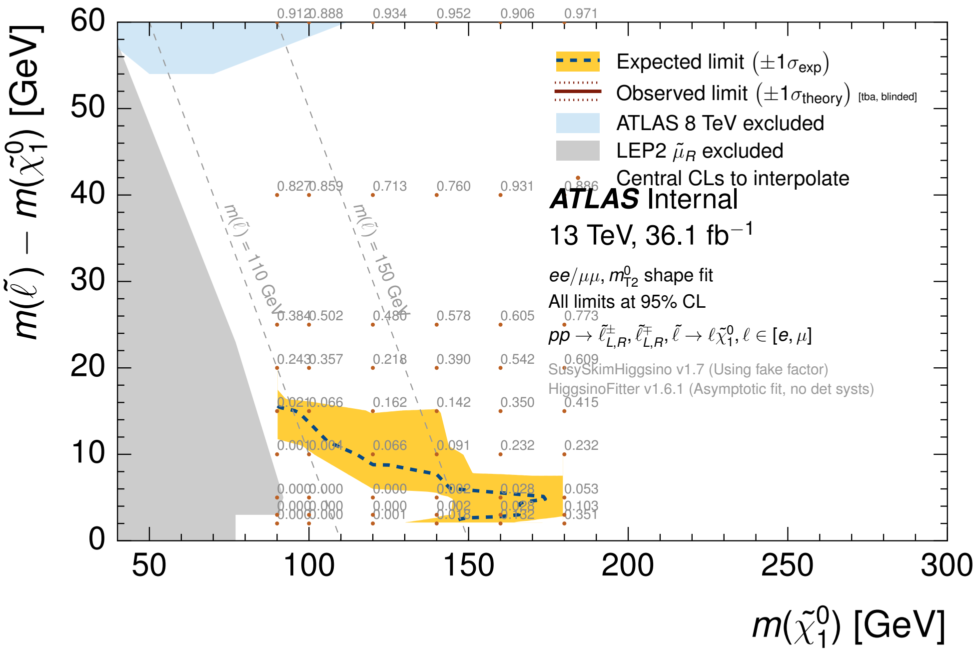

(a) m_{T2}^{0} shape fit. Using $E_{\mathrm{T}}^{\mathrm{miss}}/H_{\mathrm{T}}^{\mathrm{leptons}} > \mathrm{Max}\left(5, 15 - m_{\mathrm{T2}}^{0}/\ \mathrm{GeV}\right)$.

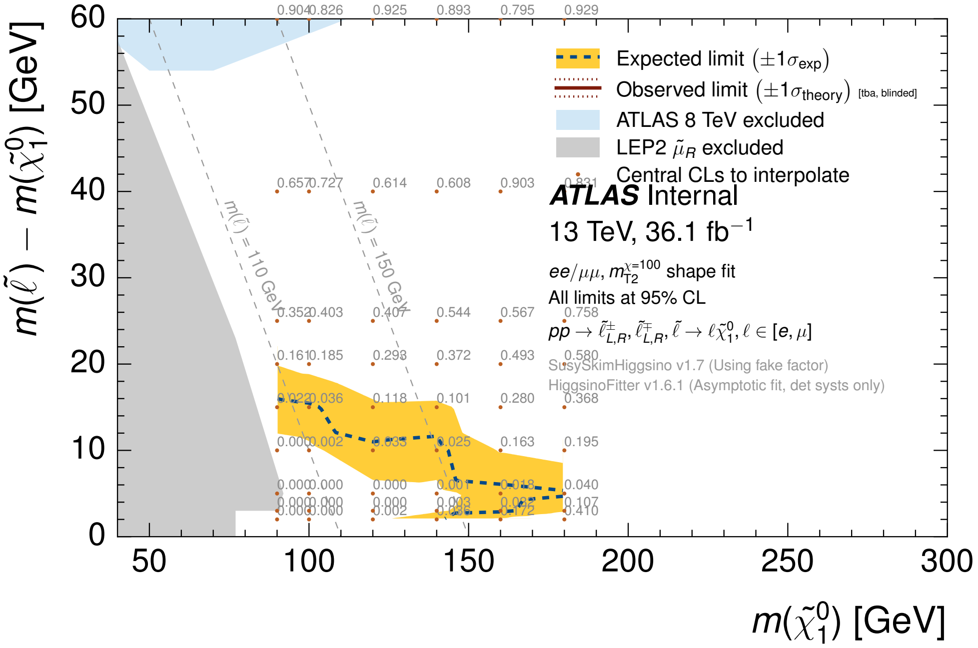

(b) m_{T2}^{50} shape fit. Using $E_{\mathrm{T}}^{\mathrm{miss}}/H_{\mathrm{T}}^{\mathrm{leptons}} > \mathrm{Max}\left(5, 15 - 2 \cdot \left[m_{\mathrm{T2}}^{50}/\ \mathrm{GeV} - 50\right]\right)$.

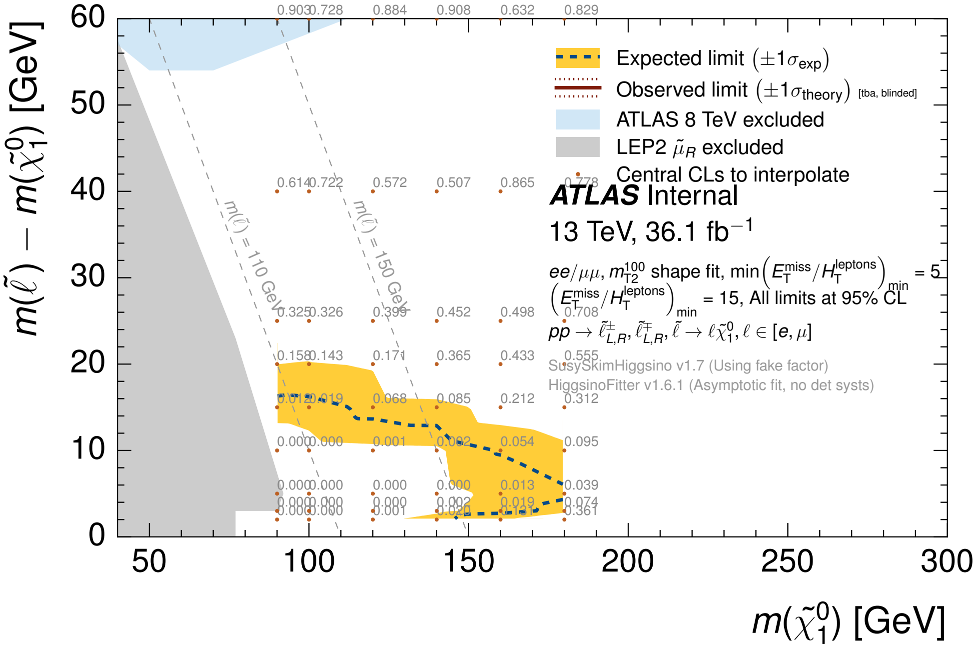

(a) m_{T2}^{100} shape fit. Using $E_{\mathrm{T}}^{\mathrm{miss}}/H_{\mathrm{T}}^{\mathrm{leptons}} > \mathrm{Max}\left(5, 15 - 2 \cdot \left[m_{\mathrm{T2}}^{100}/\ \mathrm{GeV} - 100\right]\right)$.

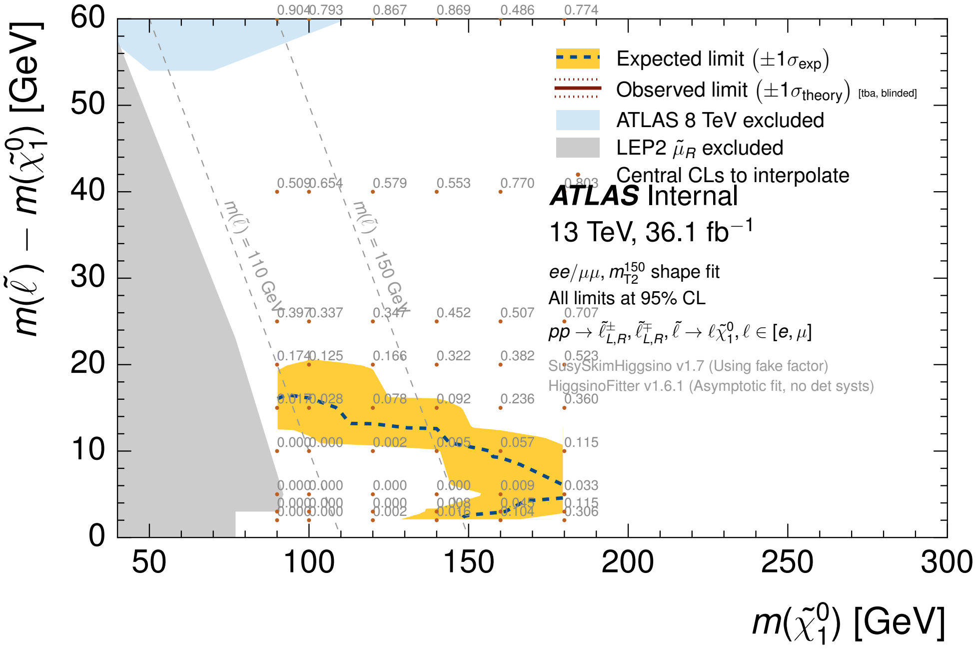

(b) m_{T2}^{150} shape fit. Using $E_{\mathrm{T}}^{\mathrm{miss}}/H_{\mathrm{T}}^{\mathrm{leptons}} > \mathrm{Max}\left(5, 15 - 2 \cdot \left[m_{\mathrm{T2}}^{150}/\ \mathrm{GeV} - 150\right]\right)$.

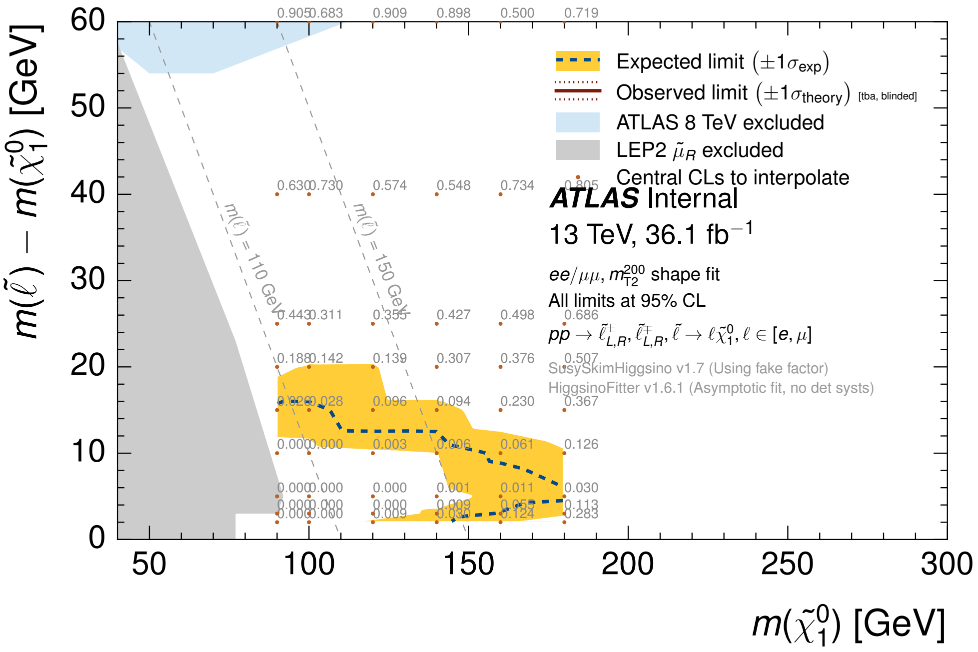

Figure B.14: m_{T2}^{200} shape fit. Using $E_{\mathrm{T}}^{\mathrm{miss}}/H_{\mathrm{T}}^{\mathrm{leptons}} > \mathrm{Max}\left(5, 15 - 2 \cdot \left[m_{\mathrm{T2}}^{200}/\ \mathrm{GeV} - 200\right]\right)$.